

NASA Conference Publication 2256

Space Photovoltaic Research and Technology 1982

***High Efficiency, Radiation Damage,
and Blanket Technology***

*Proceedings of a conference
held at NASA Lewis Research Center
Cleveland, Ohio
April 20-22, 1982*

NASA

NASA Conference Publication 2256

Space Photovoltaic Research and Technology 1982

*High Efficiency, Radiation Damage,
and Blanket Technology*

*Proceedings of a conference
held at NASA Lewis Research Center
Cleveland, Ohio
April 20-22, 1982*

NASA

National Aeronautics
and Space Administration

Scientific and Technical
Information Office

1982

FOREWORD

As has been repeated many times, the solar cell has been an indispensable element of the U.S. space program. The development of the silicon solar cell into an efficient, reliable, and commercially available device has made our many accomplishments in space possible. Not only has the silicon cell been the workhorse power source for satellites, it is now also a leading candidate for generating solar-electric power on the ground. Looking to the future, to the proposed space platform, one sees that the job of photovoltaic power generation is far from over and that the need for high efficiency, long lived, inexpensive photovoltaic devices is stronger than ever.

This meeting, the fifth of its kind, was intended to be a direction-setting forum where each invited expert was expected to express his or her judgement to (1) help set suitable goals for space solar cell research and development, (2) define the barriers preventing the attainment of these goals, and (3) bring to the surface the most viable approaches to overcome these obstacles.

This was a working meeting where strong emphasis was placed on the exchange and discussion of ideas and opinions against a background of technical presentations. The atmosphere was informal, yet structured, and individual interaction was encouraged.

The discussions at this meeting, as in the past, were focused on five areas. These areas and the individuals who generally accepted the responsibility of managing them are

Silicon research and technology, Andrew Meulenbeerg, COMSAT Laboratories
Advanced devices, Peter Borden, Varian Associates
Gallium arsenide solar cells, Edmund Conway, NASA Langley
Radiation damage, Irving Weinberg, NASA Lewis
Blanket technology, John Scott-Monck, Jet Propulsion Laboratory

An oral report from workshops in each of these areas was presented and discussed in a plenary session. Written summaries of the workshop conclusions prepared by the workshop chairmen are included in these proceedings.

The coordinated efforts of Victor Weizer, Cosmo Baraona, George Mazaris, and Shirley Livingston were responsible for the successful organization and conduct of this meeting.

Henry Brandhorst
NASA Lewis Research Center

Conference chairman

CONTENTS

FOREWORD	iii
NASA-OAST PROGRAM IN PHOTOVOLTAIC ENERGY CONVERSION Jerome P. Mullin and Dennis J. Flood, National Aeronautics and Space Administration	1
NEW SILICON CELL DESIGN CONCEPTS FOR >20 PERCENT AM1 EFFICIENCY M. Wolf, University of Pennsylvania	5
SURFACE EFFECTS IN HIGH-VOLTAGE SILICON SOLAR CELLS A. Meulenbergh, Jr., and R.A. Arndt, COMSAT Laboratories	13
RECENT DEVELOPMENTS IN THIN SILICON SOLAR CELLS F. Ho and P. Iles, Applied Solar Energy Corporation	17
LARGE AREA SPACE SOLAR CELL ASSEMBLIES M.B. Spitzer and M.J. Nowlan, Spire Corporation	25
SIMULATED SPACE FLIGHT TESTING OF COMMERCIAL TERRESTRIAL SILICON CELLS Paul M. Stella and Tetsuo F. Miyahira, Jet Propulsion Laboratory.	37
DIFFUSION LENGTH MEASUREMENTS IN SOLAR CELLS - AN ANALYSIS AND COMPARISON OF TECHNIQUES John A. Woollam, A. Azim Khan, and R.J. Soukup, University of Nebraska, and Allen M. Hermann, Solar Energy Research Institute	45
PROGRESS TOWARD CASCADE CELLS MADE BY OM-VPE Peter G. Borden, Ross A. LaRue, and Michael J. Ludowise, Varian Associates, Inc.	57
PRESENT STATUS OF AIR FORCE AlGaAs/GaAs CASCADE CELL PROGRAM W.P. Rahilly, Air Force Wright Aeronautical Laboratory.	67
DETERMINATION OF OPTIMUM SUNLIGHT CONCENTRATION LEVEL IN SPACE FOR III-V CASCADE CELLS Henry B. Curtis, NASA Lewis Research Center	69
SOLAR ENERGY CONVERSION USING SURFACE PLASMONS FOR BROADBAND ENERGY TRANSPORT Lynn Marie Anderson, NASA Lewis Research Center	79
STUDY OF GaAs DAMAGE COEFFICIENTS H.S. Rauschenbach, T.R. Simpson, R. Parthasarathy, and M. Taher-Zadeh, TRW Space and Technology Group.	89
CURRENT STATUS OF THIN-FILM CLEFT GaAs SOLAR CELLS John C.C. Fan, Carl O. Bozler, and Robert W. McClelland, Massachusetts Institute of Technology	91
AIR FORCE DEVELOPMENT OF THIN GaAs SOLAR CELLS Ken Masloski, Air Force Wright Aeronautical Laboratories.	93

PROGRESS TOWARD THIN-FILM GaAs SOLAR CELLS USING A SINGLE-CRYSTAL Si SUBSTRATE WITH A Ge INTERLAYER Y.C.M. Yeh, K.L. Wang, and S. Zwerdling, Jet Propulsion Laboratory.	99
DIFFUSED P ⁺ -N SOLAR CELLS IN BULK GaAs J.M. Borrego and S.K. Ghandhi, Rensselaer Polytechnic Institute . . .	105
ADVANCES IN LARGE-DIAMETER LIQUID ENCAPSULATED CZOCHRALSKI GaAs R.T. Chen, D.E. Holmes, and C.G. Kirkpatrick, Rockwell International	109
GaAs SOLAR CELLS FOR CONCENTRATOR SYSTEMS IN SPACE R.Y. Loo, R.C. Knechtli, and G.S. Kamath, Hughes Research Laboratories.	123
THE EFFECT OF DIFFERENT SOLAR SIMULATORS ON THE MEASUREMENT OF SHORT- CIRCUIT CURRENT TEMPERATURE COEFFICIENTS Henry B. Curtis and R.E. Hart, Jr., NASA Lewis Research Center . . .	131
DEFECTS AND ANNEALING STUDIES IN 1-MeV ELECTRON IRRADIATED (AlGa)As-GaAs SOLAR CELLS Sheng S. Li W.L. Wang, University of Florida, R.Y. Loo, Hughes Research Laboratories, and W.P. Rahilly, Air Force Aeropropulsion Laboratory.	137
DEFECT BEHAVIOR IN ELECTRON-IRRADIATED BORON- AND GALLIUM-DOPED SILICON Peter J. Drevinsky and Henry M. DeAngelis, Hanscom Air Force Base . .	145
COLD CRUCIBLE CZOCHRALSKI FOR SOLAR CELLS Terry M. Trumble, Air Force Wright Aeronautical Laboratories.	157
MICRODISTRIBUTION OF OXYGEN IN SILICON AND ITS EFFECTS ON ELECTRONIC PROPERTIES H.C. Gatos, B.-Y. Mao, K. Nauka, and J. Lagowski, Massachusetts Institute of Technology	163
EFFECTS OF INJECTION CHARGE DISTRIBUTION ON THE PERFORMANCE OF RADIATION DAMAGED, HIGH RESISTIVITY CELLS I. Weinberg, NASA Lewis Research Center, C. Goradia, Cleveland State University, and C.K. Swartz, NASA Lewis Research Center	171
RADIATION DAMAGE AND ANNEALING IN LARGE AREA n ⁺ /p/p ⁺ GaAs SHALLOW HOMOJUNCTION SOLAR CELLS D.J. Flood, D.J. Brinker, C.K. Swartz, and R.E. Hart, Jr., NASA Lewis Research Center, and John C.C. Fan, Lincoln Laboratory.	179
BASIS FOR EQUIVALENT FLUENCE CONCEPT IN SPACE SOLAR CELLS A. Meulenbergh, COMSAT Laboratories.	185
GROWN-IN DEFECTS AND DEFECTS PRODUCED BY 1-MeV ELECTRON IRRADIATION IN Al _{0.3} Ga _{0.7} As P-N JUNCTION SOLAR CELLS Sheng S. Li, K.W. Teng, D.W. Schoenfeld, University of Florida, and W.P. Rahilly, Air Force Aeropropulsion Laboratory	195

PROGRESS IN DEVELOPING HIGH PERFORMANCE SOLAR BLANKETS AND ARRAYS John Scott-Monck, Jet Propulsion Labotatory	201
MINIATURIZED CASSEGRAINIAN CONCENTRATOR CONCEPT DEMONSTRATION R.E. Patterson and H.S. Rauschenbach, TRW Space and Technology Group.	211
THE COURSE OF SOLAR ARRAY WELDING TECHNOLOGY DEVELOPMENT Paul M. Stella, Jet Propulsion Laboratory	223
A PRELIMINARY EVALUATION OF A POTENTIAL SPACE WORTHY ENCAPSULANT John Scott-Monck, Jet Propulsion Laboratory	231
MICROSTRUCTURAL ANALYSIS OF SOLAR CELL WELDS T.J. Moore, G.K. Watson, and C.R. Baraona, NASA Lewis Research Center	237
<u>WORKSHOP REPORTS</u>	
EVALUATION OF SOLAR CELL WELDS BY SCANNING ACOUSTIC MICROSCOPY S.J. Klima, W.E. Frey, and C.R. Baraona, NASA Lewis Research Center.	251
SILICON RESEARCH AND TECHNOLOGY A. Meulenber, COMSAT Laboratories.	259
ADVANCED DEVICES Peter Bordin, Varian Associates	261
GaAs SOLAR CELLS E.J. Conway, NASA Langley Research Center	265
RADIATION DAMAGE I. Weinberg, NASA Lewis Research Center	267
BLANKET TECHNOLOGY John Scott-Monck, Jet Propulsion Laboratory	269

NASA-OAST PROGRAM IN PHOTOVOLTAIC ENERGY CONVERSION

Jerome P. Mullin and Dennis J. Flood
National Aeronautics and Space Administration
Washington, D.C.

ABSTRACT

The NASA program in photovoltaic energy conversion includes research and technology development efforts on solar cells, blankets, and arrays. The overall objectives are to increase conversion efficiency, reduce mass, reduce cost, and increase operating life. The potential growth of space power requirements in the future presents a major challenge to the current state of technology in space photovoltaic systems.

INTRODUCTION

The OAST Office of Space Energy Conversion, formerly Space Power and Electric Propulsion, supports, guides, and directs programs to provide a power technology base that enables and/or enhances current and future activities in space exploration and utilization (figure 1). Within the Office of Space Energy Conversion, the Photovoltaic Energy Conversion program has the specific objective to improve conversion efficiency, reduce mass, reduce cost, and increase the operating life of photovoltaic converters and arrays. The program seeks to do so by developing and applying an improved understanding of photovoltaic energy conversion, and evaluating a broad range of advanced concepts for reducing cost and mass of photovoltaic systems.

PHOTOVOLTAIC ENERGY CONVERSION PROGRAM

Major thrusts of the program fall into three areas: (1) device research and technology; (2) low cost blanket and array technology; and (3) high performance blanket and array technology. Activities in device R&T include fundamental studies of radiation damage and annealing; development of high specific power cells; identification and demonstration of low cost technologies in cell fabrication; research on advanced devices such as the multiple bandgap cascade solar cell and surface plasmon converter; and finally, research on several types of concentrator devices such as spectro- and thermophotovoltaic converters. Low cost blanket and array activities include fundamental studies of solar cell interconnect welding, large area silicon solar cell development and a variety of planar and concentrator array approaches. High performance B&A work is at present focussed on

demonstrating reliable, space-qualifiable lightweight blanket and array technologies using the OAST 2-mil thin silicon cell. As future high performance, ultralight cells are developed, activities in this area are expected to evolve to incorporate them.

TECHNOLOGY CHALLENGES

Figure 2 is a summary of improvements in array specific power achieved over the history of the space program. Advances in array and blanket technology are presently under investigation which have the potential to enable array specific powers in excess of 150 W/Kg in the near term. A second goal within sight is demonstration of critical technology advances needed for 300 W/Kg array technology. Further advances are quite likely in the more distant future.

The trend in array specific cost over the past 20 years is shown in figure 3. It would appear that significant advances in cost-reducing technology must occur if the order of magnitude cost reduction goal is to be reached. The decreases in specific cost observed so far have resulted primarily from increases in array size during that period of time. Based on current estimates of the SEPS array specific cost, the NASA goal appears very ambitious. However, both increases in size and the introduction of new technologies can reasonably be expected to aid the drive toward lower cost. A number of studies have verified this view and the program will continue to explore promising approaches such as the cassegrainian concentrator identified in one such study.

Figure 4 shows the cumulative and annual amounts of photovoltaic power launched by NASA since the early 1960's. With the exception of Skylab, the annual rate has been on the order of 2-4 kilowatts per year, and is not expected to change much until the advent of large space stations, when multi-tens of kilowatt arrays will be required. Following that, it is possible to imagine the routine launch into LEO and other orbits of large arrays for various NASA, commercial, and military applications. Such a scenario presents a major challenge to our current technology base.

SUMMARY

The NASA-OAST program in photovoltaic energy conversion is a well-focussed, yet broadly based program designed to provide technological advances that enhance and/or enable current and future activities in space exploration and utilization. Significant improvements have been achieved in cell performance and in blanket and array specific power and lifetime. Technologies directed at reducing cost for large arrays have been identified; technologies for achieving high performance are currently under investigation. The trend toward high power requirements presents a major challenge to the current status of technology development in space photovoltaics.

SPACE POWER AND ELECTRIC PROPULSION PROGRAM CONTENT

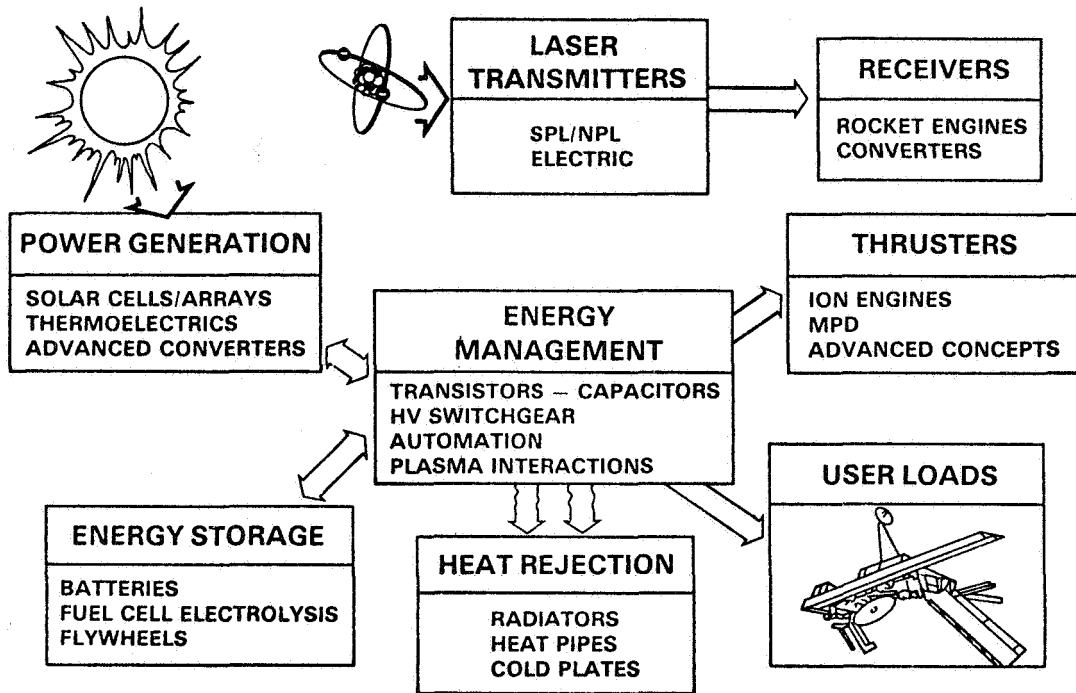


Figure 1

SPECIFIC POWER OF SOLAR ARRAYS

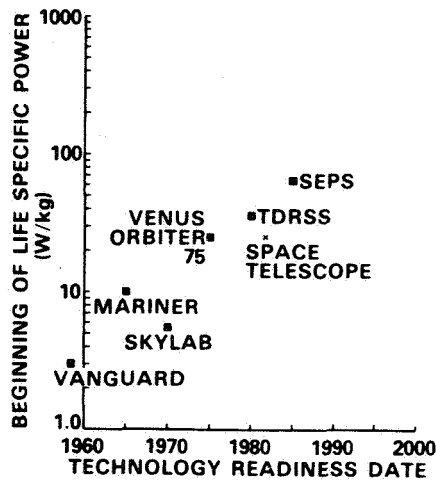


Figure 2

SPECIFIC COST OF SOLAR ARRAYS

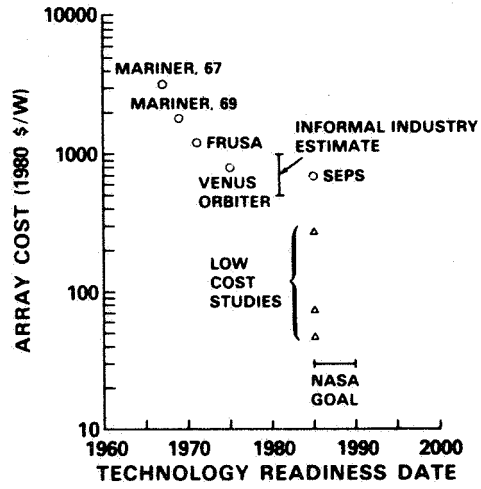


Figure 3

SOLAR POWER LAUNCHED BY NASA

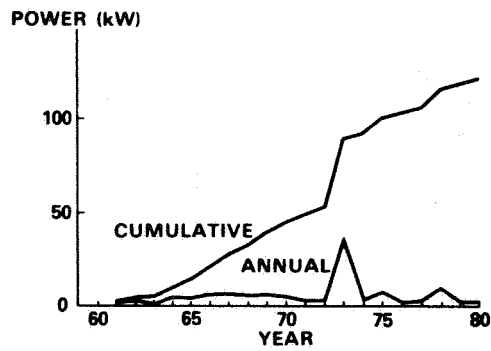


Figure 4

NEW SILICON CELL DESIGN CONCEPTS FOR >20 PERCENT AMI EFFICIENCY

M. Wolf
University of Pennsylvania
Philadelphia, Pennsylvania

SUMMARY

The basic design principles for obtaining high efficiency in silicon solar cells are reviewed. They critically involve very long minority carrier lifetimes, not so much to attain high collection efficiency, but primarily for increased output voltages. Minority carrier lifetime, however, is sensitive to radiation damage, and particularly in low resistivity silicon, on which the high efficiency design is based. Radiation resistant space cells will therefore have to follow differing design principles than high efficiency terrestrial cells.

DESIGN VIEWPOINTS DERIVABLE FROM AN IDEALIZED CELL STRUCTURE

In the simple solar cell structure, which consists only of one layer for each of the three regions (front, depletion, and base region)¹⁾, three light generated current components flow (one each from the three regions), which all need to be maximized for best collection efficiency. In addition, two injection current components flow in forward bias operation (one into the base and one into the front region) which need to be minimized to achieve high output voltages. Optimum performance for terrestrial applications or BOL space service is achieved when the surface recombination velocities both at the front and at the back surfaces are zero (Fig. 1). Then the device design involves a trade-off between light generated and open circuit voltage, to attain maximum power output. This trade-off involves primarily the thickness of the base region. The optimum design also indicates impurity concentrations just at the onset of Auger recombination, equal in both the front and the base regions, when secondary, technology dependent effects, such as series resistance related losses, are dealt with separately.

The consideration of the simple device structure shows that the basic device does not require the properties of an "emitter" for the front region, and that the open circuit voltage monotonously increases with increasing minority carrier lifetime, while the collection efficiency essentially saturates as long recognized²⁾. To gain the highest possible performance, the highest technologically achievable minority carrier lifetime is thus needed.

While, principally, improved open circuit voltages are expected from increasing dopant concentrations, the onset of direct, band-to-band Auger recombination sets a basic limit to this trend,²⁾ (Fig. 2), as does bandgap narrowing³⁾. Thus, an optimum impurity concentration will be reached just before Auger recombination causes a downturn of the power output with a further increase of the impurity concentration. In consequence of this observation, a high efficiency solar cell design should avoid very high doping concentrations at which the heavy doping effects have a significant influence on the device performance. There exist some doubts, however, on the currently accepted values of Auger recombination⁴⁾ and bandgap narrowing⁵⁾ in depen-

dence on the dopant concentration. After better information on these heavy doping effects has been attained, the solar cell design philosophies might change slightly.

Both the maximum idealized efficiency and the dopant concentration at which this efficiency is obtained, (Fig. 3), depend on the minority carrier lifetime model chosen. The three models for the dependency of the minority carrier lifetime on dopant concentration, on which the three efficiency curves of Fig. 3 are based, are shown in Fig. 4⁶⁾. (Fig. 3 is based on a more detailed solar cell model outlined in the next section, but similar curves could have been obtained with the simple model).

REALISTIC STRUCTURES FOR HIGH EFFICIENCY TERRESTRIAL SOLAR CELLS

After the considerations on the idealized structure, the question arises to what degree such high performance may be approximated in realistic cell structures?

The first obstacle to zero surface recombination velocity on the back surface, appears to be the ohmic contact which represents a surface recombination velocity near 10^6 cm s^{-1} . A suitable high/low junction structure with a third, more heavily doped base layer of significant thickness, can accomplish a transport velocity transformation from values near 10^6 cm s^{-1} down to 20 cm s^{-1} at the interface between the narrow base layer and the high/low junction (Fig. 5). This is an adequately low value for close approximation of zero surface recombination velocity at the back of the base layer.⁶⁾

For the front, however, a similar approach is not appropriate, as the relatively thick third, more heavily doped layer would diminish the collection efficiency. However, a structure as illustrated in Fig. 6 could form an appropriate remedy. Here, the third layer exists only under the ohmic contacts which are represented by the grid line and bus line pattern on the front surface of the cell. The light-exposed surface is located directly on the less heavily doped front layer. Its surface recombination velocity, as it results from the fabrication processes applied, would normally be too high to allow adequately high performance. Particularly the influence on the saturation current which determines the open circuit voltage, would reduce performance. Thus, adequate means for reduction of the surface recombination velocity to values near 100 cm s^{-1} on the open front surface will still be needed. Doped oxides or induced accumulation layers (MIS structures) may accomplish this result. MIS approaches can also be used to reduce the effect of the high surface recombination velocity of the ohmic contact, similar to the high/low junction-third layer combination.

Appropriately applying these measures in combination can achieve a performance comparable to that of the idealized device of Fig. 1. It may be noted that, in the computation of the idealized efficiency data, a textured front surface (oblique photon penetration) and an internally optically reflecting back surface were included. Also, for a realistically achievable cell, including front surface shading by metallization, series resistance losses, a non-ideal antireflection coating, etc., the performance data have to be reduced to about 90% of the values given here.

CELL DESIGN FOR HIGH PERFORMANCE AFTER ENERGETIC PARTICLE EFFECTS

The high solar cell performance discussed in the preceding paragraphs, is achievable only with very large diffusion lengths in both the front and the base regions of the device. In most space missions, however, the radiation environment rapidly reduces the minority carrier lifetime (Fig. 7) ⁷). The original curves (solid lines of Fig. 7) apply to solar cells of rather limited diffusion lengths, while the devices discussed in the preceding paragraphs would start with substantially longer values. However, they would follow the dashed curve under the influence of nuclear particle flux until their approximation to the original straight line. Thus, for 1 MeV electron equivalent nuclear radiation fluxes, at the fluence level of 10^{15} to 10^{16} cm^{-2} , no advantage would be derived from the original high diffusion lengths. In design computations for a solar cell structure corresponding to Fig. 6 ⁶), a parametric study for the optimum base layer thickness as function of the minority carrier lifetime in the base was carried out (Fig. 8), yielding both the optimum base thickness and the maximum efficiency achievable for a given minority carrier lifetime. At a 1 MeV equivalent fluence of 10^{16} cm^{-2} , the minority carrier lifetime would have decreased to 35 ns according to Fig. 7, and the corresponding efficiency would be 14% with a base layer thickness of 30 μm .

It is evident that the design for optimum EOL (end of life) performance of silicon solar cells will require very thin silicon wafers, but will still not be able to exceed a performance level near 14% (AMO). It should be noted that the prior computations were carried out for optimum cell performance under AM1 conditions. It will be necessary to carry out similar computations for an optimum performance at EOL under AMO. In fact, the 26.7% (AM1) efficient cell shows 23.9% efficiency for AMO (BOL).

While the terrestrial solar cell optimization was based on the use of low resistivity silicon, it is well known that this type of silicon is more radiation sensitive than higher resistivity material (Fig. 9). Thus, a radiation resistant design may include a trade-off towards the use of higher resistivity material. While the damage coefficient for diffusion length (Fig. 9) is reduced by approximately a factor of 3 in going from 1Ω cm ($p = 1.5 \times 10^{16}$ cm^{-3}) to 10Ω cm resistivity ($p = 1.3 \times 10^{15}$ cm^{-3}), the minority carrier mobility decreases from approximately 1000 to 750 $\text{cm}^2 \text{V}^{-1}\text{s}^{-1}$, so that the effective change in the damage coefficient for minority carrier lifetime is only approximately 2.25. Nevertheless, this difference in minority carrier lifetime damage coefficient will have a significant influence on the ultimate design of a radiation hardened, high performance silicon solar cell.

CONCLUSION

The principles of radiation resistant silicon solar cell design are opposing those of high efficiency design, particularly in the areas of selected resistivities and minority carrier lifetimes. An optimum EOL cell design needs still to be derived, but it is likely to be based on very thin silicon wafers. A disadvantage will be that the optimum EOL designs for different radiation environments will differ, and will be far from optimum at BOL. On the other hand, an optimum EOL design may not show much output degradation throughout its life.

REFERENCES

1. M. Wolf, "Updating the limit efficiency of silicon solar cells", IEEE Trans. Electron Devices, vol. ED-27, pp. 751-759, Apr. 1980.
2. H. Fischer and W. Pschunder, "Impact of material and junction properties on silicon solar cell efficiencies", in Rec. 11th IEEE Photovoltaic Spec. Conf., pp. 25-31, 1975.
3. Lindholm, F.A., Li, S.S., and Sah, C.T., "Fundamental limitations imposed by high doping on the performance of pn junction silicon solar cells", *ibid.*, pp. 3-12.
4. J. Dziewior and W. Schmid, "Auger coefficients for highly doped and highly excited silicon", Appl. Phys. Lett., vol. 31, pp. 346-348, 1977.
5. Lanyon, H.P.D., "Bandgap reduction mechanism in heavily doped semiconductors", Rec. 15th IEEE Photovoltaic Spec. Conf., IEEE Cat. No. 81CH1644-4, pp. 415-421, May, 1981.
6. Bowler, D.L., and Wolf, M., "Interactions of efficiency and material requirements for terrestrial silicon solar cells", IEEE Trans. Components, Hybrids and Manuf'g. Technol., CHMT3, pp. 464-472, Dec. 1980.
7. Tada, H.Y., and Carter, J.R., Jr., "Solar Cell Radiation Handbook", Jet Propulsion Laboratory Publ'n., 77-56, Nov. 1977.

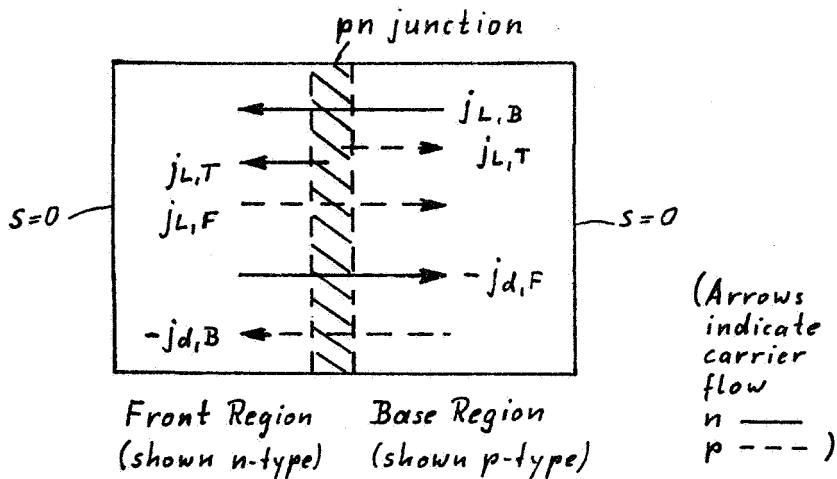


Fig. 1. Simplified ideal solar cell structure with zero surface recombination velocity at the outside boundary surfaces of both front region and base region.

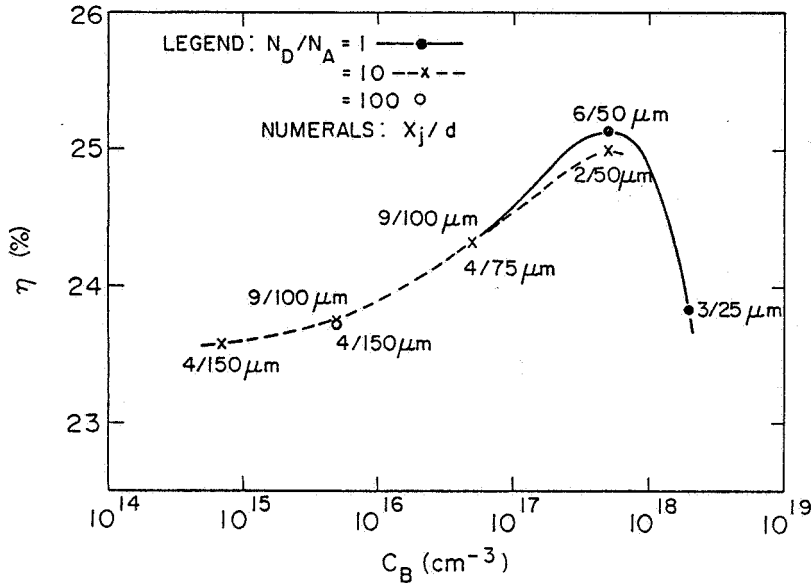


Fig. 2. Efficiency η of the idealized solar cell structure in dependence on the majority carrier concentration C_B in the base region. The numerals indicate the nominal front region thickness x_j and the total cell thickness d , at which optimum performance is achieved. Used as a parameter is the ratio of the impurity concentrations in the front (N_D) and base (N_A) regions, respectively.

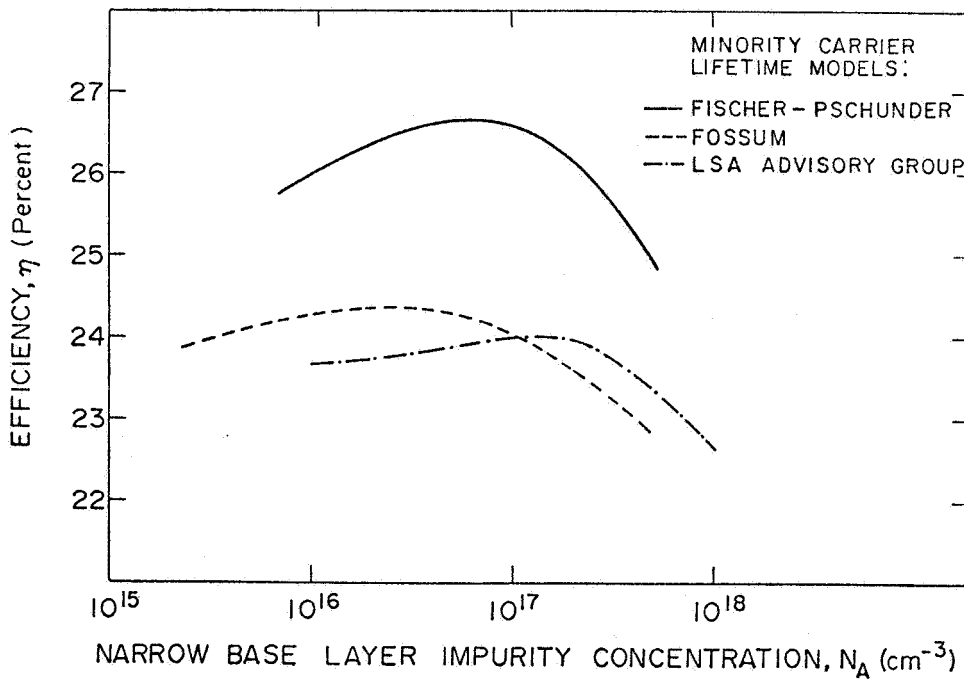


Fig. 3. Dependence of the efficiency versus base layer impurity concentration relationship on the minority carrier lifetime model used.

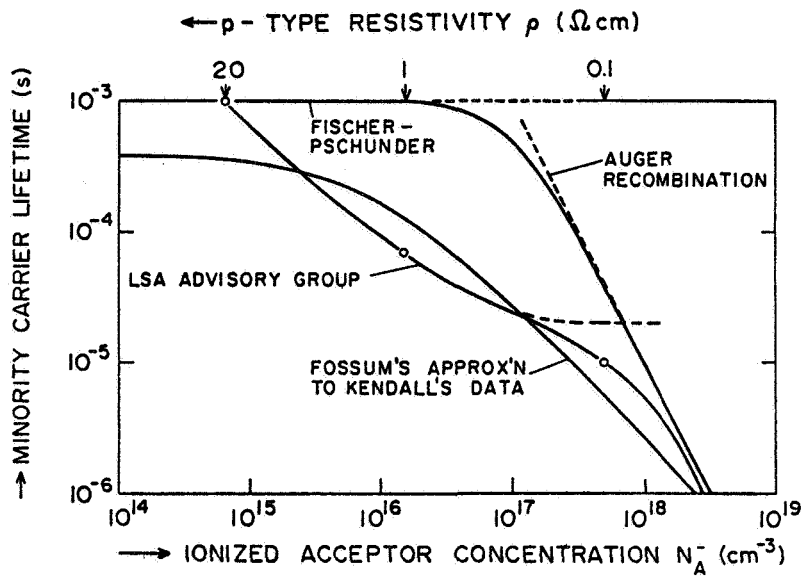


Fig. 4. The three minority carrier lifetime models used for Fig. 3. For details, see ref. 6.

		FRONT	PN	BASE 1	BASE 2	BASE 3	
u_d (←)	[cm s^{-1}]	200 (p)	52.6 (p)	225 (n)	52.8 (n)	$2.1 \cdot 10^3$ (n)	$1 \cdot 10^6$ (n)
$N_{D \text{ or } A}$	[cm^{-3}]	$5 \cdot 10^{17} - 2 \cdot 10^{18}$		$5 \cdot 10^{16}$	—	$2 \cdot 10^{18}$	
$L_{p \text{ or } n}$	[μm]	36.3		226	88.4	34.5	
E	[V cm^{-1}]	$1.93 \cdot 10^3$		0	$9.55 \cdot 10^3$	0	
u_L (→)	[cm s^{-1}]	—	$1 \cdot 10^9$ (p)	$1 \cdot 10^9$ (n)	$2.6 \cdot 10^3$ (n)	$1.03 \cdot 10^5$ (n)	—
X	[μm]	0	0.186	0.340	60	60.1	100
		$j_L = 39.79 [\text{mA cm}^{-2}]$ (C.F.) = 0.847 $V_{oc} = 0.705 [\text{V}]$ $\eta = 23.92 [\%]$		FRONT: $j_L = 6.2 [\text{mA cm}^{-2}]; j_0 = 1.3 \cdot 10^{-15} [\text{A cm}^{-2}]$ BASE: $j_L = 31.0 [\text{mA cm}^{-2}]; j_0 = 5.7 \cdot 10^{-14} [\text{A cm}^{-2}]$			

Fig. 5. Near optimum silicon solar cell structure (AM1) based on the lifetime model labeled LSA Advisory Group in Fig. 4.

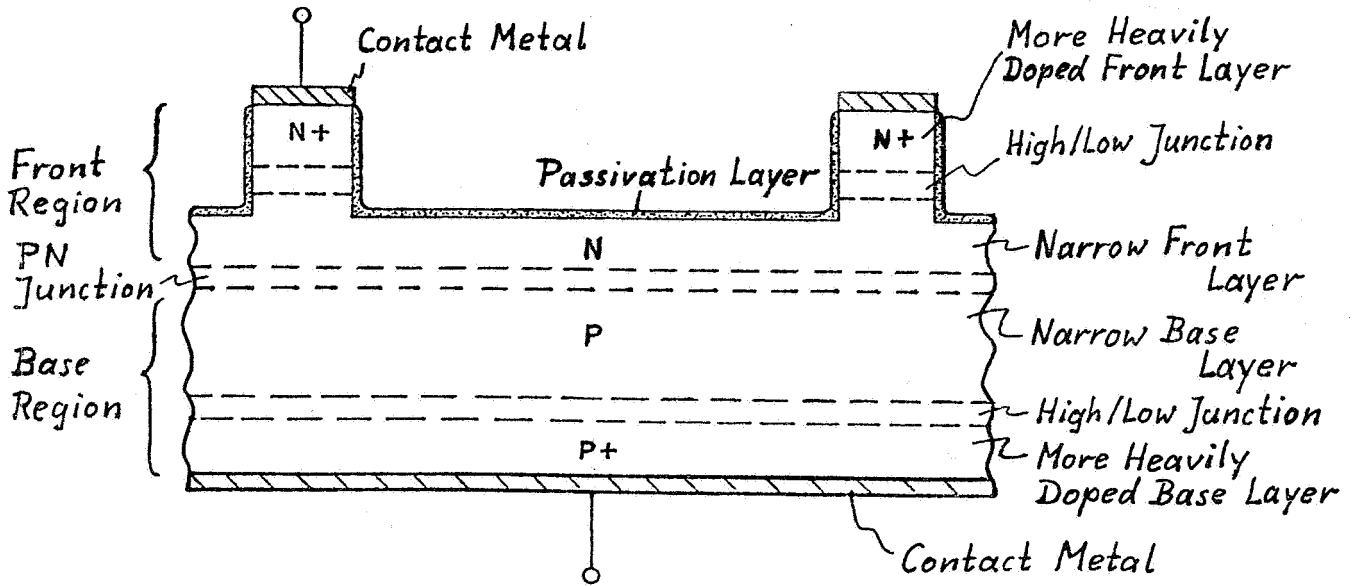


Fig. 6. Silicon solar cell structure for high efficiency.

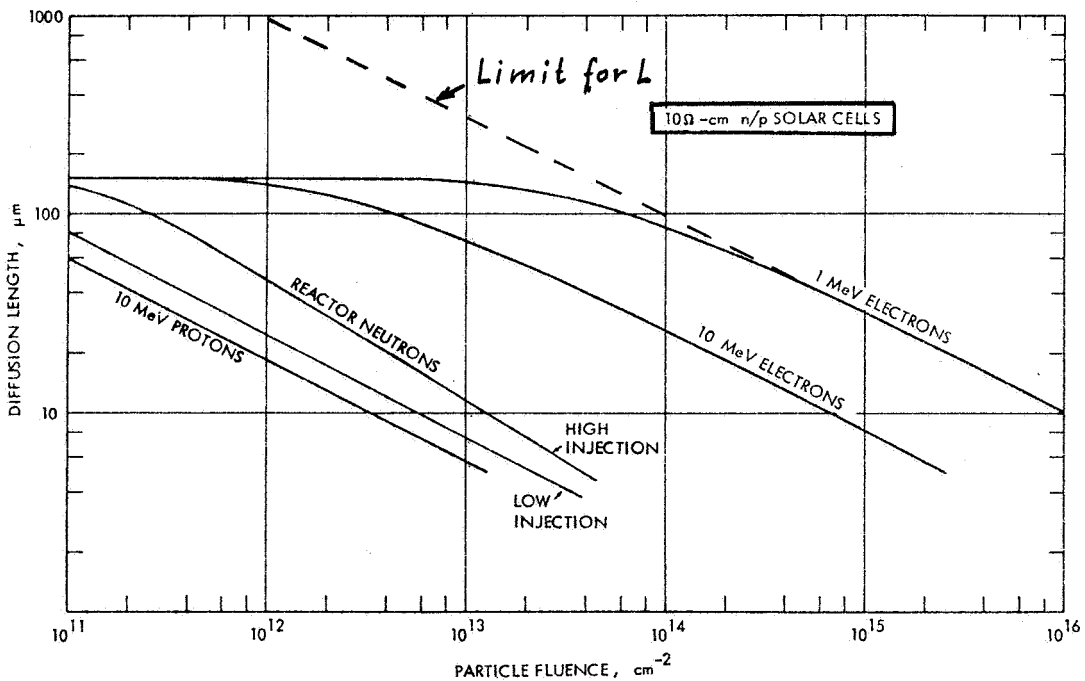


Fig. 7. Base region diffusion length L in 10Ω cm n/p Si solar cells as function of fluence for various energetic particles. From ref. 7.

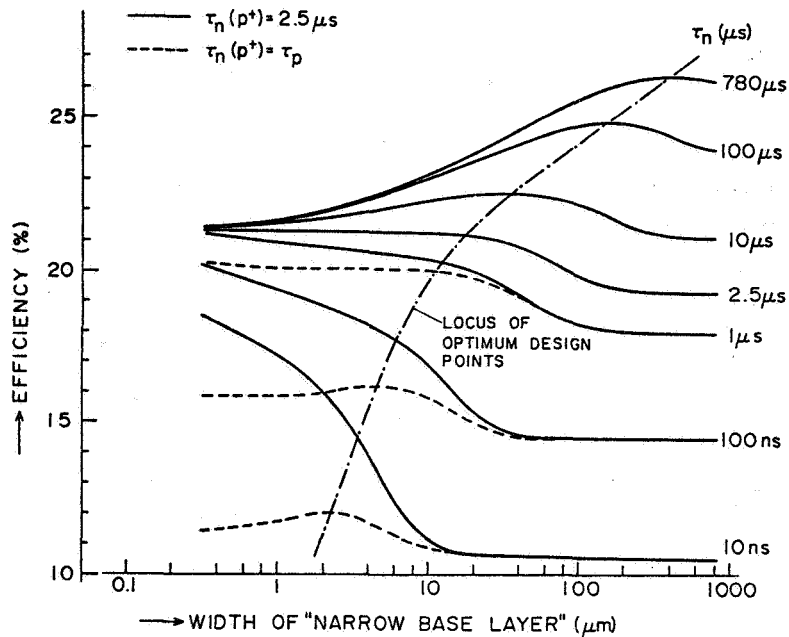


Fig. 8. Efficiency as function of the thickness of the less heavily doped base layer, with minority carrier lifetime in this layer as parameter. The dashed curves do not permit the lifetime in the more heavily doped base layer (p^+ layer) to exceed that of the p -layer. All other parameters kept constant.

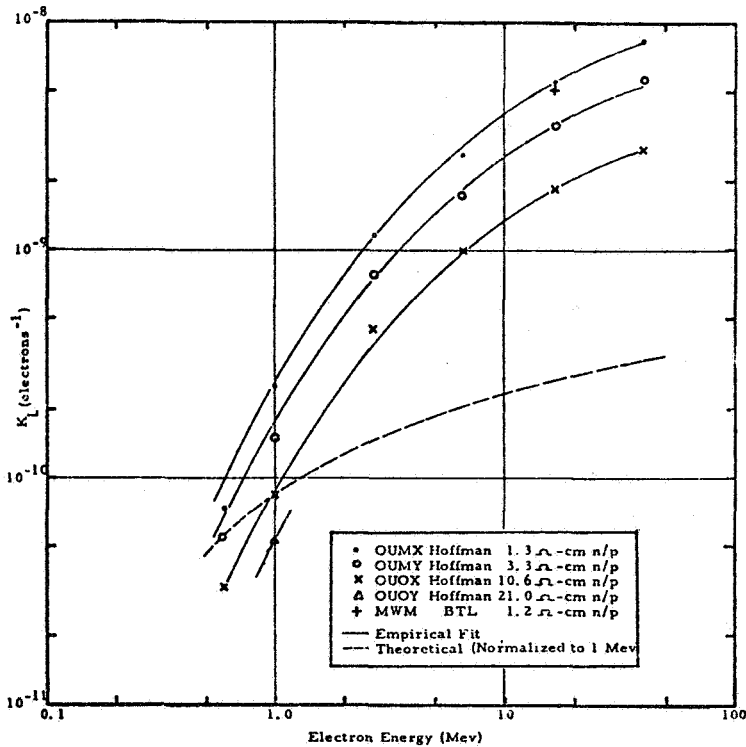


Fig. 9. Dependence of the damage coefficient K_L for diffusion length on electron energy and base region resistivity.

SURFACE EFFECTS IN HIGH-VOLTAGE SILICON SOLAR CELLS*

A. Meulenber, Jr., and R.A. Arndt
COMSAT Laboratories
Clarksburg, Maryland

EXTENDED ABSTRACT**

The influence of surface recombination velocity (SRV) on emitter dark current, and therefore on cell open-circuit voltage V_{OC} , has necessitated the use of low area "dot" contacts to reduce a major source of this dark current (ref. 1). Once the contact area is reduced sufficiently (or MIS contacts used to reduce SRV at the contacts), the major source of dark current from the emitter of a shallow junction solar cell is the oxide-silicon interface itself. (Heavy doping effects influence all cells, and Auger recombination is the major problem in deep junction solar cells.) Recombination and generation of carriers at this interface will influence both the blue response and the V_{OC} of such a cell, and therefore must be reduced as much as possible.

The SRV of a solar cell is increased and the blue response decreased by defect sites near the interface and by electric fields which draw minority carriers to the interface. The SRV contribution to the emitter dark current is also increased by heavy doping effects which create bandgap narrowing, even in the vicinity of the interface.

A series of experiments was performed in an attempt to reduce the surface recombination velocity of heavily doped silicon surfaces. Most of the effort involved diffused n^+p structures, but a comparison was also made with low doped MIS structures.

Antireflecting coatings deposited directly on a silicon surface provide poor interface characteristics so that passivating oxide generally needs to be grown prior to application of the AR coating. Solar cell processing at COMSAT Laboratories has traditionally used thermal oxidation of tantalum metal to form the AR coating and to passivate the surface simultaneously (ref. 2). During the early studies on this material, it was discovered by C-V techniques that significant negative charge was created and trapped in the Ta_2O_5 during the oxidation process (ref. 3). Cells fabricated in the early portion of this effort utilized this process without alteration.

To improve the traditional AR coating, it was found that application of positive static charge (ref. 4) to the front of the AR coating did not alter the cell characteristics. However, when the AR coating was subjected to a 750°C , 30-minute oxidation prior to forming the contact, the cell became quite sensitive to such surface charge. Figure 1 indicates the influence of positive charge on shallow junction solar cell I-V characteristics. Cells with junctions as deep as $1/5\ \mu\text{m}$ have displayed similar effects. As expected, the more

*This paper is based upon work performed at COMSAT Laboratories under the sponsorship of the Communications Satellite Corporation and supported in part by NASA Lewis under Contract NAS3-22217.

**Full text to appear in the 16th Photovoltaic Specialists Conference, San Diego, CA, September, 1982.

heavily doped surfaces showed the least response to charge. The oxidation step must either reduce or compensate the charge in the Ta_2O_5 or it must remove defect sites that pin the Fermi level locally at the interface. This oxidation step adds about 5 mV to the average open-circuit voltage even with no surface charge.

MIS cells have been fabricated (fig. 2) that exhibited dark currents lower than those in 650-mV, diffused cells.¹ The implication is that the SRV of the MIS structure is lower than that of diffused cells and/or that the inversion layer is better than the diffused layer. A third possibility is that simple oxidation of a heavily doped and/or diffused layer cannot provide a well-passivated surface.

Major conclusions of this study are as follows:

- a. Surface recombination velocity is the major limitation of shallow junction solar cells.
- b. Proper surface passivation allows significant influence on blue response and V_{OC} by use of static charge applied to the surface.
- c. Surface passivation of heavily diffused surfaces does not appear to break an apparent V_{OC} barrier for diffused cells at ~655 mV.
- d. MIS structures have shown greater potential for high V_{OC} , probably as a result of lower SRV at the oxide-silicon interface.

REFERENCES

1. Rittner, E. S.; Meulenbergh, A.; and Allison, J. F.: Dependence of Efficiency of Shallow Junction Silicon Solar Cells on Substrate Doping. *Journal of Energy*, vol. 5, no. 1, January-February 1981, pp. 9-14.
2. Revesz, A. G.; and Allison, J. H.: Electronic Properties of the Silicon-Thermally Grown Tantalum Oxide Interface. *IEEE Transactions on Electron Devices*, vol. ED-23, no. 5, May 1976, pp. 527-529.
3. Revesz, A. G.; Allison, J. F.; and Reynolds, J. H.: Tantalum Oxide and Niobium Oxide Antireflection Films in Silicon Solar Cells. *COMSAT Technical Review*, vol. 6, no. 1, Spring 1976, pp. 57-69.
4. Lam, Y. W.; Green, M. A.; and Davies, L. W.: Electrostatic Effects in Inversion-Layer Metal-Insulator-Semiconductor Solar Cells. *Applied Physics Letters*, vol. 37 (12), December 15, 1980, pp. 1087-1089.

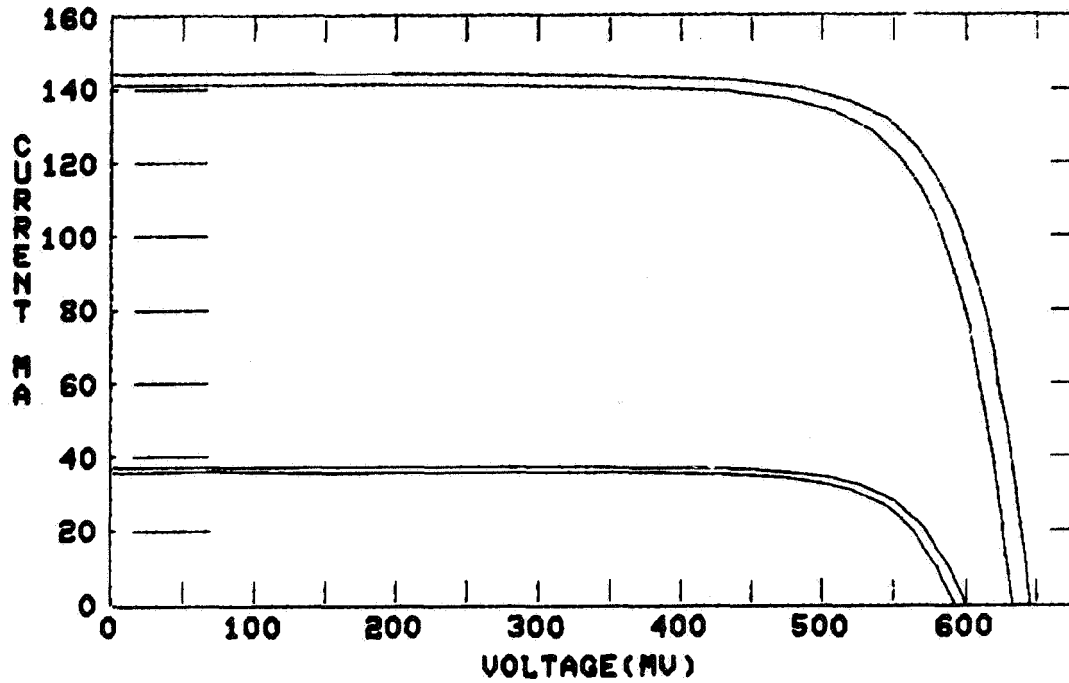


Figure 1. - The influence of positive surface charge on a shallow junction solar cell. The upper curve of each pair is for the cell when charged.

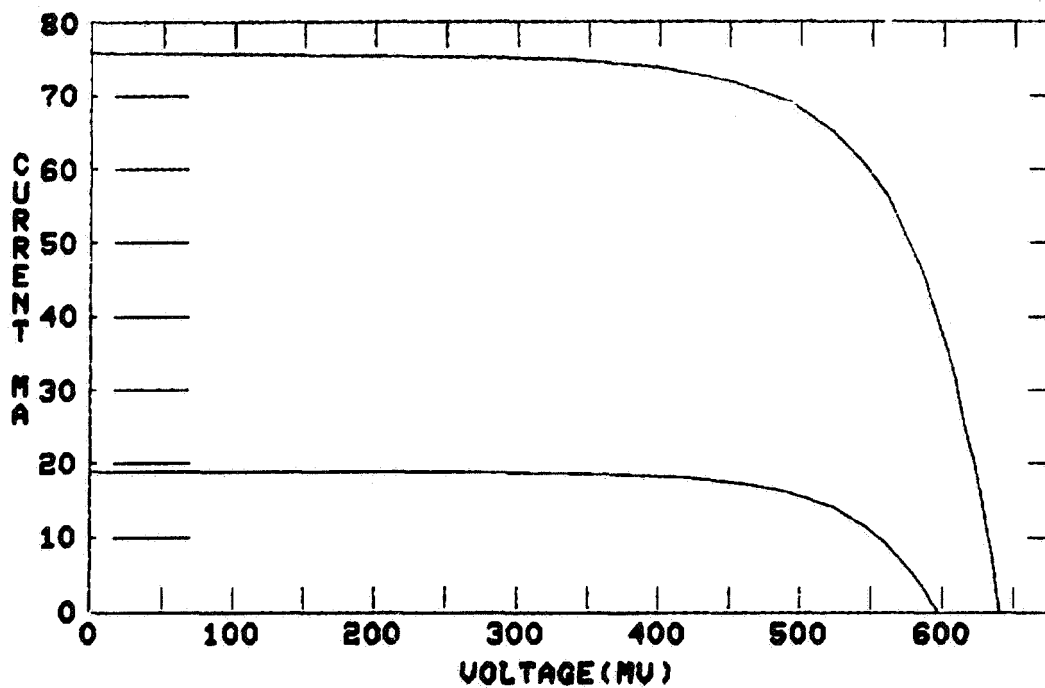


Figure 2. - The IV characteristics of an MIS cell (0.1 Ω -cm substrate, $\sim 100 \text{ \AA}$ Er + $\sim 50 \text{ \AA}$ Cr + Plated Grids, No AR Coating).

RECENT DEVELOPMENTS IN THIN SILICON SOLAR CELLS*

F. Ho and P. Iles
Applied Solar Energy Corporation
City of Industry, California

COPLANAR BACK CONTACT CELLS

50um thick cells $2 \times 4 \text{cm}^2$ area with coplanar back contacts were made with good yield, and with output equivalent to conventional top/bottom contact cells of the same thickness. A wraparound junction (WAJ) design was selected, and used successfully. The contact configurations are shown in Figure 1. The low α 's cells delivered were all above 12%, the average efficiency was 13% and the best was 14%. The overall yield was 35-40%, comparable to that for conventional 50um cells (see Table 1). The process sequence was moderately complex, but showed good reproducibility. The CBC cells performed well under several important environmental tests. High α 's CBC cells were made, with about 1% increase in conversion efficiency.

The most important design criteria were the choice of back surface N+ and P+ areas.

P+ AREA

Any giveaway P+ area introduced series resistance losses. The losses depended on both the area and the configuration of the giveaway area. This WAJ design did not allow reduction of this loss by use of the P+ BSF layer. The final design reduced this giveaway area, with minimal loss in output.

N+ AREA

The N+ layer on the edges and back surface introduced shunt losses. These were minimized by reducing the N+ area. Table 2 shows the improved cell performance (CFF) as the N+ area was decreased systematically (at the same time the P+ contact was correspondingly increased). Reduction of the N+ back surface area to $\sim 2.5\%$ also decreased shunting components in the diode dark forward current, and eliminated some inhomogeneities caused by illumination at different parts of the cell.

SILICON

FZ Si gave higher output than CZ. Cells were made with either 10 ohm-cm and 2 ohm-cm silicon; histogram plots of the output (Figure 2) show the distributions

*Most of the work described was funded by NASA-Lewis Research Center.

were similar. These two groups can be used for close comparison of the radiation resistance of CBC cells.

I-V DATA

Typical values were $I_{sc} \sim 312\text{mA}$, $V_{oc} \sim 610\text{mV}$, and $CFF \sim 0.76$. The best cell had I_{sc} 312, V_{oc} 0.619, and $FF \sim .79$; the I-V curve for this cell is shown in Figure 3. α_s was measured ~ 0.72 .

CONCLUSIONS

If the array advantages are sufficient to require 50um cells with coplanar back contacts, cells of good performance can be made, and there is further chance that the fabrication processes can be streamlined to reduce the most differential against conventional 50um thick cells.

VERY LOW α_s 50um CELLS

The goals of this program, $\alpha_s < 0.64$ with efficiency $\rightarrow 14\%$ have involved careful examination of the tradeoffs needed to combine these two goals. To reduce α_s , several cell design features are required:

- a) The front surface should not be textured (the loss of power from increased α_s offsets the increased current).
- b) The back surface must have high optical finish.
- c) A high IR reflectance back surface contact layer is required.
- d) Slight advantage can be taken of the use of high UV reflectance coatings on the coverglass.

NOTE: We have not assumed the use of a separate blue-red rejection filter.

In addition, several essential process steps are needed, especially for thin cells:

- i) A shallow diffused layer is required on the front surface.
- ii) Grid patterns with minimum shading.
- iii) Good quality AR coating.
- iv) A back surface field (BSF) is needed.

For (ii) and (iii) we estimated the tradeoff between power loss and cell α_s , for two limiting cases, namely full front surface metal coverage, and omission of AR coating. The estimated α_s values were ~ 0.25 and ~ 0.50 respectively, but the increased power available from these low α_s values was much less than the decreased power caused by these extreme conditions. We concluded by analysis and from tests, that any attempt to reduce α_s at the expense of active area or AR effectiveness was also counter productive.

PROCESS SELECTION FOR LOW α_s , 50um CELLS

(a) A suitable method is needed for thinning to 50um while maintaining high surface finish, especially on the back surface. We developed an etch-thinning process which leaves a mirror finish on the back surface, and a near specular finish on the front surface.

(b) For BSR metals, we extended earlier comparisons of metals with high IR reflectance, and selected gold for this work. Later, to improve the environmental performance we have used a very thin layer of aluminum under the gold. To ensure low contact resistance, we have returned to a structure used earlier, where the ohmic contact to the back surface is provided by a grid contact (deposited over the BSF layer) and the BSR metal is deposited on the remainder of the back surface. The grid pattern was designed to minimize series resistance at the sheet resistance levels introduced by the BSF.

(c) The BSF formation involves the major trade-offs. For thin cells, a good BSF (increased Voc, increased long wavelength response) is essential. Usually a good BSF layer involves high doping levels and reasonable depth of the layer. Often these steps reduce the optical quality of the back surface. We have avoided this possibility by using boron-diffusion, a process we have shown effective for highest output 50um cells. However, the high boron doping levels have led to another trade-off, caused by free carrier absorption in the BSF layer. This free carrier absorption (beyond 1.1um) decreases the overall reflectance, and the decrease is more serious at longer wavelengths.

We have found that the effective reflectance values can be shown to have λ^2 dependence, as predicted for free carrier absorption.

We have varied the boron doping levels systematically (keeping other factors constant) and have shown steady decrease in IR reflectance (Figure 4). In addition, we evaluated the BSF effectiveness of these varying boron conditions, and showed that to achieve $\alpha_s < 0.65$ will require loss of cell efficiency.

Figure 5 shows the present combination of I-V output and α_s achieved. At present we are fabricating 50 deliverable cells to show the best state-of-the-art.

CONCLUSIONS

It is possible to make silicon cells with α_s below ~ 0.60 . However, to maintain state-of-the-art efficiency ($> 12\%$) sets a limit to $\alpha_s \sim 0.63$, and suggests that in practice, the additional difficulties in reducing α_s to this range for thin cells, are accompanied by reduced cell output. The best compromise appears to be operation at high efficiency down to $\alpha_s < 0.67$.

WELDING TESTS

Weldable cells made on a pilot line (50um thick, 2x2cm, low $\alpha_s \sim 0.72$ and

average AMO efficiency ~13%) have been distributed to the array industry. In most cases, the cells have shown good weldability, especially after suitable handling techniques were developed. (Fuller reports on these cells will be given in other papers at this conference.)

TABLE 1
PROCESS LOSS AND YIELD SUMMARY FOR THE THREE FINAL
PILOT RUNS

PROCESS LOSS AND REJECT MODE	LOT NUMBER		
	I (%)	II (%)	III (%)
CLEANING AND ETCHING	10.2	12	10.7
SiO ₂ DEPOSITION	2	2.5	3.5
DIFFUSION (POCl ₃ , BN)	6	5.5	2
PHOTORESIST WORK	12.8	3.5	8.7
METALLIZATION	4	6	6
PLATING	6.4	8	8.5
CUTTING AND AR COATING	0.6	0.5	1.3
MECHANICAL REJECT	6.7	8	18
ELECTRICAL REJECT (< 12% AMO)	14	12.7	7.3
TOTAL YIELD (≥ 12%)	37.3	41.3	34

TABLE 2
TESTS TO DETERMINE TRADEOFF N+ AND P+ BACK
SURFACE AREA

N+ AREA (%)	P+ AREA (%)	Voc (mV)	Jsc (mA/cm ²)	CFF (%)	EFF (%)	Rs (ohm)
10.2	88.5	602	37.3	74	12.3	0.080
5.1	93.6	590	37.9	75	12.5	0.058
2.3	96.4	598	37.7	77	12.9	0.056
0	100	592	37.8	78	12.9	0.055

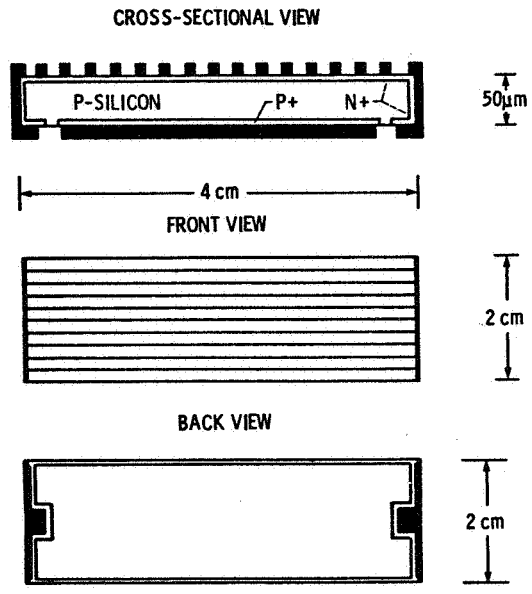
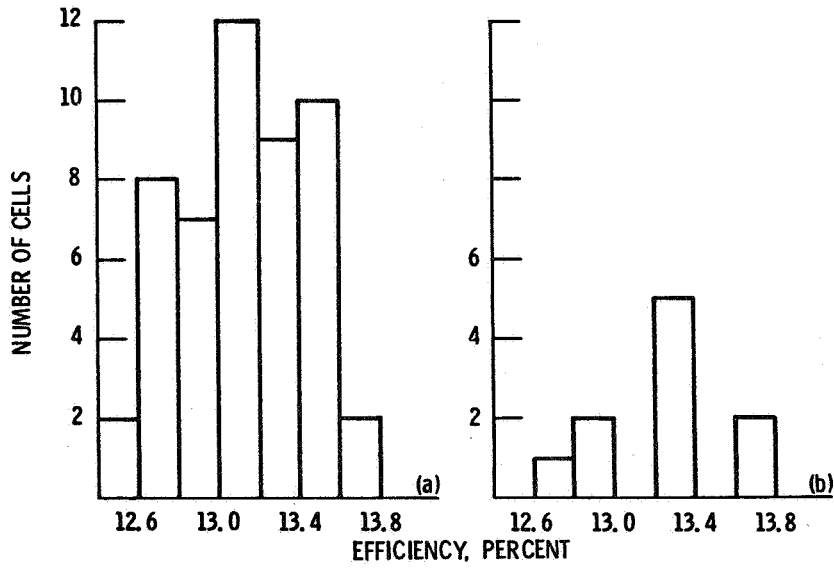


Figure 1. - 2-mil coplanar back contacts cell (WAJ).



(a) 10 ohm-cm (50 cells).
 (b) 2 ohm-cm (10 cells).

Figure 2. - Histogram plot for delivered 50- μ m CBC cells.

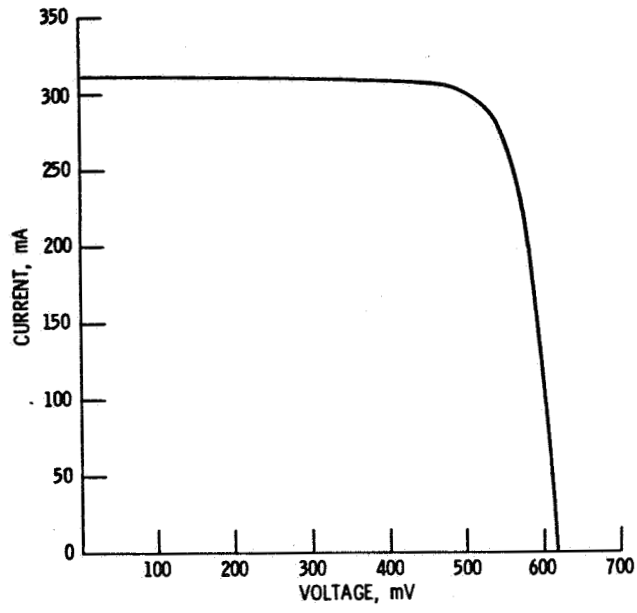


Figure 3. - Current-voltage curve for 50- μm CBC cell.

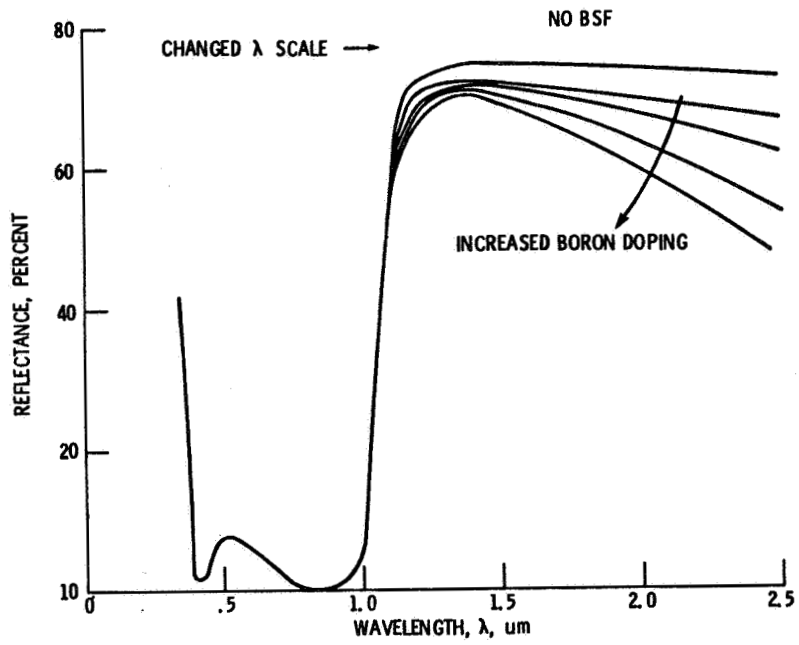


Figure 4. - Specular reflectance and wavelength (varying boron doping).

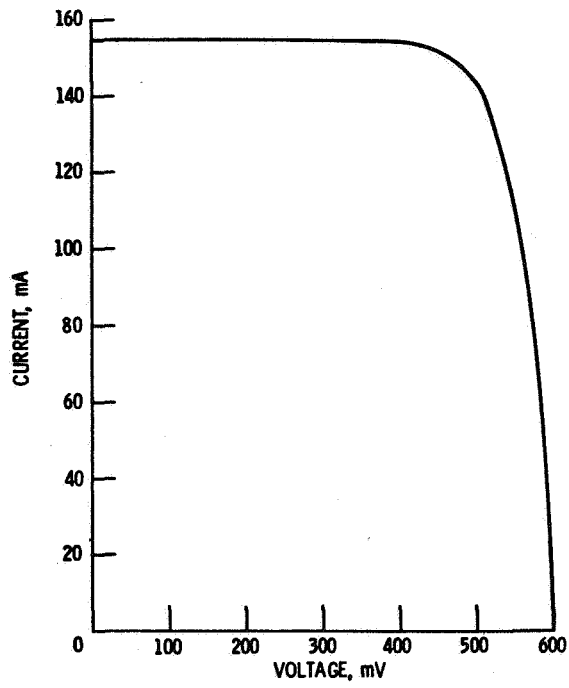


Figure 5. - Current-voltage curve for 50- μm , low α_s cells.

LARGE AREA SPACE SOLAR CELL ASSEMBLIES*

M.B. Spitzer and M.J. Nowlan
Spire Corporation
Bedford, Massachusetts

SUMMARY

Development of a large area space solar cell assembly is presented. The assembly consists of an ion implanted silicon cell and glass cover. The important attributes of fabrication are (1) use of a back surface field which is compatible with a back surface reflector, and (2) integration of coverglass application and cell fabrication.

INTRODUCTION

The economic constraints on future large space power systems will require a reduction in cell cost without compromise of cell quality. Certainly innovative cell fabrication techniques are necessary for achievement of this reduction. A further reduction may be possible with the use of low-cost terrestrial solar cell technology (ref. 1).

This paper describes the ongoing development of a low-cost large area (34.3 cm^2) n^+pp^+ solar cell assembly based on ion implantation. Whereas the cost of ion implantation is considered to be a disadvantage at current production levels, future large scale production will require an automated, effluentless, high throughput process. The development of ion implantation anticipates this need. The technical features of ion implantation and its development for terrestrial purposes are discussed in references 2 and 3. Application of the technology to space solar cell fabrication has a particular advantage arising from the ease with which back surface reflectors can be formed on the implanted back surface (ref. 4). This will be discussed more fully in the next section.

An important innovation in cell encapsulation has also been developed. In this new technique, the coverglass is applied before the cell is sawed to final size. The coverglass and cell are then sawed as a unit. In this way, the cost of the coverglass is reduced, since the tolerance on glass size is relaxed, and costly coverglass/cell alignment procedures are eliminated.

CELL DEVELOPMENT

All cell development was based on 2 ohm-cm p-type (100) silicon, with thickness of 250 μm and diameter 7.6 cm. No AR coatings were used during cell development.

* This work was supported by the NASA Lewis Research Center.

Back Surface Implantation

The implantation of $^{27}\text{Al}^+$, $^{11}\text{B}^+$ and $^{70}\text{Ga}^+$ ions was investigated for p-p⁺ BSF formation. Implant and anneal parameters are given in Table 1. After this sequence, front junctions were formed by phosphorus implantation (10 keV, 2.5×10^{15} ions/cm²) and annealed with a three-step anneal (ref. 3).

Figure 1 shows the resulting doping profiles obtained by spreading resistance analysis. The anomalous Al profile is not understood; however, the B and Ga have the abrupt profile characteristic of the implantation process. Boron yields the highest activation. Table 2 shows the measured cell performance under simulated AMO insolation. Also shown in the table are results obtained without BSF formation. These cells had a slightly different front junction anneal and a different back contact, but were fabricated from the same starting material and are included here to indicate the performance achievable without a back implant. Cells with implanted backs have slightly better FF; this is attributed to an improved electrical back contact. We infer from this data that the Al and Ga implants are not effective in providing BSF enhancement of voltage and current, even though the doping varies over two orders of magnitude at the p-p⁺ junction.

One of the major advantages of using ion implantation for back surface field formation is that implantation leaves the physical appearance of the surface unchanged. Thus, a wafer with a polished back can be used for back surface reflector (BSR) formation, without repolishing of the implanted surface. This should be contrasted with Al-paste processes, which require extensive repolishing after BSF formation.

A BSR was formed on surfaces which were boron-implanted as described above. The BSR consisted of evaporated Al-Ti-Pd-Ag and no repolishing was used prior to evaporation. The polished fronts of the samples were AR coated with TiO₂ but had neither front metallization nor front junctions. Table 3 shows the measured values of thermal alpha (courtesy of H. Curtis of NASA-LeRC) for four samples. All samples had thermal alpha values less than 0.70. It can be seen from these data that (1) contact sintering has no measurable effect on thermal alpha, and (2) boron implantation increases thermal alpha slightly.

Emitter Development

Various phosphorus and arsenic implantations were studied in order to achieve very shallow ($\leq 0.2 \mu\text{m}$) highly doped n⁺ layers. Refinements such as oxide passivation and junction tailoring (ref. 5) were not pursued at this stage of the development.

Spreading resistance profiles for three different emitters are shown in Fig. 2. The ion implantation and anneal parameters are listed in Table 4. Also listed are the measured AMO performance data of test cells fabricated with the indicated emitters. Each test cell had a boron-implanted BSF and Ti-Pd-Ag metallization. No antireflection coating was used.

The first two entries in Table 4 compare direct implantation of phosphorus to phosphorus implanted in a surface which is first rendered amorphous by silicon implantation. This "pre-implantation" was investigated because it offers complete elimination of channeling, and should also yield better epitaxial regrowth during the anneal, since the surface layer has no polycrystalline features (ref. 6).

As is evident in Figure 2, this pre-implantation does result in reduced junction depth; however, the Voc of these cells is much lower than that of the directly implanted phosphorus. Since the dark logI-V curves of the predamaged cells show a small increase in saturation current with no change in n-factor, we attribute the reduced Voc to an increase in emitter dark current resulting from a decrease in emitter diffusion length. This decrease of emitter diffusion length is attributed to unsatisfactory annealing of the implantation damage.

We have also examined arsenic implantation and very shallow junctions have been obtained as indicated in Figure 2. Spectral response measurements indicate that the blue response is enhanced, but that the red response is lower than the phosphorus-implanted cells. Various anneal cycles were investigated to determine whether the minority carrier lifetime had been compromised by the one-step anneal, but no improvement was attained. The poor performance of these cells is therefore attributed to low lifetime in the material used for arsenic studies.

Results

Large area cells were fabricated using the boron implantation and anneal as described above and phosphorus implantation (5 keV, 2.5×10^{15} ions/cm²) followed by a three-step anneal (ref. 3). Patterned Ti-Pd-Ag contacts were applied to the front and full area Al-Ti-Pd-Ag contacts were applied to the back. An evaporated antireflection coating of Ta₂O₅ was applied and cells were sawed to final size (5.9 cm x 5.9 cm). The cell shape and contact configuration were selected so as to be compatible with the encapsulation design (Fig. 3). Total cell area was 34.3 cm².

Performance under simulated AMO insolation at 25°C was measured, and the following average characteristics were obtained for a group of twenty-five cells.

	<u>Average</u>	<u>Standard Deviation</u>
V _{oc} (mV)	605	0.2
J _{sc} (mA/cm ²)	38.1	0.3
FF (%)	75.2	1.1
EFF (%)	12.8	0.2

We attribute the low fill factor in part to a shunt resistance arising at the wafer edge (part of this edge is incorporated in the final cell - see Fig. 3) and in part to contact series resistance. Improvements in cell design and fabrication techniques which will yield a fill factor of 80% without substantial increase in cell cost are being pursued.

ENCAPSULATION

A major reduction in assembly cost is achieved by a new procedure for attaching glass coverslips. Standard practice has been to bond a precisely cut coverslip to a finished cell. The demands on cell and glass tolerance and on precision alignment of coverslip with respect to the cell during assembly add substantially to the assembly cost. To reduce this cost, we have developed a process in which the glass cover is bonded to the wafer before sawing the cell to its final size. In this way, cell and glass are sawed to size as one using a wafer dicing saw. This obviates the need for precision in both coverslip preparation and alignment, without loss of registration, and so results in a major cost saving. We believe that this is the first demonstration of this technology.

Materials and Lamination

An encapsulation procedure was developed for three adhesives: ethylene vinyl acetate (EVA), FEP-Teflon sheet and Dow-Corning 93-500. Two types of glass were used: Corning 0211 (nominally 300 μm thick) and Corning 7070 microsheet (nominally 100 μm thick). The thermal expansion coefficient of Corning 7070 is quite close to that of silicon; it is therefore the best choice for use with lamination sequences involving temperature cycling.

The lamination procedures used for EVA and FEP-Teflon were straightforward. A brief description is provided here. The details can be found in reference 7. An assembly consisting of the glass, adhesive and cell are placed in an evacuated chamber. Pressure is applied ($\frac{1}{2}$ atm. for EVA, 2 atm. for FEP-Teflon) and the sample is heated (150°C for EVA, 300°C for FEP-Teflon) to allow the adhesive to flow. The assembly is then cooled slowly to room temperature.

Lamination with DC93-500 was also straightforward. The adhesive is mixed, de-aired and poured onto the center of the cell. The cell is then placed in a bell jar and the DC93-500 is de-aired a second time. A cleaned coverslip is placed over the DC93-500 and the air is pressed out manually. The assembly is then placed in an oven at 150°C for 15 minutes to speed the adhesive cure.

Complete lamination over an area of 45 cm^2 was attained with each adhesive. No delamination occurred after 10 temperature cycles between 77 K and 373 K.

Assembly Configuration

Figure 3 illustrates the contact configuration used in this work. The final cell is square with a connection pad at each corner. Note that the corners would actually extend beyond the edge of the wafer since the diagonal of the square is larger than the wafer diameter. The actual corners are therefore rounded and are formed by the edge of the original wafer. This edge is never removed.

Silver ribbon leads were welded to the connection pads and a glass cover was laminated to the assembly as described in the previous section. The dotted lines in Figure 3 indicate the locations of the saw cut. It is necessary to fold the ribbon leads over either the rounded corner or the edge of the glass so as to remain out of the path of the saw blade. A photograph of an assembly prepared for sawing is shown in Figure 4A. The leads have been taped to the coverglass. The assembly is shown after sawing in Figure 4B.

Assembly Results

Assemblies have been fabricated with each of the adhesives with good results obtained when Corning 7070 microsheet is used. Problems resulting from residual stress when Corning 0211 was used in combination with a thermal lamination process included cell bowing and spontaneous coverglass cracking.

Two wafers were removed prior to sawing from the large area cell process group described in the first section of this paper and were encapsulated with the DC93-500 lamination process and Corning 7070 microsheet. The performance under simulated AMO insolation is shown below.

Cell	V _{oc} (mV)	J _{sc} (mA/cm ²)	FF (%)	Eff (%)
31-6	600	37.0	72.8	12.0
34-3	603	37.2	75.9	12.6

There would appear to be a slight decrease in short circuit current (in comparison to the non-encapsulated cells), perhaps owing to a change in the effectiveness of the antireflection coating upon encapsulation. In general, however, the performance does not seem to be degraded by the encapsulation process.

CONCLUSIONS

Cells were fabricated using potentially low-cost ion implantation processing. Average efficiency of large area cells of 12.8% AMO was achieved. A novel encapsulation technology was investigated and found to simplify encapsulation without sacrifice of cell quality.

REFERENCES

1. Scott-Monck, J.; Stella, P.; and Berman P.: Space Applicable DOE Photovoltaic Technology - An Update, JPL Publication 81-91, November, 1981.
2. Douglas, E.; and D'Aiello, R.: A Study of the Factors Which Control the Efficiency of Ion-Implanted Silicon Solar Cells, IEEE Transactions on Electron Devices ED-27, 792 (1980).
3. Kirkpatrick, A.; Minnucci, J.; and Greenwald, A.: Low-Cost Ion Implantation and Annealing Technology for Solar Cells, Record of the 14th IEEE Photovoltaic Specialists Conference, San Diego, 1980, page 820.
4. Rasch, K.-D.; Roy, K.; Schilling, R.; and Fischer, H.; Compatibility of BSR and BSF Solar Cell Technology, Record of the 14th IEEE Photovoltaic Specialists Conference, San Diego, 1980, page 141.
5. Minnucci, J.; Kirkpatrick, A.; and Matthei, K.: Tailored Emitter, Low Resistivity, Ion Implanted Silicon Solar Cells, IEEE Transactions on Electron Devices ED-27, 802 (1980).
6. Csepregi, L.; Kennedy, E.; Lau, S.; Mayer, J.; and Sigmon, T.; Disorder Produced by High-Dose Implantation in Silicon, Appl. Phys. Lett. 29, 645 (1976); see also Crowder, B.: The Role of Damage in the Annealing Characteristics of Ion Implanted Si, J. Electrochem. Soc.: Solid State Science, May, 1970, page 671.
7. Spire Corporation, Final Report for NASA Contract NAS3-22236, Spire Report No. FR10081.

TABLE 1 - BACK SURFACE FIELD PROCESS PARAMETERS

Ion Implantation

Energy = 50 keV
 Fluence = 5×10^{15} ions/cm

Furnace Anneal

550°C for 2 hours
 Ramp to 950°C at 8°C/min
 950°C for 2 hours
 Ramp to 500°C at 5°C/min.

TABLE 2 - MEASURED PERFORMANCE OF B, Ga AND Al BSF SOLAR CELLS.

BSF (no. of cells)	V _{oc} (mV)	J _{sc} (mA/cm ²)	FF (%)	EFF (%)
Boron (35)	595 (003)	27.0 (0.4)	78.7 (1.4)	9.37 (0.24)
Gallium (11)	584 (005)	26.0 (0.3)	77.4 (4.0)	8.71 (0.59)
Aluminum (24)	584 (003)	26.2 (0.3)	78.8 (0.8)	9.00 (.14)
None (24)	582 (002)	26.3 (0.3)	76.9 (1.9)	8.7 (0.2)

Notes: Simulated AMO illumination. Cell area = 4 cm², no AR coating.
 Standard deviation shown in parenthesis. T=25°C.

TABLE 3 - MEASURED VALUES OF THERMAL ALPHA FOR FOUR BSR PROCESSES

Back Implantation	Metallization	Thermal Alpha
None	Not sintered	0.64 + 0.02
None	Sintered, 400°C	0.66 + 0.02
11B+	Not sintered	0.67 + 0.02
11B+	Sintered, 400°C	0.68 + 0.02

TABLE 4 - COMPARISON OF SHALLOW JUNCTION CELLS FORMED BY VARIOUS FRONT IMPLANTATION PROCESSES

Implantation	Furnace Anneal Cycle	Junction Depth (μm)	V_{oc} (mV)	J_{sc} (mA/cm^2)	FF (%)	AMO Eff (%)
31p+ 10 keV 2.5 x 10 ¹⁵ ions/cm ² (Direct)	550°C - 2 hours	0.18	582 (001)	26.6 (0.2)	78.1 (1.3)	9.0 (0.1)
	850°C - 15 min					
	550°C - 2 hours (flowing N ₂)					
31p+ 10 keV 2.5 x 10 ¹⁵ ions/cm ² (Si pre-implanted)	550°C - 2 hours	0.13	555 (002)	26.6 (0.1)	77.2 (2.2)	8.5 (0.3)
	850°C - 15 min					
	550°C - 2 hours (flowing N ₂)					
75As+ 30 keV 3.5 x 10 ¹⁵ ions/cm ² (Direct)	900°C - 30 min. (flowing O ₂)	0.10	567 (001)	24.2 (0.9)	77.3 (0.1)	7.9 (0.4)

Notes: Simulated AMO insolation. Cell area is 4 cm². No AR coatings. Standard deviation shown in parenthesis. T = 25°C.

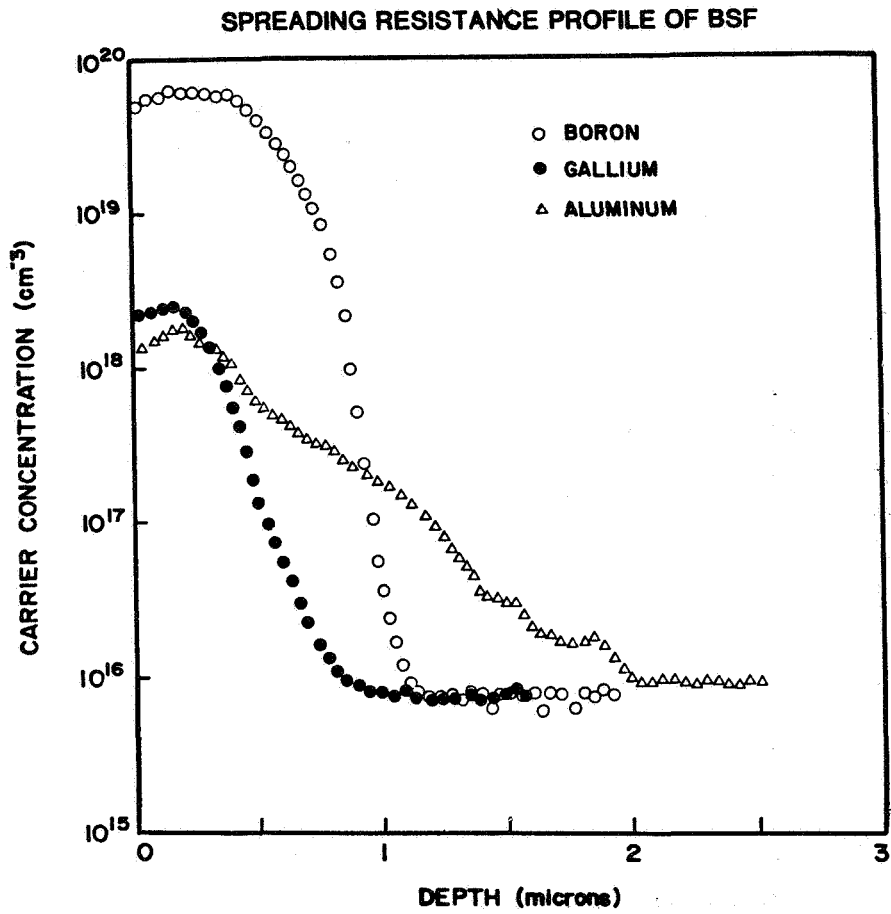


Figure 1: Spreading Resistance Profiles of Boron, Gallium and Aluminum Implants.

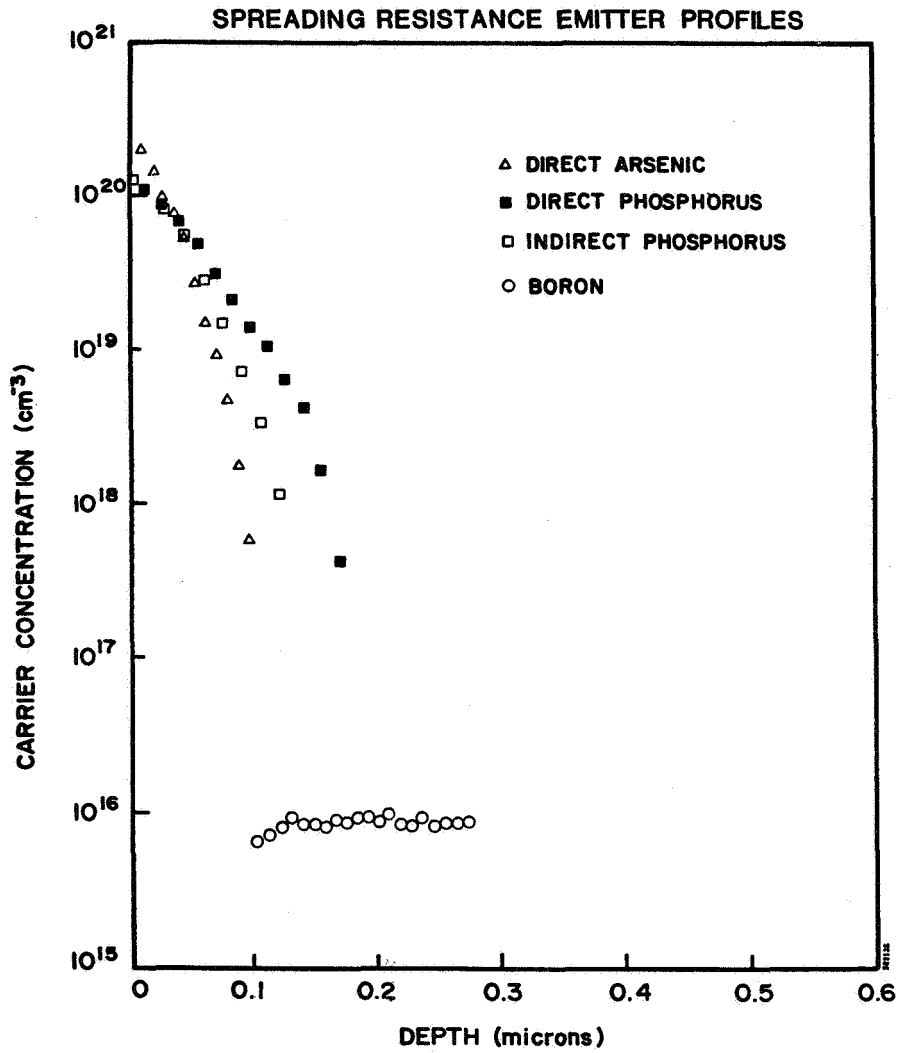


Figure 2: Spreading Resistance Profiles of Direct Arsenic, Direct Phosphorus, and Silicon Followed by Phosphorus Implants.

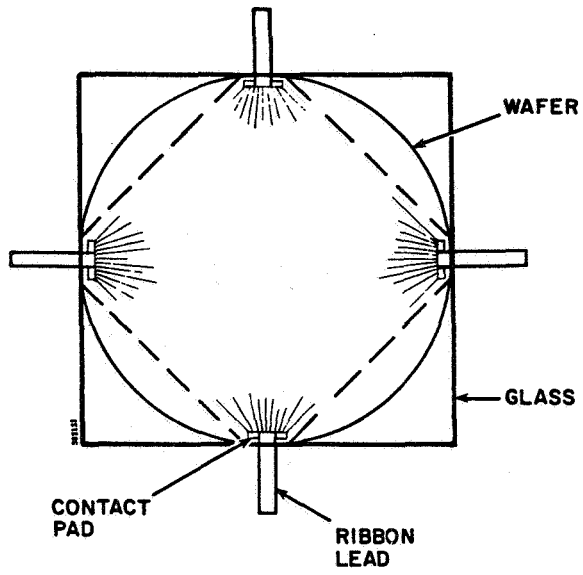


Figure 3: Configuration of Cell and Coverglass Assembly Prior to Sawing. The dotted lines indicate the saw cut positions.

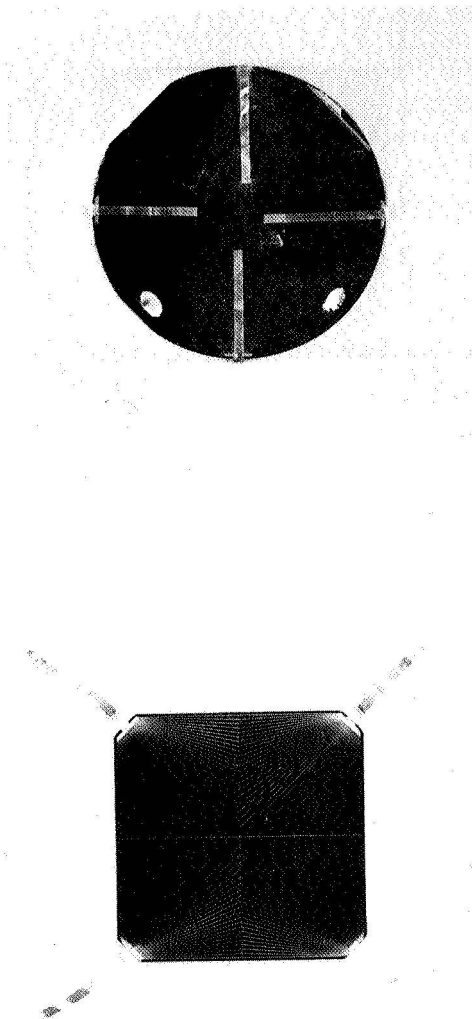


Figure 4: Photograph of the Solar Cell Assembly (a) Before sawing, with the ribbon leads folded over the front surface, and (b) after sawing, with the ribbon leads removed from the front surface.

SIMULATED SPACE FLIGHT TESTING OF COMMERCIAL TERRESTRIAL SILICON CELLS*

Paul M. Stella and Tetsuo F. Miyahira
Jet Propulsion Laboratory
California Institute of Technology
Pasadena, California

SUMMARY

Low cost silicon solar cells, manufactured for the terrestrial market, are examined for possible space flight use. The results of preliminary space environmental testing are reported and discussed. In addition, a number of possible obstacles to the use of these cells are examined. It is concluded that the terrestrial industry could provide an extremely low cost and reliable cell for space use.

INTRODUCTION

The need for new high volume, low cost solar cell and array technology necessary to support the next generation of space missions has been recognized by many (Ref. 1). The use of the shuttle will enable much more ambitious and massive payloads to be launched into Low Earth Orbit (LEO) which will create a significant increase in mission power requirements. In addressing this need NASA has sponsored the development of low cost space cells (Ref. 2). As a result of this work space cell manufacturers have developed candidate cell designs for future mission use under the Power Extension Package (PEP) program. It has been shown that a key to significant lowering of costs is through the means of large quantity production. In the case of the space cells, although a significant increase in annual volume will be required to support future needs, this demand may not be large enough to bring about dramatic cost savings. In addition, the continuing need for specialized low volume cell types will impede the space cell manufacturers from achieving the benefits of a large volume single product line.

However, the terrestrial solar cell industry would have no difficulty in producing the quantity of cells required for future space needs. Whereas the annual space cell production volume is presently measured in the tens of kilowatts, the terrestrial production volume is many megawatts. Although there are distinctly different technology drivers for the two applications many such as low cost and humidity resistance are similar. Furthermore the LEO mission application will reduce the need for a highly radiation resistant, low mass cell, requirements which would otherwise most likely exceed terrestrial cell capabilities.

* The research described in this paper presents the results of one phase of research carried out, at the Jet Propulsion Laboratory, California Institute of Technology, under Contract with the National Aeronautics and Space Administration.

This paper will address the question of whether or not the utilization of cells developed for the terrestrial market can satisfy future low cost space solar power needs. In particular, the results of space environmental testing of these terrestrial cells will be presented, and a discussion of capabilities and limitations of these cells will identify their possible potential.

TEST DESCRIPTION

For this evaluation, cells were purchased from six terrestrial manufacturers. All cells were made from single crystal P type Czochralski grown silicon. Modules are commercially available from five of these suppliers; the sixth was included due to the use of unique fabrication technology which may become commonplace within the next decade. One supplier also provided two types of cells representing different approaches commercially being offered by them. These samples represent a number of different technology approaches which are summarized in Table 1.

After receipt of the samples, mechanical and electrical characterization were performed. In this manner sizes and masses were obtained along with the necessary AMO performance, and spectral response. Samples were then selected from these groups for subsequent space type environmental testing including humidity-temperature storage, thermal vacuum soak, and 1 MeV electron irradiation. These will be described below. It should be noted that none of these cells were designed to survive space type requirements and that performance in the space type tests does not reflect upon their abilities to withstand the terrestrial requirements. In fact it is an accepted terrestrial practice to environmentally test assembled modules, and not single cells. In view of this no attempt will be made to identify a particular sample with the manufacturer.

MECHANICAL AND ELECTRICAL CHARACTERIZATION

Cell shapes vary from rectangular to round, with areas ranging from 38 cm² to nearly 98 cm², all larger than the PEP cells (36 cm²) or present space cells (4 cm² → 12 cm²). The two largest cells utilize metal conductor straps on the N⁺ surface in order to provide low resistive losses without large shadowing losses. Minimizing the cell series resistance is important in view of the large output currents which range from 1.4 to 3.3 Amps. The current densities of the samples averaged 34mA/cm² with the highest at 38mA/cm² and lowest at 30mA/cm². Cell efficiencies ranged from 8.1 percent to 12.6 percent. The performances are shown in Table 2 for each sample group. Of interest, the cell efficiencies are roughly inversely related to the cell active areas, with the exception of the large strapped samples, where resultant efficiencies fall in the mid value range of 10 percent, demonstrating the advantage of the strap concept. Fill factors (FF) generally fall below values observed on space cells, reflecting the impact of large areas and possibly less exacting contacting technologies. For these samples average fill factors varied from a low of 0.65 to a high of 0.76.

Although these efficiencies compare with a conventional 13 percent space cell, the lack of a strong terrestrial driver for low mass leads to a considerable difference in specific power. The influence of large wafer thickness and extensive solder coverage in some samples is appreciable. For samples with straps the mass of the strap external to the cell edge was excluded since this would normally be the interconnector.

The cell spectral response reflects material properties and processing variations and indicate a cell's potential performance under particulate radiation. For the samples examined here significant variations existed in the different groups' spectral characteristics, particularly in the short wavelength region (0.4 microns). For example, the highest sample's response was more than twice that of the lowest. These curves could be used to guide any necessary process or material modifications to enhance radiation resistance.

ENVIRONMENTAL TESTS

Humidity-Temperature Storage. - Selected samples were subjected to 20 days exposure at conditions of 45°C and 95 percent relative humidity. Electrical measurements were made at the end of 8 and 20 days exposure in order to evaluate changes from the initial values. With the exception of one group, no significant changes were observed during the 20 days. The sample group employing silk screened contacts showed a loss of 13 percent in power at 8 days, increasing slightly to 15 percent power loss at 20 days, the result of a significant fill factor degradation. The sample utilizing a liquid deposited AR coating showed no changes in coating appearance or output current.

High Temperature Soak. - Samples were subjected to seven days exposure at 120°C, at a pressure of less than 1×10^{-4} torr, primarily to evaluate whether any detrimental outgassing might occur from non-vacuum metallization and coating processes. No visible changes were observed and although a maximum output loss of approximately 2.5% was observed for one group this was not considered to be statistically significant.

1 MeV Electron Exposure. - Cells were irradiated in the JPL Dynamitron to a fluence of 3×10^{14} e/cm². Sample temperature was maintained at $28^\circ \pm 2^\circ\text{C}$ during the test. Inasmuch as a number of different processes normally impacting cell radiation resistance were represented among the cells, the measured losses fell in a wide range. In general, however, the losses were comparable to what is observed on a standard space cell under similar fluence. The lowest degradation was measured at a 13.4 percent power loss, whereas the greatest was 26.2 percent. These are compared to typical space cell results in Figure 1.

DISCUSSION

The results of these initial tests indicate that cells presently being produced for the terrestrial market are, with some exceptions, capable of surviving typical space acceptance tests; that the design requirements for earth use do not exclude space use. Furthermore, the terrestrial cell is expected to improve as a product in areas likely to further enhance space capabilities. For example, efficiency will be improved and mass reduced. These will be pursued independent of space needs. Efficiency is critical in reducing overall balance of systems costs such as protective coverings, shipping, etc. In the matter of mass, the less material used the lower the product cost.

The cell shape (round, rectangular) must be considered for space systems. In LEO space applications, array drag leads to a need for high packing factors to reduce the array area. In the case of a 10 cm round cell the maximum array cell area coverage will be less than 82 percent. By cutting this cell into a square, a much better array area coverage will be possible, reducing overall array size. This will introduce some additional cell cost but would be worthwhile at the overall systems level.

A primary concern in utilizing terrestrial cells is the question of contact interconnect designs capable of surviving a very large number of thermal cycles. It has been shown that solder has limited capabilities for LEO thermal cycling conditions (Ref 3). Since present terrestrial cells generally have extensive solder coverage whether they are capable of surviving the 30,000 LEO cycles of a 5 year mission is open to question. In fact, tests are presently underway to examine the terrestrial cells' contact behavior under thermal cycling, the first step in evaluating a useful interconnect approach.

CONCLUSIONS

Clearly the matter of thick, low packing efficiency cell shapes, and massive solder quantities limits the space potential of terrestrial cells. Yet these same areas are of concern to terrestrial manufacturers seeking reduced costs. Excess amounts of material mean high material costs, and low area efficiency means high system costs; so there is a trend to improvement along these lines, that should benefit space capabilities.

Commercial terrestrial solar cells appear to be capable of surviving space type environmental testing. The present cost of these cells is significantly lower than values projected for PEP cells. These cells are not however generally compatible with the requirements for efficient space solar array manufacture. It would be worthwhile to seek cell modifications that could enhance space use and to investigate what cost impacts would occur. As mentioned above, many of these modifications, such as rectangular shapes for packing factor improvement and material thickness reduction are also beneficial to the terrestrial user, and will likely be pursued by that industry. Thus, with the PEP cell work this would allow the concept of a low cost cell for space use to be approached from two directions, enhancing the possibility for solar array cost reductions. The most critical question is whether or not the low cost cell contact schemes are compatible with the need for an interconnect method that will survive tens of thousands of thermal cycles.

REFERENCES

1. Randolph, L. P., "Photovoltaic Outlook from the NASA Viewpoint", 15th IEEE PSVC proceedings, Orlando, Fl., 1981, pp 10-13.
2. Matthei, K. W., Zemmrick, D. K. and Webb, M., "Optimization of Large Area Solar Cells for Low Cost Space Application", 15th IEEE PVSC proceedings, Orlando, Fl., 1981, pp 228-232.
3. Luft, W., "Solar Cell Interconnector Design", IEEE Transactions on Aerospace and Electronic Systems, Vol. AES-7, No. 5, Sept. 1971, pp 781-791.

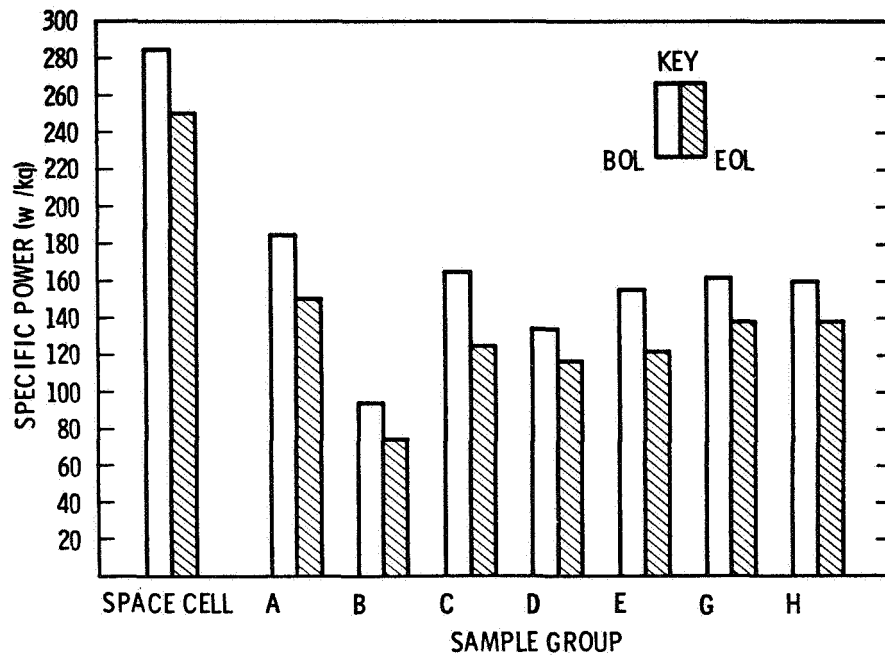
TABLE 1.
 TERRESTRIAL CELL FABRICATION TECHNOLOGIES

CELL PROCESS	TECHNOLOGY
Junction Formation	Diffusion * Ion Implantation
AR Coating	Texturing * CVD Vacuum Evaporation * Liquid-Bake
Cell Contacts	Ni Plate/Solder Evaporation * Silk Screen Ink Metal Straps

* Standard Space Cell Technologies

TABLE 2.
SAMPLE CHARACTERISTICS

Sample ID	Cell Area (cm ²)	Isc (A)	Pmax (mW)	FF	Eff 28°C AMO	Cell Mass mg/cm ²	Comments
A	46	1.56	701	.76	11.1	83	
B	79	2.34	886	.65	8.1	120	Full Solder Coverage
C	38	1.43	628	.75	12.6	101	
D	46	1.48	579	.67	9.5	94	Full Solder Coverage
E	82	2.57*	1030	.69	8.9*	88	*Textured, No AR, contact metal straps
G	98	3.27	1370	.73	10.3	86	N contact metal straps, Soldered P surface
H	68	2.30	826	.65	8.9	76	



● SPECIFIC POWER AT BOL AND EOL (3×10^{14} 1 mev ELECTRONS) *

▶ REFERENCE SPACE CELL IS 2 OHM-CM, 250 MICRONS THICK

EFFECT OF 1MEV ELECTRONS

FIGURE 1

DIFFUSION LENGTH MEASUREMENTS IN SOLAR CELLS - AN ANALYSIS AND COMPARISON OF TECHNIQUES*

John A. Woollam†, A. Azim Khan, and R.J. Soukup
Department of Electrical Engineering
University of Nebraska
Lincoln, Nebraska

Allen M. Hermann
Solar Energy Research Institute
Golden, Colorado

SUMMARY

A brief review of the major techniques for measuring minority carrier diffusion lengths in solar cells is given. Emphasis is placed on comparing limits of applicability for each method, especially as applied to silicon cells or to gallium arsenide cells, including the effects of radiation damage.

INTRODUCTION

In this paper we are undertaking a big topic, and have had to limit the number of techniques studied in-depth. In all cases we have put numbers into equations appearing in references in order to determine limits of applicability of various methods. Parameters are: material type (direct gap or indirect gap, usually GaAs or Si), range of values found in the literature for diffusion lengths including radiation damage values, doping density, optical absorption coefficient, recombination velocity, and cell dimensions. Some of our conclusions are expressions of opinion, and we welcome open discussion. A bibliography is given in the appendix.

A limited number of reviews or comparisons are in the literature. For example, Runyan's book Semiconductor Measurements and Instrumentation has a chapter on lifetime, including references. The American Society for Testing and Materials has a book Lifetime Factors in Silicon, and a publication "Minority Carrier Diffusion Length in Silicon by Measurement of Steady-State Surface Photovoltage". Reynolds and Meulenberg (1974) compared four techniques. K. O. Leedy has collected "A Bibliography on Electron Beam Induced Current Analysis of Semiconductor Devices" (1977).

We begin our analysis of minority carrier diffusion length determinations by writing down the familiar diffusion equation, assuming minority electrons are being generated in a p-type solar cell base:

*Supported by NASA Lewis Grant NAG3-120.

†Also of Universal Energy Systems, Dayton, Ohio.

$$D_n \frac{d^2 \delta n_p}{dX^2} - \frac{\delta n_p}{\tau_n} + G_n(X) = 0 \quad (1)$$

where D_n is the diffusion coefficient, τ_n the minority carrier lifetime, $G_n(x)$ the generation rate, and δn_p the density of generated excess minority electrons. The general solution is

$$\delta n_p = A \cosh \frac{X}{L_n} + B \sinh \frac{X}{L_n} - f(G_n(X)), \quad (2)$$

where f is some function, and $L_n = \sqrt{D_n \tau_n}$ is the minority carrier diffusion length.

UNIFORM GENERATION

The simplest application of equations (1) and (2) is when $G_n(x) = \text{constant}$ (uniform generation). If $\delta n_p = 0$ at the solar cell junction depletion region edge, and the surface away from the junction is described by a surface recombination velocity, then the short circuit current, J_{sc} , is a simple function of diffusion length. In the case of a perfectly efficient BSF the recombination velocity is zero, and if the cell thickness is large compared with L_n ,

$$J_{sc} = q G_n L_n. \quad (3)$$

The point to make concerning uniform generation techniques is that the relationship between current and diffusion length is generally straight forward. However, making an accurate measurement of the generation rate is more difficult. If cell geometry remains nearly the same for all cells investigated then the technique is quite useful, especially for comparative purposes. These measurements have been done using γ -rays, X-rays, and particle beams (See bibliography attached).

ELECTRON BEAM INDUCED CURRENTS

Solutions to equation (1) are more complicated when absorption depends on position. A popular technique for determining L , especially in direct gap materials is the so called EBIC technique. There are a large number of papers in this area, and for the bibliography we have selected ones that best helped us to understand fundamentals and delineate major conclusion.

In the early 1970's Hackett made a detailed analysis of electron beam excited minority carrier diffusion profiles in semiconductors. He assumed the electron beam was an ideal steady state point source

located a distance ξ beneath the semiconductor surface having a characteristic recombination velocity s . In Hackett's analysis a normalized recombination velocity $S=s/(L_b/\tau_b)$ is defined, where L_b and τ_b are diffusion length and lifetime respectively. Jastrezewski, Lagowski, and Gatos used Hackett's results to show that

$$\Delta p(\xi) = (GL_b^2/D) \left\{ 1 - [S/(S + 1)]e^{-\xi/L_b} \right\}, \quad (4)$$

where L_b is the "bulk" diffusion length (our ultimately desired L) uninfluenced by effects of surface recombination at the surface through which the beam is passing. An L_{eff} is defined as the "apparent L " observed, as is influenced by recombination. L_{eff} is determined by measuring currents, I , generated at a junction a distance X from the electron beam, and

$$I = I_0 e^{-X/L_{eff}}. \quad (5)$$

In this geometry, X and ξ are perpendicular to each other. By Eqn. (4) and a simple argument one gets

$$\frac{L_{eff}}{L_b} = \left\{ 1 - [S/(S + 1)]e^{-\xi/L_b} \right\}^{1/2}. \quad (6)$$

This is an important equation, and is plotted in Figure 1. Thus when $S = 0$, $L_{eff} = L_b$, always. If $S = \infty$, $S/(S + 1) = 1$ and $L_{eff} = L_b$, when ξ is several times larger than L_b . Intermediate cases are shown in Figure 1. ξ can be controlled by varying the electron beam energy, and this is plotted in Figure 2 for silicon and gallium arsenide. Thus, for a given energy, the electron beam penetrates considerably deeper in silicon than in gallium arsenide. Note that

$$\ln \left(1 - (L_{eff}^2/L_b^2) \right) = \ln (S/S + 1) - \xi/L_b. \quad (7)$$

So a plot of the left hand side vs. ξ gives S from the intercept and L_b from the slope. This is not as simple as it looks. To make the plot, guesses for L_b are made until a self consistent straight line plot is found. Also, S is the normalized parameter.

To better define the situation Watanabe, Actor, and Gatos showed that the true recombination velocity s can be determined from

$$s = D \left[\frac{\partial}{\partial \xi} \ln I \right]_{\xi = 0}, \quad (8)$$

where D is the diffusion coefficient. (On the basis of this they made spatial profiles of s over the surface of a representative silicon sample.) The above analysis demonstrates that bulk diffusion lengths can be determined by EBIC even when surface recombination influences experimental results.

In all measurement techniques considered in this paper, measurement of L becomes more difficult when L is comparable to material or device dimensions. This is often the situation for solar cell designs. The problem was addressed by Flat and Milnes in 1978 for the EBIC technique, and Von Roos also determined that measurements of L were especially difficult when L is comparable to or greater than layer thickness.

Thus EBIC is a very powerful and fundamental tool for determining L, but the user should be aware of the potential complications. To completely avoid surface recombination effects, Figure 1 shows that $\xi \sim 2.5 L_b$ is needed, which implies that L_b should be less than about 20 μm for silicon, and less than about 8 μm for gallium arsenide. $L < 8 \mu\text{m}$ is often the case for gallium arsenide, but 20 μm is a rather short diffusion length even in irradiated silicon. Thus to measure L using EBIC in silicon probably requires use of the analysis associated with equations (4) through (8). Even for materials with short diffusion lengths one should use structures whose dimensions are large compared with diffusion lengths.

SCHOTTKY BARRIER PHOTOCURRENT

In this technique a Schottky barrier solar cell is made on the material of interest. Monochromatic light is shined on the cell, and the cell can be reverse biased. If the cell thickness is much larger than the diffusion length, then the short circuit current is given by:

$$J(\lambda) \sim \left(1 - \frac{e^{-\alpha W}}{1 + \alpha L} \right) \quad (9)$$

where α is the optical absorption coefficient and W the depletion layer width. If experiments are done with no bias, then $W = W_0$.

Thus

$$\frac{J(\lambda)}{J_0(\lambda)} = \frac{1 + \alpha L - e^{-\alpha W}}{1 + \alpha L - e^{-\alpha W_0}} \equiv J \text{ normalized} \quad (10)$$

A plot of J_{norm} vs. αW gives a series of curves dependent on αL . Thus a comparison of calculated and measured J_{norm} vs. αW yields αL , and L, if α is known.

We have analyzed expected results from this type experiment for both silicon and gallium arsenide, and Table I shows our results.

Doping densities of 10^{14} to $10^{18}/\text{cm}^3$ are assumed. For a density of 10^{14} per cm^3 depletion widths are from $W_0 = 5 \mu\text{m}$ to $W = 10 \mu\text{m}$ at high reverse bias. For silicon and gallium arsenide the range of absorption coefficients vs. wavelength is reasonably well known. (If α is not well known spectroscopic ellipsometry is a non-destructive, accurate method to measure α). In Table I we have assumed that the experimenter can set the monochromator to get α near 200 cm^{-1} , 10^3 cm^{-1} or 10^5 cm^{-1} . Absorption edges in direct gap materials are so sharp near the band edge that getting 200 cm^{-1} may be difficult. For silicon this value is reasonable. In any case, the value of L for making $\alpha L = 1$ for each case is listed in the table. αW_0 is the simple product. Calculated sensitivities, using Eqn. 10 are given. Since we feel that $\sim 10\%$ sensitivity is needed, the range of L for which this technique is applicable is given in the table. For comparison, the last column gives the experimentally observed ranges found in silicon and gallium arsenide, including radiation damage values. We conclude that this technique is generally good for direct gap materials but will work only for very lightly doped silicon, and even then only marginally. Two words of caution: In direct gap materials α changes so rapidly with λ that great care should be taken to measure α at the wavelength of interest. Note that α is temperature and impurity sensitive near the band edge. Secondly, the width W is often measured by capacitance voltage plots. Since materials other than silicon have high interface state densities, charges in these states shift C-V curves and give erroneous values for W .

SURFACE PHOTOVOLTAGE

In this technique light of wavelength just above the band edge strikes the surface of the semiconductor exciting electron hole pairs. Because the surface is a "sink" for recombination, a potential gradient is created relative to the back surface of the material. Generally this voltage is detected capacitively (an ac coupling) by chopping the light beam at roughly 10 Hz. Measurements of the intensity necessary to make the surface photovoltage constant are made as a function of wavelength. Plots of this intensity are made vs. α^{-1} and the intercept of the zero intensity is the diffusion length. The technique was shown by Wang et al to work for pn junctions (under specified conditions), and by Stokes and Chu for solar cell short circuit currents.

The conditions for reliable use are as follows:

- (1) $\alpha d_1 \ll 1$ i.e. absorpt. in the emitter (or surface depl. reg.) is small.
- (2) $d \gg L$ i.e. the cell is thick compared to L ,
- (3) $p \gg \Delta n$ i.e. low level injection,
- (4) $d_1 \ll L$ i.e. the emitter is thin,
- (5) $\alpha d > 1$ i.e. most light is absorbed in the base,

where $\alpha = \alpha(\lambda)$ is the optical absorption coefficient, d_1 the emitter thickness for a cell geometry or surface depletion thickness in bulk material, d the total cell thickness, and L the diffusion length. To meet condition (1), α is made low by choosing λ near the band edge. Condition (2) is often the most difficult to meet for common solar cell designs. Philips showed that this condition could be relaxed, but Chu and Stokes found poor agreement if $d \sim L$. (3) is met by choosing reasonable light intensity. For most cells, $d_1 \ll L$ by deliberate design. Finally, $\alpha d > 1$ is easy to satisfy because the base of cells are often thick enough to absorb most of the light, and because α can be controlled by wavelength selection. The above statements are true for silicon cells, gallium arsenide cells, and recently for amorphous silicon cells where diffusion lengths of only a few hundred angstroms can be found. As a practical rule of thumb, the shortest diffusion length measurable is about $\frac{1}{4}$ of the $(1/\alpha)$ value at the highest α needed to make the measurement. For example, in a - Si $\alpha = 10^5 \text{ cm}^{-1}$ at 2.5 e.v. photon energies. Thus $\frac{1}{4} \times 10^{-5} \text{ cm} = 250 \text{ \AA}$! In GaAs the minimum L measurable is about 0.1 \mu m for $\alpha_{\text{max}} \sim 2 \times 10^4 \text{ cm}^{-1}$.

FINAL STATEMENTS

All techniques have the limitation that semiconductor thicknesses should be large in comparison with diffusion lengths, in order to simplify interpretation. This is often violated in solar cell designs. Each of the techniques discussed have advantages and disadvantages which must be considered. We feel it is important that the limits of applicability of particular methods be realized.

BIBLIOGRAPHY

General

1. Runyan, W. R.: Semiconductor Measurements and Instrumentation, Texas Instruments Electronics Series, McGraw-Hill Book Co., 1975.
2. Westbrook, R. D.: ASTM Special Technical Publication 712 "Lifetime Factors in Silicon", American Society for Testing and Materials, Philadelphia, 1980.
3. Reynolds, J. H., and Meulenberg, A., Jr.: "Measurement of Diffusion Length in Solar Cells", J. Appl. Phys. 45, 2582 (1974).
4. Leedy, K. O.: "A Bibliography on Electron Beam Induced Current Analysis of Semiconductor Devices", Solid State Technology, February 1977.
5. NASA Conference Publication 2020, "Solar Cell High Efficiency and Radiation Damage", National Aeronautics and Space Administration, 1977.
6. NASA Conference Publication 2169, "Space Photovoltaic Research and Technology 1980", National Aeronautics and Space Administration, 1980.

Uniform Generation Method

7. Gremmelmaier, R.: "Irradiation of pn Junctions with Gamma Rays: A Method for Measuring Diffusion Lengths", Proc. IRE 46, 1045, (1958).
8. Rosenzweig, W.: "Diffusion Length Measurement by Means of Ionizing Radiation", Bell Systems Tech. J. 41, 1573 (1962).
9. Aukerman, L. W., Millea, M. F., and McColl, M.: "Diffusion Lengths of Electrons and Holes in GaAs", J. Appl. Phys. 38, 685, (1967).

Electron Beam Induced Currents Method

10. Hackett, W. H., Jr.: "Direct Measurement of Very Short Minority-Carrier Diffusion Lengths in Semiconductors", J. Appl. Phys. 42, 3249, (July 1971).
11. Hackett, W. H., Jr.: "Electron Beam Excited Minority-Carrier Diffusion Profiles in Semiconductors", J. Appl. Physics 43, 1649, (April 1972).

BIBLIOGRAPHY (continued)

Electron Beam Induced Currents Method (continued)

12. Jastrzebski, L., et al: "Application of Scanning Electron Microscopy to Determination of Surface Recombination Velocity: GaAs", Appl. Phys. Lett. 27, 537, (November 1975).
13. Watanabe, M., et al: "Measurement of Minority-Carrier Lifetime and Surface Recombination Velocity with a High Spacial Resolution", International Elec. Devices Meeting (1976).
14. Weizer, V. G., and Andrews, C. W.: "Application of the SEM to the Measurement of Solar Cell Parameters", NASA TMX-73637, (1977).
15. Oakes, J. J., et al: "Diffusion Length Determination in Thin-Film Cu_xS/CdS Solar Cells by Scanning Electron Microscopy", J. Appl. Phys. 48, 2548, (June 1977).
16. Flat, A., and Milnes, A. G.: "Interpretation of Scanning Electron Microscope Measurements of Minority Carrier Diffusion Lengths in Semiconductors", Int. J. Elec. 44, 629, (August 1977).
17. Gatos, H. C., et al: "Surface Recombination Velocity and Diffusion Length of Minority-Carriers in Heavily Doped Silicon Layers", NASA Conf. Pub., 2020, 59, (1977).
18. Watanabe, M., et al: "Determination of Minority-Carrier Lifetime and Surface Recombination Velocity with High Spacial Resolution", IEEE Trans. Electr. Devices, ED-24, 1172, (1977).
19. Partin, D. L., et al: "Effects of Contact Metals on Minority Carrier Diffusion Lengths in GaAs", J. Elec. Materials 7, 279, (1978).
20. VonRoos, O.: "Analysis of the Interaction of an Electron Beam With a Solar Cell-I", Solid State Elec. 21, 1063, (1978).
21. VonRoos, O.: "Analysis of the Interaction of an Electron Beam With a Solar Cell-II", Solid State Elec. 21, 1069, (1978).
22. VonRoos, O.: "Analysis of the Interaction of an Electron Beam With a Solar Cell-III", Solid State Elec. 22, 773, (1979).
23. Partin, D. L., et al: "Effect of Surface Preparation and Heat-Treatment on Hole Diffusion Lengths in VPE GaAs and GaAsP", J. J. Electrochem. Soc. 126, 1581, (1979).

BIBLIOGRAPHY (continued)

Schottky Barrier Photocurrent Method

24. Lender, R. J., Tiwari, S., Borrego, J. M., and Ghandhi, S. K.: "Diffusion Length Measurements in Schottky Barrier GaAs Solar Cells", *Solid State Electronics* 22, 213, (1979).
25. Lastras-Martinez, A., Raccah, P. M., Triboulet, R.: "Minority Carrier Diffusion Length Measurements in CdTe by a Photocurrent Technique", *Appl. Phys. Letts.* 36, 469 (1980).
26. Sukegawa, T., Watanabe, T., Mizuki, T., and Tanaka, A.: "Differential Photocurrent Method for Measurement of the Optical Absorption Coefficient and the Minority Carrier Diffusion Length in a Semiconductor", *IEEE Trans. on Electron Devices* ED-27, 1251, (1980).

Surface Photovoltage Technique

27. Goodman, A. M.: "A Method for the Measurement of Short Minority-Carrier Diffusion Lengths in Semiconductors", *J. Appl. Phys.* 32, 2550, (December 1961).
28. Vilms, J., Spicer, W. E.: "Quantum Efficiency and Radiative Lifetime in p-type GaAs", *J. Appl. Phys.* 36, 2815, (Sept. 1965).
29. Phillips, W. E.: "Interpretation of Steady-State Surface Photovoltage Measurements in Epitaxial Semiconductors Layers", *Solid State Elec.* 15, 1097, (1972).
30. Wang, E. Y., Baroana, C. R., and Brandhorst, H. W., Jr.: "Surface Photovoltage Method Extended to Silicon Solar Cell Junction", *J. Electrochem. Soc.*, 973, (July 1974).
31. Li, S. S.: "Determination of Minority-Carrier Diffusion Length in Indium Phosphide by Surface Photovoltage Measurement", *Appl. Phys. Letts.* 29, 126, (July 1976).
32. Stokes, E. D., and Chu, T. L.: "Diffusion Lengths in Solar Cells From Short Circuit Current Measurements", *Appl. Phys. Letts.* 30, 425, (1977).
33. Chu, T. L., and Stokes, E. D.: "A Comparison of Carrier Lifetime Measurements by Photoconductive Decay and Surface Photovoltage Methods", *J. Appl. Phys.* 49, 2996, (May 1978).
34. Brandhorst, H. W., Jr., Acampora, F. L., and Potter, A. E., Jr.: "High Photovoltages in Cadmium Sulfide Films", *J. Appl. Phys.* 39, 6071, (December 1978).

BIBLIOGRAPHY (continued)

Surface Photovoltage Technique (continued)

35. American Society for Testing and Materials F391-73T, "Minority Carrier Diffusion Length in Silicon by Measurement of Steady-State Surface Photovoltage" ASTM.

Table I - Schottky Barrier Photocurrent Technique

Doping Density	Depletion Region Width		Assumed Absorption Coeff., α	L to make $\alpha L = 1$	αW_0	Sensitivity $\frac{\Delta J}{J}$, %	Measurable Range of L	Observed Ranges of L
	W_0 (zero bias)	W (with bias)						
$10^{14}/\text{cm}^3$ ($> 100 \Omega\text{cm}$ in Si)	5 μm	10 μm	200 cm^{-1}	50 μm	0.1	8%	5 to 30 μm	20 to 500 μm in Si (2 to 100* in GaAs)
			10^3	10	0.5	17		
			10^4	1	1.5	10		
$10^{16}/\text{cm}^3$ (1 Ωcm Si 2 Ωcm GaAs)	0.5 μm	1 μm	200 cm^{-1}	50 μm	0.01	1%	0.3 to 2 μm	10 to 300 μm in Si 0.5 to 3 μm in GaAs
			10^3	10	0.05	4		
			10^4	1	0.50	17		
			3×10^4	0.3	1.5	10		
$10^{18}/\text{cm}^3$ ($< 0.1 \Omega\text{cm}$ Si 0.3 Ωcm GaAs)	0.1	0.3	200 cm^{-1}	50 μm	0.002	$<< 1\%$	$\leq 1 \mu\text{m}$ only	3 to 30 μm in Si 0.2 to 2 μm in GaAs
			10^3	10	0.01	1		
			10^4	1	0.1	8		
			5×10^4	0.2	0.5	17		

*Diffusion lengths this large in GaAs are quite rare: See Nelson's papers.

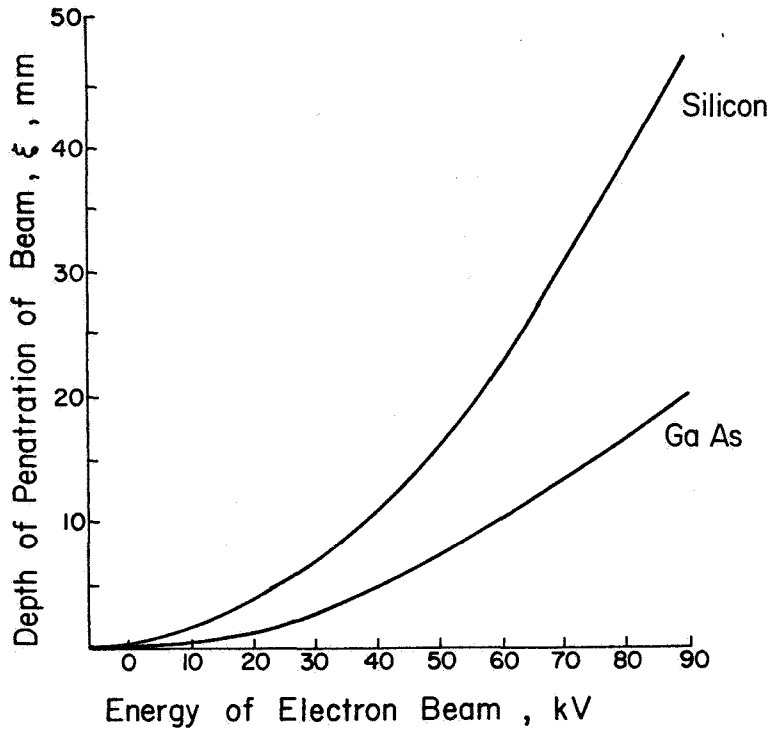


Fig. 1: Normalized diffusion length L_e/L_b vs. normalized depth ξ/L_b , for various values of normalized surface recombination velocity.

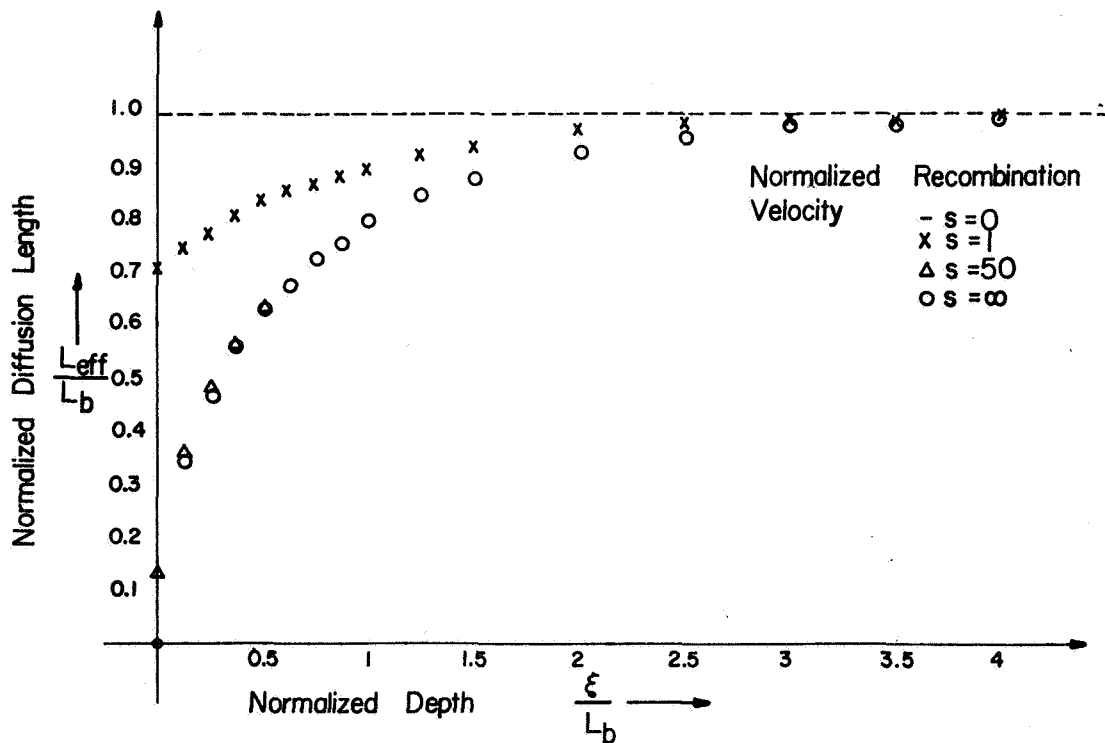


Fig. 2: Electron beam penetration depth as a function of beam energy for Si and GaAs.

PROGRESS TOWARD CASCADE CELLS MADE BY OM-VPE*

Peter G. Borden, Ross A. LaRue, and Michael J. Ludowise
Varian Associates, Inc.
Palo Alto, California

SUMMARY

OM-VPE has been used to make a sophisticated monolithic cascade cell, with a peak AM0 efficiency of 16.6%, not corrected for 14% grid coverage. The cell has 9 epitaxial layers. The top cell is 1.35 microns thick with a 0.1 micron thick emitter. Both cells are heteroface n-p structures. The cascade cell uses metal interconnects. Details of growth and processing are described.

INTRODUCTION

This paper describes the design, fabrication, and testing of a high efficiency monolithic cascade cell made using Organometallic Vapor Phase Epitaxy (OM-VPE), and interconnected using the MIC² structure. A number of significant results have been obtained, including

- 16.6% AM0 efficiency at a concentration of 10.7 suns, uncorrected for the 14% obscuration (19.3% active area efficiency).
- .5 cm² active area (.71 cm by .71 cm), with wafer yields in excess of 4 cm² per processed wafer.
- A 1.35 micron thick 30% AlGaAs heteroface top cell with an emitter only 0.1 microns thick.
- An n-on-p heteroface GaAs bottom cell stable enough to endure the 20 minute, 780 °C growth of the top cell.

The cell design and structure will be described first. The fabrication process follows, followed by a presentation of experimental results.

Cell Design

The cell structure is listed in Table 1. It is based on a computer optimized design for 400 suns AM2 and experimental iterations to optimize the quantum yield of the top cell. As can be seen, heteroface structures are used for both the top and bottom cells. The entire structure contains nine layers. These are formed in continuous sequence under computer control in the OM-VPE reactor. Uniformity over a 1.5 x 2 inch wafer is typically $\pm 7.5\%$.

An n-on-p structure is used for the bottom cell. Typically, n-type dopants are slow diffusers in GaAs; this gives the GaAs cell an inherent stability during the growth of the top cell. The n-on-p structure has other advantages for space applications, including long base diffusion lengths for better radiation hardness¹. The low resistivity of the n-type emitter reduces emitter sheet resistance, an important consideration in cells using MIC² interconnects.

The top cell is composed of six layers, the junction occurring in 30% AlGaAs, with a bandgap of 1.82 eV. From the top down, these are a GaAs contact layer, used in the contacting process. Next is an 80% AlGaAs window layer and an emitter 0.10 microns thick. This is the thinnest emitter ever reported for a heteroface cell, and is required because of the relatively short diffusion length in n⁺ 30% AlGaAs. The p-type base is about 1 micron thick, and collects most of the photons used by the top cell. Below the base is a back surface field (BSF) layer, required to prevent carriers from leaking out the back of the thin base. The remaining layer is used for contacting during the interconnect process.

Note that the top cell is extremely thin, and is, to the knowledge of the authors, the thinnest single crystal solar cell ever reported. The motivation is as follows: To properly current match an AlGaAs/GaAs cascade cell, the top cell should have a bandgap of about 1.9 eV. The problem is that key properties of AlGaAs, such as mobility and diffusion length, degrade rapidly as the direct-indirect transition at 1.95 eV is approached. An alternative strategy is to make the top cell so thin that it is semi-transparent, allowing some of the near gap photons to penetrate through to the bottom cell. In this manner, a current matched structure with a lower gap top cell is possible. A careful tradeoff of practical material parameters, bandgap, and efficiency places an optimum gap for the top cell at about 1.82 eV.

Figures 1 and 2 show quantum yields for top and bottom cells made with this design strategy. Figure 1 shows the quantum yield of a 1.82 eV AlGaAs cell. This is corrected for both AR coating reflection and grid coverage. The downward slope of the red response is partially due to the semi-transparency. Figure 2 shows the quantum yield of a GaAs bottom cell. This is corrected for AR coating reflection, but not grid coverage. Note the sharp cut-off at the bandgap of the top cell. But note also that some light above the top cell bandgap energy leaks through.

Figure 2 attests to the stability of the bottom cell. This plot is not corrected for the 14% grid obscuration, so that the internal quantum yield is flat at about 90%. This cell has been exposed to a temperature cycle of 780°C for 20 minutes.

FABRICATION PROCESS

The MIC² interconnect process has been used with this cell. This has been described elsewhere², and will be summarized here. In this process, narrow grooves are etched through the top cell to the emitter of the bottom cell. Metal deposited in these grooves shorts the emitter of the bottom cell to the base of the top cell. This interconnect is particularly useful in the development of cascade cells because it requires no tunnel junction and allows divert probing of the top and bottom cells.

Figure 3 outlines the MIC² process. Two selective etches are used. One etch attacks GaAs and 30% AlGaAs, but not 80% AlGaAs. HF etches 80% AlGaAs, but not the other materials. The process proceeds as follows: Following masking, the two etches are used to etch down to the contact layer below the top cell BSF. The cell is remasked, and a narrower groove etched in the bottom of the first groove through to the emitter of the bottom cell. The same mask is used to deposit an n-type ohmic contact on the top of the cell and the emitter of the bottom cell. Finally, a p-type contact placed in the groove connects the n-type contact metal to the buried contact layer. The cell is alloyed, cap stripped, and AR coating applied.

The grooves are nominally 13 microns wide, on 202 micron centers. The top contact stripes are nominally 7 microns wide on the same centers, for an obscuration of 10%. This design is appropriate for 400 suns AM2. Low concentration or 1 sun designs have contacts spaced typically 5 or more times further apart, and obscuration is negligible. In practice, the grooves and grids are 19 and 10 microns wide respectively, increasing obscuration to 14%. This can be reduced considerably through further process enhancements.

We have used AuGa/Ni/Au for n-type contacts and Al/Mg/Au contacts for p-type. These are chosen because they alloy at the same temperature and time, and thus amenable for use in a two-layer contact.

Anti-reflection coating is applied by selective etching of the GaAs cap layer, followed by plasma deposition of a single layer of Si₃N₄. Two-layer coatings will significantly improve performance. The single layer has been used at this stage of development because of its simplicity and yield.

PERFORMANCE RESULTS

Cells are typically made on 1.5 x 2 inch wafers, with the mask providing 6 devices per wafer. Each device has an active area 0.5 cm², with dimensions .71 x .71 cm. The entire chip active area measures .77 cm², with two large contact busses taking up the remaining area. This is an optimized design for 400 suns, AM2. The cells have a single Si₃N₄ AR coating. The top contact grid is not plated.

Cells have been tested in a Spectrolab XT-10 simulator with an AM0 filter set. Intensity is set to one sun, using a GaAs calibration cell. A glass lens provides concentration. The cell has no cooling, and the nominal ambient temperature is 24°C. The concentration is measured by taking the ratio of the cascade cell short circuit current at concentration to the one sun short circuit current.

Table 2 shows the efficiency at various concentrations. Table 3 lists other cell parameters. Figure 4 shows the cell IV characteristics. The efficiency assumes a 0.5 cm² cell area. In Table 2, three columns tabulate the measured efficiency (14% obscuration), the internal efficiency (no obscuration) and efficiency corrected to 5% obscuration, as might be typical for a 1 sun cell. The efficiency at 10.7 suns is close to that of a very good GaAs cell.

This cell has about 17% current mismatch, with the bottom cell short circuit current greater than the top. This can be determined by illuminating with a He-Ne laser. Such light, which is absorbed in the top cell alone, improves the short

circuit current by about 35%. This mismatch is due to the cell being an AM2 design, that we are only using a single layer AR coating, and that more work is needed to optimize the top cell thickness to properly exploit its semi-transparency.

CONCLUSION

This work has demonstrated that cascade cells can be made with areas approaching those required for space applications, and that high efficiencies are realizable. To achieve these efficiencies, several design techniques have been employed, including:

- use of thin, semi-transparent top cells to enhance current matching while maintaining top cell quantum yield.
- use of n-p cells to maintain stability of the bottom cell during growth of the top cell.
- use of top cell BSF to prevent carriers from spilling out the back of the base.

It is anticipated that considerable improvements are possible through such steps as use of a 2-layer AR coating, plating of grids to improve fill factor, and better current matching through an optimized AR coating and proper thickness top cell. Improvements of this sort, none of which require new technology development, should increase efficiency well beyond that of the best GaAs cell.

* Different aspects of this work were supported by NASA Contract NAS3-22232 and by DOE through SERI subcontract XP-0-8081-1.

REFERENCES

1. Flood, D. J., Swartz, C. K. and Hart, Jr., R. E., GaAs Homoijunction Solar Cell Development, In Space Photovoltaic Research and Technology 1980, NASA Conference Publication 2169, p. 239.
2. Borden, P. G., LaRue, R. A., Ludowise, M. J., Saxena, R. and Gregory, P. E., A Metal-Interconnected Cascade (MIC²) Solar Cell, IEDM Technical Digest, 150 (1981).

TABLE I.-CELL STRUCTURE

<u>LAYER</u>	<u>PURPOSE</u>	<u>TYPE</u>	<u>MATERIAL</u>	<u>THICKNESS</u>
9	Contact	n^+	GaAs:Se	0.5 μm
8	Window	n^+	$\text{Al}_{.8}\text{Ga}_{.2}\text{As:Se}$	0.15
7	Emitter	n^+	$\text{Al}_{.3}\text{Ga}_{.7}\text{As:Se}$	0.1
6	Base	P	$\text{Al}_{.3}\text{Ga}_{.7}\text{As:Zn}$	1.0
5	BSF	P	$\text{Al}_{.8}\text{Ga}_{.2}\text{As:Zn}$	0.1
4	Contact	P^+	$\text{Al}_{.32}\text{Ga}_{.68}\text{As:Zn}$	0.2
3	Window	n	$\text{Al}_{.8}\text{Ga}_{.2}\text{As:Se}$	0.1
2	Emitter	n	GaAs:Se	0.5
1	Base	p	GaAs:Zn	2.0
0	Substrate	p	GaAs:Zn	12 mils

TABLE II.-MIC² AMØ EFFICIENCY

<u>Concentration</u> <u>(suns)</u>	<u>Efficiency at Obscuration of</u>		
	<u>14%</u>	<u>5%</u>	<u>0%</u>
1	13.2%	14.6%	15.3%
3.97	15.4%	17.0%	17.9%
8.79	16.5%	18.2%	19.2%
10.67	16.6%	18.3%	19.3%

14% obscuration (grooves, top contact)
 .5 cm² active area (.71 x .71 cm)
 30% AlGaAs top cell
 GaAs bottom cell

TABLE III.- CELL PERFORMANCE

<u>Conc. (Suns)</u>	<u>V_{oc} (V)</u>	<u>I_{sc} (mA)</u>	<u>FF</u>	<u>η (%)</u>
1	2.15	6.1	.681	13.2
3.97	2.27	24.2	.753	15.4
8.79	2.32	53.6	.786	16.5
10.67	2.33	65.1	.782	16.6

.5 cm² active area
 14% obscuration
 AMO, simulated
 Single layer Si₃N₄ AR coating

30M-276 CAP OFF
MEASURED 11/23/81 SLITS: 5NM

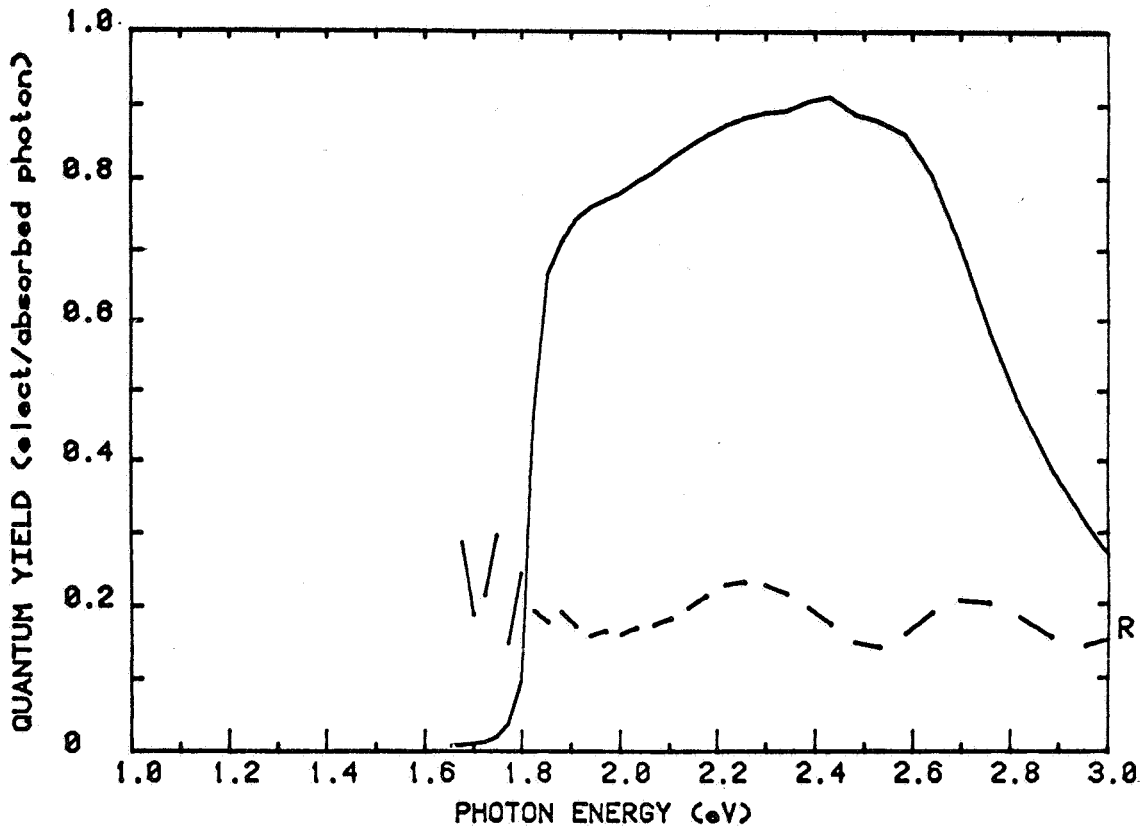


Figure 1

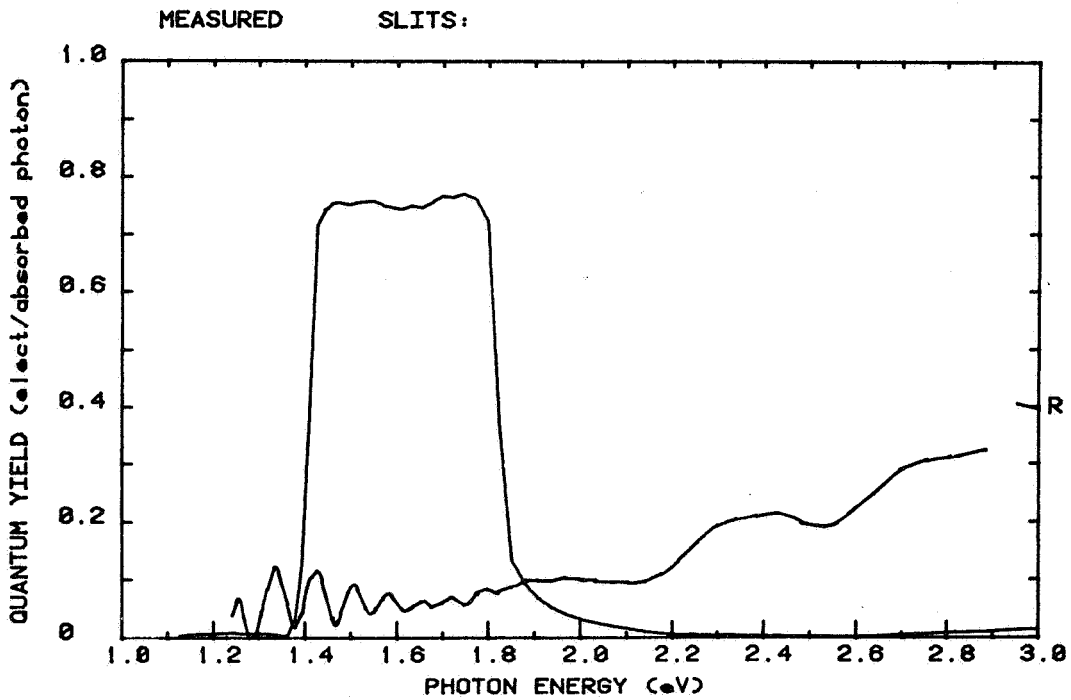


Figure 2

MIC² CELL PROCESS

NOTE: Drawings are not to scale. Top cell layers are about 1.5 microns thick in total, bottom cell is about 2.5 microns thick. Top grid bars are spaced about 150 microns for a concentrator cell, about 1000 microns for a 1 sun cell. Top groove is about 10 microns wide.

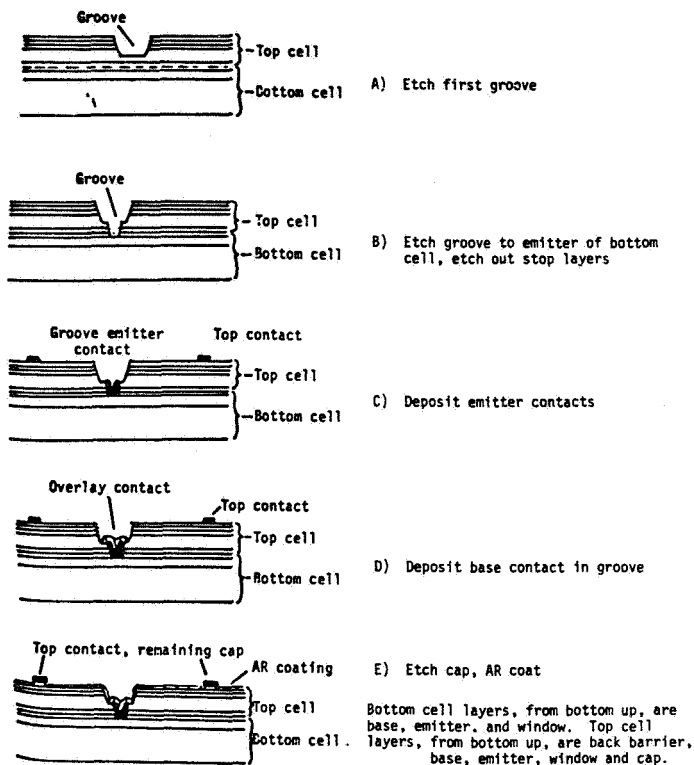


Figure 3

CASCADE CELL IV AT VARIOUS CONCENTRATIONS

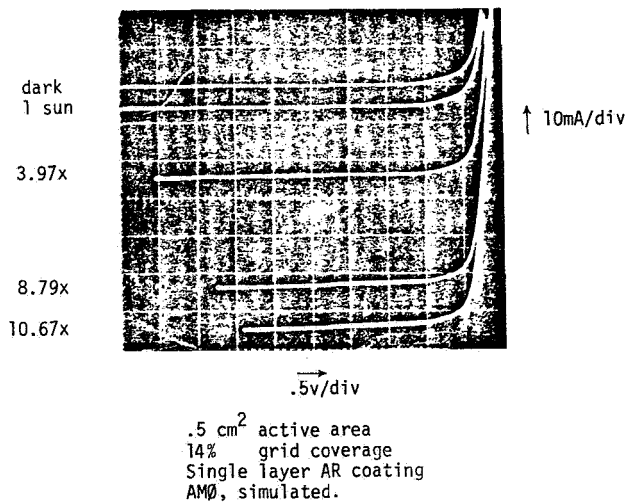


Figure 4

PRESENT STATUS OF AIR FORCE AlGaAs/GaAs CASCADE CELL PROGRAM

W.P. Rahilly
Air Force Wright Aeronautical Laboratory
Wright Patterson Air Force Base, Ohio

ABSTRACT

The status of the AF AlGaAs/GaAs cascade cell program is summarized. Recent results show that liquid phase epitaxy is a superior fabrication approach. Specific technical difficulties are addressed and approaches to solve them are described. The plans for follow-on programs based on these results are also described.

DETERMINATION OF OPTIMUM SUNLIGHT CONCENTRATION LEVEL IN SPACE FOR III-V CASCADE SOLAR CELLS

Henry B. Curtis
NASA Lewis Research Center
Cleveland, Ohio

ABSTRACT

The optimum range of concentration levels in space for III-V cascade cells has been calculated using a realistic solar cell diode equation. Temperature was varied with concentration using several models and ranged from 55° C at 1 sun to between 80° and 200° C at 100 suns. A variety of series resistance and internal resistances were used. Coefficients of the diffusion and recombination terms are strongly temperature dependent. The study indicates that the maximum efficiency of 30 percent occurs in the 50 to 100 sun concentration range provided series resistance is below 0.015 ohm-cm² and cell temperature is about 80° C at 100 suns.

INTRODUCTION

Cascade solar cells, especially those made using III-V materials, have the potential for much greater conversion efficiency than conventional single junction solar cells. The increased efficiency is mainly due to the better utilization of the solar spectrum by the two or three junctions of the cascade cell. An advantage of III-V material cascade cells is their low rate of decrease in power with increasing temperature. This indicates that III-V cascade cells should benefit from concentrated sunlight and be able to operate without forced cooling. The concentration level where the cell efficiency peaks depends on several factors, such as resistance losses and cell temperature as a function of concentration. Previous studies have calculated the efficiency of two and three junction cascade cells at various temperatures and concentrations (refs. 1 and 2), however, there was no definite relation between cell temperature and concentration. In an earlier study (ref. 3), the performance of gallium arsenide cells was calculated as cell temperature increased with concentration in specific difference functional relationships. The purpose of this effort is to expand the work of reference 3 to the case of III-V cascade cells.

METHOD OF CALCULATION

Current voltage curves were calculated for each cell in the cascade structure using the solar cell diode equation and the principle of superposition. Terms for the light-generated current, diffusion current, space charge recombination current, and series and shunt resistances are included. Cell current density J (in A/cm²) is given by

$$J = J_L - J_{01} \left(\exp \frac{V + JAR_s}{V_T} - 1 \right) - J_{02} \left(\exp \frac{V + JAR_s}{2V_T} - 1 \right) - \frac{V + JAR_s}{AR_{sh}} \quad (1)$$

where

A	cell area, cm ²
J _L	light-generated current density, A/cm ²
J ₀₁	coefficient of diffusion current term, A/cm ²
J ₀₂	coefficient of space charge region recombination current term, A/cm ²
R _s	series resistance, ohm
R _{sh}	shunt resistance, ohm
V _T	=kT/q = 25.85 mV at T = 300 K
V	cell output voltage

The individual current-voltage curves are added in series with ohmic resistance losses for the cell interconnects to obtain the cascade cell performance.

Before any calculations are possible, we must do the following:

- (1) Determine the initial values (at 300 K) for J_L, J₀₁, and J₀₂ for each junction in the cascade cell structure.
- (2) Determine the temperature dependence of the above quantities.
- (3) Determine the relationship between cell temperature and concentration.

In a series connected cascade cell, the current in each junction must be equal. This constraint is met by proper choice of the band gaps of the individual cells. For this study it was assumed that a III-V direct gap cell of band gap E_g, used as the top cell in a cascade structure, has a light-generated current equal to 80 percent of a "perfect" cell of the same band gap (quantum yield = 1 above the band gap and zero below the gap). The 20 percent loss can be attributed to grid coverage, surface reflection, recombination, etc. Integrating the quantum yield of a perfect cell against the Labs and Neckel AMO spectrum, gives the data in figure 1, which shows light-generated current for a perfect 1-cm² cell as a function of cutoff wavelength, λ_c:

$$\lambda_c = \frac{1.24}{E_g}$$

For a gallium arsenide cell of 0.867 μm cutoff wavelength, the 80 percent assumption leads to a value of 31.1 mA/cm² for light-generated current, in good agreement with the literature (ref. 4). For the second and third junctions, it was assumed that the light-generated current was 85

percent of a perfect cell (adjusted for absorption in the upper cells). Lower losses are assumed in the lower junctions due to decreased reflection and recombination losses. Using the above assumptions, the equal light-generated currents in each junction and the band gaps corresponding to any top cell band gap are uniquely determined.

The coefficients of the diffusion and recombination terms, J_{01} , and J_{02} , are determined for each band gap by assuming the following:

- (1) The diode quality factor n is equal to 1.2 at 1-sun concentration and at 300 K
- (2) Voltage V_{oc} is 70 percent of the band gap (eV).

The diode quality factor can be determined by using equation (1) and plotting an $I_{sc} - V_{oc}$ curve. The slope of this curve at 300 K and at current levels corresponding to 1-sun illumination leads to an n value that is dependent on the relative values for J_{01} and J_{02} . For example, if J_{02} is zero, then the cell is completely diffusion limited, and $n = 1.0$. By adjusting the relative value of J_{01} and J_{02} , an n value of 1.2 can be obtained. The final value of the two constants is determined by $V_{oc} = 0.7 E_g$. The value of $n = 1.2$ is assumed to be typical of current III-V cells (refs. 5 and 6). For GaAs 70 percent of E_g is 1 V, which value is typical of a good GaAs cell.

The temperature dependence of the various band gaps was assumed to be similar to that of gallium arsenide. The gallium arsenide temperature dependence can be obtained from the literature (ref. 7).

The J_{01} and J_{02} vary with the square of the intrinsic concentration and the intrinsic concentration, respectively. Hence,

$$J_{01} \propto T^3 \exp(-E_g/kT) \quad (2)$$

and

$$J_{02} \propto T^{3/2} \exp(-E_g/2kT) \quad (3)$$

The temperature dependences of J_{01} and J_{02} are calculated from equations (2) and (3).

The light-generated current of a solar cell increases with increasing temperature for two reasons: (1) the smaller band gap means more photons are collected, and (2) material properties such as lifetime improve with increasing temperatures (ref. 8). It was assumed that the band gap change accounted for most of the increase in light-generated current with temperature, and a value of 0.020 percent/K was assigned to the "better material properties" portion of increased current. Since band gaps were varied with temperature in this study, the calculated light-generated current already reflects this effect. For a gallium arsenide cell, this resulted in a $25 \mu A/cm^2-K$ temperature coefficient, which is in substantial agreement with published results (ref. 9).

The operating temperature of a solar cell in space is dependent on many factors. These include the incident irradiance, the absorptance and emittance of the cell and radiator surface, the thermal transfer between cell and

radiator, the size and orientation of the radiator, and the orbit of the spacecraft. It was beyond the scope of this study to calculate temperature variations with concentration for a nearly infinite set of starting assumptions. Instead actual data for 1-sun operation and other studies for data at concentrated sunlight levels were used.

For 1-sun operation in space, a cell temperature of 328 K (55° C) is typical of present photovoltaic arrays (ref. 10). These arrays use passive cooling, and the cells are producing power. There were no actual data available for cell temperature at elevated concentration levels in space, so the results of two studies were used to determine the range of operating temperatures expected. For the first study, which did not limit cell size and had no active cooling, a cell temperature of 398 K (125° C) at 50 suns was computed. A nearly 14-K margin for error is included, making this cell temperature value conservative. For the second study (ref. 12) much lower cell temperatures were computed for space solar cells: 353 K (80° C) for a 100-sun irradiance level. This study used very small cells (4 mm diam) to maximize the heat transfer from cell to radiator.

These low cell temperatures at concentration are similar to earlier work on small silicon cells at several hundred AM1 concentrations for terrestrial purposes. (ref. 13) Passive cooling was assumed in all the above work. Because of the usual dependences observed in space between irradiance and temperature, a T^4 relationship to concentration ratio ($T^4 = A_1CR + A_2$) was fitted to the 328 K - 1-sun point and to each of the higher concentration points. This lead to two different temperature dependences with concentration, a high temperature dependence and a low temperature dependence. A third, intermediate dependence curve is obtained by arbitrarily using a temperature level of 398 K (125° C) at 100 suns. The three temperature dependences are summarized below.

	Temperature, K	CR
High temperature	398	50
Intermediate temperature	398	100
Low temperature	353	100

Figure 2 shows temperature as a function of concentration for these three temperature dependences.

RESULTS AND DISCUSSION

Current-voltage curves were generated for cascade cell structures for sunlight concentration levels up to 250x (AM0). Figure 3 shows a typical three-junction cascade cell curve as well as the individual curves for each junction. Cell temperature was varied with concentration as described above, and efficiencies were calculated as a function of concentration level for a variety of series resistance, cell interconnection resistance, and top band gap values.

As seen from equation (1), the quantities AR_S and AR_{Sh} may be treated as independent variables. The same holds true for AR_C , where R_C

is the interconnect resistance between cells, whose ohmic voltage drop is subtracted from the cascade cell performance. Hence, for the remainder of the study series resistance, shunt resistance, and interconnect resistance were treated in terms of ohm-cm^2 .

As in the previous work (ref. 3) the effect of shunt resistance at higher concentration levels was negligible. Because the main focus of this study is on higher concentration ratios, a value of 2500 ohm-cm^2 for shunt resistance was used throughout.

Figure 4 shows efficiency as a function of concentration for three interconnect resistance values for a three junction cascade cell with a top band gap of 2.07 eV . The low-temperature dependence was used and $AR_S = 0.015 \text{ ohm-cm}^2$. Note the falloff in efficiency above about 100 concentration and the fairly broad maximum over the 30 to 100 range. The value of 50 m ohm-cm^2 (the center curve) for cell interconnect resistance resulted in a voltage drop of 75 mV at each interconnection at 100 AMO. This was somewhat less than the 100-mV drop assumed in reference 1, but probably within future technology. The top band gap was 2.07 eV . The corresponding band gaps for the second and third cells are 1.55 and 1.17 eV . This is not the optimum choice of band gaps; however, for direct gap materials of the same lattice constant, data from references 14 and 15 indicate that it is the only choice. Since the ability to grow individual cells in a monolithic stack of different lattice constants is considered improbable (ref. 1), the more realistic choice is 2.07 eV as top band gap, even though efficiencies could be about 3 percentage points higher with a more optimum band gap combination.

The effect of varying series resistance of the individual junctions is shown in figure 5. The effect of series resistance is less than the interconnect resistance due to the smaller values used in the calculation. The value of 15 m ohm-cm^2 should be readily achievable since similar and lower values have already been produced in single gallium arsenide cells (refs. 16 and 17).

Figure 6 shows efficiency as a function of concentration for the three temperature dependences. The efficiencies are equal at 1 sun and change as concentration and temperature are increased. The benefit of operating the cell at lower temperatures at concentration is readily evident. At 100 suns, the high temperature dependence results in an efficiency value lower than at 1 sun, due to the high operating temperature. Also at 100 suns, the difference in efficiency between the high- and low-temperature dependence curves is about 5.7 percentage points (29.67 and 23.97 percent). This is considerably more than the change in efficiencies in figures 4 and 5 due to the range of series and interconnect resistances studied. Hence, the effect of decreasing the operating temperature is the most important factor in raising the efficiency of cascade cells operating at high concentration levels.

The effect of mismatch in the currents of the individual cells is shown in table I. The first source of mismatch arises from the band gaps being chosen at one temperature and the cell being operated at a different temperature. For temperature differences of 30 to 40 K, this mismatch effect was negligible, with changes in efficiency of 0.1 percentage point. Since any cascade cell will be designed for the concentrator it will be used in, this

mismatch error can be neglected. The second mismatch error results from the uncertainty of our knowledge of the AMO spectrum. The Labs and Neckel spectrum was used throughout this study to determine light-generated currents and band gaps. The other recognized AMO spectrum was that of Thekaekara. Data were generated using band gaps chosen by the Labs and Neckel spectrum and light-generated currents chosen using the Thekaekara spectrum. The differences were small, about 0.4 percentage point difference in efficiency, which resulted in approximately a 1.3 percent drop in maximum power.

The third mismatch arises from radiation damage in space. For proton irradiation of sufficiently low energy we can assume that the current in the top cell is reduced by 10 percent. This results in approximately a 7-1/2 percent drop in efficiency of the cascade cell.

CONCLUSIONS

The optimum concentration level for III-V cascade cells is about 50 suns (with a range of 10 to 100 suns), where the efficiency falls off by less than 1 percentage point, provided the following conditions are met:

(1) An optical concentrator-passive cooling system must be provided which maintains cell temperature as low as possible. Some concepts presently under study indicate temperatures of 80° C at 100-sun concentration appear feasible through use of small cells to obtain good heat transfer to a radiating surface. The small cell concept has already been demonstrated in terrestrial concentrators to yield low operating temperatures.

(2) The resistance losses due to series resistance in the individual cells and the cell interconnects are kept at reasonable values. A value of 15 m ohm-cm² for individual cell series resistance should be an achievable value since gallium arsenide cells have been made with this on lower series resistance values. A value of 50 m ohm-cm² represents a goal for cell interconnect resistance. There is no known experimental data on such values at present. In any event, the drop in efficiency due to increased resistance losses at 100-sun concentration is considerably less than the loss due to higher operating temperatures.

REFERENCES

1. Maloney T J 1981, Projected performance of III-V epitaxial multijunction solar cells in space, Sol. Energy Mater. 4, 1981, pp. 359-372.
2. Lamorte M F and Abbott D H 1980, Computer modeling of a two-junction, monolithic cascade solar cell, IEEE Trans Electron Devices 27 (1), 231-249.
3. Curtis H B 1981, Determination of optimum sunlight concentration level in Space for gallium arsenide solar cells, 15th Photovoltaic Specialists Conference, Kissimmee, Florida, 12-15 May 1981, 52-56.
4. Kamath S et al 1979, Fabrication of high efficiency and radiation resistance GaAs solar cells, Solar Cell High Efficiency and Radiation Damage, Cleveland, OH, 13-14 June 1979, NASA-CP-2097, 209-216.
5. Fan J C C et al 1980, GaAs shallow-homojunction solar cells, 14th. Photovoltaic Specialists Conference, San Diego, CA, 7-10 Jan. 1980, 1102-1105.
6. Turner C W et al 1980, Indium phosphide homojunction solar cells, 14th. Photovoltaic Specialists Conference, San Diego, CA, 7-10 Jan. 1980, 351-353.
7. Yang E S 1978, Fundamentals of semiconductor devices, New York, McGraw-Hill.
8. Hovel H J 1975, Solar cells, New York, Academic Press.
9. Swartz C K and Hart R E Jr 1979, Temperature and intensity dependence of the performance of an electron-irradiated (AlGa)As/GaAs solar cell, Solar Cell High Efficiency and Radiation Damage, Cleveland, OH, 13-14 June 1979, 217-226.
10. J. Scott-Monck, J A 1980, "Prospects for Enhancing SEP Array Performance," Space Photovoltaic Research and Technology 1980, Cleveland, OH, 15-17 Oct. 1980, 351-361.
11. Peterson D M and Pleasant R L. 1981, Study of multi-megawatt technology needs for photovoltaic space power systems, vol. 2, GDC-AST-81-019-VOL-2 (General Dynamics/Convair)
12. Patterson R E et al 1981, Low cost, high concentration ratio solar cell array for space applications, Intersociety Energy Conversion Engineering Conference, 16th., Atlanta, GA, 9-14 Aug. 1981, 383-389.
13. Napoli L S and Swartz G A. 1978, Design and development of a 300-watt solar photovoltaic concentrator, SAND-78-7027 (Wisconsin Univ.)
14. Glisson T H et al 1978, Energy band gap and lattice constant contours of III-V quaternary alloys, J. Elec. Mater. 7 (1), 1-16.

15. Williams C K et al 1978, Energy band gap and lattice constant contours of III-V quaternary alloys of the form $A_xB_yC_zD$ or $AB_xC_yD_z$, J. Elec. Mater. 7 (5), 639-646.
16. Sahai R. et al 1978, High efficiency AlGaAs/GaAs concentrator solar development, 13th. Photovoltaic Specialists Conference, Washington, D.C., 5-8 June 1978, 946-952. Efficiency AlGaAs/GaAs
17. Ewan J et al 1978, GaAs solar cells for high solar concentration applications, 13th. Photovoltaic Specialists Conference, Washington, D.C., 5-8 June 1978, 941-945.

TABLE I. - EFFECTS OF VARIOUS CURRENT MISMATCHES ON CASCADE CELL POWER OUTPUT

Source of mismatch	Percent drop in P_{max}
$\Delta T \sim 30^\circ$ between cell operation and band gap optimization	Negligible, 0.3 percent
Uncertainty of AMO spectrum Labs and Neckel/Thekaekara	Small, 1.3 percent
Radiation damage 10 percent drop in one cell current	6 to 7.5 percent

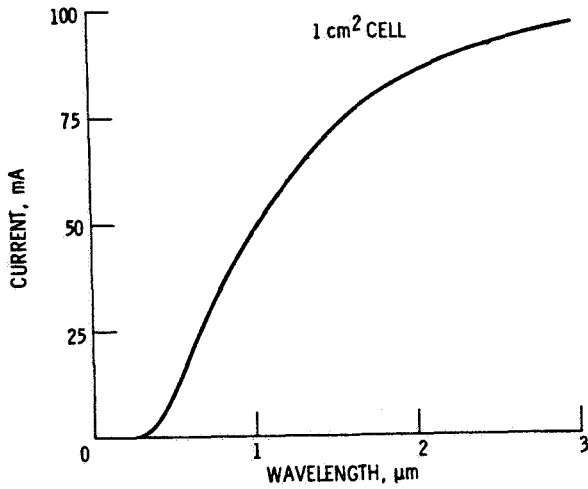


Figure 1. - Variation of short-circuit current of perfect cell with cutoff wavelength.

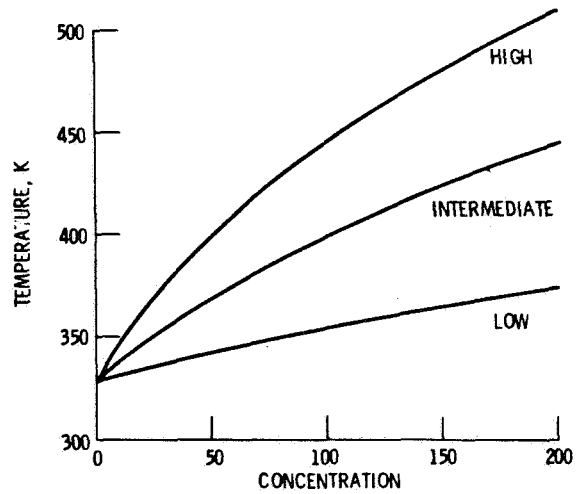


Figure 2. - Variation of temperature with concentration for different temperature dependences.

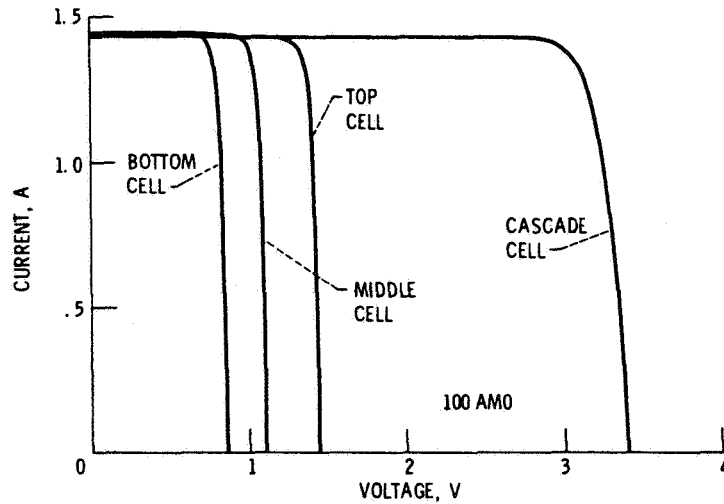


Figure 3. - Series addition of individual I-V curves.

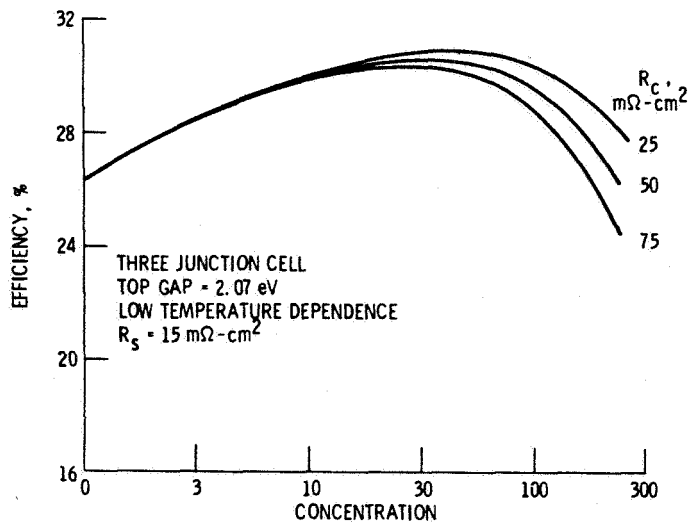


Figure 4. - Variation of efficiency with concentration for different interconnect resistances.

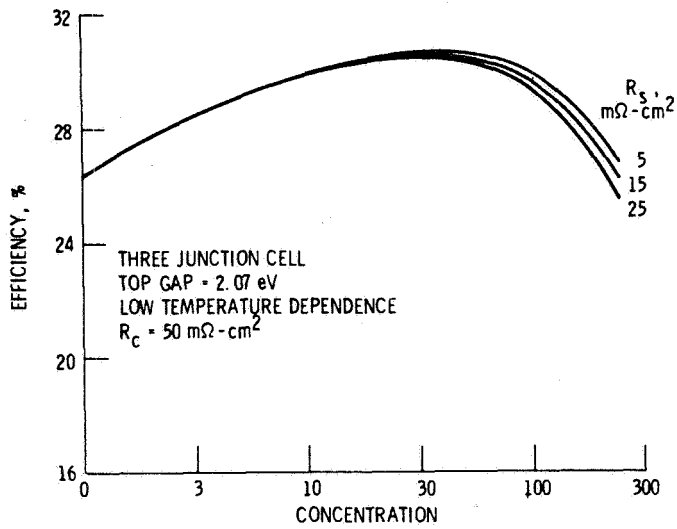


Figure 5. - Variation of efficiency with concentration for different series resistances.

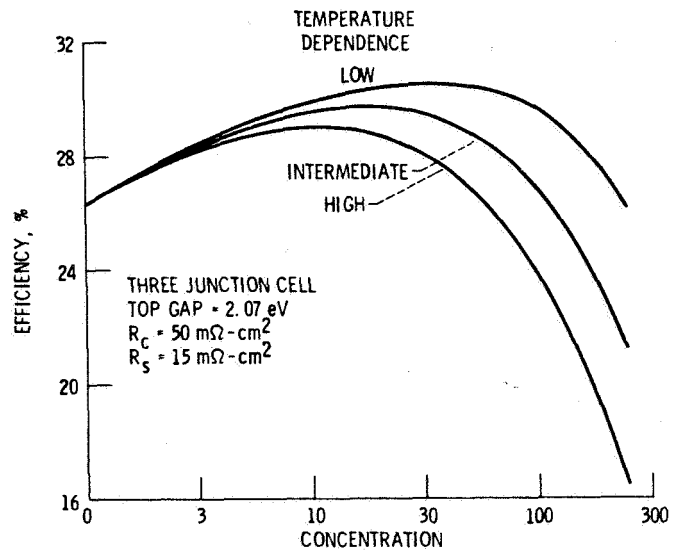


Figure 6. - Variation of efficiency with concentration for different temperature dependences.

SOLAR ENERGY CONVERSION USING SURFACE PLASMONS FOR BROADBAND ENERGY TRANSPORT

Lynn Marie Anderson
NASA Lewis Research Center
Cleveland, Ohio

SUMMARY

This paper introduces a new strategy for efficient solar energy conversion based on parallel-processing with surface plasmons. The approach is unique in identifying: (1) a broadband carrier with suitable range for energy transport, and (2) a technique to extract more energy from the more energetic photons, without sequential losses or unique materials for each frequency band. The aim is to overcome the fundamental losses associated with the broad solar spectrum and to achieve a higher level of spectrum splitting than has been possible in semiconductor systems.

INTRODUCTION

In conventional silicon solar cells, 56 percent of the incident power is wasted because monoenergetic conduction electrons are used to transport a broad solar energy spectrum. In cascade and spectrophotovoltaic systems, spectral mismatch losses are reduced by using different semiconductors to support different energy carriers. However, the increased complexity and sequential losses offset incremental efficiency gains when more than two or three frequency channels are used.

A preferred route is to parallel process different carriers in the same material. The missing ingredient has been the identification of a broadband carrier with suitable range for energy transport. In the search for long-lived excited states, little attention has been paid to less stable, but relativistic waves, like the surface plasmon. Perhaps these collective modes were overlooked because their properties are unfamiliar, or more likely, they were ruled out due to a prevalent misconception that wave approaches are unsuited for incoherent light.

SURFACE PLASMONS

Surface plasmons (refs. 1 to 4) are guided electromagnetic waves, which can be supported on thin films of common metals, like aluminum or silver. Thicker substrates may also be used, and there may be native oxides or dielectric overlayers. However, an interface can not support surface plasmons unless the dielectric function has opposite sign in the two materials. Negative dielectric functions occur in the Reststrahlen band or high reflectivity region of most metals and semiconductors.

The surface plasma wave (fig. 1) consists of a propagating wave of surface charge (polarized valence electrons) accompanied by transverse and longitudinal electromagnetic fields, which decay exponentially with distance from the metal interface. Typically, the fields extend a tenth to several thousand micrometers

above the metal, but only penetrate a few hundred angstroms into the substrate, permitting integration with back surface diodes. This also allows an extremely lightweight system for space use or a materials-conservative device on a low-cost substrate for terrestrial applications.

The surface plasmon spectrum is broad and continuous from the infrared to cut-offs which lie in the visible or ultraviolet depending on the material. The velocities are relativistic except near cut-off. For broadband energy transport, we are primarily interested in the relativistic waves, rather than the better known quasistatic ones, which are nearly monoenergetic.

Surface plasmons have finite range due to substrate absorption mechanisms like collision-broadening and interband transitions, as well as radiative loss induced by surface roughness. Landau-damping, or electron acceleration, can also be important but not for the relativistic waves. On an open surface the relativistic plasmons have field patterns in which most of the energy travels just above the metal, reducing substrate absorption (refs. 3 and 4). The range is excellent for device purposes, typically, 75 to 5000 micrometers at solar frequencies and centimeters in the infrared (refs. 5 to 7). This allows some compromise on materials quality and leaves room to design graduated structures which shift fields into the tunnel diodes, where energy is extracted. For plasmons propagating along the interfaces of the metal-barrier-semiconductor tunnels, the range may be only a few micrometers at the blue end of the spectrum, but this should be adequate.

These properties make surface plasmons ideal for broadband energy transport. Two questions remain: how to couple sunlight into the waves, and how to extract power to do work on a load.

ENERGY CONVERSION

There are three steps in the energy conversion process (fig. 2):

(1) Sunlight excites surface plasmons when its fluctuating electric fields polarize surface charge on the metal. Coherent light is not required, but a prism, grating, or textured surface must be used to provide phase-matching between photons and slightly slower surface plasmons of the same energy.

(2) The surface plasmons transport energy to an array of tunnel diodes, tuned to extract maximum power from waves in a different frequency bands. Diodes differ in geometry and operating voltage, but all share the same materials. The simplest type is an MIS diode formed from the conducting substrate, its native oxide, and a buried or front surface semiconductor electrode.

(3) Energy is extracted by inelastic tunneling, a one-step process in which an electron from the low voltage (semiconductor) electrode simultaneously absorbs a surface plasmon and tunnels to higher potential in the metal. Ideally, the semiconductor bandgap prevents backflow by eliminating unwanted final state energy levels. In a circuit, the tunneling current and load resistance supply the operating voltage. Current flows in the power quadrant as inelastic tunneling raises electrons to higher potential, enabling them to do work on the load.

COUPLING TO SUNLIGHT

Coupling sunlight to surface plasmons poses unique design problems since the light is unpolarized, uncollimated and broadband. Sunlight can excite surface plasmons when fluctuating solar fields polarize surface charge on the conductor. S-polarized photons, which have purely tangential electric fields, can not induce charge on a smooth surface, but "deep" surface texture, on the scale of the wavelength, should allow effective coupling of both polarizations (refs. 8 to 10).

Given charge fluctuations at a surface plasmon frequency, the collective response can not be excited unless parallel momentum is also conserved. Two primary techniques are used to phase-match photons to slightly slower surface plasmons of the same energy:

(1) A slow-wave structure, such as diffraction grating, (refs. 11 to 13) creates photon harmonics with parallel momentum shifted by multiples of the inverse period. When one diffracted order satisfies the phase-matching condition, energy is withdrawn from all orders proportionately. A rough or discontinuous surface (refs. 14 to 19) acts like a superposition of gratings, allowing phase-matching over a broad frequency range.

(2) Alternatively, photons may be slowed by a medium of high refractive index. In a prism-coupler (refs. 20 and 21), phase-matching occurs at specific incidence angles, which typically vary a few degrees across the solar band.

Coupling to surface plasmons is resonant and can be virtually complete in phase-matched structures. As early as 1902, Wood observed anomalies in the scattered light from gratings (refs. 20 to 25) which Lord Rayleigh explained as diffraction into a pair of superficial waves (ref. 26). Fano explained the anomalously large amplitude of the surface wave with an analogy to resonances in a mechanical system (ref. 27). With prism-couplers, 99 percent conversion of monochromatic, p-polarized light to surface plasmons has been demonstrated experimentally on a variety of substrates (refs. 28 to 30), while experimental evidence for strong coupling on gratings and rough surfaces (refs. 31 to 33 and 34 to 37, respectively) has also been shown.

Since the surface plasmon velocity varies with frequency, a range of grating periods or prism incidence angles is required to couple the solar spectrum. One strategy shown in figure 3 would use a prism or lens to disperse the spectrum over a fixed grating near parallel incidence. Angular dispersion controls the effective grating period and directs the surface plasmons towards appropriately tuned diodes. A guided wave approach appears most compatible with miniature concentrators, since collimation and focusing are required. Requisite periods depend on incidence angles and geometry but visible wavelengths are normally required. Fortunately, perfect collimation and phase-matching are not required as any structure has built-in momentum uncertainty, which is inversely proportional to the parallel dimension.

Alternatively, natural sunlight with a range of incidence angles could be coupled to surface plasmons on a textured surface. This has the virtue of simplicity and potential low-cost for large-area systems without concentration or tracking. Since waves of different frequencies are co-excited without preferred direction, the collecting diodes should be filtered for response to specific frequency bands.

ENERGY EXTRACTION BY INELASTIC TUNNELING

As shown in figure 4, the surface plasmons transport energy to an array of tunnel diodes tuned to extract maximum power from waves in different frequency bands. Although the diodes differ in geometry and operating voltage, all share the same materials. The simplest tunnel diode would be a metal-barrier-semiconductor junction formed from the conducting substrate, its native oxide, and a buried or front surface semiconductor electrode. The metal and semiconductor are at different potentials with the oxide serving as a barrier to inhibit electron flow.

Energy is extracted from the surface plasmons by inelastic tunneling (refs. 38 to 45), a one-step process in which an electron from the low voltage (semiconductor) electrode simultaneously absorbs a surface plasmon and tunnels to higher potential in the metal. The semiconductor is doped heavily p^+ , so its Fermi level lies close to the valence band. Thus, almost all the energy can be extracted from surface plasmons with energy slightly more than the operating voltage: the surface plasmon excites an electron from the semiconductor valence band into an empty state just above the metal Fermi level, where there is little excess to be lost to heat.

Ideally, the semiconductor bandgap prevents backflow by eliminating the final state energy levels which could otherwise be reached by conventional elastic tunneling (ref. 45) or by inelastic tunneling with emission of surface plasmons whose energy is less than the operating voltage. Some backflow through surface states and defects is unavoidable.

In a steady-state circuit, load resistance times the net tunneling current results in the impressed voltage across the diode. Current flows in the power quadrant as inelastic tunneling raises electrons to higher potential, enabling them to do work on the load. Since the diode voltage determines the fraction of surface plasmon energy extracted, the load should be regulated to maintain constant voltage as the current varies with solar flux.

PRECEDENT: TUNABLE LIGHT-EMITTING DIODES

Tunable light-emitting diodes based on inelastic tunneling were first demonstrated in 1976 by Lambe and McCarthy (refs. 47 to 49). The fabrication is straight-forward (refs. 50 to 56): A thin film of aluminum is evaporated on a glass or ceramic substrate, encouraged to form the native oxide, and crossed with a counter-electrode, typically 200 Å of silver, to form a tunnel junction of millimeter-square area. A voltage is applied across the junction to cause inelastic tunneling with emission of surface or junction plasmons. These waves can radiate visible light if phase-matching is provided by roughening the electrode surface with chemical etches, abrasion, or deposition of small metallic particles or by growing the whole diode structure on an irregular surface (e.g., CaF_2 islands) or a holographic grating. When the voltage is varied from 2 to 4 volts, the color changes from red through blue-white, with uniform glow across the outer electrode surface. Although still extremely inefficient, these are room temperature, reasonably stable devices with intriguing prospects for thin film video displays.

In present LED's, the glow can only be seen in a dark room - implying efficiencies less than 10^{-5} percent. What went wrong? The applied voltage

causes a current of tunneling electrons which have a very high (order one) probability to excite slow junction plasmons, which propagate along the tunnel interfaces (refs. 38 to 40). Unfortunately, most of the junction plasmons are absorbed by the substrate before they can radiate through the silver electrode. The mean free paths for substrate absorption and radiation differ by five orders of magnitude, which seems to explain the low efficiency (refs. 38 to 40). When diodes are grown on visible frequency holographic gratings (refs. 55 and 56), the plasmons are emitted on the outer electrode surface where they can radiate effectively. This time the efficiency is low (10^{-5} percent) due to weak coupling to the tunneling electrons (ref. 57).

The situation should be easier for photodiodes than it is for LED's, since the controlling mean free paths are different. Surface plasmons can be efficiently excited by light. Their long range leaves room to design graduated structures which shift fields into the tunnels. Alternatively, phase-matching structures might be used to link surface and junction plasmons through some type of bulk mode. Both techniques are used with high efficiency, nearly 100 percent in some cases, for closely related surface acoustic wave devices (refs. 58 to 60). Junction plasmons have shorter range, typically a few micrometers, but preliminary calculations from a Berkeley grant suggest a comparable range for junction plasmon capture by tunneling electrons. This would be a good starting point for efficient diodes; however, quite a bit more theoretical modeling and experimental characterization is necessary before we are confident of our understanding of processes occurring in the tunnel diodes.

CLOSING REMARKS

This paper has introduced an advanced concept for direct conversion of sunlight to electricity, which aims at high efficiency by tailoring the conversion process to separate energy bands within the broad solar spectrum. The objective is to obtain a high level of spectrum-splitting without sequential losses or unique materials for each frequency band. In this concept, sunlight excites a spectrum of surface plasma waves which are processed in parallel on the same metal film. The surface plasmons transport energy to an array of metal-barrier-semiconductor diodes, where energy is extracted by inelastic tunneling. Diodes are tuned to different frequency bands by selecting the operating voltage and geometry, but all diodes share the same materials.

Surface plasmons should lend themselves to an exciting new class of electro-optic devices, operating over a broad frequency range (IR through UV). The waves can be supported on common metals, like aluminum or silver, with only a thin film required. This allows extremely lightweight systems for space use, or materials-conservative devices on low-cost substrates for terrestrial applications. The long surface plasmon range allows some compromise on materials quality and leaves room to design graduated structures which shift fields into the tunneling region. Surface plasmons have strong coupling to both light and tunneling electrons; the challenge will be to accomplish both in the same device.

REFERENCES

1. R. H. Ritchie, Phys. Rev. 106, 874 (1957).
2. E. A. Stern and R. A. Farrett, Phys. Rev. 120, 130 (1960).
3. R. H. Ritchie, Surf. Sci. 34, 1 (1973).
4. D. L. Mills and E. Burstein, Rep. Prog. Phys. 37, 817 (1974).
5. A. S. Barker Jr., Phys. Rev. Lett. 28, 892 (1972).
6. A. S. Barker Jr., Phys. Rev. B8, 5418 (1973).
7. J. Schoenwald, E. Burstein, and J. M. Elson, Sol. State Comm. 12, 185 (1973).
8. C. H. Palmer, J. O. S. A. 42, 269 (1952).
9. C. H. Palmer, J. O. S. A. 46, 50 (1956).
10. C. H. Palmer, 51, 1438 (1961).
11. A. Hessel and A. Oliner, App. Optics 4, 1275 (1965).
12. D. L. Mills, Phys. Rev. B15, 3097 (1977).
13. D. L. Mills, B23, 4963 (1981).
14. R. H. Ritchie and R. E. Wilems, Phys. Rev. 178, 372 (1969).
15. J. Crowell and R. H. Ritchie, J. O. S. A. 64, 794 (1970).
16. J. M. Elson and R. H. Ritchie, Phys. Lett. 32A, 255 (1970).
17. D. L. Mills, Phys. Rev. B12, 4036 (1975).
18. D. L. Mills and A. A. Maradudin, Phys. Rev. B12, 2943 (1975).
19. A. A. Maradudin and D. L. Mills, Phys. Rev. B11, 1392 (1975).
20. A. Otto, Z. Physik 216, 398 (1968).
21. A. Otto, Optical Properties of Solids, New Developments, p. 677-727, B. O. Seraphim, Ed. (North-Holland, New York, 1976).
22. R. W. Wood, Proc. Phys. Soc. (London) 18, 396 (1902).
23. R. W. Wood, Phil. Mag. 4, 396 (1902).
24. R. W. Wood, 23, 310 (1912).
25. R. W. Wood, Phys. Rev. 48, 928 (1935).
26. Lord Rayleigh, Phil. Mag. 14, 60 (1907).
27. U. Fano., J. O. S. A. 31, 213 (1941).
28. G. T. Sincerbox and J. C. Gordon II, App. Optics 20, 1491 (1981).
29. M. R. Philpott and J. D. Swalen, J. Chem. Phys. 69, 2912 (1978).
30. M. R. Philpott, A. Brillante, I. R. Pockrand, and J. D. Swalen, Ml. Cryst. Liq. Cryst. 50, 139 (1979).
31. J. G. Endriz and W. E. Spicer, Phys. Rev. B4, 4144 (1971).
32. S. O. Sari, D. K. Cohen, and K. D. Scherkoske, Phys. Rev. B21, 2162 (1980).
33. E. Shiles, T. Sasaki, M. Inokuti, and D. Y. Smith, Phys. Rev. B22, 1612 (1980).
34. M. Fleischmann, P. J. Hendra, and A. J. McQuillan, Chem. Phys. Lett. 26, 163 (1974).
35. M. Fleischmann, P. J. Hendra, and A. J. McQuillan, J. Chem. Soc. Chem. Comm. 3, 80 (1973).
36. D. L. Jeanmarie and R. P. Van Duyne, J. Electroanal. Chem. 84, 1 (1977).
37. M. Albrecht and J. A. Creighton, J. Am. Chem. Soc. 99, 5215 (1977).
38. B. Laks and D. L. Mills, Phys. Rev. B20, 4962 (1979).
39. B. Laks and D. L. Mills, B21, 5175 (1980).
40. D. L. Mills and M. Weber, Tunneling Spectroscopy: Capabilities, Application and New Techniques, Ch. 5, P. K. Hansma, Edit. (Plenum Press, 1982).
41. K. L. Nagi, E. N. Economou, M. H. Cohen, Phys. Rev. Lett. 22, 1375 (1969).
42. K. L. Nagi and E. N. Economou, Phys. Rev. B4, 2132 (1971).
43. L. C. Davis, Phys. Rev. B16, 2482 (1977).
44. D. Hone, B. Muhlshlegel, and D. J. Scalapino, App. Phys. Lett. 33, 205 (1978).

45. R. W. Rendell, D. J. Scalapino, and B. Muhlschlegel, Phys. Rev. Lett. 41, 1746 (1978).
46. T. L. Hwang, S. E. Schwarz, and R. K. Jain, Phys. Rev. Lett. 36, 379 (1976).
47. J. Lambe and S. L. McCarthy, Phys. Rev. Lett. 37, 923 (1976).
48. S. L. McCarthy and J. Lambe, App. Phys. Lett. 30, 427 (1977).
49. S. L. McCarthy and J. Lambe, 33, 858 (1978).
50. K. Parvin and W. Parker, Solid State Comm. 37, 629 (1981).
51. R. K. Jains, S. Wagner, and D. H. Olson, App. Phys. Lett. 32, 62 (1978).
52. P. K. Hansma and H. P. Broida, App. Phys. Lett. 32, 545 (1978).
53. A. Adams, J. C. Wyss, and P. K. Hansma, Phys. Rev. Lett. 42, 912 (1979).
54. A. Adams and P. K. Hansma, Phys. Rev. B23, 3597 (1981).
55. J. R. Kirtley, T. N. Theis, and J. C. Tsang, App. Phys. Lett. 37, 435 (1980).
56. J. R. Kirtley, T. N. Theis, and J. C. Tsang, Phys. Rev. B24, 5650 (1981).
57. B. Laks and D. L. Mills, Phys. Rev. B22, 5723 (1980).
58. P. K. Tien, Rev. Mod Phys. 49, 361 (1977).
59. J. Melngailis, H. A. Haus, and A. Lattes, App. Phys. Lett. 35, 324 (1979).
60. I. Pockrand, J. D. Swalen, R. Santo, A. Brillante, and M. R. Philpott, J. Chem. Phys. 69, 4001 (1978).

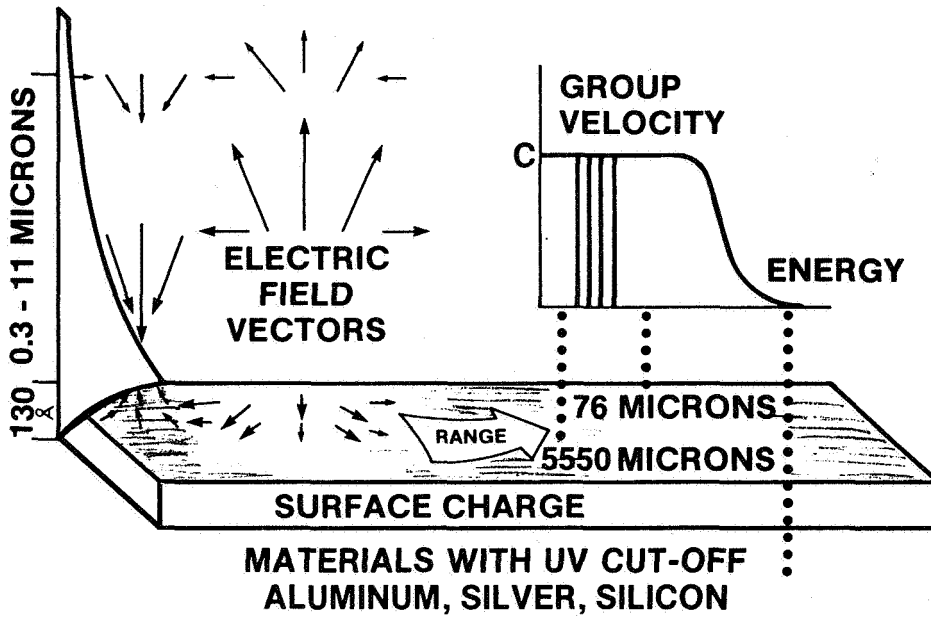


Figure 1. - Surface plasma waves.

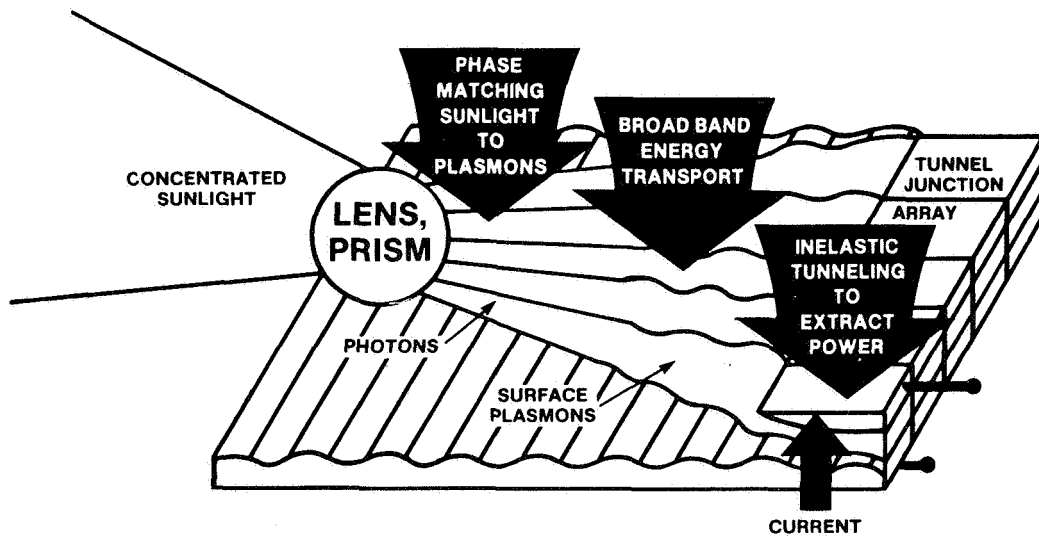


Figure 2. - Parallel processing with surface plasma waves.
Status: early conceptual phase.

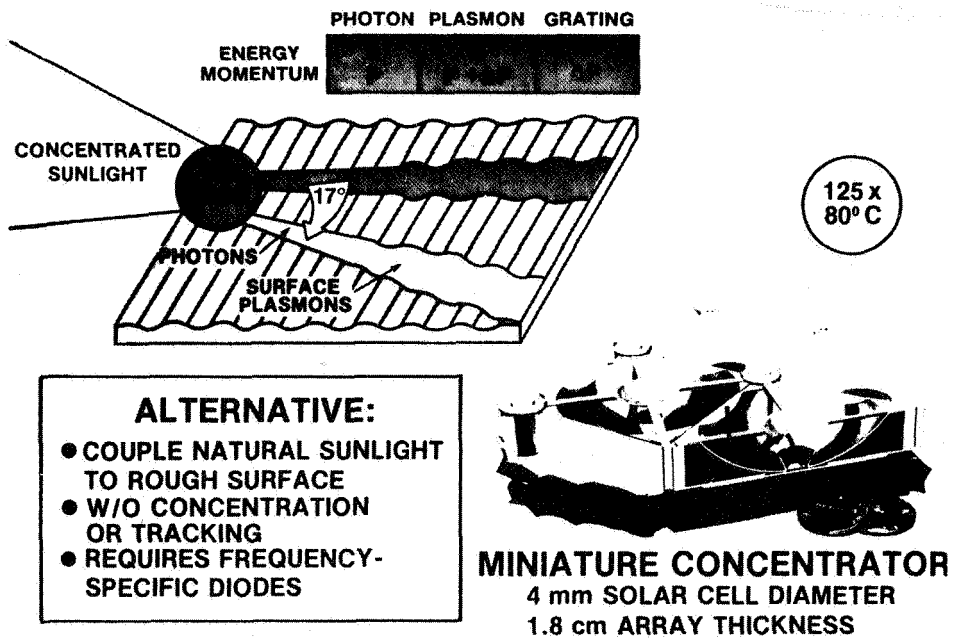
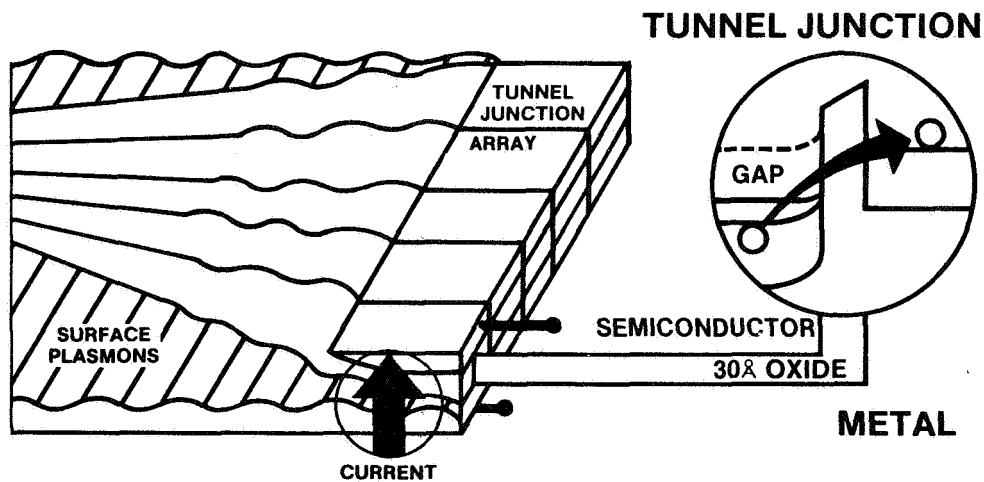


Figure 3. - Coupling to sunlight.



- INELASTIC TUNNELING ABSORBS PLASMONS TO PUMP ELECTRONS TO HIGHER POTENTIAL
- VOLTAGE SUPPLIED BY TUNNEL CURRENT AND LOAD RESISTANCE
- SEMICONDUCTOR BANDGAP LIMITS BACKFLOW

Figure 4. - Extracting power from surface plasmons.

STUDY OF GaAs DAMAGE COEFFICIENTS

H.S. Rauschenbach, T.R. Simpson, R. Parthasarathy, and M. Taher-Zadeh
TRW Space and Technology Group
Redondo Beach, California

The development of GaAs solar cells has advanced to the point where it can be considered as a potentially enabling technology for a range of future missions. Since an adequate set of radiation characterization test data for GaAs solar cells does not exist, the sparse existing solar cell data was combined with general GaAs device radiation damage coefficients reported in the literature. These damage coefficients were then applied to GaAs solar cell radiation damage analysis for a number of characteristic orbits. The study showed that for orbits where penetrating electron radiation dominates, GaAs damage is similar to Si damage. However, in orbits where damage from lower energy protons dominates, the degradation of thinly shielded GaAs cells is more severe than the damage of equally shielded Si cells, while the degradation of thickly shielded GaAs cells is less severe than the degradation of equally shielded Si cells. The most significant conclusions from the study are that (i) the damage-equivalent 1-MeV fluence for GaAs is, in general, different from that for Si cells for the same shielding thickness, same orbit and same orbital exposure time, and (ii) the damage coefficients of GaAs cells are functions of total accumulated fluence, indicating a reduced rate of damage as the fluence increases.

CURRENT STATUS OF THIN-FILM CLEFT GaAs SOLAR CELLS*

John C.C. Fan, Carl O. Bozler, and Robert W. McClelland
Lincoln Laboratory
Massachusetts Institute of Technology
Lexington, Massachusetts

Single-crystal GaAs layers as thin as 5 μ m have been grown and separated from reusable GaAs substrates by the CLEFT process. This process has been used in fabricating a 17% (AM1) GaAs solar cell, only 10 μ m thick, that is bonded to a glass substrate. The procedure for preparing CLEFT cells will be described. The thin-film technique eliminates the cost and limited availability of GaAs as major obstacles to utilization of GaAs solar cells. In addition, by using CLEFT cells with lightweight packaging it should be possible to produce panels with specific power of several kW/kg. The potential utilization of CLEFT cells in a high-efficiency tandem-cell structure will be discussed.

*This work was sponsored by the National Aeronautics and Space Administration and the Department of the Air Force.

AIR FORCE DEVELOPMENT OF THIN GaAs SOLAR CELLS

Ken Masloski
Air Force Wright Aeronautical Laboratories
Wright Patterson Air Force Base, Ohio

INTRODUCTION

The advantages of gallium arsenide (GaAs) over silicon (Si) type solar cells are many and have been well documented. However, two major disadvantages are weight and cost. Several ideas have recently surfaced that, if successful, will diminish these disadvantages. The CLEFT peeled film technique introduced by John Fan at Massachusetts Institute of Technology and the galicon cell being developed at the Jet Propulsion Laboratory are two of the more promising approaches. Presently, the Air Force is funding a program with Varian Associates, reference 1, to develop low weight, low cost, high efficiency GaAs solar cells. This paper will summarize the work under this program entitled "Low Cost GaAs Solar Cell Development".

PROGRAM GOALS

The specific goals of this program are the development of GaAs solar cells with at least an 18% conversion efficiency at beginning-of-life (BOL) and at least 13.5% after 5×10^{15} (1 Mev) electrons/cm². The cost and weight goals are \$300/watt and 550 watts/kg respectively, both at the cell level without a cover. These goals are considerably beyond the current state-of-the-art and represent a difficult but realizable challenge that must be attained to meet future power requirements of 25 kW and higher.

The only logical way to achieve such goals is to significantly reduce the cell thickness. Since the collection process in a GaAs cell takes place in the first few microns, theoretically such a cell could be made with a thickness on the order of 2 to 3 microns. However, thick substrates do provide physical strength to the cell so there are limits as to how thin cells can be fabricated before breakage becomes a very serious problem. In this program, the thickness goal was set at 50 microns or less. It is very unlikely the other goals will be met if the thickness exceeds 50 microns.

The \$300/watt cost goal translates to slightly less than \$30 per 2 x 2 cm² cell. It is not the intention of this program to fabricate cells at this cost, but to identify fabrication processes that could reduce GaAs cell costs to this level on a large quantity scale. While cell cost is important, it is secondary to the power to weight ratio.

VARIAN APPROACH

The approach chosen by Varian on this program is to first optimize a thick (~300 μ m) AlGaAs/GaAs structure using the organometallic vapor phase epitaxy (OM-VPE) growth method. The OM-VPE process allows superior control in the growth of the various cell layers. Techniques such as a graded junction and base plus a back surface field (BSF) are expected to increase efficiency. Any combination of these is possible with OM-VPE plus the option of growing n on p or p on n devices. The optimum structure will be identified through a combination of material growths and an advanced computer model.

Since currently existing GaAs computer models do not account for effects such as junction grading and base grading, a more advanced model is to be developed. The approach is to divide the cell into 50 or so thin layers with the doping, composition, mobility, etc., assumed constant in each. The layers are then coupled by their boundary conditions, and the solution to each layer is analytic in form. The model will be verified and modified to incorporate the results from the initial experimental material growths. It will then be used as an analytical aid in developing the optimum structure with further material growths verifying the results.

The optimized AlGaAs structure will be thinned via a stop etch technique which has been used in the production of photocathodes at Varian. The idea is to grow a thin AlGaAs stop etch layer on the substrate at an appropriate position to get the desired thickness. The cell active layers are grown, front contacts are attached, an AR coating is formed, and the cell is then glass bonded. The substrate is then chemically etched away to the stop etch layer. The result is a thin glass bonded cell that must only be back contacted. An alternate approach is to simply polish the substrate to between 30 to 50 microns. Both methods will be employed and compared to determine the yield vs performance tradeoff.

The method may seem costly; however, a detailed study by Varian indicates otherwise. Also, a gallium recovery process would be possible in a large scale production facility. A cost study is planned toward the end of this program.

PROGRESS

Considerable progress has already been made in the first six months of the program. Most of the work has been fabricating and testing of various material growths to determine the optimum structure. While grading the doping level in the base and the use of a BSF have proved effective, the graded windows have reduced cell performance. Based on the spectral response curve, it appears the graded windows are absorbing too much blue. The best cell had a BSF and graded base. Work is now underway to determine the most optimum way to utilize these features.

The basic cell structure is shown in figure 1. It is an OM-CVD grown p on n GaAs solar cell. The n type base layer is linear graded from 7×10^{17} to 2×10^{18} Se atoms/cm³. Earlier material growths indicate the base grading should begin within the first micron from the junction. This can be modeled analytically by computer if exponential grading is assumed, thereby providing a constant electric field in the base. It is felt a graded base will build a field to force minority carriers towards the junction thereby improving efficiency.

A BSF is formed by inserting a thin (1300Å) layer of AlGaAs within the base and 1-1.5 microns from the junction. The BSF can be modeled as a zero recombination velocity boundary condition to the base. The purpose of the BSF is to confine carriers in the base, so they can be collected rather than lost to the substrate.

The p type emitter layer thickness is 1000Å, 2000Å or 3000Å in selected samples. The dopant is 2×10^{18} zinc atoms/cm³. The top window layer is approximately 1300Å in thickness and is a Al_{0.8}Ga_{0.2}As composition doped with 1×10^{18} zinc atoms/cm³.

The alternative n on p structure is currently being considered and several material growths are being fabricated. Because of the higher mobility of n-type GaAs, the n doped emitter layer can be made much thinner. The emitter layer thickness for the n on p device will be 400Å to 800Å in selected samples. The n on p structures will be carefully evaluated to determine if any advantages exist over p on n structures.

Thinning via the polish back method and the stop etch technique is scheduled to begin by early spring 1982.

BLANKET TECHNOLOGY

In the near future, the Air Force plans to combine the thin GaAs cell with other technologies to develop light weight, hardened solar blankets. The other technologies include adhesiveless covers such as the plasma Activated Source (PAS) integral covers and Electrostatic Bonding (ESB), high temperature contacts and welded interconnects to reduce the vulnerability to laser threats. The objective is the development of a blanket with a BOL power to mass ratio of 250 watts/kg and at least 200 watts/kg after 1×10^{15} (1 Mev) electrons/cm².

Using current technology with 200 micron thick Si cells, a blanket level power to mass ratio of 116 watts/kg at BOL and 85 watts/kg after 1×10^{15} (1 Mev) electrons/cm² is considered good, reference 2. Unfortunately, the current technology cannot meet the higher power requirements expected for the near future. Since covered cells account for three quarters or more of the total blanket weight, it is obvious that the blanket power to weight ratio goals can only be met with thin, high efficiency solar cells with low mass covers. Such cells combined with high temperature contacts, and welded interconnects can meet the power to weight goals and significantly increase the

military hardness without incurring additional weight.

Using the following weight assumptions, the blanket level goals can be put into perspective with the successful development of the thin 2 mil GaAs cell.

.0279 g/cm ²	2 mil GaAs solar cell
.0670 g/cm ²	12 mil 7940 fused-silica
.0027 g/cm ²	1 mil DC-93-500 adhesive
.0099 g/cm ²	3 mil Kapton-Al blanket
.0042 g/cm ²	Aluminum interconnect weight
<u>.1117 g/cm²</u>	Total blanket weight

Assuming an 18% BOL, 13.5% EOL efficient cell provides a blanket level power to weight ratio of 217 watts/kg BOL and 163 watts/kg EOL. It should be noted the major weight cost is in the coverslide. The cover provides significant attenuation of proton irradiation, and the amount of protection is directly related to the glass thickness. Tradeoffs between coverglass thickness and EOL efficiency must be made for each mission to optimize EOL power to weight ratios. Clearly these numbers indicate a need for low areal density covers that are effective against particulate irradiation.

CONCLUSIONS

The work being performed at Varian represents a relatively straight forward approach towards the development of thin, high efficiency GaAs solar cells. The Air Force has a very strong interest in the development of light weight space power systems. Eventually, the thin cell technology will be combined with other appropriate technologies towards the development of light weight, military hardened solar array blankets.

REFERENCES

1. Low Cost GaAs Solar Cell Development - Air Force Contract #F33615-81-C-2025, Varian Associates, Pala Alto CA, Principle Investigator - Peter Borden
2. High Voltage High Power Solar Power Systems Study - Air Force Contract #F33615-79-C-2042, Lockheed Missiles and Space Company, (interim presentation)

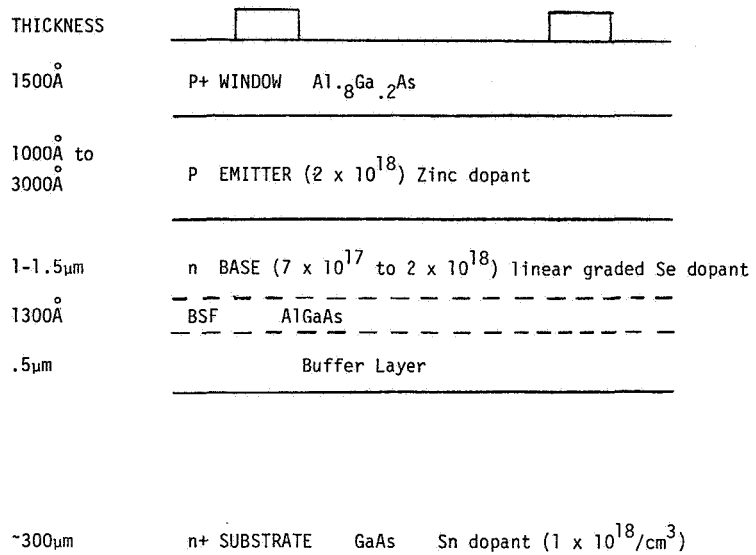


FIGURE 1 CELL STRUCTURE

PROGRESS TOWARD THIN-FILM GaAs SOLAR CELLS USING A SINGLE-CRYSTAL Si SUBSTRATE WITH A Ge INTERLAYER*

Y.C.M. Yeh, K.L. Wang, and S. Zwerdling
Jet Propulsion Laboratory
California Institute of Technology
Pasadena, California

EXTENDED ABSTRACT

INTRODUCTION

The objective of our research program is to develop a technology for fabricating light-weight, high-efficiency, radiation-resistant solar cells for space applications. The approaches currently adopted are to fabricate shallow homojunction n^+/p as well as p/n AlGaAs-heteroface GaAs solar cells by organometallic chemical vapor deposition (OM-CVD) on single-crystal Si substrates using in each case, a thin Ge epi-interlayer first grown by CVD. This approach maintains the advantages of the low specific gravity of Si as well as the high efficiency and radiation-resistant properties of the GaAs solar cell which can lead to greatly improved specific power for a solar array. The intermediate goals of the program are to investigate the growth of single-crystal GaAs epilayers on Ge epi-interlayers on Si substrates and to develop related solar cell fabrication technology. This paper reports on our progress toward these intermediate goals.

EXPERIMENTAL

In the experiment involving the growth of a GaAs/Ge/Si structure, Ge epi-interlayers were first grown on (100) single-crystal Si substrates in a vertical quartz CVD reactor at 700-725°C with a growth rate of about 0.1 micrometer/min by pyrolysis of GeH_4 in a H_2 gas mixture. Subsequently, the growth of GaAs layers on the Ge epi-interlayer were conducted in a horizontal quartz CVD reactor at similar temperature range with a growth rate of about 0.2 micrometer/min by pyrolysis of trimethyl gallium (TMG) and arsine (AsH_3) in a H_2 gas mixture.

*The research described in this paper was performed at the Jet Propulsion Laboratory, California Institute of Technology, and was sponsored by the National Aeronautics and Space Administration, Office of Aeronautics and Space Technology, under Contract NAS7-100 with the Jet Propulsion Laboratory, and the United States Air Force (at Wright-Patterson AFB) through an agreement with the National Aeronautics and Space Administration.

In the development of the n⁺/p GaAs shallow-homojunction baseline structure, GaAs p- and n-type layers were produced by alternately adding dimethylzinc and hydrogen sulfide, respectively, to the OM-CVD gas stream, as the dopants. The active p-layer, about 2 micrometers thick, was doped to $1-2 \times 10^{17}/\text{cm}^3$, whereas the n⁺ layer about 40 nm thick was doped to $4 \times 10^{18}/\text{cm}^3$ for low sheet resistance. Electroplated gold was used for grid and back surface contact coating, and the anti-reflection coating was made by vacuum deposition of Sb₂O₃.

RESULTS AND DISCUSSION

During the last Conference here at NASA Lewis, we reported the first successful growth of thin epitaxial layers of GaAs by OM-CVD onto a Ge epi-interlayer which was in turn grown onto a (100) Si substrate, with all epi-growth done by the CVD process. The structures thus produced were smooth, bright and shiny. However, some stress-induced cleavage lines and a high surface micropit density (about $10^5/\text{cm}^2$) were observed by SEM and optical microscopy. The high micropit density of the GaAs films were a consequence of the initial high micropit density (about $6 \times 10^7/\text{cm}^2$) of the Ge epi-interlayer.

In order to improve the Ge surface for subsequent GaAs growth, pulsed laser annealing experiments were first conducted. A Nd:YAG laser system at the laboratories of the Lockheed Missiles and Space Systems Division, Sunnyvale, California was used for these annealing studies. Annealing experiments were performed on Ge/Si samples with energy densities ranging from 0.35 to 0.79 J/cm² with a pulse width of less than 150 ns at a wavelength of 1.06 micrometers. The results at low energy density (0.35 J/cm²) showed that the annealed Ge epi-layer possessed a smoother surface morphology, but had a surface micro-pit density similar to the unannealed Ge films. On the other hand, at high energy density (0.79 J/cm²), some surface damage was evident. The best results were obtained when a laser energy density of about 0.64 J/cm² was used. This led to a 10-fold reduction of the surface micropit density on the Ge layer from the original value of about $10^7/\text{cm}^2$ (Fig. 1) to a value of about $10^6/\text{cm}^2$ (Fig. 2) and a considerably smoother surface. Although the improvement in surface morphology of Ge is significant, the micropit density value was still too high. Therefore, experiments were conducted with the aim of improving surface morphology by modifying the Ge interlayer growth technique.

The following steps were taken to improve Ge-crystal growth: 1) improving the leak-tightness of the CVD Ge growth system, 2) reducing the surface boundary layer thickness during Ge film growth by modification of the reactor design, and 3) a more effective initial purging of the system to minimize residual O₂ and H₂O vapor contamination. Thus a reduction of surface micropit density by four orders of magnitude for the Ge interlayers was achieved. A photomicrograph (Fig. 3) of typical Ge/Si samples thus produced shows a surface micropit density corresponding to about $5 \times 10^3/\text{cm}^2$.

Subsequently, GaAs films were deposited on those improved Ge/Si samples by OM-CVD. When a Ge/Si sample with a 0.5-micrometer thick Ge interlayer was used as the substrate wafer, a smooth epi-GaAs film with low micropit density (less than $5 \times 10^3/\text{cm}^2$) and without cleavage lines, and having a large surface area (2cm x 2cm) can be made routinely by OM-CVD. A photomicrograph of such a GaAs/Ge/Si sample is shown in Fig. 4. This low micropit density value should

be adequate for solar cell (and other) applications, in view of the fact that, typically, a good single-crystal GaAs exhibits similar values of surface etch-pit density.

In the development of the n^+/p shallow-homojunction GaAs baseline solar cell technology, further improvement in energy conversion efficiency has been achieved. The solar cell samples grown showed AMO efficiencies between 15% and 16%. Light I-V characteristics of the best cell with an area of 1 cm^2 is shown in Fig. 5. The AMO energy conversion efficiency for this GaAs solar cell measured at 28°C is about 16% using a Spectrolab model XT-10 AMO simulator. This efficiency value is comparable to that reported by others employing the same n^+/p shallow-homojunction GaAs solar-cell structure. The AMO values of V_{oc} , J_{sc} and FF for this cell were about 0.99V, 26.6 mA/cm^2 and 0.81, respectively.

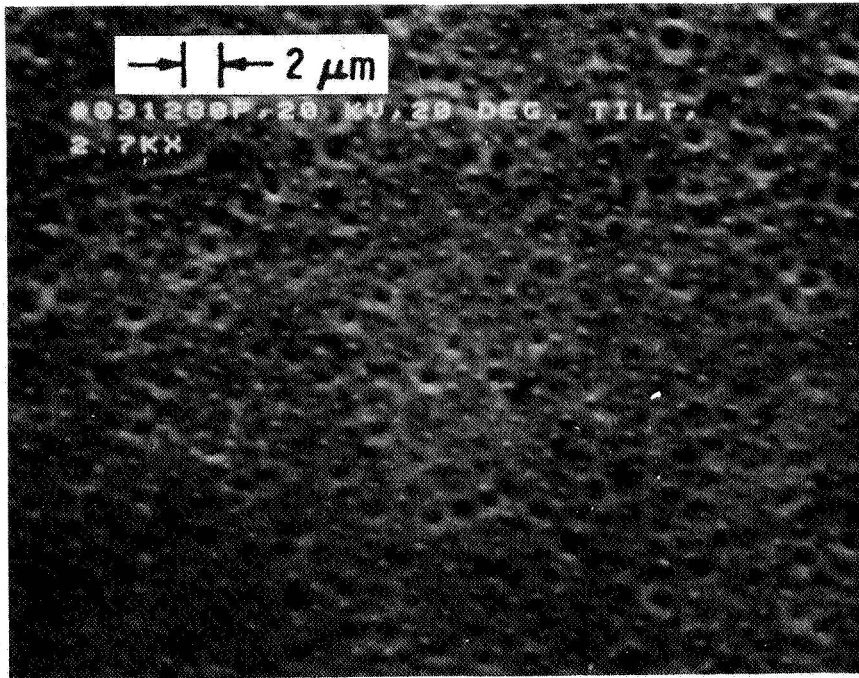


Fig. 1. SEM photomicrograph of a typical Ge film grown at 700°C on a (100) Si substrate, before laser annealing.

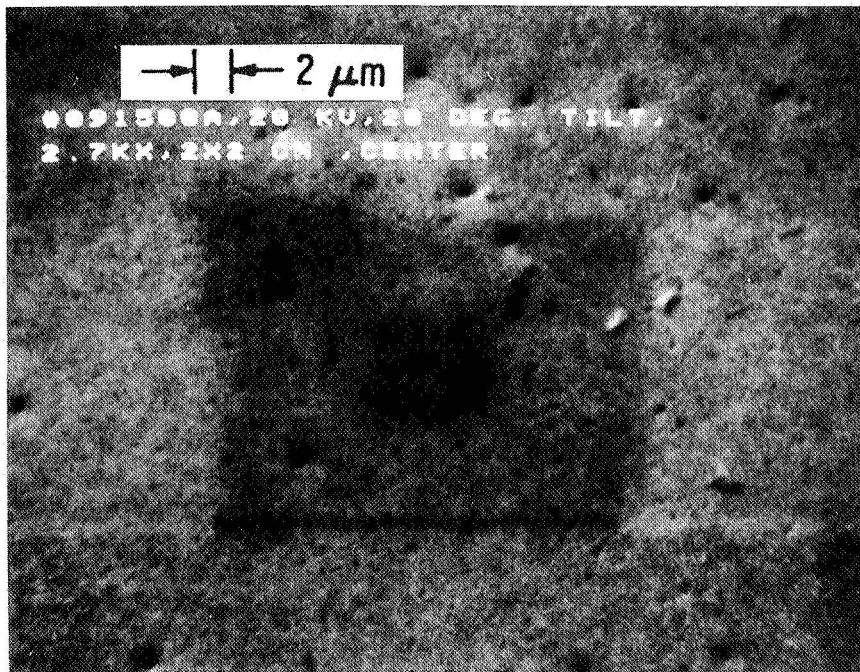


Fig. 2. SEM photomicrograph of the Ge/Si sample annealed at an average energy-density of about 0.64 J/cm².

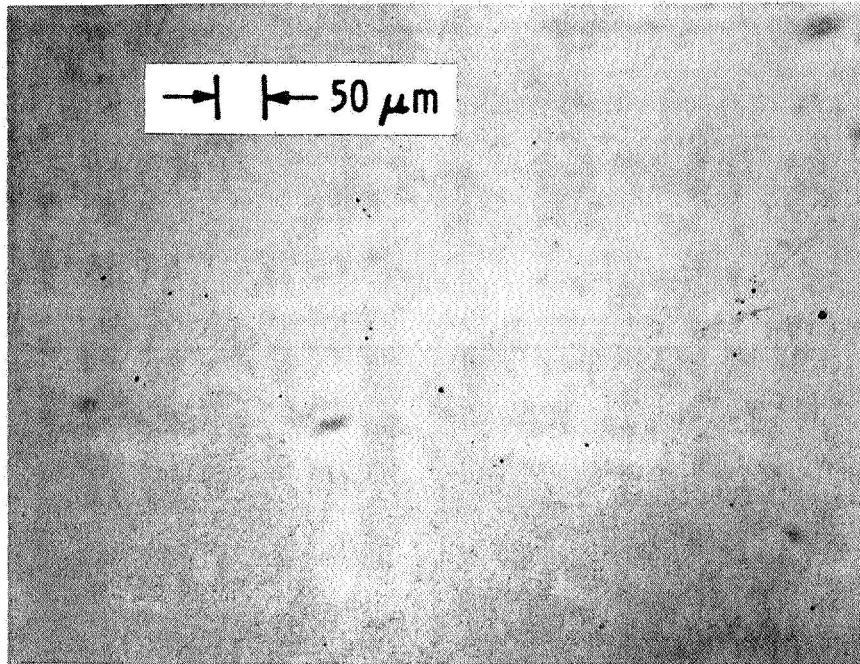


Fig. 3. Photomicrograph of a typical Ge film grown at 700°C on (100) Si substrate using the improved Ge-growth technology.

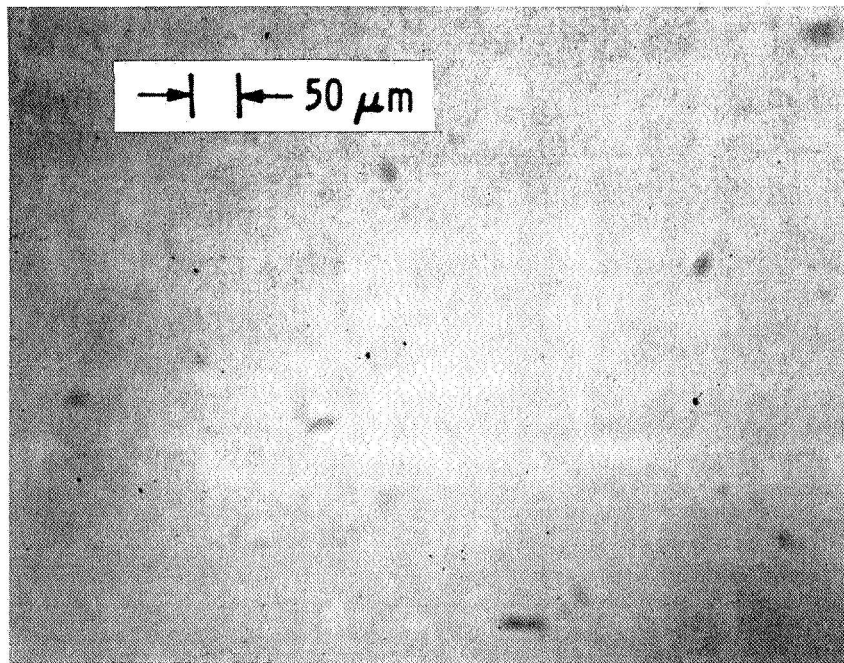


Fig. 4. Photomicrograph of a GaAs/Ge/Si sample with OM-CVD grown GaAs on a CVD-grown Ge interlayer.

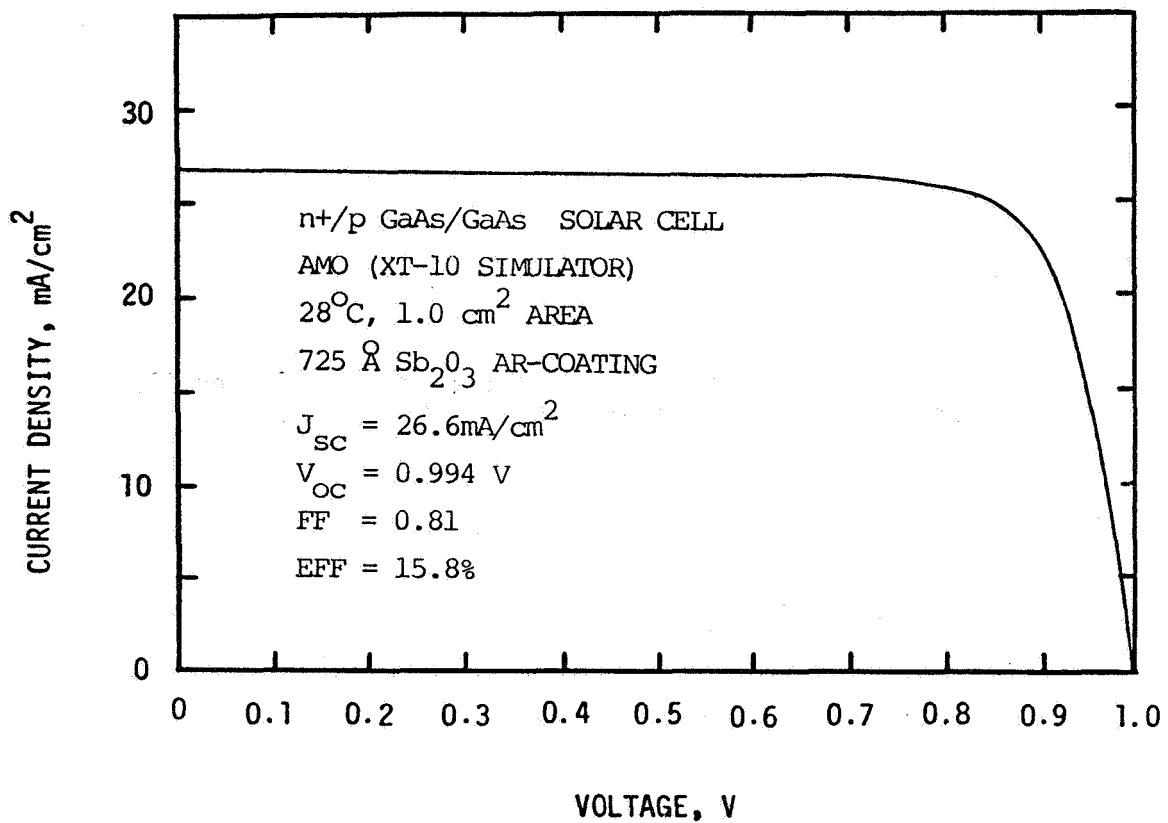


Fig. 5. Light I-V characteristics of a 1cm x 1cm - area n⁺/p GaAs/GaAs solar cell.

DIFFUSED P⁺-N SOLAR CELLS IN BULK GaAs*

J.M. Borrego and S.K. Ghandhi
Rensselaer Polytechnic Institute
Troy, New York

SUMMARY

Recently melt grown GaAs, made by liquid encapsulation techniques, has become available. This material is of sufficiently good quality to allow the fabrication of solar cells by direct diffusion. This talk will describe results obtained with p⁺-n junction solar cells made by zinc diffusion, and will evaluate the quality of bulk GaAs for this application.

INTRODUCTION

Gallium arsenide solar cells are conventionally made by the epitaxial growth of a junction structure on a heavily doped substrate. This process has been necessitated by the poor quality of starting bulk material, which is highly defected. Recently, however, melt grown GaAs made by liquid encapsulated Czochralski (LEC) techniques combined with in-situ compounding, has become available (ref. 1,2). These materials are of sufficiently good quality to allow the fabrication of solar cells by direct diffusion.

This paper outlines results obtained with large area (0.5 cm²) p⁺-n junction solar cells formed in this way, using precisely controlled p⁺-diffusions made by an open tube process.

EXPERIMENTAL

Tellurium-doped n-type gallium arsenide of (100) orientation and $5 - 8 \times 10^{16} \text{ cm}^{-3}$ concentration, made by the LEC process, was used for this study. Slices were cut into suitable pieces, and given a brief Caro's etch ($\text{H}_2\text{SO}_4 : \text{H}_2\text{O}_2 : \text{H}_2\text{O} = 10 : 1 : 1$ by volume) before use.

The diffusion technique has been detailed previously (ref. 3), and will be summarized here. First, samples were placed on the platform of a resistance-heated susceptor in a cold wall reactor held at 350°C. A 1000 Å layer of ZnO-SiO₂ was

* Performed on NASA-Lewis Research Center Grant No. NAG3-188.

deposited on the samples, by the simultaneous pyrolysis of diethylzinc $[(C_2H_5)_2Zn]$ and silane (SiH_4) in oxygen. This served as a doped oxide source for the subsequent diffusion step.

Next, without removing the samples, a 2000 Å cap layer of $P_2O_5-SiO_2$ was grown over the doped oxide layer. This layer was also grown at 350°C by the simultaneous pyrolysis of phosphine (PH_3) and SiH_4 in oxygen.

Diffusions were made in an open tube furnace with flowing nitrogen gas, and at temperatures from 500°C to 600°C. Junction depths from 500-1000 Å were obtained in this manner. No PSG cap layer was used on the back face because of the low temperatures involved. However, the back face of the slices was subsequently etched to remove surface damage caused during diffusion. Ohmic contacts were made by evaporating 1000 Å of Au-Ge of eutectic composition (12% Ge by wt), and heat treating in a N_2/H_2 gas mixture of 450°C for 1 minute.

Solar cells of 0.5 cm² area, were made as follows: After diffusion, positive photoresist was applied to delineate a grid patterned cell, and buffered HF used to cut the underlying glass layers. The grid structure was then electrolytically plated in a gold bath. A second photoresist layer was applied to define a rectangular pattern and the uncovered oxide regions were etched in BHF. Next, a rectangular mesa was etched in the GaAs, using Caro's etch. The cell was coated with 800 Å of Sb_2O_3 , after the removal of the remaining photoresist and glass layers. This film is easily deposited, and serves as an antireflective coating.

A number of small area cells of both the Schottky and p^+-n junction type were also made for diagnostic purposes. These were used to test the quality of starting materials and its stability to thermal processing.

The photoresponse of large area cells was measured in our laboratory at AMI (simulated with an ELH source and a detector calibrated against a Bureau of Standards secondary standard). Some cells were measured by NASA at AMO as well. Finally, spectral response measurements were made on the large area devices.

RESULTS AND DISCUSSION

The Schottky devices, made on as-purchased GaAs, provided a baseline for the starting material. Schottky devices, on which the processing associated with the diffusion was simulated, provided information on the changes undergone by the GaAs due to this heat treatment. The short circuit current density for these cells, measured with no AR coating under simulated AMI conditions, was found to be only slightly changed (from 13.1-13.6 mA/cm²) after thermal processing at 600°C for 30 minutes under the PSG cap layer. Small area p^+-n cells, on the other hand, exhibited a consistently higher value of short circuit current (15.6 mA/cm²). The reasons for this improvement, caused by the in-diffusion of zinc, are under investigation at the present time.

Table I shows the measured performance of a large area AR-coated cell made by this diffusion process. Both data at AMI and AMO are provided for comparison purposes. As expected, the short circuit current density is 24% larger under AMO

conditions, but the fill factor and efficiency are essentially unchanged. Analysis of $\ln I$ vs. V characteristics has shown that the relatively low fill factor in these cells is caused by a high value of ideality factor ($n \approx 1.6$) which was typical for p^+-n junctions in the LEC material.

Figure 1 shows the results of spectral response measurements on a large area cell, as well as a computer simulation based on a device with the following parameters:

Junction depth	= 1000 Å
Zero-bias depletion layer width	= 1000 Å
Surface recombination velocity	= 10^6 cm/sec
Hole diffusion length	= 1.4 μm

Experimental measurements of junction depth and hole diffusion length (ref. 4) agree well with those used in the model. Computer simulations have also indicated where device design and material properties must be altered (improved) in order to optimize this cell structure.

CONCLUSION

This work has demonstrated the feasibility of making large area solar cells in bulk GaAs, by a simple open tube diffusion process. A cell efficiency of 12.2% has been achieved for AMO conditions, even though no attempts have been made to optimize the cell design or the AR coating. Computer simulation has shown directions for obtaining improved cell performance. Further work, involving deep level transient spectroscopy, is in progress to understand the effects of zinc diffusion into gallium arsenide.

REFERENCES

1. Fairman, R. D., Chen, R. T., Oliver, J. R., and Ch'en, D. R., "Growth of High-Purity Semi-Insulating Bulk GaAs for Integrated Circuit Applications", IEEE Trans. Electron Devices, ED-28, 135 (1981).
2. Hobgood, H. M., Eldridge, G. W., Barrett, D. L., and Thomas, R. N., "High-Purity Semi-Insulating GaAs Material for Monolithic Microwave Integrated Circuits", IEEE Trans. Electron Devices, ED-28, 140 (1981).
3. Ghandhi, S. K., and Field, R. J., "Precisely Controlled Shallow p^+ Diffusions in GaAs", Appl. Phys. Lett. 38(4), 267 (1981).
4. Lender, R. J., Tiwari, S., Borrego, J. M., and Ghandhi, S. K., "Diffusion Length Measurements in Schottky Barrier GaAs Solar Cells", Solid State Electronics, 22, 213 (1979).

TABLE 1: RESPONSE OF LARGE AREA GaAs SOLAR CELL

Conditions	J_{sc} (mA/cm ²)	V_{oc} (V)	FF	Efficiency (%)
AM1	19.1	0.894	0.75	12.6
AM0 (NASA)	23.6	0.921	0.77	12.2

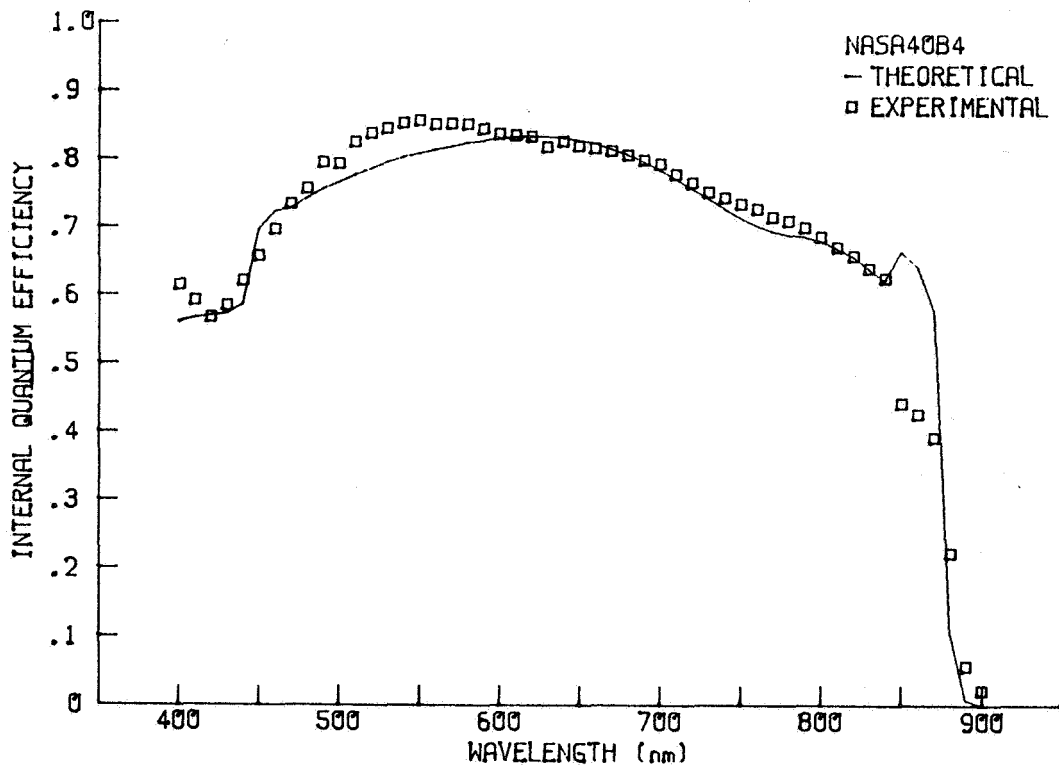


FIGURE 1

ADVANCES IN LARGE-DIAMETER LIQUID ENCAPSULATED CZOCHRALSKI GaAs*

R.T. Chen, D.E. Holmes, and C.G. Kirkpatrick
Rockwell International
Microelectronics Research and Development Center

SUMMARY

We have evaluated the purity, crystalline perfection, and electrical properties of n- and p-type GaAs crystals grown by the liquid encapsulated Czochralski (LEC) technique. This study included the determination of the dislocation density, incidence of twinning, microstructure, background purity, mobility, and minority carrier diffusion length. The properties of the LEC GaAs crystals are generally comparable to, if not superior to those of small-diameter GaAs material grown by conventional bulk growth techniques. As a result, LEC GaAs is suitable for application to minority carrier devices requiring high-quality and large-area substrates.

INTRODUCTION

The availability of high quality, large-diameter GaAs substrates is the key to the successful development and production of high-speed GaAs integrated circuits and high efficiency minority carrier devices, such as solar cells. The liquid encapsulated Czochralski (LEC) technique (refs. 1-6) has provided a means for producing large-diameter GaAs with reproducible and thermally-stable semi-insulating properties suitable for GaAs integrated circuits and microwave devices. The purpose of this work was to further demonstrate the capability of the LEC growth technique to produce large-diameter, high-quality GaAs substrates suitable for minority carrier device applications. Attention was focused on materials properties relevant to minority carrier devices, including the dislocation density, incidence of twinning, microstructure, background impurities, mobility, and minority carrier diffusion length. We have evaluated these properties in n- and p-type 3-inch-diameter LEC GaAs crystals, and the results were compared with those from small-diameter GaAs crystals grown by conventional bulk growth techniques.

LEC CRYSTAL GROWTH

The doped and undoped, 3-inch diameter GaAs crystals used in this study were grown in a high pressure "Melbourn" (Metals Research Ltd.) puller using the LEC technique. The LEC growth configuration is shown in Figure 1. The crystals were grown in the $\langle 100 \rangle$ direction from 6-inch-diameter quartz and pyrolytic boron nitride (PBN) crucibles. The GaAs melt was prepared by in-situ synthesis (ref. 1), starting with a charge of high purity (6-9's) Ga and As weighing 3 Kg. The crystals typically weighed from 2.2 to 2.4 Kg. The ambient pressure (Argon) during growth

*Supported in part by NASA under Contracts # NAS3-22224 and NAS3-22235.

was typically 300 psi. The seed and crucible were both rotated counter-clockwise at 6 and 15 rpm, respectively. For n- or p-type doping, zone-refined Si, high purity (5-9's) Ga₂Se₃, or Zn₃As₂ was added to the charge. The resulting carrier densities ranged from 1×10^{15} to 1×10^{19} cm⁻³.

The crystal diameter was controlled by adjusting the heater temperature and the cooling rate in response to changes in the differential weight signal obtained from the "load cell", a special weighing device on which the pull shaft was mounted. An increase or decrease of the differential weight indicated a corresponding expansion or contraction of the crystal. Growth was typically initiated by reducing the diameter of the crystal below that of the seed. This procedure is referred to as Dash-type seed necking (ref. 7). The diameter was then allowed to expand controllably, forming the "cone". Expansion was terminated at the "shoulder", and the diameter of the crystal was held constant for the remainder of the growth process, forming the "body".

Figure 2 shows a 3.6 Kg, 3-inch diameter, (100) LEC GaAs ingot grown at our laboratory illustrating the excellent diameter control ($\leq \pm 2$ mm) that can be achieved. Approximately 130, (100) wafers with a thickness of about 0.025 inch can be obtained from such an ingot.

CHARACTERIZATION METHODS

The crystals were evaluated in terms of crystalline perfection, electrical properties and purity. The wafers used for analysis were cut from the front, middle and tail of the crystals, then lapped and polished on both sides. Dislocation densities and distributions were evaluated by preferential etching (KOH for 25 min. at 400°C). This etch attacks dislocations intersecting the surface of the sample, forming hexagonal etch pits. The microstructures were examined by transmission electron microscopy (TEM). A chemical jet etching technique using 10HCl:1H₂O₂:1H₂O etching solution was applied to produce TEM foils with thicknesses less than 4000Å. The background impurities were determined by secondary ion mass spectrometry (SIMS). Carbon was determined by infrared localized vibrational mode (LVM) absorption measurement (ref. 8). The carrier concentration and mobility were determined by Hall effect measurement, and the minority carrier diffusion length by SEM-EBIC measurement (refs. 9-12).

RESULTS AND DISCUSSION

Reduction of Dislocation Density

A principal cause of dislocations in bulk GaAs crystals is stress induced by thermal gradients (refs. 13-16) during crystal growth. The relatively high dislocation density observed in large diameter (> 2 inch) LEC GaAs has been a source of some concern in applying large-diameter material to minority carrier devices. In the present study, we have investigated optimum growth parameters to substantially reduce the dislocation density in 3-inch LEC GaAs crystals.

The distribution of dislocations across wafers exhibits four-fold symmetry indicative of the $\langle 100 \rangle$ crystallographic orientation, as shown in figure 3. A microscopic view of the dislocation distribution, as shown in figure 4, clearly shows large variations in etch pit density (EPD). The main features of the distribution are: (1) minimum EPD occurs over a large annulus between the center and

edge (Region 1, or "ring" region); (2) intermediate EPD occurs in the center (Region 2, or "center" region); (3) maximum EPD occurs at the edge (Region 3, or "edge" region). In addition, the EPD in the ring and edge regions is greater along the $\langle 100 \rangle$ than the $\langle 110 \rangle$ direction (See figure 4). Figure 5 indicates measured EPD distributions across the full diameter of wafers which typically followed a "W"-shaped profile, and invariably increased from front to tail, indicating that the overall level of stress increased along the crystal, or that the dislocations multiplied after growth, or both. It is important to note that the EPD values at the center and ring regions represent over 75% of the area of the wafer. Therefore, the averaged EPD from these two areas is indicative of the EPD value for the entire wafer. Our experimentally determined radial EPD distributions are consistent with theoretical thermoelastic analyses of Czochralski crystals by Penning (ref. 13) and Jordan et al. (refs. 15, 16).

Through the use of good quality seeds (EPD $< 5000 \text{ cm}^{-2}$), seed necking (if EPD $> 5000 \text{ cm}^{-2}$), shallow cone shaping ($\sim 30^\circ$), thicker B_2O_3 encapsulant layers, and good diameter controls ($< \pm 3\text{mm}$), we have routinely produced 3-inch undoped LEC GaAs crystals with significantly reduced dislocation densities as shown in table I. Further reductions have been attained at the front of the crystal using a slightly As-rich melt, low ambient ($\sim 3 \text{ atm}$) pressures (see table I), or Se-doping ($[\text{Se}] \sim 3 \times 10^{18} \text{ cm}^{-3}$) (see table II). Dislocation densities as low as 6000 cm^{-2} were observed, which is the lowest density reported for 3-inch diameter LEC GaAs wafers. Finally, substantial reduction in dislocation density ($\sim 3.5 \times 10^4 \text{ cm}^{-2}$) has also been achieved at the tail of the crystal through a slow pull-free process, as shown in table I. In contrast to the regular fast pull-free process used to terminate the crystal growth process, the pull-rate did not increase in the slow pull-free process in order to significantly reduce the thermal shock during the pull-free process.

No dislocation reduction effect was observed for Si or Zn doping up to 2×10^{18} and $1 \times 10^{19} \text{ cm}^{-3}$, respectively. In contrast to Bridgman growth (ref. 17), a higher dislocation density was observed in Si-doped LEC GaAs crystals as compared to that of the undoped crystals. The result can be explained by the viscosity reduction in the B_2O_3 encapsulant (i.e. increasing thermal stress) due to the increase of Si content in B_2O_3 (ref. 18).

Our EPD results observed in the present study (see tables I and II) are comparable to commercial 2-inch, undoped D-shaped Bridgman-grown GaAs, as shown in table III. Moreover, the observed values are at least 5 to 10 times lower than commercial 2-inch and 3-inch LEC GaAs crystals (see table III).

Reduction of Twinning

A major problem which has affected the yield of GaAs material suitable for device processing has been the incidence of twin formation. We have found that the melt stoichiometry is an important parameter in controlling the formation of twins in 3-inch-diameter, (100) LEC GaAs crystals. The results of our study show that the incidence of twinning is considerably reduced when undoped or doped crystals are grown from As-rich, near stoichiometric melts. Only 4 or 12 (33%) undoped crystals grown from Ga-rich melts were single. On the other hand, 11 of 13 (85%) undoped crystals and 8 of 9 (90%) doped crystals grown from As-rich melts were single. Furthermore, the incidence of twinning could not be correlated with other growth parameters, such as the wetness of B_2O_3 (for $[\text{H}_2\text{O}] < 500 \text{ ppm}$), the

cone angle, the fluctuation in the diameter of the crystal, or the type of the crucible. The achievement of high single crystal yield (~ 90%) in the LEC GaAs crystals indicates a significant advantage over the conventional Bridgman growth technique, in which the single crystal yield is usually substantially reduced by the crystal sticking to the boat.

Microstructures Observed by TEM

In general, microstructures free of stacking faults, low-angle grain boundaries and dislocation loops, except a few dislocations, can be observed for all undoped LEC GaAs crystals, as well as crystals with Se, Si and Zn doping up to 2×10^{18} , 3×10^{18} and $1 \times 10^{19} \text{cm}^{-3}$, respectively. However, as the Se doping increases to greater than $2 \times 10^{18} \text{cm}^{-3}$, stacking faults and dislocation loops, as shown in figure 6, can be observed. Our results are consistent with that of high-quality Bridgman-grown materials.

Background Impurities

The averaged concentrations of background shallow-donor (Si, S, Se and Te) and metal (Mg, Cr, Mn, Fe and B) impurities in the 3-inch-diameter LEC GaAs grown from both quartz and PBN crucibles as determined by SIMS measurements are shown in table IV. With the exception of Si and B the impurity concentration levels are exceedingly low. Many measurements are either at or below the typical background sensitivity of SIMS technique, suggesting that LEC material in some cases is purer element-by-element than the standard used to check the SIMS background sensitivity. The concentration of both Si and B range from 1×10^{14} to $3 \times 10^{16} \text{cm}^{-3}$, and from 6×10^{14} to $2 \times 10^{18} \text{cm}^{-3}$, respectively. B is the isoelectronic impurity in GaAs, no indication of the electrical activity of B in LEC GaAs has been observed. C as determined by LVM measurements is present at levels varying from about less than $\sim 1 \times 10^{15} \text{cm}^{-3}$ (detection limit) to $1.3 \times 10^{16} \text{cm}^{-3}$. Therefore, C is expected to be a dominant acceptor in LEC material.

We have found that the variability in Si and B levels is dependent on variations in the H_2O content of the B_2O_3 (ref. 19). H_2O in the encapsulant reduces the transport of Si through the B_2O_3 from the quartz crucible to the melt. In addition, the presence of H_2O reduces the pick-up by the melt of B from the B_2O_3 . Si-doped, n-type LEC GaAs with an electron density less than $5 \times 10^{16} \text{cm}^{-3}$ can, therefore, only be grown from quartz crucibles using "dry" B_2O_3 ($[\text{H}_2\text{O}] < 500 \text{ ppm}$).

Our analysis of the background metal impurities, such as Fe, Cr, and Mn, shows virtually no difference between LEC and Bridgman material, as indicated in table IV. The background concentration of the residual donor S is also comparable. Although the Si concentration varies in LEC material grown from quartz crucibles, Si contamination is virtually eliminated by growing from PBN crucibles. As a result, the background Si concentration in LEC GaAs is typically more than one order of magnitude lower than in Bridgman material. Our highest purity material had a concentration of total donors and acceptors ($N_D + N_A$) of about $4 \times 10^{15} \text{cm}^{-3}$, but the typical purity is about $1-2 \times 10^{16} \text{cm}^{-3}$.

Mobility

The dependence of the electron mobility on the free carrier concentration of our material is shown in figure 7. The Se-doped LEC samples have a mobility of approximately 4000 and 2500 cm^2/Vsec corresponding to electron densities of 1×10^{17} and $1 \times 10^{18} \text{cm}^{-3}$, respectively. A slightly lower mobility is observed for the Si-doped samples indicating higher compensation. In general, the mobility curves show a peak for an electron density of $\sim 10^{17} \text{cm}^{-3}$. The reduced mobilities at lower electron concentrations are probably due to compensation controlled by background impurities or native defects. Our mobility results are consistent with statistical analysis of hundreds of crystals grown by conventional bulk-grown methods reported recently by Mullin et al. (ref. 20). In addition, a comparison of our results to the theoretical mobility-electron concentration relationship for GaAs, indicates that our material is characterized by low compensation ratios (0.3 to 0.4) consistent with the statistical behavior of other bulk GaAs materials.

Good mobility was also observed for the p-type LEC GaAs, as shown in figure 8. Hole mobilities as high as 330 cm^2/Vsec (for hole concentration $\sim 1 \times 10^{16} \text{cm}^{-3}$) were observed for the LEC material grown from undoped Ga-rich melt using a PBN crucible. Mobilities as high as 210 cm^2/Vsec were observed for Zn-doped material with $\sim 4 \times 10^{17} \text{cm}^{-3}$ hole concentration. Elliott et al. (ref. 21) have explained the p-type conduction of the undoped LEC GaAs in terms of the 77 meV acceptor (ref. 22). The origin of this acceptor is probably the Ga_{As} antisite defect. Our mobility results for the p-type LEC GaAs are also comparable to the commercially-available, high-purity, small-diameter Bridgman-grown GaAs, as shown in figure 8.

Minority Carrier Diffusion Length

Good hole diffusion lengths (as high as 1.3 μm) have been observed for n-type (Se- or Si-doped), 3-inch-diameter LEC GaAs crystals, as shown in figure 9. The measured values are comparable to those of n-type bulk GaAs grown by conventional methods reported by Sekela et al. (ref. 12). The electron diffusion length has only been determined for one p-type undoped LEC GaAs crystal grown from Ga-rich melt in a PBN crucible (table V). A diffusion length as high as 5.3 μm is observed in the material. This value is close to the 8 μm electron diffusion length reported for both p-type high-purity MOCVD and LPE layers (refs. 10, 11 and 23).

No correlation was observed between the dislocation density and diffusion length for either n- or p-type LEC GaAs. A similar observation has been reported by Sekela et al. (ref. 12) for n-type bulk GaAs. Finally, it is of interest to note that the hole diffusion length as well as the hole concentration across the full-diameter wafer decrease towards the edge, as shown in table V. Since a constant hole mobility was observed across the wafer and no correlation between the diffusion length and dislocation density was detected, the decrease of the diffusion length may be attributed to an increase of an unknown donor concentration toward the edge of the wafer. Further work is still needed in this area.

CONCLUSION

We have shown that large-diameter, n- and p-type LEC GaAs can be grown with a low-dislocation-density, high purity, long minority carrier diffusion lengths, and high mobility. A high single crystal yield (~ 90%) and clean microstructures have also been achieved in these materials. The properties are comparable to small-diameter GaAs crystals grown by conventional bulk growth techniques. Our results showing low dislocation densities and long diffusion lengths indicate that the dislocation density will not be a limiting factor for the application of 3-inch-diameter LEC GaAs crystals to minority carrier devices, such as solar cells. The low background impurities, consistent with high mobility and long diffusion length, also ensure the use of these materials as both passive and active substrate materials in these devices. We, therefore, conclude that for minority carrier devices requiring high-quality and large-area substrates, the 3-inch-diameter LEC GaAs crystals are indeed an excellent material for such applications.

REFERENCES

1. AuCoin, T.R.; Ross, R.L.; Wade, M.J.; and Savage, R.O.: Liquid Encapsulated Compounding and Czochralski Growth of Semi-Insulating Gallium Arsenide, *Solid State Technology*, vol. 22, no. 1, 1979, pp. 59-62.
2. Mullin, J.B.; Heritage, R.J.; Holliday, C.H.; and Straugham, B.W.: Liquid Encapsulation Crystal Pulling at High Pressure, *J. Crystal Growth*, vol. 3-4, 1968, pp. 281-285.
3. Fairman, R.D.; Chen, R.T.; Oliver, J.R.; and Ch'en, D.R.: Growth of High-Purity Semi-Insulating Bulk GaAs for Integrated-Circuit Applications, *IEEE Transactions on Electron Devices*, vol. ED-28, no. 2, 1981, pp. 135-140.
4. Holmes, D.E.; Chen, R.T.; Elliott, K.R.; and Kirkpatrick, C.G.: Stoichiometry-Controlled Compensation in Liquid Encapsulated Czochralski GaAs, *Appl. Phys. Lett.*, vol. 40, no. 1, 1982, pp. 46-48.
5. Holmes, D.E.; Elliott, K.R.; Chen, R.T.; and Kirkpatrick, C.G.: Stoichiometry-Related Centers in LEC GaAs, 2nd Conference on Semi-Insulating III-V Materials, Evian, France, April 19-21, 1982.
6. Thomas, R.N.; Hobgood, H.M.; Eldridge, G.W.; Barrett, D.L.; and Braggins, T.T.: Growth and Characterization of Large Diameter Undoped Semi-Insulating GaAs For Direct Ion Implanted FET Technology, *Solid-State Electronics*, vol. 24, 1981, pp. 387-399.
7. Dash, W.D.: Growth of Silicon Crystals Free of Dislocations, *J. Appl. Phys.*, vol. 28, no. 8, 1957, p. 882.
8. Brozel, M.R.; Clegg, J.B.; and Newman, R.C.: Carbon, Oxygen and Silicon Impurities in Gallium Arsenide, *J. Phys. D, Appl. Phys.*, vol. 11, 1978, pp. 1331-1339.

9. Hackett, W.H., Jr.: Electron-Beam Excited Minority-Carrier Diffusion Profiles in Semiconductors, J. Appl. Phys., vol. 43, no. 4, 1972, pp. 1649-1654.
10. Shen, C.C.; Pande, K.P.; and Pearson, G.L.: Electron Diffusion Lengths in Liquid-Phase Epitaxial p-GaAs:Ge Layers Determined by Electron-Beam-Induced Current Method, J. Appl. Phys. vol. 53, no. 2, 1982, pp. 1236-1237.
11. Wight, D.R.; Oliver, P.E.; Prentice, T.; and Steward, V.W.: Diffusion Lengths In p-type MOCVD GaAs, J. Crystal Growth, vol. 55, 1981, pp. 183-191.
12. Sekela, A.M.; Feucht, D.L.; and Milnes, A.G.: Diffusion Length Studies in Gallium Arsenide, Inst. Phys. Conf. Ser. No. 24, 1975, pp. 245-253. (The Fifth International Symposium on Gallium Arsenide and Related Compounds, Deauville, France, 24-26 September 1974).
13. Penning, P.O., Philips Research Reports, vol. 13, 1958, p. 79.
14. Mil'vidskii, M.G.; and Bochkarev, E.P.: Creation of Defects During the Growth of Semiconductor Single Crystals and Films, J. Crystal Growth, vol. 44, 1978, pp. 61-74.
15. Jordan, A.S.; Caruso, R.; and Von Neida, A.R.: A Thermoelastic Analysis of Dislocation Generation in Pulled GaAs Crystals, The Bell System Technical Journal, vol. 59, no. 4, 1980, pp. 593-637.
16. Jordan, A.S.: An Evaluation of the Thermal and Elastic Constants Affecting GaAs Crystal Growth, J. Crystal Growth, vol. 49, 1980, pp. 631-642.
17. Suzuki, T.; Akai, S.I.; Kohe, K.; Hishida, Y.; Fujita, K.; and Kito, N.: Development of Large Size "Dislocation-Free" GaAs Single Crystal, Sumitomo Electric Technical Review, no. 18, December 1978, pp. 105-111.
18. Rasa Co. Japan, Private communication.
19. Oliver, J.R.; Fairman, R.D.; Chen, R.T.; and Yu, P.W.: Undoped Semi-Insulating LEC GaAs: A Model and A Mechanism, Elec. Letts., vol. 17, no. 22, 1981, pp. 839-841.
20. Mullin, J.B.; Royle, A.; and Benn, S.: A Study on the Relationship Between Growth Technique and Dopants on the Electrical Properties of GaAs With Special Reference to LEC Growth, J. Crystal Growth, vol. 50, 1980, pp. 625-637.
21. Elliott, K.R.; Holmes, D.E.; Chen, R.T.; and Kirkpatrick, C.G.: Infrared Absorption of the 78 meV Acceptor in GaAs, Appl. Phys. Lett., May, 1982.
22. Yu, P.W.; Holmes, D.E.; and Chen, R.T.: Photoluminescence Study in LEC GaAs, Int. Symp. on GaAs and Related Compounds, Oiso, Japan, September 20-23, 1981.
23. Casey, H.C.; Miller, B.I.; and Pinkas, E.: Variation of Minority-Carrier Diffusion Length with Carrier Concentration in GaAs Liquid-Phase Epitaxial Layers, J. Appl. Phys., vol. 44, no. 3, 1973, pp. 1281-1287.

TABLE I. DISLOCATION DENSITY REDUCTION IN UNDOPED 3-INCH LEC GaAs

Front (cm ⁻²)	Tail (cm ⁻²)
1) 12×10^3 (6×10^3 *)	9.0×10^4 (3.3×10^4 *)
2) 1.8×10^4 (1.3×10^4 *)	1.0×10^5 (3.5×10^4 *)
3) 2.0×10^5 (9×10^4 *)	2.2×10^5 (1.1×10^5 *)

*Grown by low ambient pressure (~ 3 atm)

+Grown by slow pull-free process

TABLE II. DISLOCATION DENSITY REDUCTION IN DOPED 3-INCH LEC GaAs*

Front (cm ⁻²)	Tail (cm ⁻²)
1) 6×10^3	1) 6.1×10^4
2) 1.1×10^4	2) 1.2×10^5
3) 1.7×10^5	3) 1.7×10^5

*Se-doping ($n_e \sim 2 \times 10^{18} \text{ cm}^{-3}$)

TABLE III. DISLOCATION DENSITY FOR COMMERCIALY AVAILABLE 2-OR 3-INCH BRIDGMAN AND LEC GaAs CRYSTALS

	E.P.D. (cm ⁻²)
2 INCH - Bridgman (D-shaped) LEC	$\sim 2 \sim 3 \times 10^4$ $> 4 \times 10^4$
3 INCH - LEC	$> 4 \times 10^4$ (Front) $> 3 \times 10^5$ (Tail)

TABLE IV. BACKGROUND IMPURITY ANALYSIS OF LEC GaAs

GROWTH TECHNIQUE	CRUCIBLE	S	Se	Te	Mg	Cr	Mn	Fe	C*	Si	B
LEC ^a	QUARTZ	1.3e15	<1e14	<1e14	<5e14	<5e14	<1e15	<3e15	~3e15 (ND-9e15)	5e14- 3e16	4e14- 2e17
LEC ^b	PBN	1.1e15	<5e14	<5e13	2e14	<5e14	<1e15	<3e15	2-13e15	<1e15	4e14- 2e17
BRIDGMAN ^c	QUARTZ	3e15	3e14	4e13	5e14	<5e14	5e14	5e15	ND	2e16	<2e14

^a 7 CRYSTALS ANALYZED AND AVERAGED.

^b 12 CRYSTALS ANALYZED AND AVERAGED.

^c 4 CRYSTALS ANALYZED AND AVERAGED.

*CARBON DETERMINED BY LVM.

TABLE V. ELECTRON DIFFUSION LENGTH IN P-TYPE LEC GaAs

WAFER NO.	CRUCIBLE	DOPANT	SAMPLE LOCATION	FREE HOLE CONCENTRATION (cm ⁻³)	DIFFUSION* LENGTH (μm)	MOBILITY (cm ² /Vsec)
R20-F	PBN	NONE	CENTER	1.33 x 10 ¹⁶	5.3	315
		(Ga-RICH MELT)	RING	1.10 x 10 ¹⁶	4.1	315
			NEAR EDGE	1.05 x 10 ¹⁶	2.3	316

*ELECTRON DIFFUSION LENGTH ~ 8 μm REPORTED FOR BOTH p-TYPE MOCVD AND LPE LAYERS.

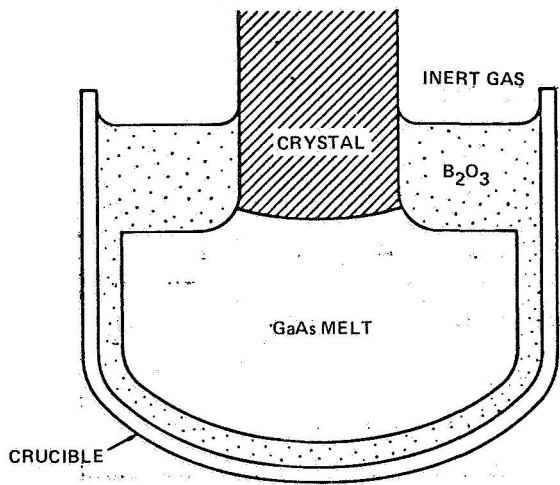


Figure 1. Configuration for LEC Growth System.



Figure 2. A 3.6 Kg, 3-inch Diameter, (100) LEC GaAs Crystal with Diameter Variation Less Than ± 2 mm.

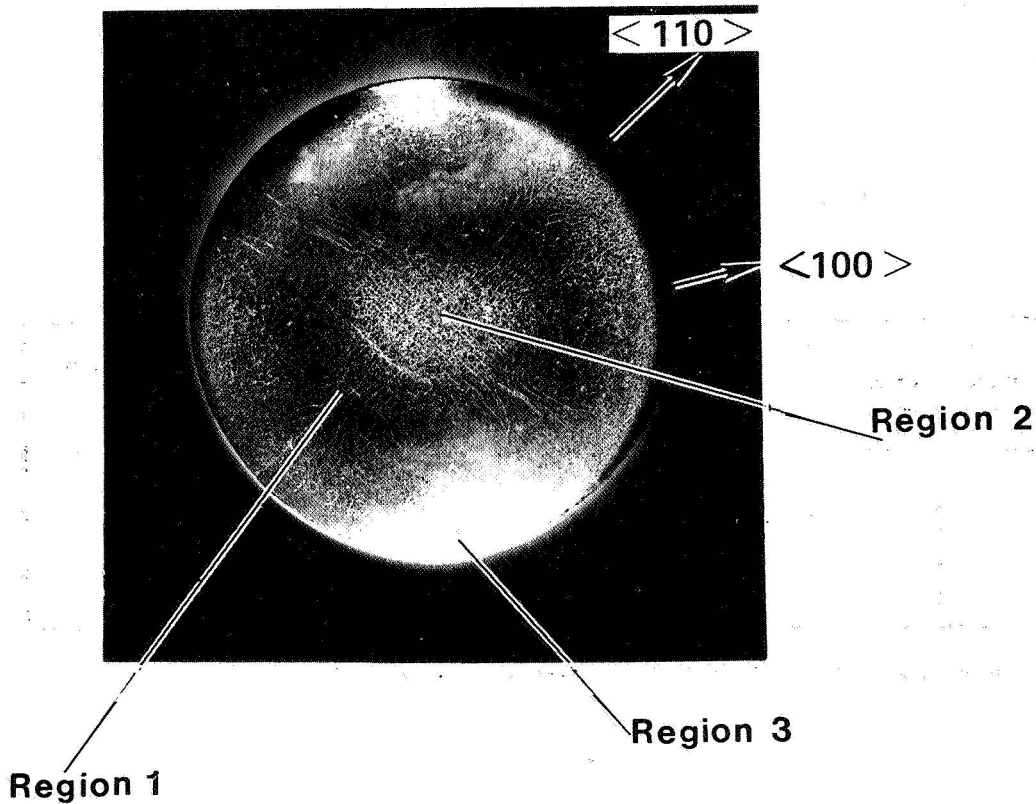


Figure 3. Radial Dislocation Density Map for 3-inch GaAs LEC wafers.

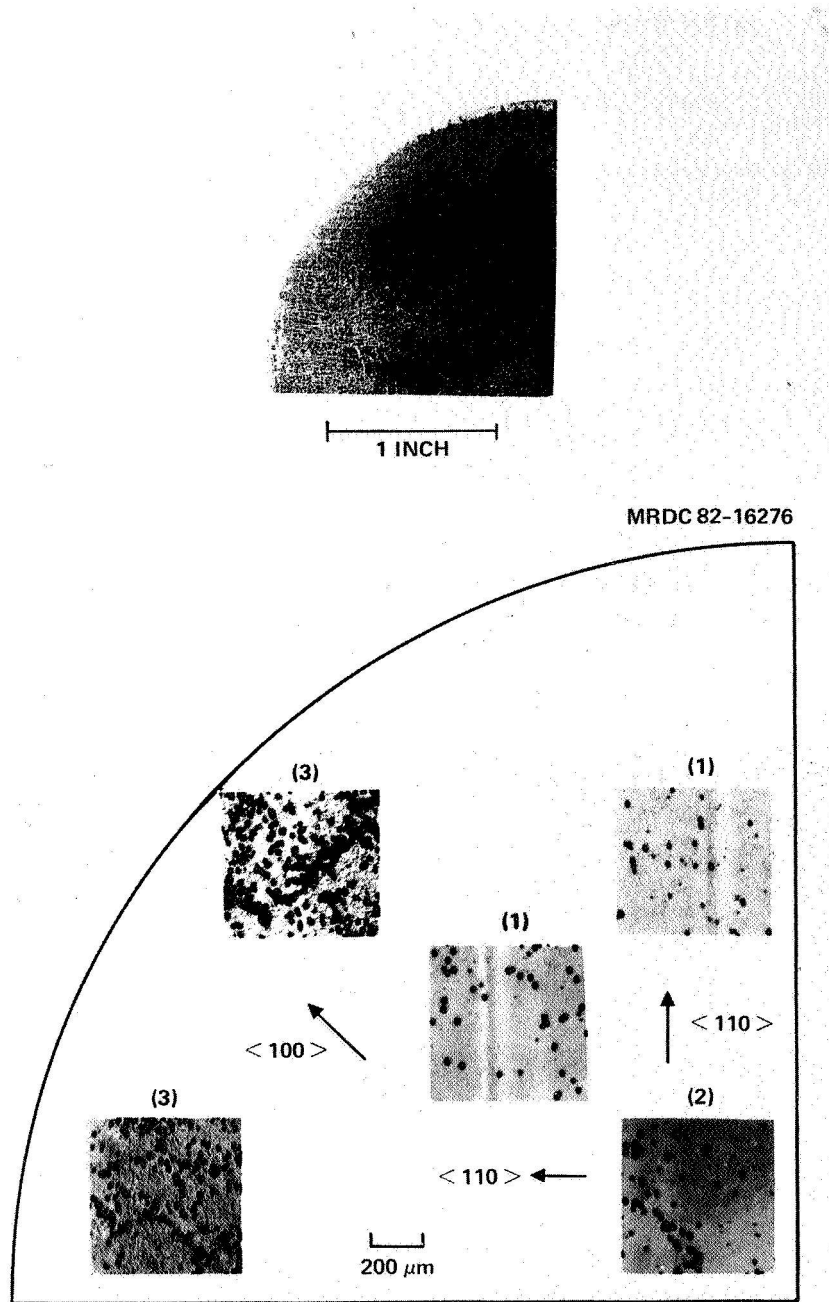


Figure 4. Etch Pit Density Map for a (100) LEC GaAs Wafer.

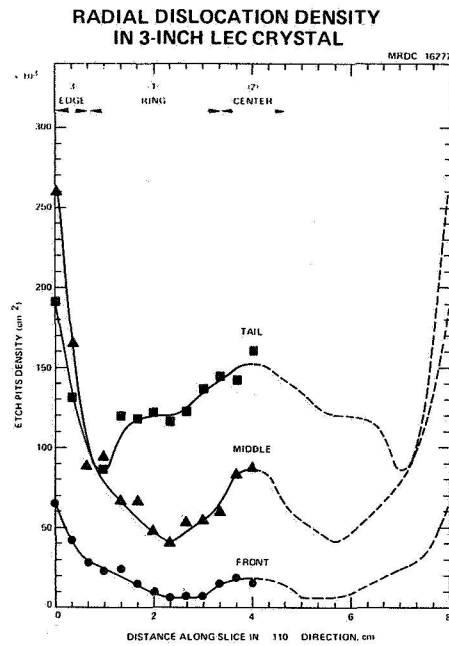


Figure 5. Radial and Longitudinal Dislocation Density for Large-diameter LEC GaAs Crystal.

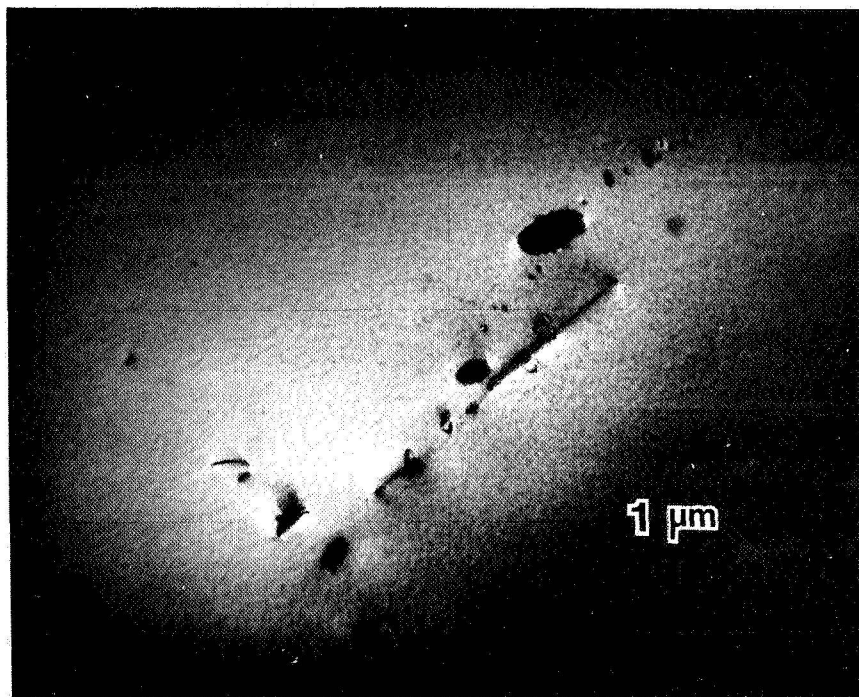


Figure 6. B.F. Micrograph for a Se-doped LEC GaAs sample with $[Se] \sim 7 \times 10^{18} \text{ cm}^{-3}$.

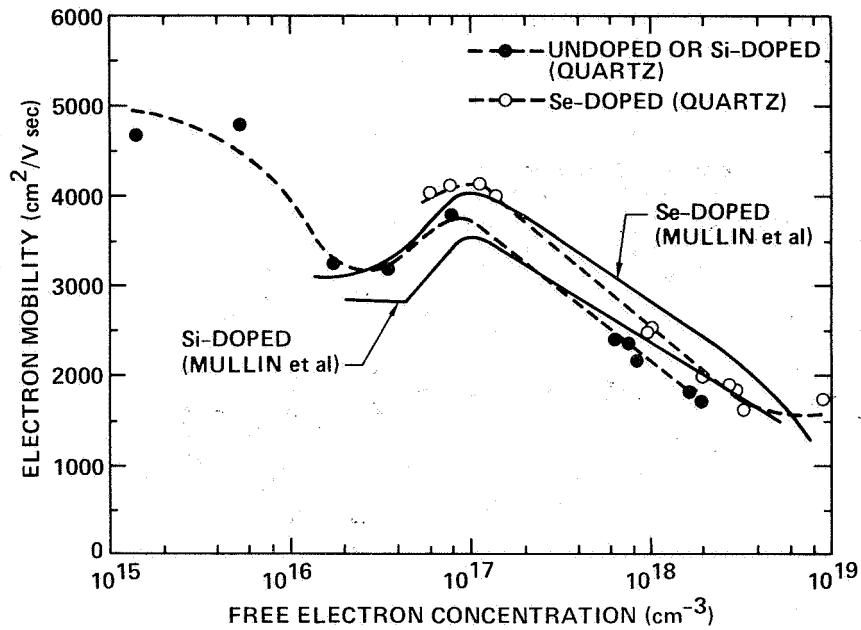


Figure 7. Mobility vs. Free Electron Concentration for n-type LEC GaAs.

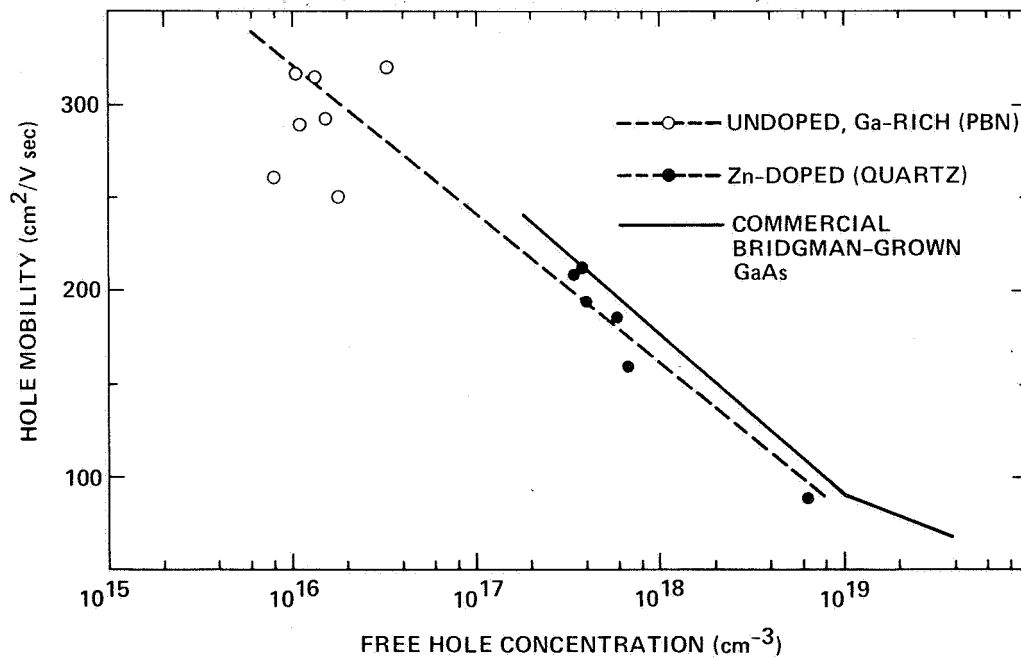


Figure 8. Mobility vs. Free Hole Concentration for p-type LEC GaAs.

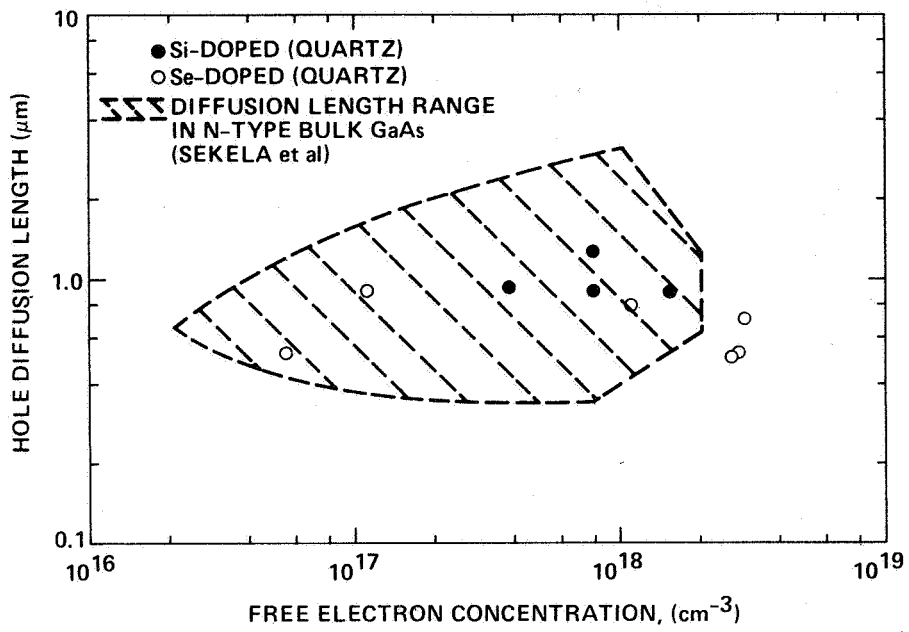


Figure 9. Hole Diffusion Length vs. Free Electron Concentration for n-type LEC GaAs.

GaAs SOLAR CELLS FOR CONCENTRATOR SYSTEMS IN SPACE*

R.Y. Loo, R.C. Knechtli, and G.S. Kamath
Hughes Research Laboratories
Malibu, California

ABSTRACT

A number of solar cell systems operating with concentrated sunlight are being considered for space applications. GaAs solar cells are specially attractive for such systems. Even modest solar concentration ratios lead to substantial increases in the efficiency of the GaAs cells. This compounds the superior efficiency which these cells already exhibit in the absence of solar concentration.

We have made cells for operation in space up to more than 100 suns and have obtained an AMO efficiency of 21% at 100 suns with these cells. The increased efficiency resulted not only from the higher open circuit voltage associated with the higher light intensity (higher short circuit current); it also benefitted from the increase in fill factor caused by the lower relative contribution of the generation recombination current to the forward bias current when the cell's operating current density is increased.

Another attractive feature of these GaAs concentrator solar cells is their ability to retain a good efficiency up to high temperatures. The experimental cells mentioned above exhibited an AMO efficiency close to 16% at 200°C. The prospect of exploiting this capability for the continuous annealing of radiation damage or for high temperature missions (e.g., near sun missions) remains therefore open.

Space systems with concentration ratios on the order of 100 suns are presently under development. We will show that the tradeoff between increased concentration ratio and increased loss due to the cell's series resistance remains attractive even for space applications at a solar concentrator ratio of 100 suns. In the design of contact configuration with low enough series resistance for such solar concentration ratios, the shallow junction depth ($<0.5 \mu\text{m}$) needed for good radiation hardness and the thin AlGaAs layer thickness needed to avoid excessive optical absorption losses have to be retained. This leads to some constraints which are more severe for space cells than for terrestrial applications. However, even with these constraints, high AMO efficiencies remain attainable at 100 suns for space cells, as shown above.

INTRODUCTION

Concentrator solar cell systems are of interest for space applications because of the prospects of providing lower cost systems with longer life in the radiation environment representative of practical space missions. The GaAs solar cells are especially attractive for this purpose because of their superior efficiency and resistance to radiation damage, together with their ability to operate efficiently at higher temperatures than silicon solar cells. One important observation is that the GaAs solar cells' efficiency, which is already high in the absence of solar concentration, increases even further with increasing solar concentration. Another important property of the GaAs solar cells is their ability to substantially recover from

* Work supported by NASA LeRC, Contract No. NAS3-22227

radiation damage by annealing at temperatures as low as 200°C. One consequence of these features is the possibility of combining both the high solar concentration and high temperature properties of GaAs solar cells so that they can be operated continuously in space for long periods of time. An alternate option is to provide capabilities for periodic annealing of the cells.

While several groups have had an active interest in the development of GaAs solar cells for concentrator applications^{1,2}, most of this work had been directed to terrestrial applications. Our own work is specifically directed to space applications. This means that we are interested in AMO efficiency rather than AM1 or AM2 performance. Furthermore, the need to minimize radiation damage limits us to consider only cells with relatively shallow junction depth ($\leq 0.5 \mu\text{m}$). Finally, because of the difficulty of cooling in space, we have an additional incentive to operate at relatively high temperatures.

In this report we consider specifically two cell designs: a large square 2 cm x 2 cm cell for space systems operated at relatively low solar concentration ratios (on the order of 10 suns), and a small concentrator cell with 4 mm diameter circular active area for high solar concentration systems operated at ≥ 100 suns.

CELL DESIGN

Figure 1 shows the baseline design for our space concentrator cell. This design follows the same guidelines as the space qualified GaAs cells reported in our earlier work.³ As indicated above, the special features of our concentrator cells are the thin (AlGa)As window layer ($\leq 0.5 \mu\text{m}$) and shallow junction depth ($0.5 \mu\text{m}$). Figure 2 shows the calculated efficiency of our GaAs cells as a function of solar concentration ratio with normalized series resistance R_{s1} as a parameter. This provides the guidelines needed for the design of our cells' contacts. More specifically, figure 2 shows that we have to keep $R_{s1} \leq 0.1 \Omega \text{ cm}^2$ for our large 2 cm x 2 cm cells to avoid excessive penalty in efficiency for concentration ratios up to $X = 10$ suns. Alternately, for our small 0.4 cm diameter cell designed for operation at $X = 100$ suns, we wish to keep $R_{s1} \leq 0.01 \Omega \text{ cm}^2$.

The gridline designs adopted to satisfy these requirements are shown on figure 3. The large cell (2 cm x 2 cm) has 80 guidelines running in parallel to each other. Each finger linewidth is 20 μm wide. There are two bus bars connecting the fingers at each end of the cell. The small circular cell has 90 radial gridlines extending from a radius of 2 mm down to 0.75 mm, 36 radial fingers from a radius of 0.75 to 0.50 mm and 12 radial fingers from a radius of 0.50 mm to 0.25 mm. The width of all fingers is tapered from 10 μm at the outer radius to 5 μm at the inner radius. The finger height is nominally 3 μm in all cells (Ag overlay). The corresponding contact finger metal resistivity is $2 \times 10^{-6} \Omega \text{ cm}$. The average resistivity of the semiconductor p-layer is $2 \times 10^{-2} \Omega \text{ cm}^2$. The metal-semiconductor interface resistance (normalized to the actual contact finger area, not to the total solar cell areas) is taken to be equal to $1 \times 10^{-3} \Omega \text{ cm}^2$. This latter value falls within the range of values measured on our experimental cells. With these values and the contact configuration described above, the calculated normalized series resistances are $0.04 \Omega \text{ cm}^2$ for the 2 cm x 2 cm cell and $0.01 \Omega \text{ cm}^2$ for the 0.4 cm diameter cell. These calculated values fall within the range specified above by inspection of figure 2.

CELL FABRICATION

Our GaAs concentrator solar cells were fabricated with the same infinite melt liquid phase epitaxial growth (LPE) technique now routinely used for the batch fabrication of our conventional 2 cm x 2 cm space qualified cells. We used photolithography for the fabrication of the front contact. We have selected to make direct contact to the (AlGa)As layer even though this is more difficult to do with

conventional techniques than making contact to the GaAs. We have overcome the difficulty of contacting to (AlGa)As by using sputter-deposition of the initial layers of AuZn on the (AlGa)As. For the back contact, we use conventional vapor deposition of Au Ge Ni. A 3 μm thick Ag overlay is plated to both front and back sides of the metallization in order to reduce the finger gridline resistance. Finally, the cells are coated with 650 \AA of Ta₂O₅ for antireflection coating.

TEST RESULTS

Figure 4 shows a set of measurements performed on the large 2 cm x 2 cm cells designed for operation at a concentration of $X = 10$ suns; figure 5 shows the measurements of the small cells (0.4 cm diameter active area) designed for operation at $X = 100$ suns. The efficiencies shown on figure 4c and figure 4d at concentration ratio up to $X = 10$ suns for our 2 cm x 2 cm concentrator cells are relatively low and compare unfavorably in the absence of concentration with our conventional 2 cm x 2 cm GaAs solar cells. While the cause for this deficiency has been identified (inadequate AR coating), no additional cells of this type were made to correct this deficiency prior to this meeting. Higher priority was given to the development of the smaller cells for operation at 100 suns. This led to the rewarding results (high AMO efficiencies) shown on figure 5c and 5d for operation at 100 suns with those cells.

The effect of temperature on the short-circuit current of our cells is shown on figure 4a and 5a. The increase of short-circuit current with temperature exhibited by these measurements is explained in part by the narrowing of the bandgap of GaAs with increasing temperature ($dE_g/dT \approx -5 \times 10^{-4}$ eV/ $^{\circ}\text{K}$). This feature is helpful insofar as it partly compensates the loss of open-circuit voltage caused by increasing temperature. The loss of open-circuit voltage with increasing temperature is shown on figure 4b and 5b. It is found to be $dV_{oc}/dT = -2$ mV/ $^{\circ}\text{K}$ and closely matches the theoretically calculated value. The loss of efficiency with increasing temperature results from the combination of the changes in open-circuit voltage, short-circuit current and fill factor with increasing temperature. The measured values of efficiency versus temperature are shown on figure 4c and 5c. We observe that in the absence of solar concentration, the efficiency obtained at an elevated temperature of 200 $^{\circ}\text{C}$ is still 11% for both types of cells. Furthermore, this efficiency becomes even higher when the solar concentration ratio is increased above unity.

The increase in efficiency with increasing solar concentration results not only from the increased open-circuit voltage, it also benefits from the increased fill factor. The latter results from the decreasing relative contribution of the generation current in the depletion region at the junction when the GaAs solar cell operates at higher current densities. These beneficial effects are off-set at increasing solar concentrations by the growing power loss due to the series resistance. As shown below, our measurements confirm that this contribution becomes important at concentration ratios in excess of 100 suns for our small cells. The measured data is shown on figure 4d and 5d, where the AMO efficiency is shown as a function of concentration ratio for the 3 temperatures of 25 $^{\circ}\text{C}$, 100 $^{\circ}\text{C}$, and 200 $^{\circ}\text{C}$. Alternately, the AMO efficiency of our cells has already been shown as a function of temperature with the concentration ratio as a parameter in figure 4c and 5c. It is especially rewarding to observe (figure 5c) that an AMO efficiency close to 16% is obtained at a temperature as high as 200 $^{\circ}\text{C}$ with a cell suitable for operation in space.

A final task is to compare the experimental results obtained to date with the theoretical calculations. More specifically, the curve of efficiency versus concentration ratio measured at 25 $^{\circ}\text{C}$ and shown as one of the curves of figure 5d can be compared with the theoretical curves shown on figure 2. Two observations are to be made in this context:

- 1) At high concentration ratios ($X = 100$), the measured and calculated efficiencies (21%) are in close agreement, provided the series resistance of the

experimental cell is $R_s < 10^{-2} \Omega \text{cm}^2$. This falls within the range of measured series resistances for our small cells.

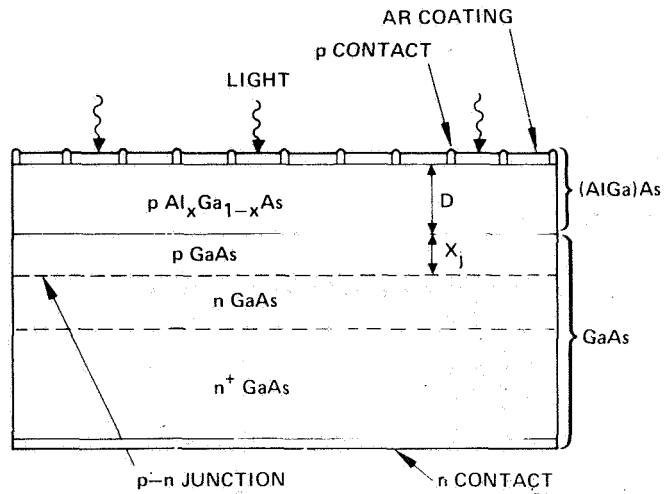
2) At low concentration ratios ($X = 1$), the calculated efficiency is substantially higher than the measured value (19% versus 16%). We have been able to trace this back to the poor fill factor exhibited at low concentration ratio on the measured set of small cells. This was caused by excessive edge-leakage current, a defect which has been overcome since those measurements were performed. This defect becomes inconsequential at the higher concentration ratios, which explains the improved agreement between theory and measurements observed at the high concentration ratios.

CONCLUSIONS

We have established that GaAs solar cells designed for operation in space under concentrated sunlight are attractive for concentration ratios up to more than 100 suns. AMO efficiencies in excess of 20% were obtained at 100 suns. Operation at elevated temperatures was found to be possible at AMO efficiencies in excess of 16% with a temperature as high as 200°C. The cells providing this performance had the shallow junction depth and thin AlGaAs window layer thickness required for good radiation hardness and favorable spectral response under AMO illumination in space.

REFERENCES

1. R. Sahai, et al, "High Efficiency AlGaAs/GaAs Concentrator Solar Cell Development," Proc. 13th IEEE Photovoltaic Specialists Conference, p. 946 (1978).
2. P.E. Gregory, et al., "Performance and Durability of AlGaAs/GaAs Concentrator Cells," Proc. 15th IEEE Photovoltaic Specialists Conference, p. 147 (1981).
3. R.C. Knechtli, et al., "Development of Space - Qualified GaAs Solar Cells," Proc. 2nd European Symposium on Photovoltaic Generators in Space, ESA SP-147, p. 121 (1980).



p CONTACT: Au-Zn-Ag
 n CONTACT: Au-Ge-Ni-Ag
 AR COATING: Ta_2O_x
 p $Al_xGa_{1-x}As$: $x > 0.85$
 $D + X_j \leq 1.0 \mu m$

Figure 1. The (AlGa) As-GaAs solar cell: baseline structure.

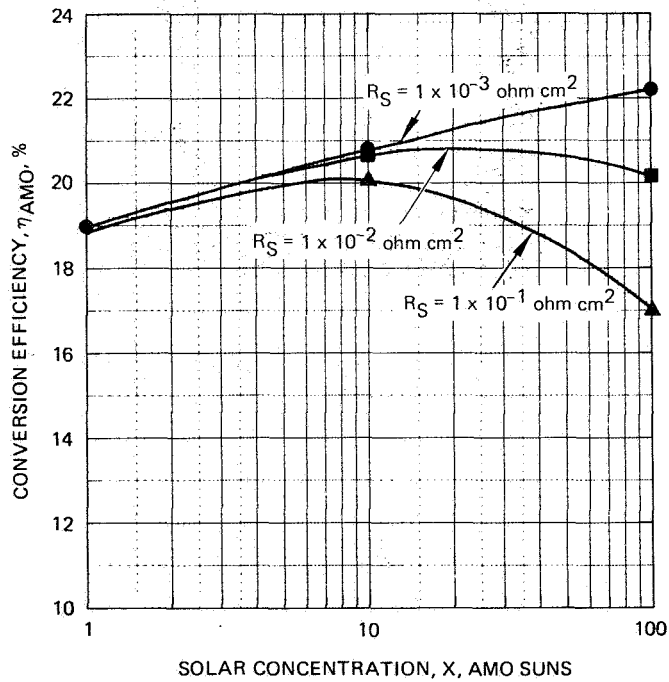
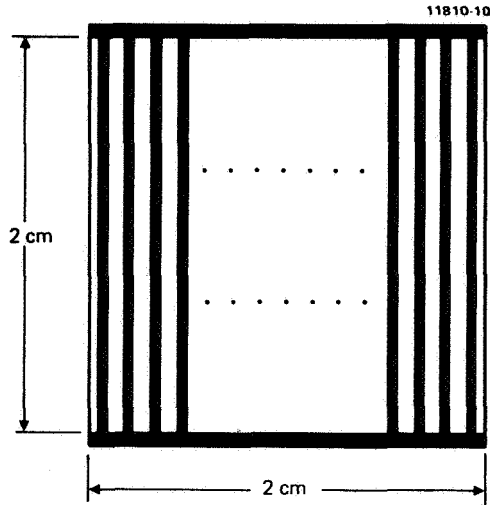
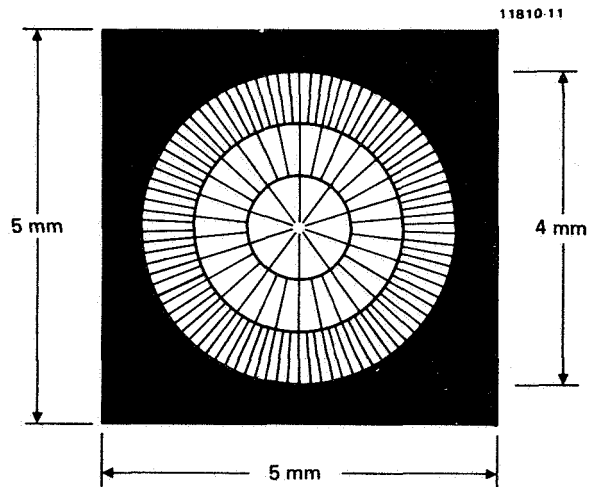


Figure 2. GaAs solar cells: calculated AMO efficiency vs solar concentration

(A) SQUARE GRIDLINE DESIGN FOR THE
2 cm x 2 cm GaAs CONCENTRATOR CELL



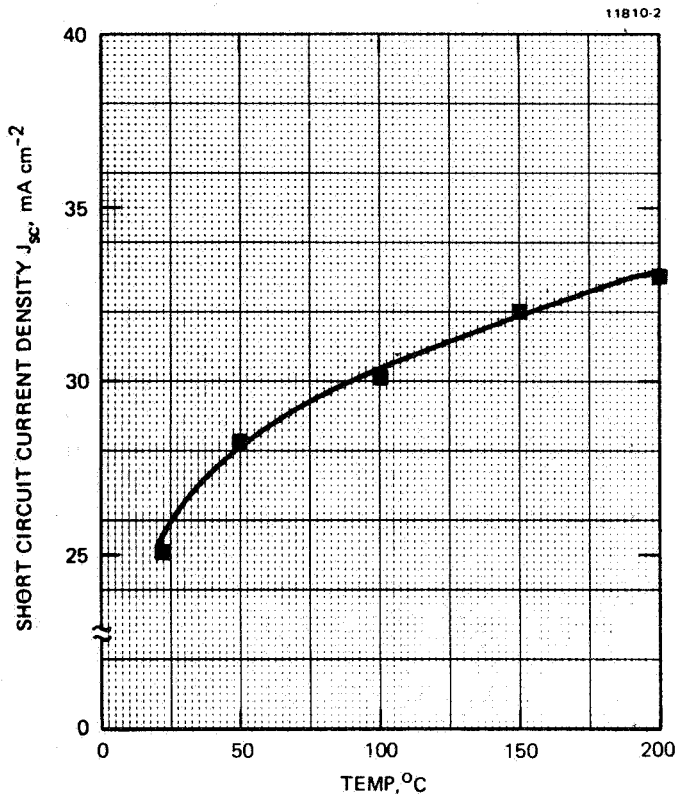
(B) CIRCULAR GRIDLINE DESIGN FOR THE 4 mm
DIAMETER SPOT SIZE GaAs CONCENTRATOR CELL



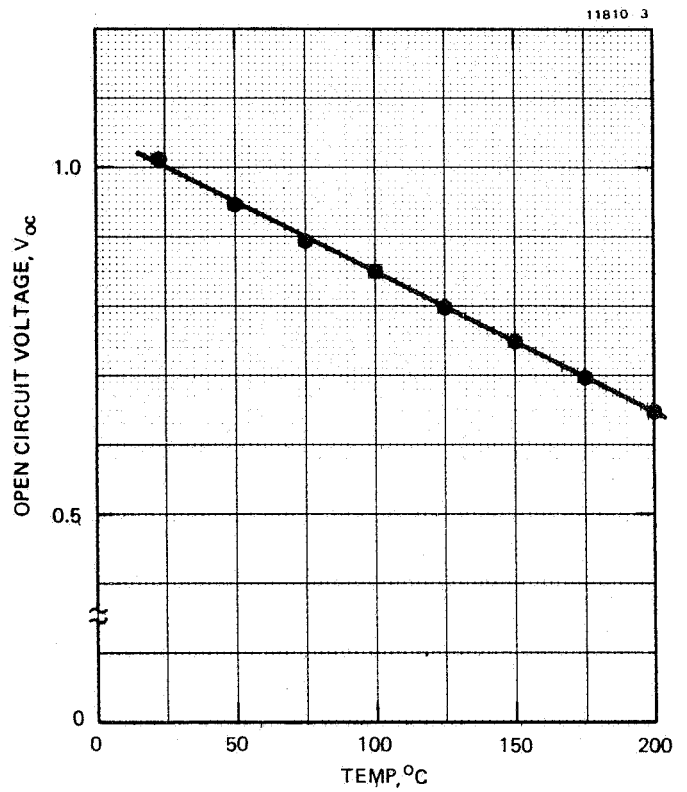
NOTE: SEE TEXT FOR FINGER NUMBERS AND
DIMENSIONS FOR BOTH DESIGNS

Figure 3. Grid line designs.

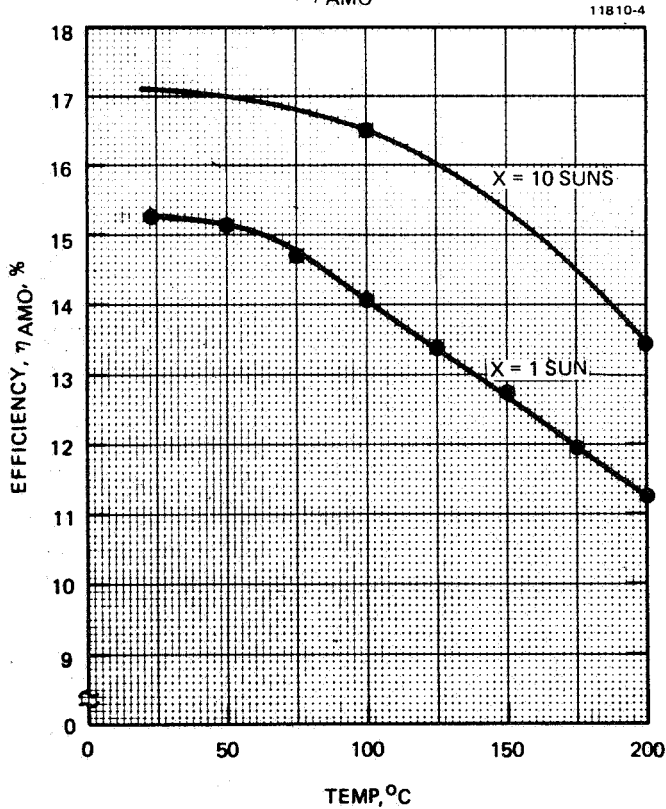
(A) SHORT CIRCUIT CURRENT DENSITY vs TEMPERATURE



(B) OPEN CIRCUIT VOLTAGE vs TEMPERATURE



(C) EFFICIENCY, η_{AMO} , vs TEMPERATURE



(D) EFFICIENCY, η_{AMO} , vs SOLAR CONCENTRATION

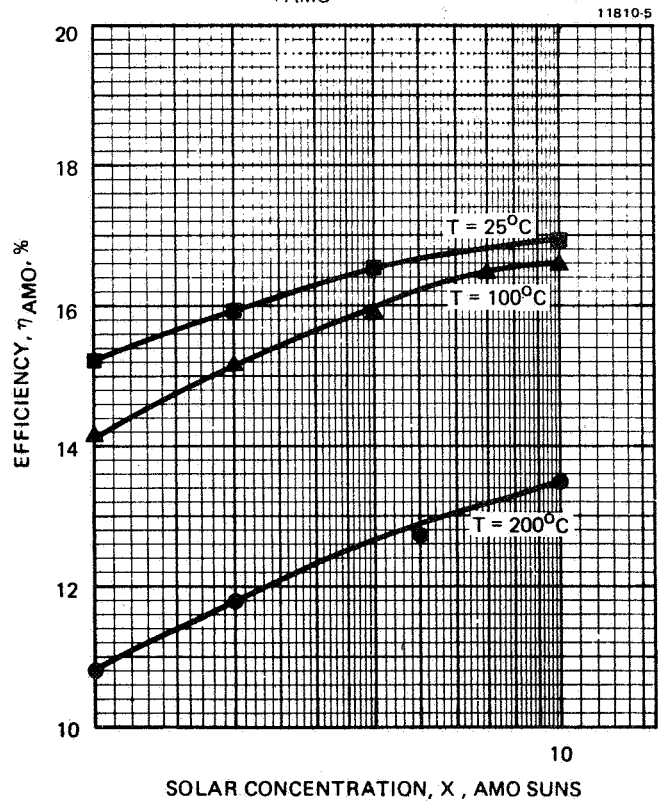


Figure 4. Large area 2 cm x 2 cm GaAs space concentrator cell characteristics.

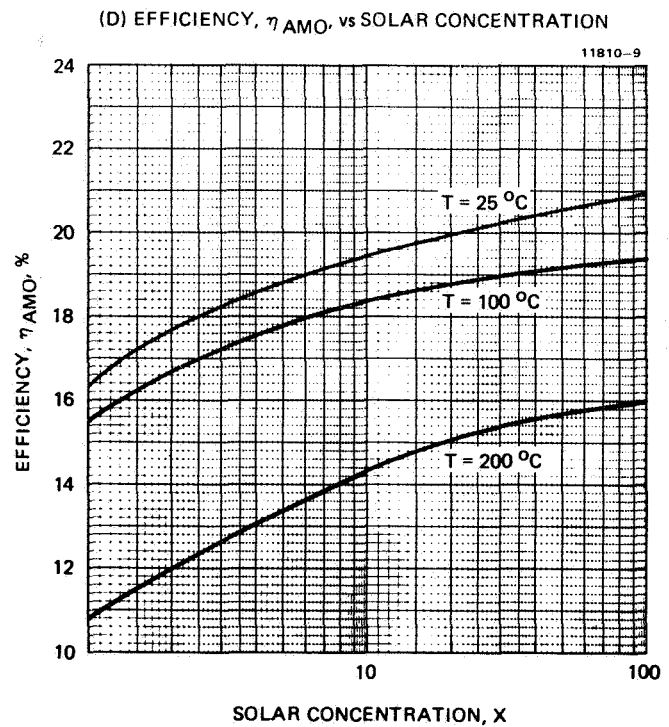
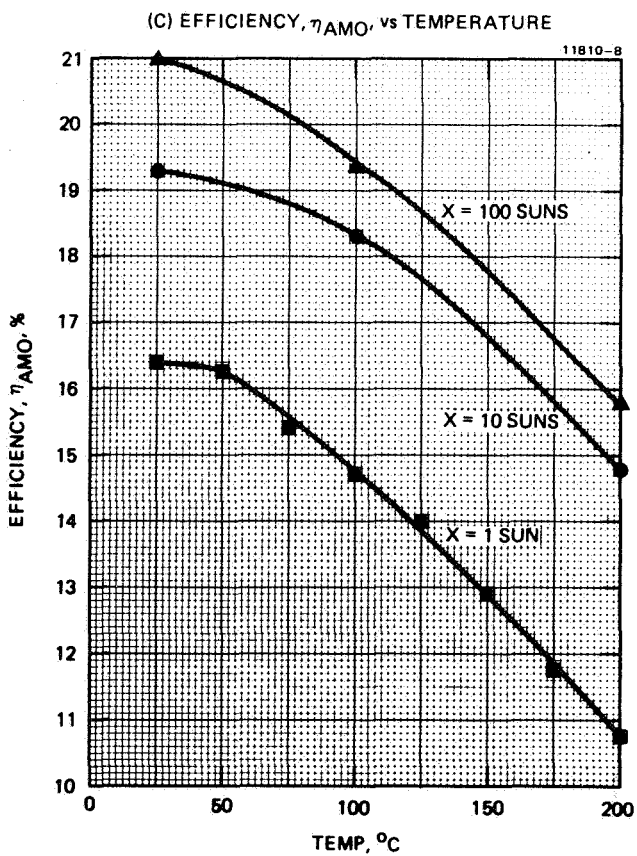
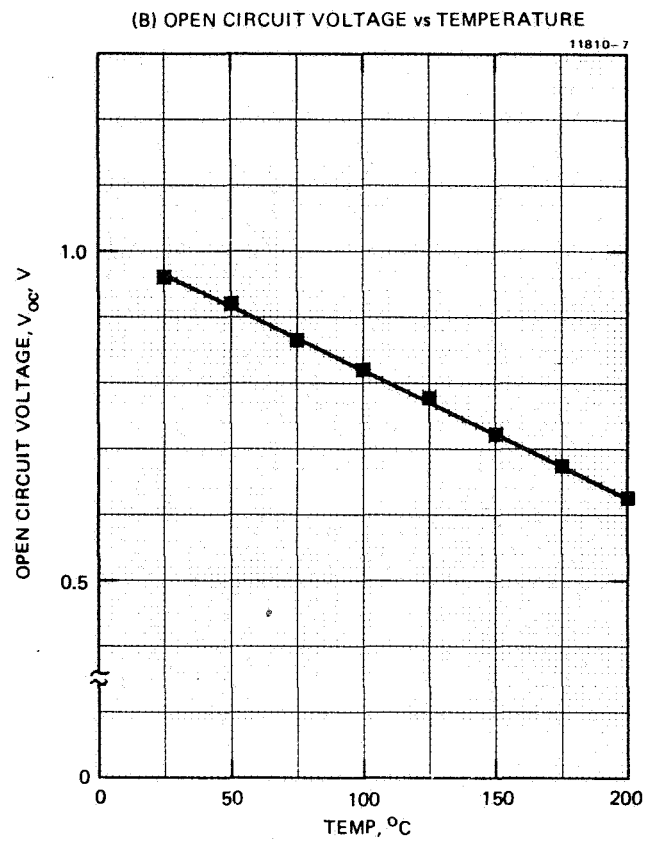
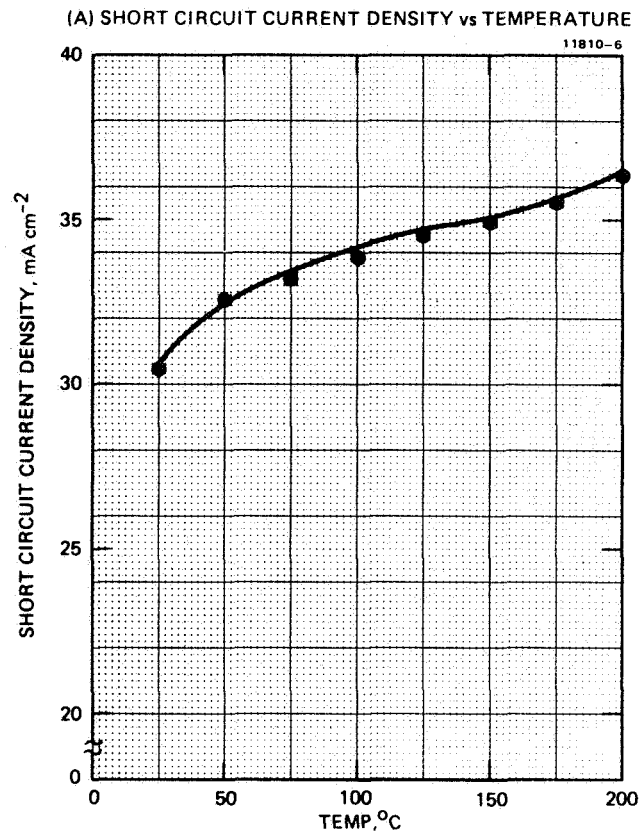


Figure 5. Small circular GaAs space concentrator cell characteristics.

THE EFFECT OF DIFFERENT SOLAR SIMULATORS ON THE MEASUREMENT OF SHORT-CIRCUIT CURRENT TEMPERATURE COEFFICIENTS

H.B. Curtis and R.E. Hart, Jr.
NASA Lewis Research Center
Cleveland, Ohio

SUMMARY

Gallium arsenide solar cells are being considered for several high temperature missions in space. Both near-Sun and concentrator missions could involve cell temperatures on the order of 200° C. Performance measurements of cells at elevated temperatures are usually made using simulated sunlight and a matched reference cell. Due to the change in bandgap with increasing temperature at portions of the spectrum where considerable simulated irradiance is present, there are significant differences in measured short circuit current at elevated temperatures among different simulators. To illustrate this, both experimental and theoretical data are presented for gallium arsenide cells.

INTRODUCTION

The use of gallium arsenide solar cells in space is being considered for several reasons. One reason is their high temperature operation, thus allowing near-Sun or high concentration missions. Before high temperature (200° C) gallium arsenide cells can be used, however, further development work will be required. There will also be many required measurements at temperatures ranging from about room temperature to over 200° C. Some recent data have indicated that the increase in measured short circuit current, α , with increasing temperature depends strongly on the type of solar simulator used. The temperature coefficient of α can vary by a factor of more than 5 depending on the incident irradiance. The tentative answer to why α varies with incident irradiance depends on the bandgap of gallium arsenide. As the temperature is increased, the decrease in bandgap is at portions of the spectrum where the irradiance of simulators and sunlight is both fairly high and varies from simulator to simulator. Hence the temperature coefficient can vary widely. In an effort to test this hypothesis, NASA Lewis performed an experimental and theoretical study using gallium arsenide cells, a variety of solar simulators, and the known bandgap temperature characteristics of gallium arsenide.

THEORETICAL CALCULATIONS

The increase in α with temperature results from two effects. The smaller bandgap allows more incident photons to be collected, and secondly, there can be an improvement in the lifetime of the cell material (ref. 1). Since we are concerned here with the effects of different simulators, we will only look at the change in bandgap effect, because any increase in lifetime will give a similar current increase for each simulator. The change in bandgap for gallium arsenide is well known (ref. 2) and can be utilized to generate a series

of spectral response curves. In Figure 1 we have plotted spectral response curves for gallium arsenide at several temperatures. The 300 K curve is measured data, and the higher temperature curves are generated by shifting the cutoff wavelength corresponding to the change in bandgap.

The short circuit current can be calculated for any spectral distribution of irradiance by using the following equation:

$$I_{SC} = A \int J(\lambda)R(\lambda)d\lambda \quad (1)$$

where $J(\lambda)$ is the spectral distribution of incident irradiance, $R(\lambda)$ is spectral response, A is cell active area, and the integration is over the solar wavelength (λ) region. Figures 2 to 6 show spectral distributions for AMO sunlight and four solar simulators. Equation (1) was used to calculate α at several temperatures for gallium arsenide solar cells under the different spectral irradiances of figures 2 to 6. Figure 7 shows calculated α as a function of temperature for three of the incident irradiances, AMO, Filtered xenon, and unfiltered xenon. Note that the increase in current is not necessarily linear with increasing temperature. Note also the large differences between the unfiltered xenon curve and the AMO and filtered xenon curves. The curves were normalized to the AMO value at 300 K (112.7mA for a 4 cm² cell) for direct comparison.

The temperature coefficients of α were calculated using the data of figure 7 and similar data for the two other simulators (pulsed xenon and dichroic filtered tungsten (ELH) and are presented in table I. The AMO value near 20 μ A/cm²-K is in agreement with published data on similar cells (refs. 3 and 4). In all cases the temperature coefficient is higher in the 400 to 500 K range than in the 300 to 400 K range. Note the extremely high values of temperature coefficient for the unfiltered xenon simulator. This is due to the very high irradiance in the wavelength interval near the gallium arsenide bandgap for the unfiltered xenon simulator.

MEASURED DATA

In an effort to experimentally verify the calculated data, measurements were made on two gallium arsenide cells at various temperatures and under different simulators. The cells were manufactured by Hughes Research Lab under an existing NASA Lewis contract, using the liquid phase epitaxy growth technique. They are p/n cells with an AlGaAs window. At Lewis measurements were made at 200° C (473 K) using a xenon pulsed simulator and at 150° C (423 K) using a filtered xenon simulator and an ELH lamp simulator. Data at 200° C (473 K) under an unfiltered xenon simulator were supplied by Hughes. The measured data are summarized in table II with current at the highest temperature measured for each simulator and the calculated temperature coefficients reported. Data were taken only to 150° C under the filtered xenon and ELH simulators due to limitations in the temperature capabilities of the test apparatus.

The measured data are in fairly good agreement with calculated data of table I. For the three xenon simulators, filtered, unfiltered, and pulsed, the measured temperature coefficients are 10 to 30 percent higher than the calculated values. However, the calculated values do not reflect any increase in α due to improved lifetime at higher temperatures. Accounting for this would make the measured and calculated temperature coefficients agree quite well for the three xenon simulators. For the ELH lamp simulator, the calculated value of temperature coefficient is larger than the measured value.

This is attributed to variations in output of ELH lamps. The spectral distribution of figure 6 may not be the same as that of the ELH lamp used in the measurements. In any case, the temperature coefficient measured using an ELH lamp simulator is considerably lower than the true value.

CONCLUSIONS

Both calculated and measured data indicate a strong dependence on incident spectral irradiance for the measured temperature coefficient of short circuit current for GaAs solar cells. Values of as high as $80\mu\text{A}/\text{cm}^2\text{ K}$ using an unfiltered xenon simulator, or as low as $10\mu\text{A}/\text{cm}^2\text{ K}$ using an ELH lamp simulator may be obtained. The reason for the spread in values results from the bandgap change with temperature occurring at portions of the spectrum where simulators can differ widely.

REFERENCES

1. Hovel, H.J.: Solar Cells. Vol. 11, Semiconductors and Semimetals. Academic Press, 1975.
2. Sze, S.M.: Physics of Semiconductor Devices. Wiley-Interscience, 1981.
3. Anspaugh, B.E., et al.: Characteristics of Solar Cells for Space Applications. Vol. XIII, JPL Publication 78-15, June 1980.
4. Swartz, C.K., and Hart, R.E., Jr.: Temperature and Intensity Dependence of the Performance of an Electron-Irradiated (AlGa) As/GaAs Solar Cell. Solar Cell High Efficiency and Radiation Damage, 1979. NASA CP-2097, 1979, pp. 217-22.

TABLE I.- CALCULATED VALUES OF SHORT-CIRCUIT CURRENT

TEMPERATURE COEFFICIENTS

Spectrum	Temperature coefficients, $\mu\text{A}/\text{cm}^2 \text{ K}$, at -	
	300 - 400 K	400 - 500 K
AM0	18.6	21.2
Filtered xenon	15.6	22.7
Unfiltered xenon	49.2	62.2
Pulsed xenon	20.9	27.2
ELH	10.4	10.8

TABLE II.- SUMMARY OF MEASURED DATA

Simulator	Short circuit current I_{SC} , mA	Temperature coefficient, $\mu\text{A}/\text{cm}^2 \text{ K}$
Filtered xenon	125.2 at 150° C	25.0
Unfiltered xenon	168.9 at 200° C	80.3
Pulsed xenon	134.0 at 200° C	30.4
ELH	116.2 at 150° C	7.0

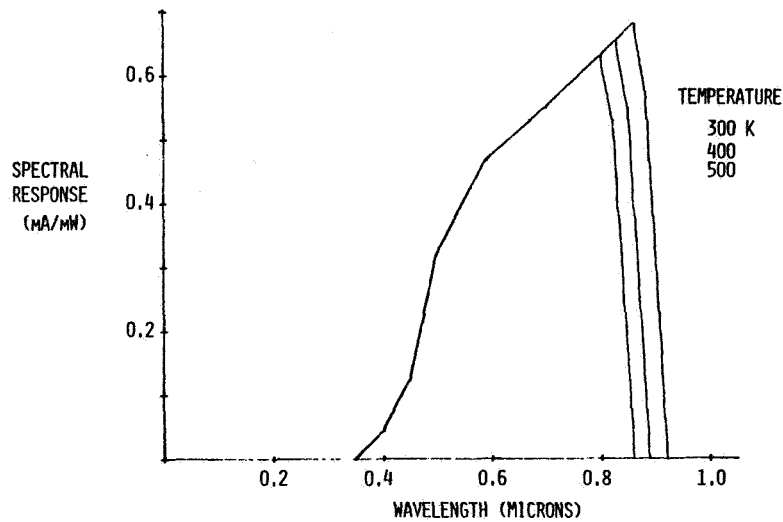


Fig. 1 Spectral response of gallium arsenide

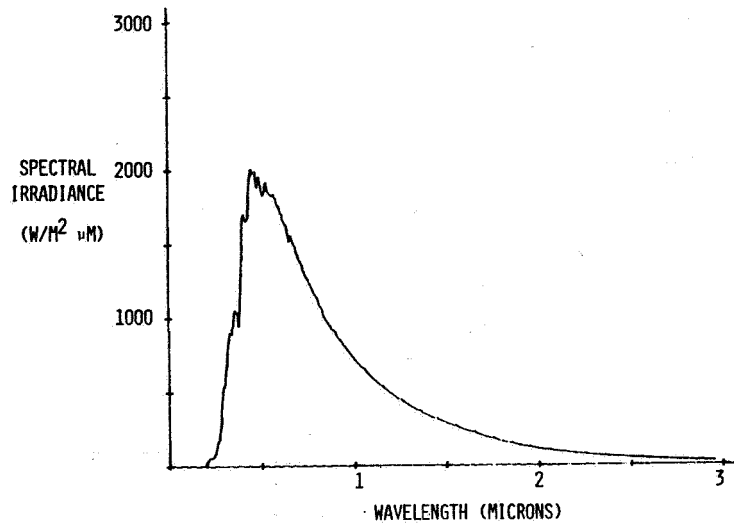


Fig. 2 Labs & Neckel AMO spectrum

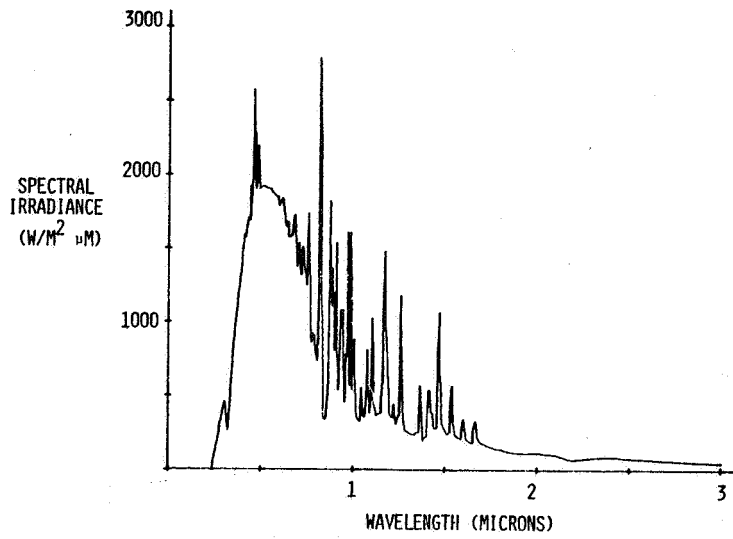


Fig. 3 Filtered xenon spectrum

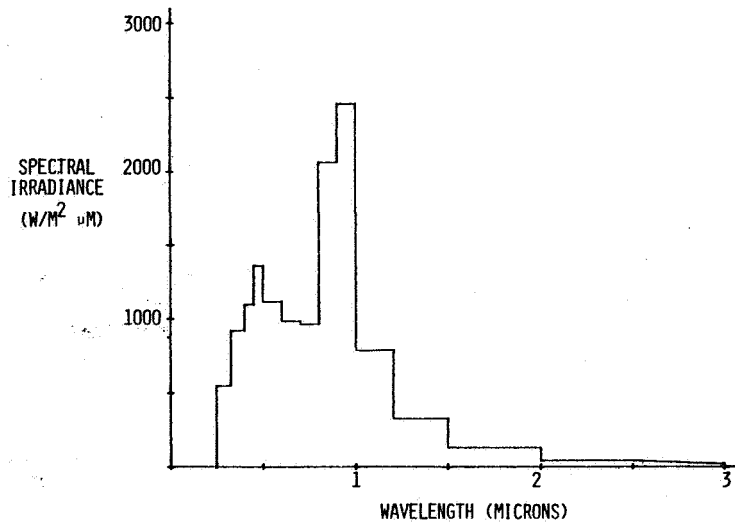


Fig. 4 Unfiltered xenon spectrum

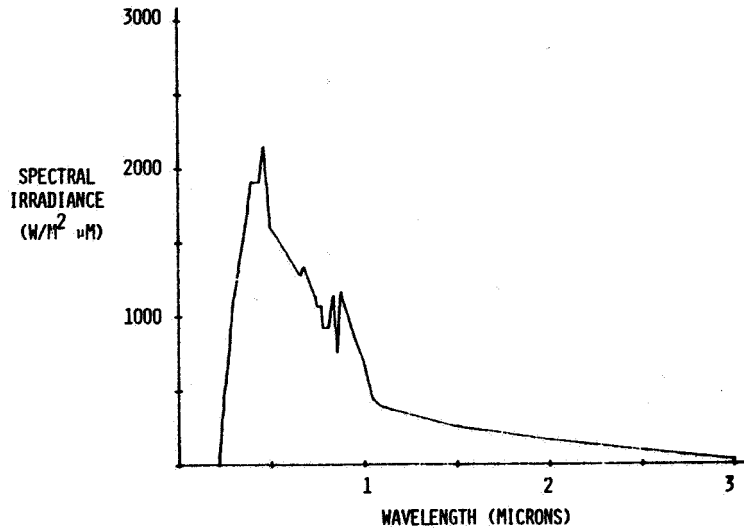


Fig. 5 Pulsed xenon spectrum

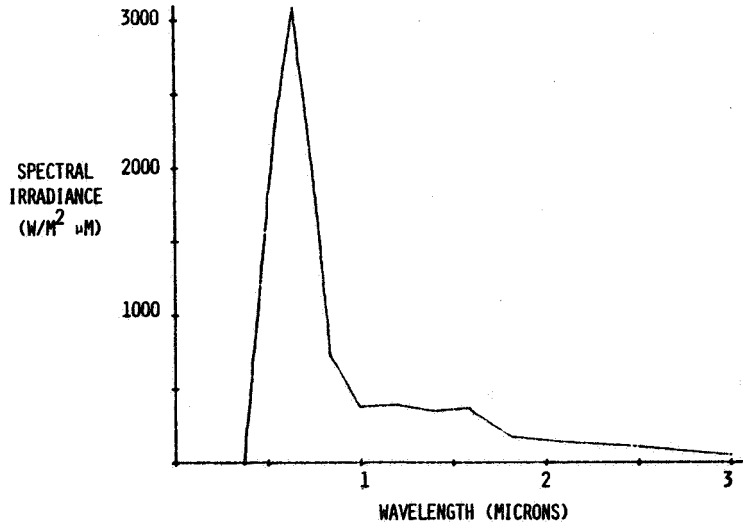


Fig. 6 ELH lamp spectrum

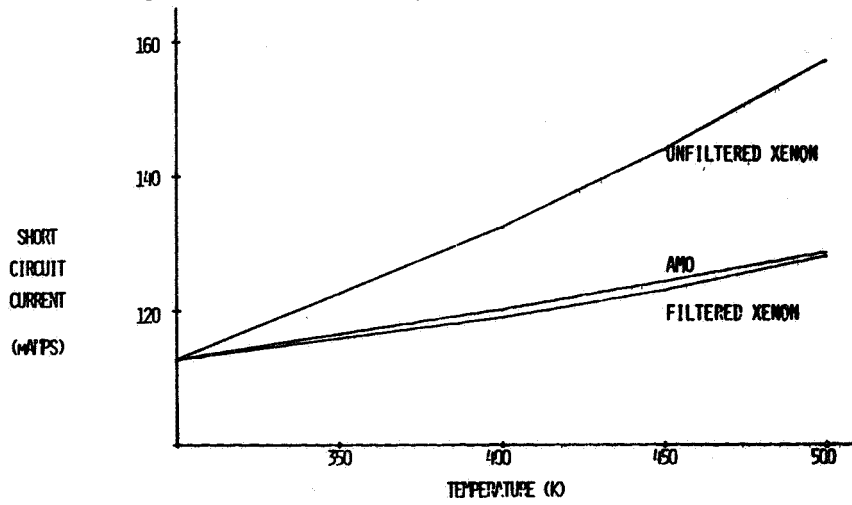


Fig. 7 Variation of calculated I_{sc} with temperature

DEFECTS AND ANNEALING STUDIES IN 1-MeV ELECTRON IRRADIATED
(AlGa)As-GaAs SOLAR CELLS*

Sheng S. Li* and W.L. Wang*
University of Florida
Gainesville, Florida

R.Y. Loo[†]
Hughes Research Laboratories
Malibu, California

W.P. Rahilly
Air Force Aeropropulsion Laboratory
Wright-Patterson Air Force Base, Ohio

EXTENDED ABSTRACT

The purpose of this paper is to present the results of our study on the deep-level defects and recombination mechanisms in the one-MeV electron irradiated (AlGa)As-GaAs solar cells under various irradiation and annealing conditions. Deep-level transient spectroscopy (DLTS) and capacitance-voltage (CV) techniques were used to determine the defect and recombination parameters such as energy levels and defect density, carrier capture cross sections and lifetimes for both electron and hole traps as well as hole diffusion lengths in these electron irradiated GaAs solar cells. GaAs solar cells used in this study were prepared by the infinite solution melt liquid phase epitaxial (LPE) technique at Hughes Research Lab., with $(Al_{0.9}Ga_{0.1})$ As window layer, Be-diffused p-GaAs layer on Sn-doped n-GaAs or undoped n-GaAs active layer grown on n⁺-GaAs substrate. Mesa structure with area of 5.86×10^{-4} cm² was fabricated for our DLTS and CV study. The Sn-doped n-GaAs active layer has a dopant density of 5×10^{16} cm⁻³, and the undoped n-GaAs layer has a carrier density of 1.5×10^{15} cm⁻³. Three different irradiation and annealing experiments were performed on these solar cells: (1) one-MeV electron irradiation was done at room temperature on Sn-doped (AlGa)As-GaAs solar cells for electron fluences of 10^{14} , 10^{15} , and 10^{16} cm⁻², and subsequently annealed at 230°C for 10, 20, 30, and 60 minutes. (2) Same type of GaAs cells was irradiated at 150°C and 200°C cell's temperature and fluence of 10^{15} cm⁻² using two different flux rates (4×10^{10} e/cm²-s and 2×10^9 e/cm²-s). (3) one-MeV electron irradiation was performed on the undoped GaAs solar cells at 200°C cell's temperature for fluence of 10^{14} and 10^{15} cm⁻². DLTS and C-V measurements were made on the cells described above, and the results are discussed next.

Fig. 1 and Fig. 2 show the DLTS scan of electron and hole traps in the (AlGa)As-GaAs cells irradiated with 10^{16} e/cm² electron fluence and annealed at 230°C in vacuum for 20, 30, and 60 minutes, respectively. Three electron traps with energies of $E_C - 0.31$, 0.71, and 0.90 eV and one hole trap with energy of $E_V + 0.71$ eV were observed in these samples. The DLTS data showed that density of each defect level was reduced as a result of the 230°C thermal annealing. Note that the "E₃" electron trap has the largest reduction in its density followed by the 230°C annealing for 60 minutes. Significant reduction in the trap density was also observed for the $E_V + 0.71$ eV hole trap from the 230°C annealing process (see Fig. 2). A similar result for both electron and hole traps was also obtained for cells irradiated by the 10^{15} e/cm² electron fluence. Table 1 and table 2 summarize the results deduced from the DLTS and C-V measurements for the Sn-doped GaAs solar cells irradiated at room temperature

with fluences of 10^{15} and 10^{16} e/cm² and annealed at 230°C for 20, 30, and 60 minutes. Hole diffusion lengths calculated from the DLTS data were found to vary between 1.5 to 2.44 μm for $\phi_e = 10^{15}$ e/cm² fluence. The effects of incident flux rate and cell's irradiation temperature on the defect parameters were studied on Sn-doped GaAs cells irradiated with 10^{15} e/cm² fluence. Fig. 3 and Fig. 4 show respectively the DLTS scans of electron and hole traps for the Sn-doped GaAs solar cells irradiated by 10^{15} e/cm² fluence, with flux rates of 4×10^{10} e/cm²-s and 2×10^9 e/cm²-s and irradiated at 150 and 200°C cell's temperature. The results show that the dominant electron trap is due to $E_C - 0.71$ eV level, and the dominant hole trap is due to $E_V + 0.71$ eV. The density for both traps increases with increasing flux rate and reducing cell's temperature. For cells irradiated at 4×10^{10} e/cm²-s flux rate, two additional electron traps (i.e., E_3 and E_5) were also detected. The defect and recombination parameters calculated from the DLTS data for these cells are summarized in table 3 and table 4. Note that the DLTS data shown in Fig. 1 through Fig. 4 are for the Sn-doped GaAs solar cells. The DLTS scans of electron and hole traps for the undoped GaAs solar cells irradiated at 200°C are shown in Fig. 5 and Fig. 6, respectively. Fig. 5 shows the DLTS scan of electron traps for cells irradiated with 10^{14} and 10^{15} e/cm² fluence, respectively; four electron traps with energies of $E_C - 0.13$, 0.41, 0.71, and 0.90 eV were observed in these two cells. Note that $E_C - 0.13$ eV and $E_C - 0.41$ eV electron traps are not detected in the Sn-doped GaAs cells shown in Fig. 1. Fig. 6 shows the DLTS scan of hole traps for the same cells shown in Fig. 5; two hole traps with energies of $E_V + 0.29$ and $E_V + 0.71$ eV were observed for cells irradiated with 10^{15} e/cm², and only one hole trap with energy of $E_V + 0.71$ eV was observed in 10^{14} e/cm² irradiated cells. In both figures it is noted that increasing electron fluence will increase the density of both electron and hole traps in these cells. Defect and recombination parameters deduced from the DLTS and C-V data for cells shown in Fig. 5 and Fig. 6 are summarized in table 5 and table 6. Fig. 7 shows the defect annealing rate for the " E_3 " electron trap for electron fluence of 10^{16} e/cm² and for the " E_5 " electron trap for electron fluence of 10^{15} e/cm², for GaAs cells shown in Fig. 1 and table 1. From the study of deep-level defects and their annealing behavior, it is concluded that (i) one-MeV electron irradiation on GaAs cells grown by the infinite solution melt LPE technique will in general produce three to four electron traps and one to two hole traps if the electron fluence is greater than 10^{14} e/cm²; (ii) defect density will increase with increasing incident flux rate and fluence; (iii) increasing annealing temperature and annealing time will reduce the density of both electron and hole traps; (iv) increasing the cell's temperature during electron irradiation will effectively reduce the trap density; (v) low temperature thermal annealing is more effective in annealing out the shallower traps than the deeper traps; (vi) the recombination enhanced annealing^[1] was found to be effective for reducing the density of deep-level recombination centers; (vii) the activation energy for the " E_3 " electron trap was found slightly different in the undoped GaAs than that of the Sn-doped GaAs solar cells (i.e., $E_C - 0.41$ eV vs. $E_C - 0.31$ eV), and (viii) the ($E_V + 0.29$ eV) hole trap observed in the undoped GaAs cells was not detected in the Sn-doped GaAs solar cells under same irradiation conditions.

*Research supported by the Aeropropulsion Lab., AFWAL, subcontract through Universal Energy System Inc., Ohio.

†Supported by NASA Lewis Research Center.

[1] J. D. Weeks, J. C. Tully, and L. C. Kimerling, Phys. Rev. B, 12, 3286 (1975).

Annealing time & Temperature	$\phi_e = 10^{16} \text{ e/cm}^2$				10^{15} e/cm^2				
	E_T (eV)	N_T (cm ⁻³)	σ_n (cm ²)	τ_n (s)	E_T (eV)	N_T (cm ⁻³)	σ_n (cm ²)	τ_n (s)	
Unannealed	$E_2 = E_c - 0.20$	9×10^{12}	1×10^{-16}	2.77×10^{-5}	230°C 10 min.)	E_2	7.9×10^{12}	1×10^{-16}	-
	$E_3 = E_c - 0.31$	2.9×10^{14}	1.8×10^{-14}	4.26×10^{-9}		E_3	-	-	-
	$E_4 = E_c - 0.71$	3.2×10^{14}	5.1×10^{-14}	1.25×10^{-9}		E_4	5.7×10^{13}	5.1×10^{-14}	7.64×10^{-9}
	$E_5 = E_c - 0.90$	3.4×10^{14}	5.8×10^{-14}	1.04×10^{-9}		E_5	1.1×10^{14}	5.8×10^{-14}	3.2×10^{-9}
230°C for 20 min.	E_3	1.4×10^{14}	1.8×10^{-14}	9.92×10^{-9}	E_3	2.6×10^{13}	1.8×10^{-14}	4.75×10^{-8}	
	E_4	9.5×10^{13}	5.1×10^{-14}	4.39×10^{-9}	E_4	5.4×10^{13}	5.1×10^{-14}	8.07×10^{-9}	
	E_5	1.2×10^{14}	5.8×10^{-14}	2.93×10^{-9}	E_5	6.1×10^{13}	5.8×10^{-14}	5.77×10^{-9}	
230°C for 30 min.	E_3	1.2×10^{14}	1.8×10^{-14}	1.01×10^{-8}	E_3	2.4×10^{13}	1.8×10^{-14}	5.1×10^{-8}	
	E_4	7.7×10^{13}	5.1×10^{-14}	5.41×10^{-9}	E_4	2.5×10^{13}	5.1×10^{-14}	1.6×10^{-8}	
	E_5	6.2×10^{13}	5.8×10^{-14}	5.68×10^{-9}	E_5	3.1×10^{13}	5.8×10^{-14}	1.14×10^{-8}	
230°C for 60 min.	E_3	2.7×10^{13}	1.8×10^{-14}	4.57×10^{-8}	E_3	7.2×10^{12}	1.8×10^{-14}	5.6×10^{-7}	
	E_4	6.2×10^{13}	5.1×10^{-14}	6.45×10^{-9}	E_4	1.8×10^{13}	5.1×10^{-14}	2.22×10^{-8}	
	E_5	1.6×10^{14}	5.8×10^{-14}	2.19×10^{-9}	E_5	2.2×10^{13}	5.8×10^{-14}	1.6×10^{-8}	

Table. 1 Electron trap parameters in one-MeV electron irradiated (AlGa)As-GaAs solar cells annealed at 230 °C for 10,20,30, and 60 min. $N_D = 5 \times 10^{16} \text{ cm}^{-3}$ (Sn-doped n-GaAs)

Table. 2 Defect parameters of Hole Traps in one-MeV Electron Irradiated (AlGa)As-GaAs Solar Cells vs. Annealing Time

Fluence (e/cm ²)	N_D (cm ⁻³)	Annealing Time & Temp.	Hole Trap				
			E_T (eV)	N_T (cm ⁻³)	σ_p (cm ²)	τ_p (ns)	L_p (μm)
10^{15}	5.5×10^{16}	20 min. at 230°C	$E_V + 0.71$	9×10^{13}	4.01×10^{-13}	2.25	1.50
		30 " "	"	6.8×10^{13}	"	2.65	1.72
		60 " "	"	3.4×10^{13}	"	5.30	2.44
10^{16}	3.5×10^{16}	20 min. at 230°C	$E_V + 0.71$	9×10^{14}	4.01×10^{-13}	0.20	0.47
		30 " "	"	6.2×10^{14}	"	0.29	0.57
		60 " "	"	1.1×10^{14}	"	1.64	1.35

Table. 3 Electron Trap Parameters vs. Flux Rate in one-MeV Electron Irradiated (AlGa)As-GaAs Solar Cells for $\phi_e = 10^{15} \text{ e/cm}^2$

Samples	N_D (cm ⁻³)	Flux Rate (e/cm ² -s)	Annealing Temp. (°C)	Electron Traps			
				E_T (eV)	N_T (cm ⁻³)	σ_n (cm ²)	τ_n (s)*
1	5.35×10^{16}	4×10^{10}	200	$E_3 = E_c - 0.31$	1.24×10^{13}	1.8×10^{-14}	1×10^{-7}
				$E_4 = E_c - 0.71$	5.84×10^{13}	5.1×10^{-14}	6.85×10^{-9}
				$E_5 = E_c - 0.90$	1.35×10^{13}	5.8×10^{-14}	2.6×10^{-8}
2	5.56×10^{16}	2×10^9	150	E_4	4.85×10^{13}	5.1×10^{-14}	8.25×10^{-9}
3	5.69×10^{16}	2×10^9	200	E_4	3.61×10^{13}	5.1×10^{-14}	1.11×10^{-8}

Table.4 Hole Trap Parameters vs. Flux Rate in one-MeV Electron Irradiated (AlGa)As-GaAs Solar Cells for $\phi_e = 10^{15} \text{ e/cm}^2$

Samples	$N_D \text{ (cm}^{-3}\text{)}$	Flux Rate ($\text{e/cm}^2\text{-s}$)	Annealing Temp. ($^{\circ}\text{C}$)	Hole Traps				
				$E_T \text{ (eV)}$	$N_T \text{ (cm}^{-3}\text{)}$	$\sigma_p \text{ (cm}^2\text{)}$	$\tau_p \text{ (s)}^*$	$L_p \text{ (}\mu\text{m)}^*$
1	5.35×10^{16}	4×10^{10}	200	$E_B = E_V + 0.71$	4.94×10^{13}	4.0×10^{-13}	3.6×10^{-9}	2.01
2	5.56×10^{16}	2×10^9	150	$E_V + 0.71$	4.02×10^{13}	4.0×10^{-13}	4.46×10^{-9}	2.23
3	5.69×10^{16}	2×10^9	200	$E_V + 0.71$	3.06×10^{13}	4.0×10^{-13}	5.84×10^{-9}	2.58

$$*\tau_p = (N_T \sigma_p V_{th})^{-1}, L_p = (\tau_p D_p)^{1/2}; D_p = 11.2 \text{ cm}^2/\text{s}.$$

Table. 5 Electron and Hole Traps in one-MeV Electron Irradiated (at 200°C) (AlGa)As-GaAs Solar Cells. *

Electron Fluence (cm^{-3})	$N_D^* \text{ (cm}^{-3}\text{)}$	Electron Traps		Hole Traps	
		$E_T \text{ (eV)}$	$N_T \text{ (cm}^{-3}\text{)}$	$E_T \text{ (eV)}$	$N_T \text{ (cm}^{-3}\text{)}$
0	1.5×10^{15}	-	-	-	-
10^{14}	1.45×10^{15}	$E_c - 0.13$	3.2×10^{13}	$E_V + 0.29$	0
		$E_c - 0.41$	1.3×10^{13}	-	-
		$E_c - 0.71$	1.2×10^{12}	$E_V + 0.71$	6.4×10^{12}
		$E_c - 0.90$	1.6×10^{12}	-	-
10^{15}	1.05×10^{15}	$E_c - 0.13$	2.2×10^{14}	$E_V + 0.29$	6.9×10^{12}
		$E_c - 0.41$	1.3×10^{13}	-	-
		$E_c - 0.71$	7.8×10^{12}	$E_V + 0.71$	2.0×10^{13}
		$E_c - 0.90$	9.5×10^{12}	-	-

*Carrier removal rate = $\Delta n / \phi_e = 0.5 \text{ cm}^{-1}$.
undoped n-GaAs LPE layer.

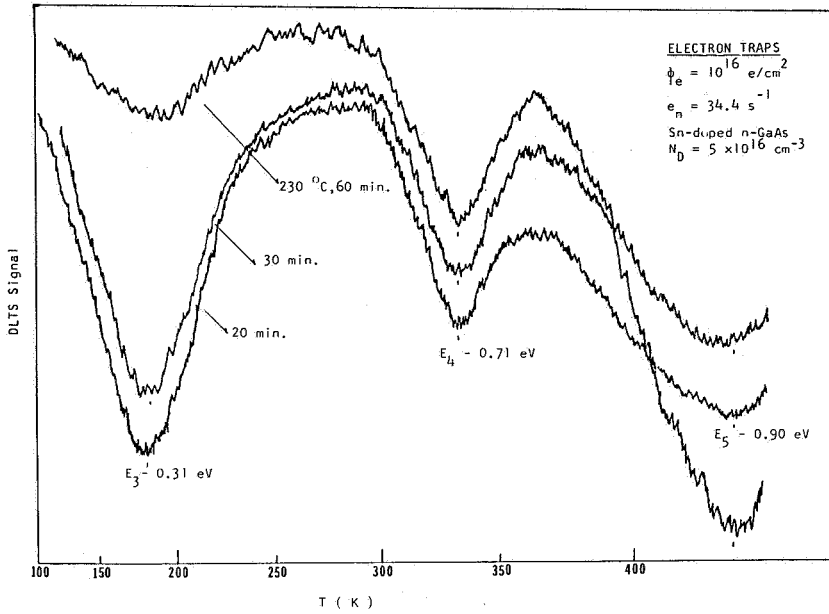


Fig. 1 DLTS scan of electron traps in one-MeV electron irradiated (AlGa)As-GaAs solar cells as a function of annealing (230 °C) time.

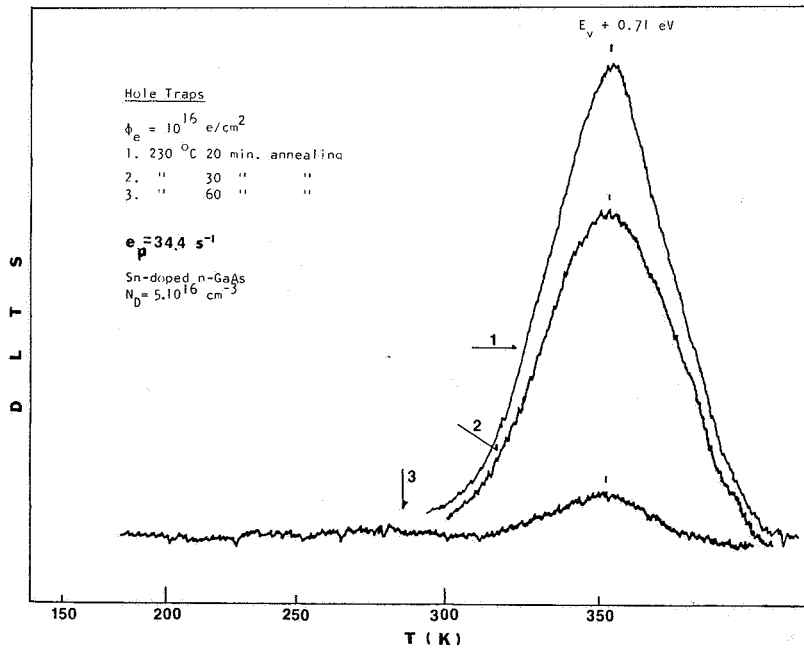


Fig. 2 DLTS scan of hole traps in one-MeV electron irradiated (AlGa)As-GaAs solar cells for different annealing times.

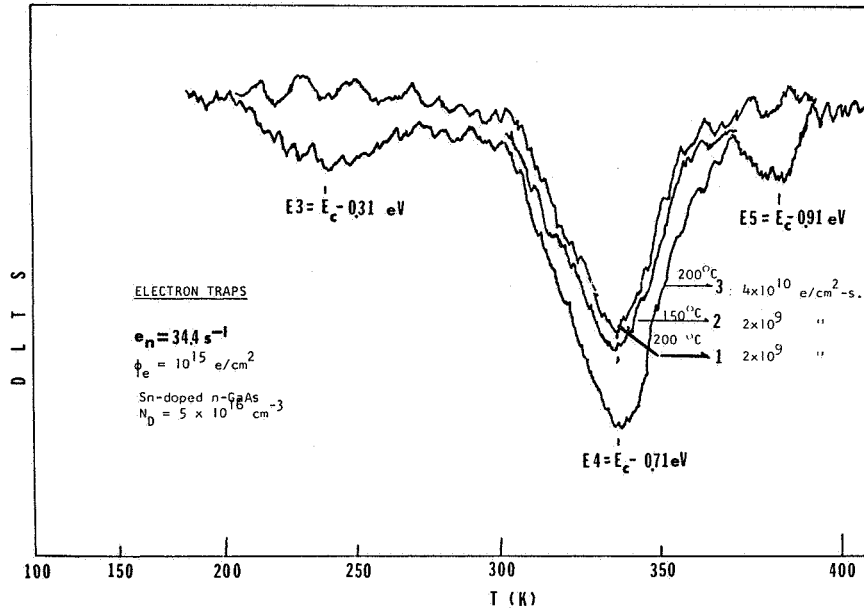


Fig. 3 DLTS scan of electron traps in one-MeV electron irradiated (AlGa)As-GaAs solar cells vs incident flux rate and annealing temperature.

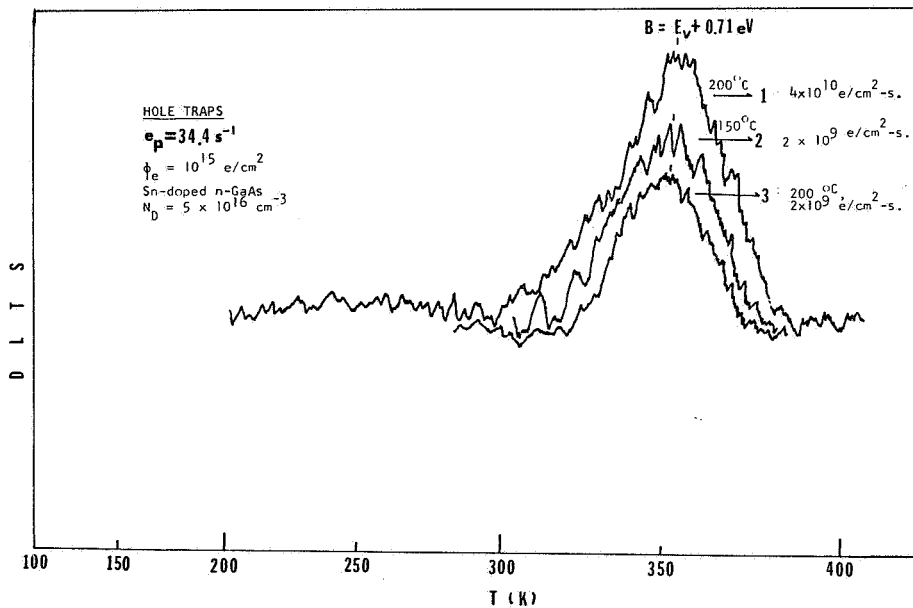


Fig. 4 DLTS scan of hole traps in one-MeV electron irradiated (AlGa)As-GaAs solar cells vs incident electron flux rate and annealing temperature.

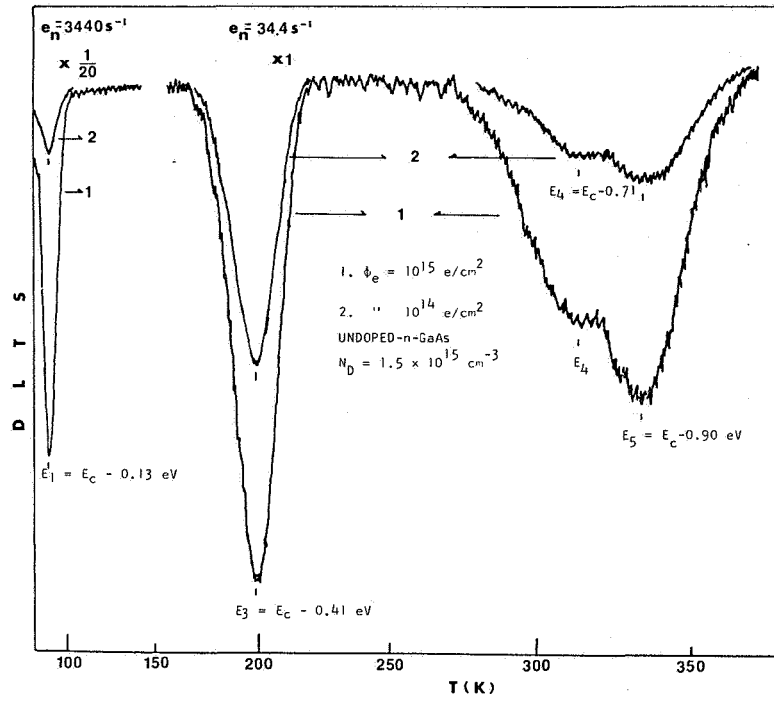


Fig. 5 DLTS scan of electron traps in one-MeV electron irradiated (at 200 °C) (AlGa)As-GaAs solar cells as a function of electron fluence.

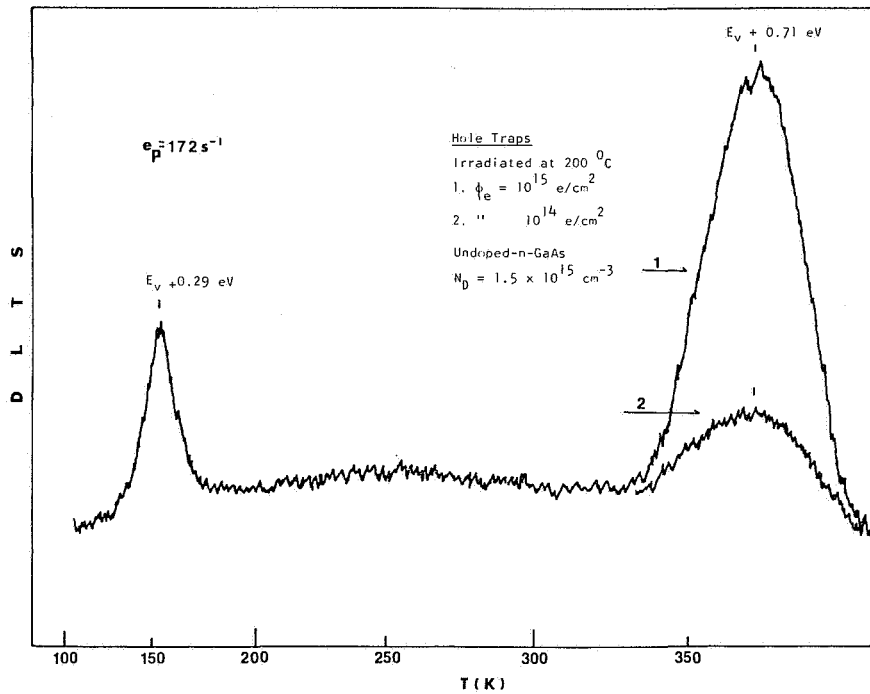


Fig. 6 DLTS scan of hole traps in one-MeV electron irradiated (at 200 °C) (AlGa)As-GaAs solar cells as a function of electron fluence.

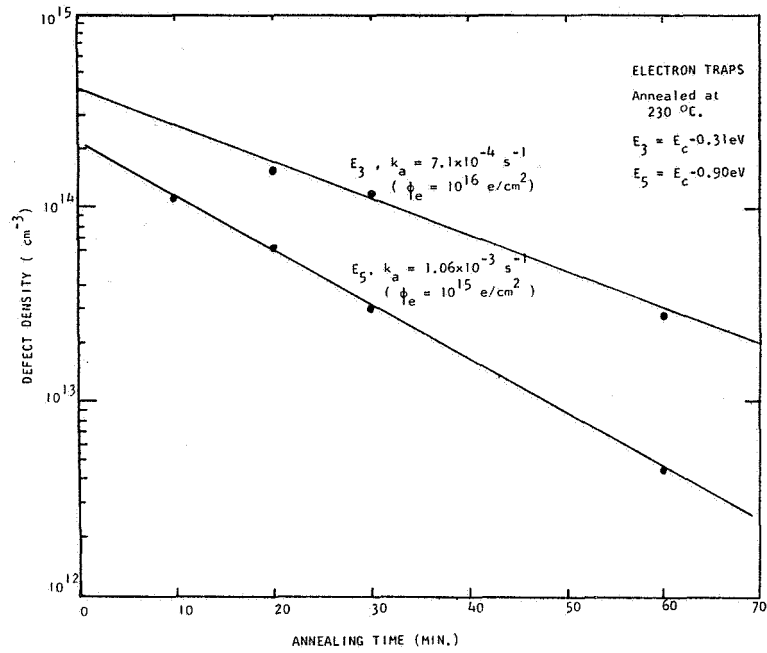


Fig.7 Annealing rate of E_3 and E_5 electron traps in one-MeV electron irradiated (AlGa)As-GaAs solar cells.

DEFECT BEHAVIOR IN ELECTRON-IRRADIATED BORON- AND GALLIUM-DOPED SILICON

Peter J. Drevinsky and Henry M. DeAngelis
Rome Air Development Center
Hanscom Air Force Base, Massachusetts

ABSTRACT

Production and anneal of defects in electron-irradiated, float-zone silicon solar cells were studied by DLTS. In boron- and gallium-doped, n^+ -p cells, dominant defects were due to the divacancy, carbon interstitial, and carbon complex. Results suggest that the DLTS peak normally ascribed to carbon complexes also involves gallium. For gallium- and, to a lesser extent, boron-doped samples, damaged lifetime shows substantial recovery only when the carbon-complex peak has annealed out at 400°C. In boron-doped, n^+ -p- p^+ cells, a minority carrier trap (E1) was also observed by DLTS in cells with a boron p^+ , but not in those with an aluminum p^+ back. A level at $E_V + 0.31$ eV appeared upon 150°C annealing (E1 out) in both p^+ back types of samples.

INTRODUCTION

In electron-irradiated electronic devices such as solar cells, interactions between dopant, intrinsic impurities, and point defects can lead to the formation of damaging complexes. Irradiation of boron-doped silicon, for example, can produce various defects involving boron, carbon, oxygen, vacancies, and interstitials. Techniques such as Deep Level Transient Spectroscopy (DLTS) have been used (refs. 1 to 3) for defect detection. Weinberg and Swarz (refs. 4 and 5), in correlating the annealing behavior of defects observed by DLTS (ref. 3) with short circuit current (J_{SC}), attributed the observed reverse anneal of J_{SC} to the emergence of the $E_V + 0.30$ eV level. Rohatgi (ref. 6) also concluded from DLTS measurements that this defect is responsible for reverse annealing in irradiated boron-doped cells.

This report describes results of our DLTS studies of defects in electron-irradiated solar cells fabricated from float-zone silicon. Since irradiated gallium-doped cells have shown a potential for greater recovery after anneal than boron-doped cells (ref. 7), we have compared radiation-induced defects in high purity, n^+ -p silicon cells doped with gallium and boron. Results of defect annealing studies are presented and minority carrier lifetime measurements are correlated with defect anneal. Defect production and annealing behavior have also been studied in a set of boron-doped, n^+ -p- p^+ silicon cells, which were fabricated with either an aluminum p^+ or a boron p^+ back surface.

EXPERIMENTAL

Diffused junction, n^+ - p cells, doped with either gallium (2, 10, and 20 ohm-cm) or with boron (2 ohm-cm), were fabricated by Spectrolab, Inc. from high purity, float-zone silicon (ref. 8). A second set consisted of diffused junction, n^+ - p - p^+ cells doped with boron (1 and 10 ohm-cm) and fabricated by Comsat Laboratories from float-zone silicon. Cells for each base resistivity had an aluminum and boron p^+ back surface and these will be referred to as Al p^+ and B p^+ , respectively. Processing conditions were: All Al p^+ cells - no pre-oxidation, single-step phosphorus front and aluminum back diffusion at 850°C for 30 min., and no post, or final, anneal; 10 ohm-cm, B p^+ cells - no pre-oxidation, boron back diffusion at 950°C for 30 min., phosphorus front diffusion at 850°C for 15 min., and post anneal at 450°C for 14 hrs.; 1 ohm-cm, B p^+ cells - identical to the 10 ohm-cm, B p^+ cells except for pre-oxidation at 1050°C for 30 min. Cells were diced into chips 0.25 cm on edge and these were mesa-etched to minimize leakage current, mounted on TO-5 headers with silver epoxy, and top-contacted by ultrasonic bonding (refs. 9 and 10).

Defects were detected by DLTS (ref. 11) by using the lock-in amplifier version of the technique (ref. 12). For bias pulse voltages and base resistivities used, the regions approximately 0.3 to 3 micrometers below the metallurgical junction could be examined. Minority carrier lifetime was measured by a diode reverse recovery technique and deeper levels unobservable by DLTS were monitored by capacitance-voltage measurements. Short circuit current was measured on either 1x1 cm or 1x2 cm cell pieces with the use of a Spectrolab solar simulator.

Samples were irradiated in air at room temperature with 1-MeV electrons to fluences ranging from 1.0×10^{15} to 1.6×10^{16} e^-/cm^2 , measured within one day after irradiation, and stored in dry ice. Lower fluences were used on cells and on companion samples for accompanying DLTS scans and minority carrier lifetime measurements. Samples were isochronally annealed to 100°C in air and continued to about 425°C in a nitrogen atmosphere for periods of either 20 or 30 minutes at temperature.

RESULTS AND DISCUSSION

Principal DLTS peaks in irradiated samples were found to be majority carrier traps associated with levels at $E_v + 0.21\text{eV}$ (H1, divacancy), $+0.27\text{eV}$ (H2, carbon interstitial), and $+0.34\text{eV}$ (H3, carbon complex). A minority carrier trap at $E_v - 0.26\text{eV}$ (E1, boron complex) was observed for boron-doped, B p^+ samples and upon annealing at 150°C, this level disappeared and another majority carrier trap at $E_v + 0.31\text{eV}$ (H4) emerged.

n^+ - p cells

Figure 1 shows DLTS spectra of 2, 10 and 20 ohm-cm (6.5×10^{15} , 1.4×10^{15} , and 5.9×10^{14} cm^{-3} , respectively), gallium-doped silicon samples irradiated to a fluence of 5×10^{15} e^-/cm^2 . The three dominant majority carrier traps H1, H2, and H3 are attributed to the divacancy (ref. 2), carbon interstitial (ref. 2), and carbon

complexes, respectively. The identity of these carbon complexes is uncertain and they have been described as a carbon interstitial-substitutional pair (C_I-C_S) in reference 2 and as a vacancy-oxygen-carbon complex (V-O-C) in reference 3. It is apparent that the amplitude of H3 is gallium concentration dependent, increasing as the gallium content increases. It is interesting to note that the relative concentrations of H2 to H3 decrease with increasing gallium concentration. The introduction rate for H1 is essentially constant for all three sample resistivities. It should be noted that boron-doped samples showed H1 and H2, but little or no production of H3.

Isochronal anneals from 50° to 100°C indicate that the gallium content apparently influences the anneal of the carbon interstitial, which disappeared more rapidly in the order of decreasing resistivity. We have not observed similar behavior in float-zone, boron-doped silicon. Peak H3 grew during this annealing sequence, and the largest increase occurred in the 20 ohm-cm samples.

The most dramatic example of the effect of gallium on annealing behavior is given in figure 2 which shows the anneal of peak H3. The annealing data were normalized to the amplitude of peak H3 after the 100°C annealing step. It is clearly seen that peak H3 involved at least two defects as an annealing stage centered at about 175°C appears and becomes more pronounced with increasing gallium concentration. Peak H3 may contain a carbon complex, but it also contains another defect which involves gallium in some way. Continuing the anneal, one finds a significant growth in peak H3, again showing a greater fractional growth for the lower gallium concentration. Note that this behavior was observed in other gallium-doped float-zone as well as crucible-grown, samples separately prepared from 1 and 10 ohm-cm silicon wafers. A detailed analysis of peak H3 at the 100°C step, at and after the 175°C annealing stage, and at the maximum growth point of 300°C has not yet been done. Essentially complete recovery is achieved after the 400°C anneal. The divacancy annealed out at 250°C to 300°C. It should be noted that an unidentified majority carrier trap, shallower than H3, emerged during the anneal at about 200°C and disappeared after the 400°C step.

Degradation and recovery of minority carrier lifetime was followed after each irradiation and annealing step for all gallium-doped samples. The data for 20 ohm-cm samples are shown in figure 3 which depicts the annealing behavior of peak H3, the lifetime, and the recovery of "deeper levels" not observable by DLTS but monitored by capacitance-voltage measurements. It is noted that the substantial growth in peak H3 coincides with the complete anneal of the deeper levels. Lifetime shows no significant recovery until H3 has annealed out at the 400°C step at which point it recovered to about 60 percent of its pre-irradiation value. The recovery of lifetime in the 2 and 10 ohm-cm, gallium-doped samples followed a similar pattern.

Figure 4 shows defect annealing data and lifetime measurements as a result of isochronal anneals from 50°C to 400°C for the 2 ohm-cm, boron-doped silicon. The anneal of peak H2, attributed primarily to the carbon interstitial, is essentially complete by about 75°C. No explanation for the residual which persists at 100°C can be given at this time. The growth of H3 is evident, but not significant until one exceeds 225°C. No secondary annealing stage appears as in gallium-doped samples. Peak H3 reaches a maximum at 350°C and anneals out by 400°C. The peak H4 was first observed after the 150°C anneal and it has been suggested that it is either a boron-oxygen-vacancy (B-O-V) in reference 3 or a silicon interstitial pair (Si_I-Si_I) in reference 2. It continues to grow, peaks at 350°C, and anneals out at 400°C. Annealing behavior was found to be similar in crucible-grown, boron-doped silicon.

It is important to note that lifetime does not recover until the 400°C anneal step at which point H3 and H4 are gone and even then only to about 20 percent of the pre-irradiation values. Our lifetime measurements on these boron-doped samples give no suggestion of a reverse anneal.

n⁺-p-p⁺ cells

Figure 5 shows typical DLTS spectra, taken under injection conditions, of 10 ohm-cm, boron-doped, Al p⁺ and B p⁺ samples irradiated to a fluence of 1×10^{15} e⁻/cm². The most striking difference is the presence of a minority carrier trap (E1) in B p⁺ and its absence in Al p⁺ samples. It is important to note that DLTS samples of both types of cells were well-behaved diodes with similar dark current-voltage and injection characteristics. Also, cells had been prepared from the same silicon ingot. In spite of being identical samples, except for back surface type and processing, only B p⁺ showed E1. Figure 5 also shows evidence for peak H3 in both sample types, quite suppressed in Al p⁺. Peaks H1 and H2 appear in comparable quantities in both types.

The absence of a distinct reverse anneal in irradiated, high-purity, boron-doped silicon (see fig. 4) as followed by lifetime measurements with the diode reverse recovery technique led to a study of cell annealing behavior. Companion 10 ohm-cm cells and DLTS samples were irradiated simultaneously. Figure 6 shows the isochronal anneal, using J_{SC} measurements, of four types of cells including a 10 ohm-cm, gallium-doped cell for comparison. It is clear that the Al p⁺ and B p⁺ cells show similar trends and recovery characteristics, with a reverse anneal in the 200° to 300°C region and virtually complete recovery after annealing at 400°C. The 2 ohm-cm crucible-grown cell behaves similarly. The gallium-doped cell does not show the pronounced reverse anneal and, in fact, recovers in the 200° to 300°C region. Generally, this annealing behavior is similar to that reported earlier (ref. 13) in an extensive study of annealing performance of solar cells. Companion DLTS samples showed spectra similar to those presented in figure 7 and defect annealing behavior similar to that shown in figure 8. Although these figures show data for more heavily-irradiated samples, they demonstrate that deeper levels, H3, and H4 are present in significant concentrations during the reverse anneal experienced by the boron-doped cells.

In figure 7, typical DLTS spectra for 10 ohm-cm, B p⁺ samples after irradiation to a fluence of 1.6×10^{16} e⁻/cm² and after three representative annealing steps are shown. Al p⁺ samples gave similar spectra, except for the absence of E1. The fractional original minority carrier lifetime (τ/τ_0) is given in parentheses under the irradiation fluence and the annealing temperature. Note that the spectrum after the 427°C anneal was taken at ten times greater sensitivity than that for the other three spectra. Each given peak is labeled once as it first appears. The prominent peaks observed after irradiation are identical to those obtained for the more lightly-irradiated B p⁺ shown in figure 5. When these anneal out, a new generation of defects appears in lower concentration. At 177°C, H2 is gone, H3 has grown, and H4 has come in at a temperature associated with the disappearance of E1. H1 is still present in its post-irradiation concentration. At 355°C lifetime begins to show recovery and it is important to note that capacitance-voltage measurements show that deeper levels have now annealed out. The spectrum shows a loss in H3 and the appearance of small quantities of unidentified defects, H5 and H6. At 427°C, the spectrum at greater sensitivity shows the loss

of essentially all of the initial radiation-produced defects and the presence of additional, unidentified H7, H8, and H9 defects. Lifetime has begun to show substantial recovery in this boron-doped sample. Other boron-doped samples have shown as much as 30 percent recovery at this temperature.

Figure 8 shows the annealing behavior of defects introduced by irradiating 10 ohm-cm, B p⁺ samples to a fluence of 1.6×10^{16} e⁻/cm². Except for the absence of E1 and smaller production of H3, defects in 10 ohm-cm, Al p⁺ samples showed similar annealing behavior for this fluence. The total radiation-induced defect concentration for each p⁺ type is nearly the same and estimated to be about 4×10^{14} cm⁻³ for these samples.

CONCLUDING REMARKS

We have observed significant differences in the defect production and annealing behavior of float-zone silicon, comparably doped with gallium and boron. The recovery of J_{SC} in limited annealing studies of gallium- and boron-doped silicon solar cells reflects some of these differences.

In n⁺-p-p⁺ samples, a minority carrier trap located at $E_C - 0.26$ eV was observed in those with a B p⁺ back, but not observed in those with an Al p⁺ back surface. The differences in processing of these cells does introduce oxygen into the B p⁺ cells. There may be sufficient oxygen in these samples to produce the B_I-O_I complex suggested in reference 3. We clearly observed the minority carrier trap in crucible-grown silicon, comparably doped with boron. Regardless of whether we observe the minority carrier trap or not in n⁺-p-p⁺ samples, $E_V + 0.31$ eV grows in. Both B p⁺ and Al p⁺ show the influence of this growth in the reverse anneal.

Additional study is needed on diodes fabricated from float-zone, boron-doped silicon which is of high purity and low carbon content. Diodes should be fabricated such that oxygen is not introduced in processing or introduced in a carefully controlled manner.

REFERENCES

1. Lang, D. V.: Deep-Level Transient Spectroscopy: A New Method to Characterize Traps in Semiconductors. J. Appl. Phys., Vol. 45, no. 7, July 1974, pp. 3023-3032.
2. Kimerling, L. C.: Defect States in Electron-Bombarded Silicon: Capacitance Transient Analysis. Radiation Effects in Semiconductors, N. B. Urli and J. W. Corbett, eds., Institute of Physics Conference Series No. 31, Institute of Physics (London), 1977, pp. 221-230.
3. Mooney, P. M.; Cheng, L. J.; Suli, M.; Gerson, J. D.; and Corbett, J. W.: Defect Energy Levels in Boron-Doped Silicon Irradiated with 1-MeV Electrons. Phys. Rev. B, vol. 15, no. 8, Apr 15, 1977, pp. 3836-3843.

4. Weinberg, I.; and Swarz, C. K.: Reverse Annealing in Radiation-Damaged, Silicon Solar Cells. NASA Conference Publication 2097, 1979, pp 161-171.
5. Weinberg, I.; and Swartz, C. K.: Origin of Reverse Annealing in Radiation-Damaged Silicon Solar Cells. Appl. Phys. Lett., vol. 36, no. 8, Apr. 15, 1980, pp. 693-695.
6. Rohatgi, A.: Radiation Tolerance of Boron Doped Dendritic Web Silicon Solar Cells. NASA Conference Publication 2169, 1980, pp. 281-288.
7. Rahilly, W. P.; Scott-Monck, J.; Anspaugh, B.; and Locker, D.: Electron and Photon Degradation in Aluminum, Gallium and Boron Doped Float Zone Silicon Solar Cells. Twelfth Photovoltaic Specialists Conference - 1976, IEEE, 1976, pp. 276-281.
8. Fodor, J.; and Opjorden, R.: Advanced Silicon Materials for Space Solar Cells. Fourteenth Photovoltaic Specialists Conference - 1980, IEEE, 1980, pp. 882-886.
9. Drevinsky, P. J.; Schott, J. T.; DeAngelis, H. M.; Kirkpatrick, A. R.; and Minnucci, J. A.: Detection of Processing- and Radiation-Induced Defects in Solar Cells by Transient Capacitance Spectroscopy. Thirteenth Photovoltaic Specialists Conference - 1978, IEEE, 1978, pp. 1232-1237.
10. Drevinsky, P. J.; DeAngelis, H. M.; Schott, J. T.; and Rahilly, W. P.: DLTS Spectra and Defect Effects on Irradiated Silicon Solar Cells. Fourteenth Photovoltaic Specialists Conference - 1980, IEEE, 1980, pp. 835-839.
11. Miller, G. L.; Lang, D. V.; and Kimerling, L. C.: Capacitance Transient Spectroscopy. Ann. Rev. Mater. Sci., vol. 7, Annual Reviews, Inc., 1977, pp. 377-448.
12. Schott, J. T.; DeAngelis, H. M.; and Drevinsky, P. J.: Capacitance Transient Spectra of Processing- and Radiation-Induced Defects in Silicon Solar Cells. J. Elec. Mater., vol. 9, no. 2, 1980, pp. 419-434.
13. Scott-Monck, J. A.; and Anspaugh, B. E.: Effects of Dopants on Annealing Performance of Silicon Solar Cells. NASA Conference Publication 2097, 1979, pp. 173-183.

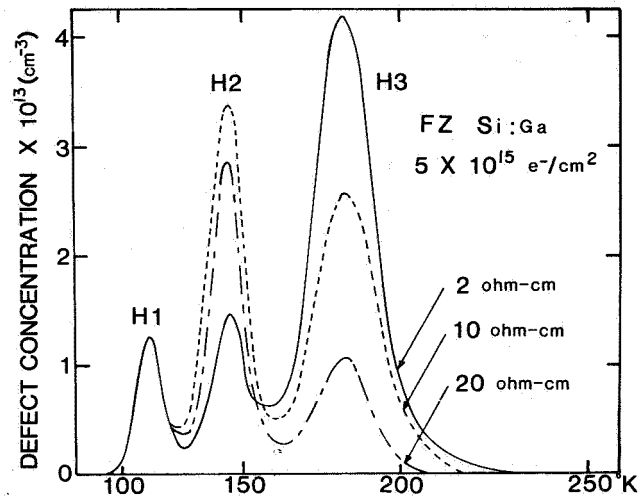


Figure 1. DLTS spectra of 1-MeV electron-irradiated, float zone silicon at various gallium doping levels.

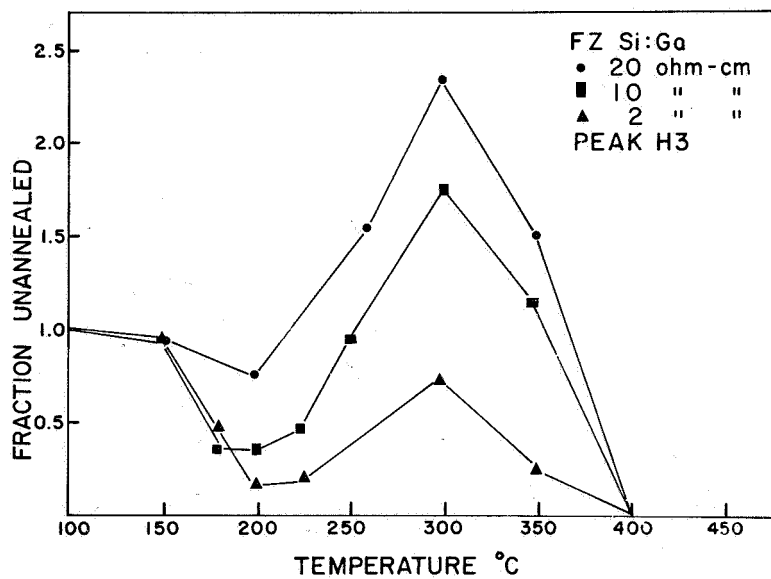


Figure 2. Isochronal anneal of the carbon-related peak (H3) in gallium-doped silicon irradiated with 1-MeV electrons ($5 \times 10^{15} \text{ e}^-/\text{cm}^2$).

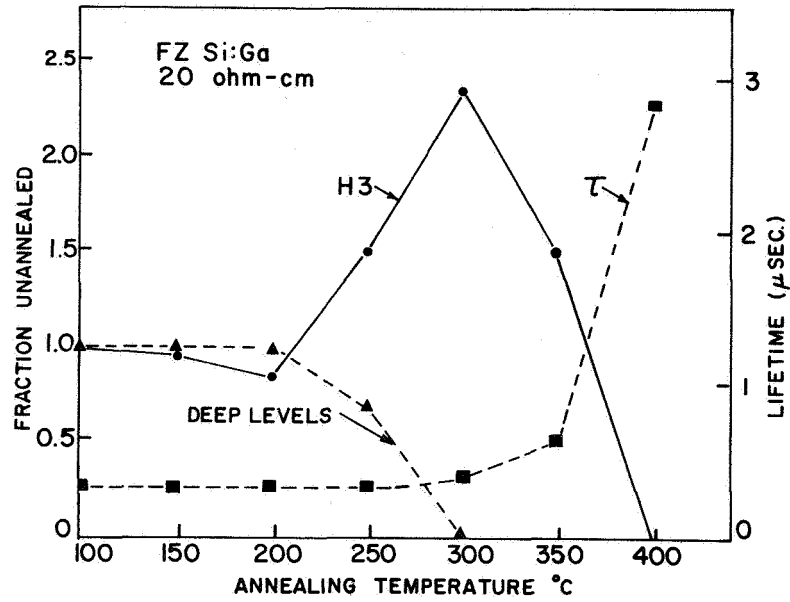


Figure 3. Isochronal anneal of the carbon-related peak (H3) in 1-MeV electron irradiated (5×10^{15} e-/cm²) 20 ohm-cm, gallium-doped silicon as well as anneal of deep levels and recovery of lifetime.

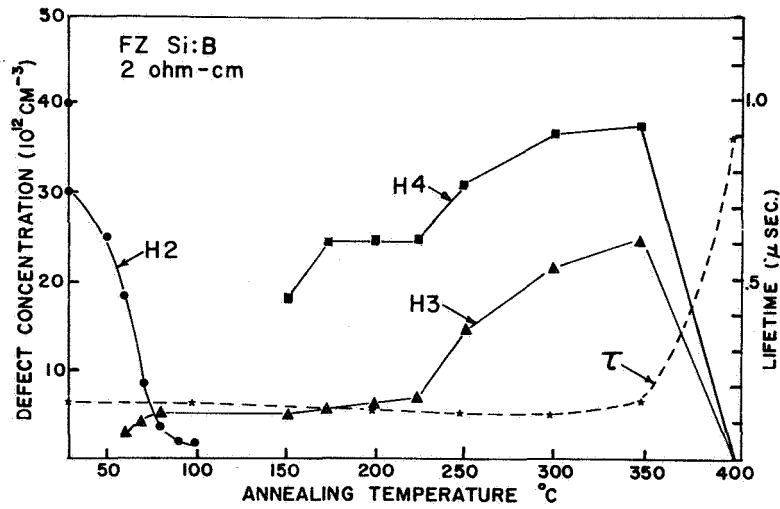


Figure 4. Isochronal anneal of 1-MeV electron irradiated (5×10^{15} e/cm²) 2-ohm-cm, boron-doped silicon showing behavior of three peaks (H2, H3, and H4) and recovery of lifetime.

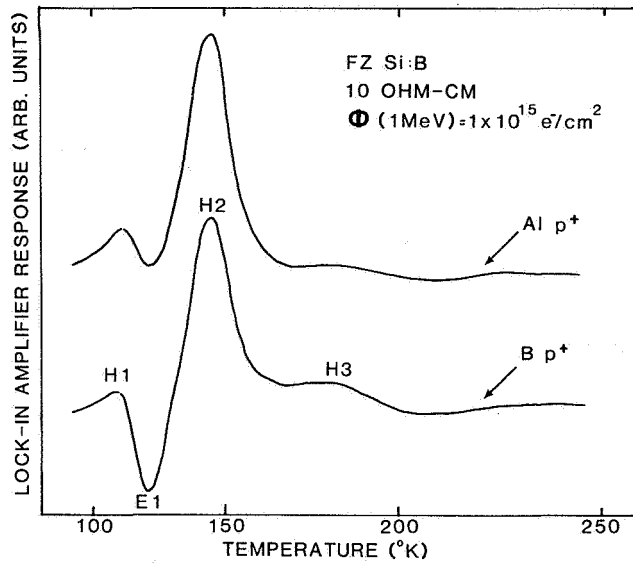


Figure 5. Comparison of DLTS spectra of electron-irradiated Al p⁺ and B p⁺ back surface samples from n⁺-p-p⁺ cells.

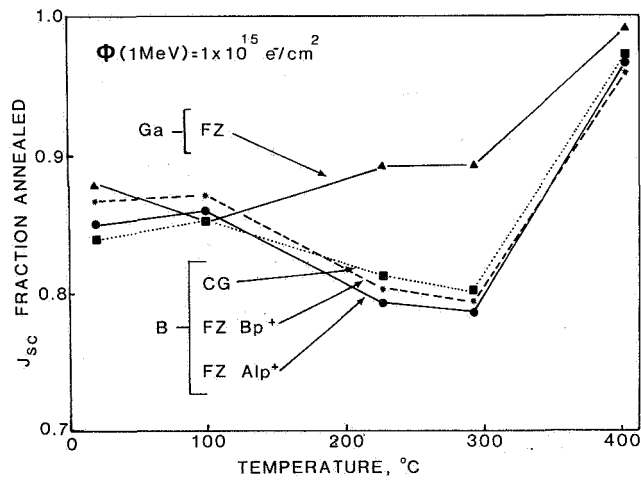


Figure 6. Isochronal anneal of short circuit current (J_{sc}) in electron-irradiated, silicon solar cells. Crucible-grown cell is 2 ohm-cm. All other cells are 10 ohm-cm.

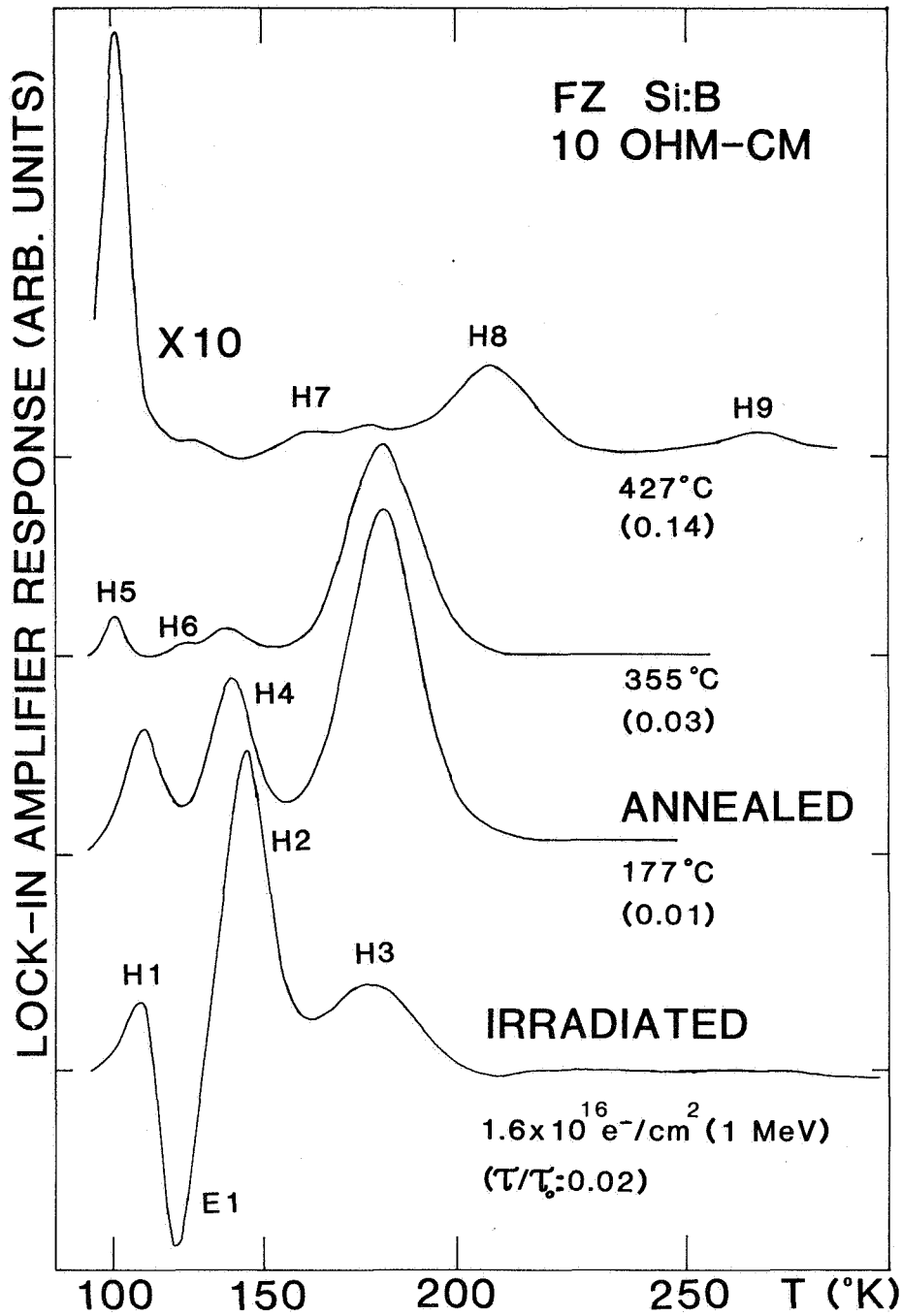


Figure 7. Typical DLTS spectra of boron-doped, B p⁺ silicon cells after electron irradiation and several annealing steps. The fractional pre-irradiation lifetime is given in parenthesis.

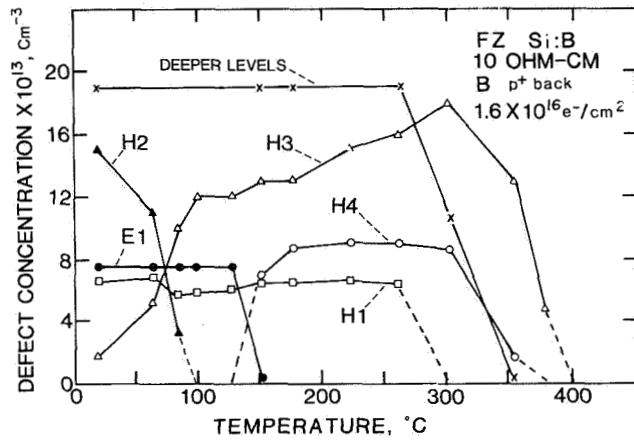


Figure 8. Isochronal anneal of principal defects and of deeper levels in electron-irradiated, boron-doped silicon.

COLD CRUCIBLE CZOCHRALSKI FOR SOLAR CELLS

Terry M. Trumble
Air Force Wright Aeronautical Laboratories
Wright-Patterson Air Force Base, Ohio

INTRODUCTION

The efficiency and radiation resistance of present silicon solar cells are a function of the oxygen and carbon impurities and the boron doping used to provide the proper resistivity material. The standard Czochralski (CZ) process used to grow single crystal silicon contaminates the silicon stock material due to the use of a quartz crucible and graphite components. The use of a process which replaces these elements with a water cooled copper to crucible has provided a major step in providing gallium doped (100) crystal orientation, low oxygen, low carbon, silicon. This paper provides a discussion of the Cold Crucible Czochralski (C³Z) process and recent Float Zone (FZ) developments.

PROGRAM GOALS

The goal of this program is to provide high efficiency, low cost, radiation resistant solar cells by providing high purity, low dislocation count, single crystal silicon. The two major impurities to be removed are carbon and oxygen with a maximum concentration of 1×10^{12} for oxygen and 5×10^{16} for carbon. Minority carrier lifetime should be 100 microseconds or greater for 1 ohm-cm material. Solar cell performance goals are 18% efficiency (AMO) at 25°C with 15% end of life efficiency at 25°C after exposure to an electron fluence of 1×10^{15} e/cm² at 1 MeV.

APPROACH

The standard Czochralski method is a well proven process for growing several million kilograms of silicon a year. The major drawback of this process is due to the contamination of the melt from the quartz crucible. The crucible contributes boron, aluminum, phosphorous and oxygen contaminants to the melt along with other minor constituents. The Cold Crucible Czochralski (C³Z) eliminates this problem by replacing the quartz crucible with a water cooled copper crucible (fig. 1). A very pure silicon charge is placed in the copper crucible and subsequently heated using a susceptor. Once the silicon begins to melt, the RF field couples into the silicon to complete the melt. The RF field then levitates the silicon away from the water cooled fingers as shown in figure 2. A seed crystal is brought in contact with the surface of the melt, and after adhering to the liquid silicon, the rotating crystal is drawn up out of the melt and the single crystal silicon allowed to solidify. The (100) crystal growth is based upon the orientation of seed crystal. The diameter and dislocation count are a function of the thermodynamic exchanges between the single crystal rod, the turning and pulling rate and the frequency and power in the RF field.

PROGRESS

As early as September 1980, moderate success in growing a 1" diameter (100) single crystal was achieved. It was approximately 1800 ohm-cm p-type that twinned in the neck region, producing an orientation slightly off (111). Maximum dislocation densities were about $5 \times 10^4 / \text{cm}^2$ in the center and 6×10^5 at the edge. Dislocation densities were further reduced to $5 \times 10^4 / \text{cm}^2$ at the edge and as low as $6 \times 10^7 / \text{cm}^2$ at the center of the seed end. Dislocations are linear imperfections in crystal lattices associated with extraneous, missing or warped planes of atoms. The program is oriented toward the growth of three resistivities, 0.1, 1.0 and 10.0 ohm-cm so that gallium doped pure silicon can be properly evaluated. Initial attempts to grow 10 ohm-cm material resulted in an 8 ohm-centimeter crystal with a resistivity variation of +3, -6% over a 5 cm long crystal. Refinements in the crystal growth process made it possible to more accurately dope the crystals on subsequent runs.

Recently, 3 crystals of 2.54 cm diameter were grown from a 350 gm charge in 2.5 cm to 3.3 cm lengths. Good single crystals were grown at resistivities of 700 ohm-cm and 1500 ohm-cm (p-type).

Presently, wafers sliced from 0.1, 1.0 and 10 ohm-centimeter material are being made into solar cells. Additional wafers are being analyzed by FTIR to determine the amount of oxygen, carbon and gallium in the material. Table 1 shows two typical gallium doped wafers which are presently being evaluated.

Recently, studies have been conducted with single pass FZ and regular CZ silicon material made into N+/P solar cells. Low resistivity cells made with boron or gallium doping were irradiated at a fluence of $1 \times 10^{14} \text{ e/cm}^2$ at 1 MeV and exposed to photon radiation for 10 hours. For the 2 ohm-centimeter boron doped solar cells, P/P_0 was 0.728, for the gallium doped cells it was 0.818 which confirms the fact that gallium doped pure silicon is better than boron doped silicon.

FUTURE WORK

Although it was possible to make 2.54cm diameter C³Z silicon, hardware problems caused by RF arcing, hardware design, and other system unknowns caused reconsideration of redesigning the system for 6.3cm diameter silicon. During the past year, an AFWAL Material Laboratory Manufacturing Technology program to Hughes Industrial Products Division has resulted in the ability to manufacture vacuum FZ in large quantities at reduced costs. This success spurred an effort to replace C³Z by 3 pass FZ and start with extremely pure polysilicon rods costing upwards of \$750 per kilo. From this material 0.1, 1.0 and 10 ohm-cm (100) crystals will be grown.

Wafers will be analyzed by conventional methods to determine oxygen and carbon content, gallium distribution, dislocation count, resistivity, mobility and radiation damage. Solar cells made from additional wafers will be characterized using IV curves and will be subsequently radiation tested at fluences up to $1 \times 10^{15} \text{ e/cm}^2$ at 1 MeV.

CONCLUSIONS

The gallium doped C^3Z or FZ material could be a mission enabling technology. Gallium arsenide solar cells with 17% to 18% BOL efficiencies will not be available in production quantities until the 1985-1986 time period. Until then, the 13.5% efficient silicon solar cell with a 9% EOL efficiency due to radiation damage cannot be expected to provide the longer life in high radiation orbits without costly replacement of satellites.

REFERENCES

1. Investigation of High Purity Czochralski Grown Silicon for Solar Cell Applications, Air Force Contract F33615-81-C-2025, Spectrolab, Sylmar CA. Principal Investigator: William Taylor.
2. "Growth of High Purity Oxygen-Free Silicon by Cold Crucible Techniques" Air Force Contract F-19628-80-C-0104, Ceres Corp, Waltham MA. Principal Investigator: Joseph F. Wenkus.
3. Solar Cell Radiation Handbook. JPL publication 77-56. Jet Propulsion Laboratory, California Institute of Technology, Pasadena CA.
4. Low Resistivity - High Lifetime Single Crystal Silicon Investigation F33615-77-C-2045 Spectrolab, Sylmar CA. Principal Investigators J. Fodor and R. W. Opjorden.

TABLE 1

COLD CRUCIBLE GROWN CRYSTALS

Crystal No.	CC 814901	CC 815001
Nominal Resistivity	1.0 ohm-cm	10 ohm-cm
Type	p	p
Dopant	Ga	Ga
Growth Date	12-9-81	12-18-81
Polysilicon Lot	CB021199	CB021199
Poly Data:		
Boron	.06 ppb	.06 ppb
Donors	.25 ppb	.25 ppb
Crystal Diameter	0.6 inches	0.3 to 0.8 inches
Length (Approx.)	2.7 inches	1 inch
<u>Resistivity vs. Distance</u>		
<u>From Seed (cm)</u>		
1	.951 ohm-cm	11.7 ohm-cm
2	.848	12.6
3	.856	
Dislocation Density	(to be determined)	

COLD CRUCIBLE CZOCHRALSKI STARTUP

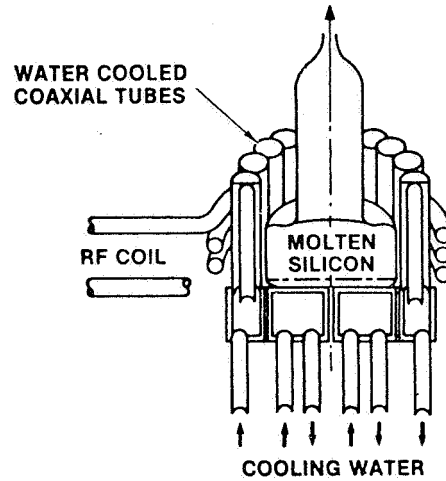


Figure 1

COLD CRUCIBLE CZOCHRALSKI CRYSTAL GROWTH

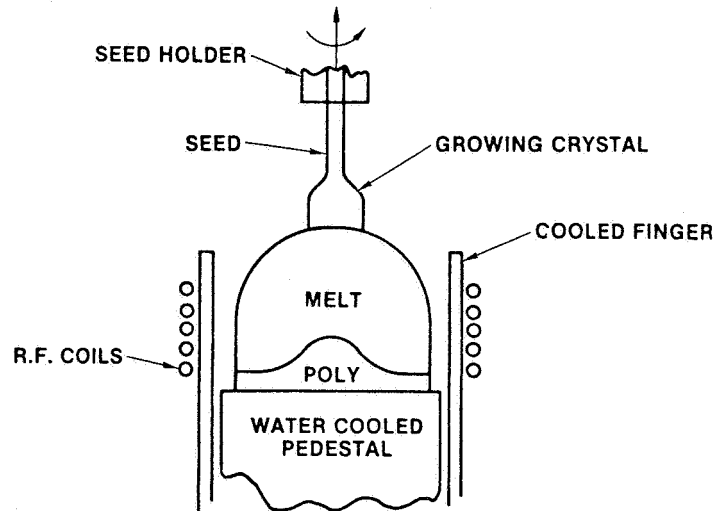


Figure 2

MICRODISTRIBUTION OF OXYGEN IN SILICON AND ITS EFFECTS ON ELECTRONIC PROPERTIES*

H.C. Gatos, B.-Y. Mao, K. Nauka, and J. Lagowski
Massachusetts Institute of Technology
Lexington, Massachusetts

ABSTRACT

The effects of interstitial oxygen on the electrical characteristics of Czochralski-grown silicon crystals were investigated for the first time on a micro-scale. It was found that the generation of thermal donors is not a direct function of the oxygen concentration. It was further found that the minority carrier lifetime decreases with increasing oxygen concentration, on a microscale in "as-grown" crystals. It was thus shown, again for the first time, that oxygen in "as grown" crystals is not electronically inert as generally believed. Preannealing at 1200°C commonly employed in device fabrication, was found to suppress the donor generation at 450°C and to decrease the deep level concentrations.

INTRODUCTION

Oxygen, invariably present in Czochralski-grown crystals, is a most undesirable impurity, as it has not only adverse, but also unpredictably complex effect on Si devices (ref. 1).

Interstitial oxygen in "as grown" crystals has been generally considered to be electronically inert. Upon heat treatment at 450°C, it becomes electronically active and leads to the generation of donors which have been attributed to the formation of Si-O complexes (ref. 2). The concentration of these donors has been related directly to the oxygen concentration (ref. 3). These donors can be annihilated at higher temperatures. Eventually prolonged heat treatment at temperatures exceeding 1000°C leads to microprecipitates of SiO_x (ref. 4).

In our studies we have developed techniques for the direct comparison of oxygen concentration and thermally activated donors on a microscale (ref. 5). Most recently we developed a technique for determining the minority carrier lifetime on a microscale, and thus the means of comparing directly the oxygen concentration to the lifetime. We have found that the thermally activated donors are not necessarily a direct function of the oxygen concentration. More importantly, we found that interstitial oxygen or oxygen in "as grown" crystals is not electronically inert, but it has a pronounced effect on the minority carrier lifetime. Furthermore, heat treatments do not just control the donor concentration, but cause complex electronic interactions with direct implication to Si devices, including photovoltaics.

EXPERIMENTAL

Czochralski-grown B-doped ($\sim 10^{15} \text{ cm}^{-3}$) crystals with an oxygen concentration of about 10^{18} cm^{-3} were employed for the study of the effects of oxygen concentration or oxygen concentration variations on the electronic properties. Longitudinal slices of Si were employed, since pronounced oxygen concentration variations are present

*This work was supported by NASA Lewis Research Center, Grant No. NSG 3017.

along the growth direction (ref. 6). On the other hand, the effects of heat treatment on energy levels within the energy gap were investigated on slices cut perpendicular to the growth direction in which the oxygen concentration variations are relatively small.

Oxygen microprofiles were obtained with scanning IR absorption (ref. 7) and carrier concentration profiles with high resolution spreading resistance measurements.

Lifetime and oxygen concentration microprofiles were obtained with a newly developed double laser arrangement as shown in Fig. 1. The CO₂ laser (9.17 μm wavelength) was employed for obtaining a transmissivity profile from which the oxygen concentration profiles could be determined. A second transmissivity profile--over the identical area--was obtained employing both the CO₂ laser and a YAG laser (10.6 μm wavelength). This transmissivity profile reflected the variation of excess carriers (generated by the YAG laser) superimposed to the variations of oxygen concentration. By subtracting the contribution of the oxygen absorption from the composite transmissivity profile we obtained the variation of the excess carrier concentration. Since the intensity of YAG laser, I, was maintained constant from the variation in excess carrier concentration, Δn, the variation in carrier lifetime, τ, could be directly determined, since

$$\Delta n = (1-R)I\tau$$

where R is the reflectivity coefficient.

Energy levels were determined by Hall-effect measurements as a function of temperature and by deep level transient spectroscopy, DLTS.

RESULTS AND DISCUSSION

In previous communications (ref. 5) we reported that oxygen concentration variations (on microscale) are not directly related to the thermally activated donor concentration variations, and it has been shown that microdefects play an important role in the generation of thermal donors. The analysis of these results is summarized in Fig. 2. The experimental points were obtained from numerous microprofiles of oxygen and thermal donor concentrations (ref. 5b). The line represents the proposed dependence of thermal donor concentration on the fourth power of oxygen concentration (ref. 3). It is seen that measurements on a microscale do not support this dependence and that macroscale measurements do lead to erroneous conclusions.

It has been generally assumed that oxygen in "as grown" Si crystals is electronically inert. For obvious reasons, critical testing of this assumption could not be carried out on the basis of macroscale measurements. However, employing double laser scanning IR absorption revealed, for the first time, that indeed oxygen is electronically active, as seen in Fig. 3. It is seen that the minority carrier lifetime, determined as outlined above, is significantly affected by oxygen. Maxima in the lifetime correspond to minima in oxygen absorption (i.e., in oxygen concentration).

These results are very surprising, as they indicate that interstitial oxygen cannot as yet be understood on a theoretical basis. It must, thus, be assumed, at this time, that oxygen-Si or oxygen-point defect complexes are present along with the interstitial oxygen species.

Attempts were made to study the lifetime variations on a microscale after 450°C heat treatment. However, a pronounced overall decrease in the lifetime made the determination of its variations essentially impossible.

Thus, a series of experiments were initiated to determine the effects of heat treatment at various temperatures (300 to 750°C) on the lifetime employing macroscale measurements. Preliminary results showed that, in general, the lifetime decreases with increasing annealing temperature. However, for a given annealing temperature the lifetime values vary significantly as a function of lifetime measurement temperature (10 to 300 K). Apparently, recombination centers of a different nature are introduced at the various heat treatment temperatures. Work is being pursued to determine the characteristics of the various recombination centers and will be reported in a future communication.

In another series of experiments the effects of preannealing at 1200°C for 30 minutes on subsequent low temperature annealing and on the deep levels in Si were investigated. This type of preannealing is usually employed prior to device fabrication. The results of these experiments are shown in figures 4, 5, and in Table I.

It is seen in Fig. 4 that preannealing decreases the rate of thermal donor generation at 450°C. In fact, conversion from n- to p-type, which takes place without preannealing, does not take place upon preannealing, even after heat treatment for 200 hrs.

In an attempt to clarify the role of high temperature preannealing, the deep level concentrations were determined in "as grown" crystal segments and preannealed. As seen in Fig. 5, two distinct acceptor deep levels were observed in "as grown" Si. The concentration of these levels decreased significantly upon preannealing, as shown in Table I, indicating that these levels do not originate in impurity atoms, but rather in impurity atom-point defect complexes. Although the relationship between the results of Fig. 4 and Table I is not clear at present, it points to the conclusion that the thermal donor generation is a point defect-assisted process.

In summary, oxygen in "as grown" Si or upon heat treatments, employed in device processing, has pronounced effects on electronic properties controlling device performance. These effects appear to be the result of oxygen interactions with point defects or point defect complexes. Identifying the nature and achieving control of these interactions should prove of paramount importance in optimizing device performance and stability.

REFERENCES

1. See, for example, Semiconductor Silicon 1981, edited by Huff, H.R.; Krieger, R.J.; and Takeishi, Y.: The Electrochemical Society, Pennington, N.J.
2. Kaiser, W.: Electrical and Optical Properties of Heat-Treated Silicon. Phys. Rev., vol. 105, no. 6, 1957, pp. 1751-1756.
3. Kaiser, W.; Frisch, H.L.; and Reiss, H.: Mechanism of the Formation of Donor States in Heat-Treated Silicon. Phys. Rev., vol. 112, no. 5, 1958, pp. 1546-1554.
4. Yang, K.H.; Anderson, P.; and Kappert, H.: Identification of Oxide Precipitates in Annealed Silicon Crystals. Appl. Phys. Lett., vol. 33, no. 3, 1978, pp. 225-227. Murgai, A.; Chi, J.-Y.; and Gatos, H.C.: Microdistribution of

Oxygen in Silicon. J. Electrochem. Soc., vol. 127, no. 5, 1980, pp. 1182-1186.

5. (a) Rava, P.; Gatos, H.C.; and Lagowski, J.: Correlation of Oxygen Concentration and Activated Oxygen Donors in Silicon Crystals on a Microscale. J. Appl. Phy. Letters, vol. 38, no. 4, 1981, pp. 274-276. (b) Gatos, H.C.; Rava, P.; and Lagowski, J.: Distribution of Oxygen in Silicon and Its Effects on Electronic Characteristics on a Microscale. Space Photovoltaic Research and Technology, 1980. NASA Conference Publication 2169.
6. Murgai, A.; Gatos, H.C.; and Westdorp, W.A.: Effect of Microscopic Growth Rate on Oxygen Distribution and Swirl Defect Distribution in Czochralski-Grown Silicon. J. Electrochem. Soc., vol. 126, no. 12, 1979, pp. 2240-2245.
7. Jastrzebski, L.; Lagowski, J.; and Gatos, H.C.: Quantitative Determination of the Carrier Distribution in Semiconductors by Scanning IR Absorption: Si. J. Electrochem. Soc., vol. 126, no. 2, 1979, pp. 260-263.

TABLE I. - DEEP ACCEPTOR LEVELS IN Si AND THE EFFECT OF PREANNEALING AT 1200°C FOR 30 MINUTES

	Sample	0.19 eV	0.43 eV
As Grown	A	2.4×10^{11}	1.2×10^{11}
	A'	2.7×10^{11}	1.2×10^{11}
Preannealing	B	7.2×10^{10}	7.2×10^{10}
	B'	undetectable	undetectable

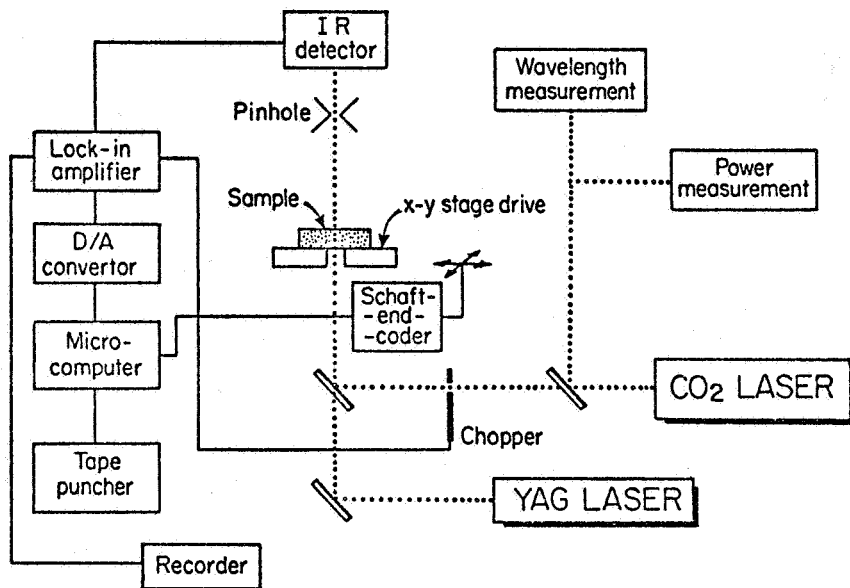


Figure 1. Schematic representation of double laser scanning absorption.

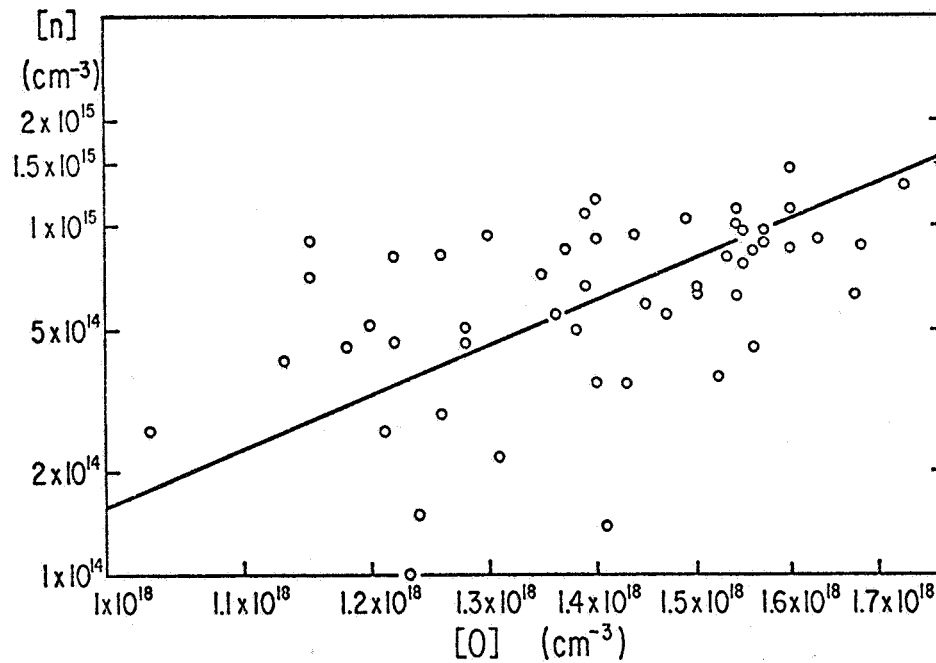


Figure 2. Thermal donor concentrations activated by heat treatment at 450°C for 4 hrs as a function of oxygen concentration. Straight line represents proposed relationship between thermal donor and oxygen concentrations (ref. 3).

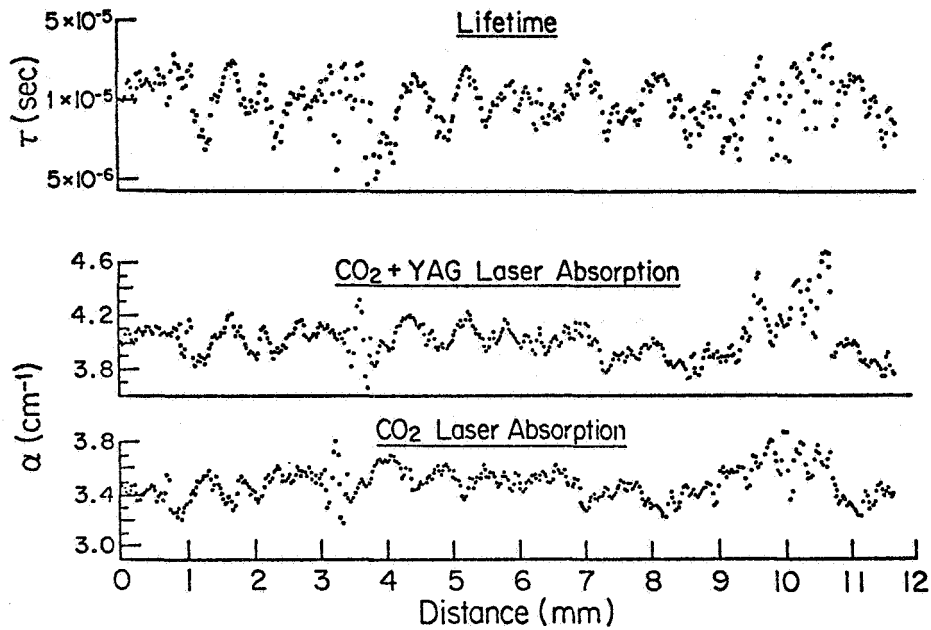


Figure 3. Variation of oxygen concentration (CO_2 laser absorption) and lifetime as a function of distance along the growth direction (see text).

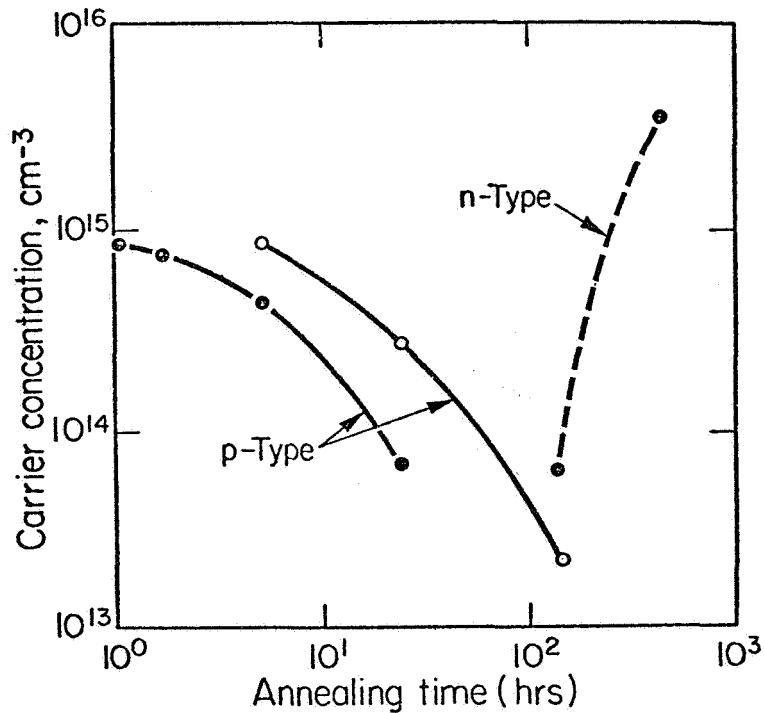


Figure 4. Carrier concentration as a function of annealing time at 450°C
 ● "as grown" Si; ○ preannealed at 1200°C for 30 minutes.

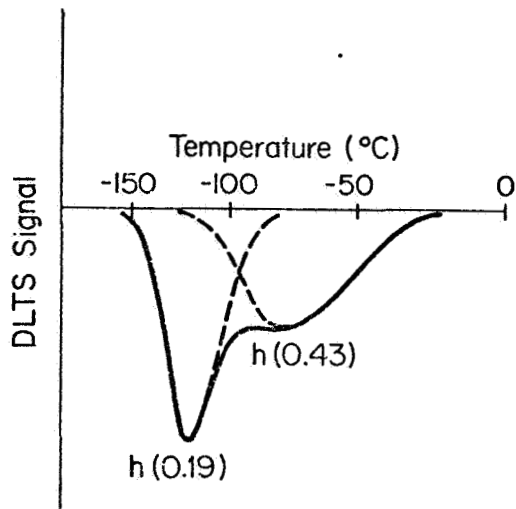


Figure 5. DLTS spectrum of "as grown" Si.

EFFECTS OF INJECTION CHARGE DISTRIBUTION ON THE PERFORMANCE OF RADIATION DAMAGED, HIGH RESISTIVITY CELLS

I. Weinberg, C. Goradia*, and C.K. Swartz
NASA Lewis Research Center
Cleveland, Ohio

Extended Abstract

Previous results indicate that, contrary to expectations, for sufficiently high cell base resistivities, the radiation resistance of silicon solar cells decreases as cell resistivity increases (ref. 1). This result was observed for n^+pp^+ cells of 84 and 1250 Ω -cm base resistivities, the data being analyzed using a theory valid only under open circuit conditions (ref. 2). From this a qualitative argument was presented to show that the increased degradation was due primarily to an increased voltage drop in the cells' base region (ref. 1). In the present case we use an analytical model, valid over all cell voltages, to place our previous qualitative conclusions on a firmer quantitative basis. Since loss of conductivity modulation is attributable to the behavior of the base injected charge distribution (ref. 3), we pay particular attention to this factor in our present treatment of the data.

Normalized maximum power as a function of fluence, after irradiation by 1 MeV electrons, is shown in figures 1 and 2. Also shown in figure 1 are the data for a 10 Ω -cm silicon cell with BSF (ref. 4). From both figures it is readily seen that in the resistivity range shown, as cell base resistivity increases the radiation induced degradation increases. This is the reverse of the behavior usually observed for cells in the lower resistivity ranges (ref. 4).

Base majority carrier concentrations, in the present unirradiated cells, are lower than the injected minority carrier concentrations at air mass zero. Hence, the usual low injection models do not apply. For this reason, we have developed a model, valid for both high and low injection levels, to use in treating the present data. Additional details have been presented in a previous publication (ref. 5). The model takes into account nonuniform optical carrier generation, band gap narrowing, generation, and recombination in the n^+p space charge region, wavelength-dependent reflection coefficients, and ohmic and Debye voltage contributions in the base region.

Schwartz et al. (ref. 3) have shown the importance of the base minority carrier distribution as a factor in cell degradation under high injection conditions. Calculations for a BSF cell under these conditions show that, with increasing cell current, the injected carrier concentration at the back junction decreases, with the region of low concentration progressively extending toward the front junction (ref. 3). In the present case, a similar situation holds for the high resistivity cell as diffusion length decreases with fluence (fig. 3). At the lower fluences the cell of figure 3 is in high injection. With increased fluence, the injected carrier concentration decreases, and portions of the cell near the back junction are in low

*Dept. of Electrical Engineering, Cleveland State University, Cleveland, Ohio.

injection. As the injected carrier concentration is lowered, the ohmic voltage drop across the cells' base region is anticipated to contribute significantly toward cell degradation. However, as cell thickness decreases, the diffusion lengths are still large enough, compared with cell thickness, that one does not encounter the gradient of injected carrier concentration seen in figure 3. This is illustrated in figure 4 for the thinnest higher resistivity cell. In this case, although the injected carrier concentration is higher than the base concentration, the cell base resistivity is still high enough to contribute a significant ohmic drop in the cells' base region. Behavior of the injected carrier concentration for the thicker 84 Ω -cm cell is shown in figure 5. In this case the cell is near the high injection condition at low fluence, the entire cell being in low injection at the higher fluences. Similar calculations of charge densities were carried out for all cells except the 10 Ω -cm cell of figure 1. These served as the basis for calculating components of the cell output voltage V where

$$V = V_1 + V_2 - V_{DEM} - V_{ohmic} - IR_s \quad (1)$$

where V_1 and V_2 are the front and rear junction voltages, V_{DEM} is the Dember potential, V_{ohmic} is the ohmic voltage drop across the cells' base region and IR_s is the remaining series resistance voltage drop due to cell components other than the base. The computed voltage drops are shown in figures 6 and 7 for the thicker cells of both resistivities. The ohmic drop is seen to be the dominant factor in degradation of the higher resistivity cell. As expected, the ohmic contribution diminishes with decreased cell resistivity but remains a significant factor in the thicker low resistivity cell. As shown in figure 8, this component diminishes with cell thickness, but is still significant in the thinner high resistivity cell, and is nontrivial in the thinner lower resistivity cell.

The present results indicate that as cell resistivity increases, the base injected minority carrier distributions, leading to lack of conductivity modulation, are increasingly significant factors in radiation-induced cell degradation. Although, for the cells presented here, degradation increases with increased resistivity, cells of lower resistivity show decreased degradation with increased resistivity (ref. 4). Thus, there appears to be a trade-off between decreased radiation-induced degradation due to decreased dopant concentration and the degrading effects of ohmic voltage drops.

REFERENCES

1. Weinberg, I.; Goradia, C.; Swartz C. K.; and Herman, A. M.: Performance of High Resistivity n^+pp^+ Silicon Solar Cells Under 1 MeV Electron Irradiation. Proc. 15th IEEE Photovoltaic Specialists Conference, 1981, pp. 484-489.
2. Wu, C.-Y. and Shen, W-Z: The Open Circuit Voltage of Back-Surface-Field (BSF) p-n Junction Cells in Concentrated Sunlight. Solid State Electron., vol. 23, 1981, pp. 219-216.
3. Schwartz, R. J.; Lundstrom, M. S.; and Nasby, R. D.: The Degradation of High-Intensity BSF Solar-Cell Fill Factors Due to a Loss of Base Conductivity Modulation. IEEE Trans. on Electron Devices, vol. ED-28, 1981, pp. 264-269.
4. Tada, H. Y.; and Carter, J. R., Jr.: Solar Cell Radiation Handbook. NASA JPL Publication 77-56, Chapt. 3, 1977.
5. Goradia, C.; Weinberg, I.; and Baraona, C.: A Theory of the N-I-P Silicon Solar Cell. Proc. 15th IEEE Photovoltaic Specialists Conference, 1981, pp. 855-860,

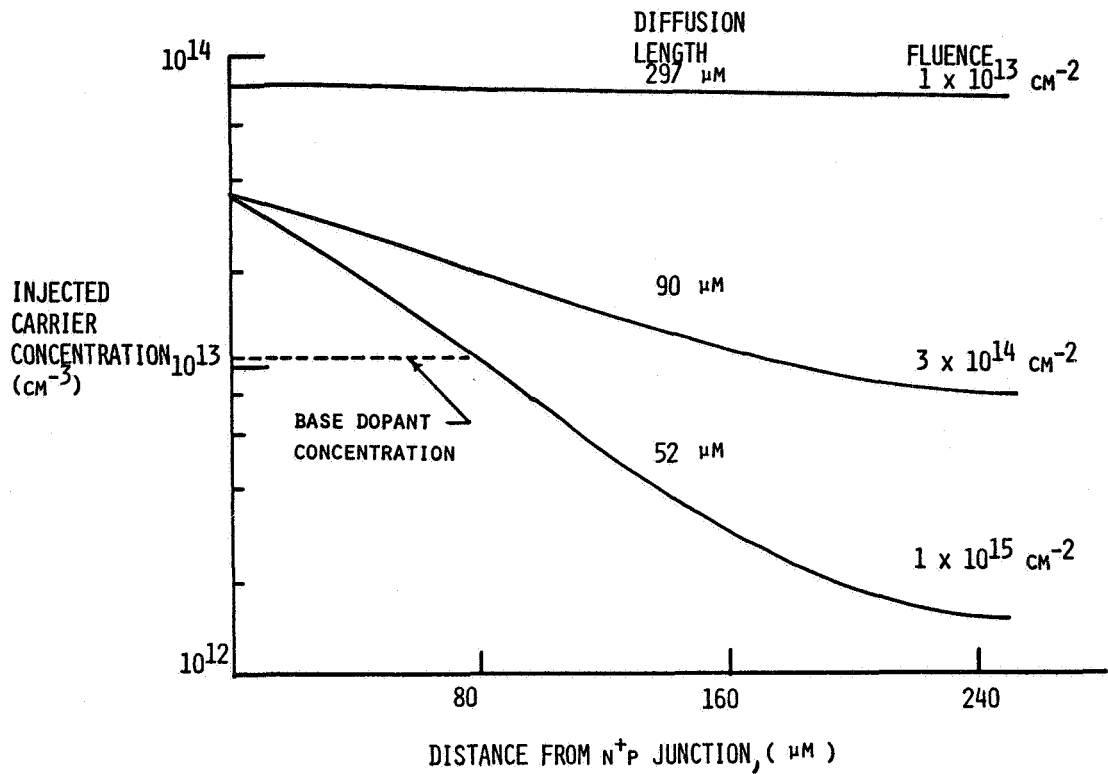


Figure 3. - Injected carrier concentration in cell's base region at P_{max} .
 $\rho = 1250 \Omega\text{-cm}$; thickness = $250 \mu\text{m}$.

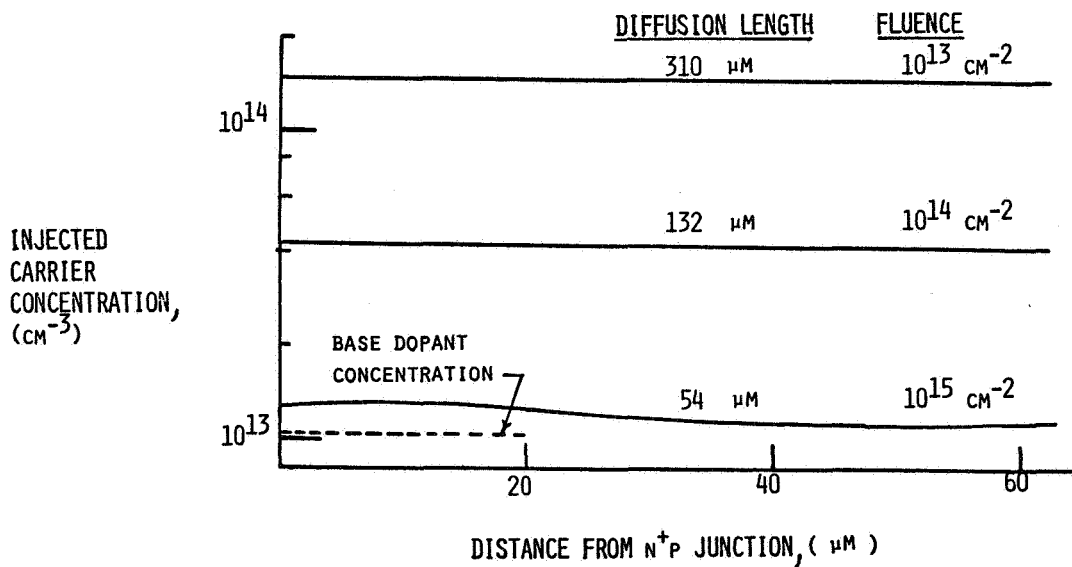


Figure 4. - Injected carrier concentration in cell's base region at P_{max} .
 $\rho = 1250 \Omega\text{-cm}$, thickness = $61 \mu\text{m}$.

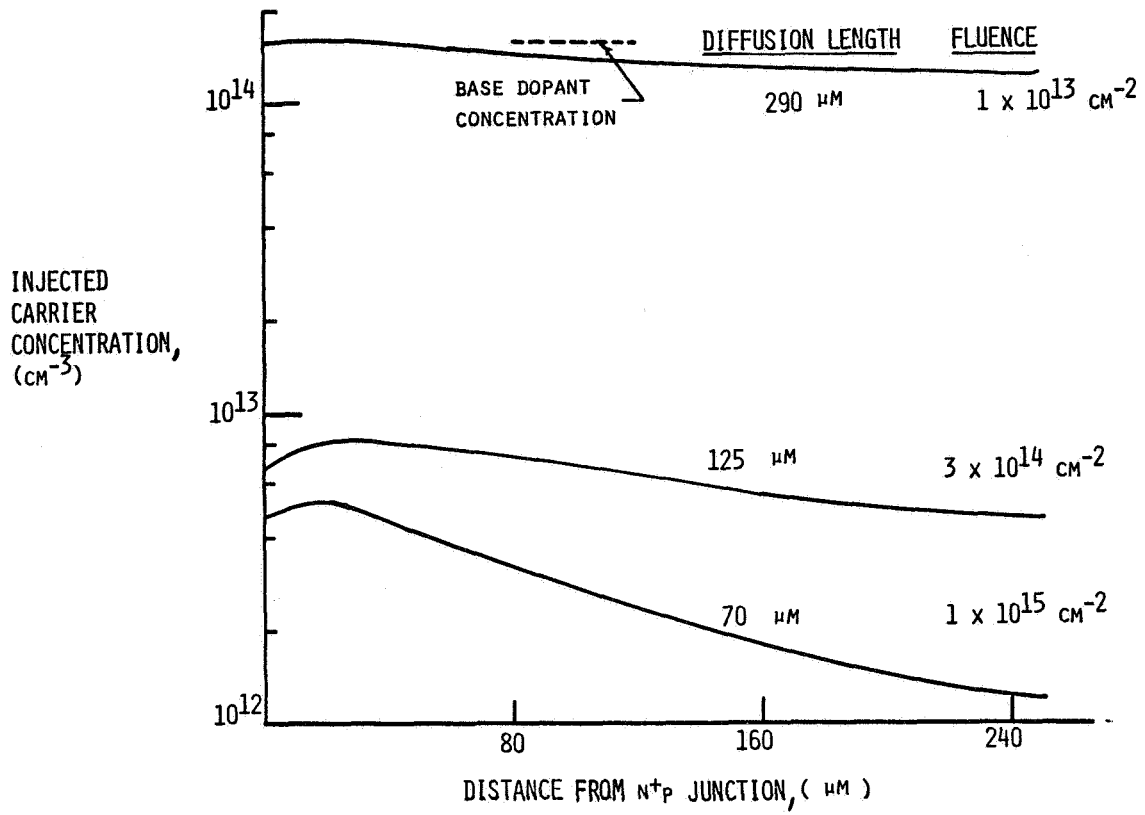


Figure 5. - Injected carrier concentration in cell base. $\rho = 84 \Omega\text{-cm}$; $t = 250 \mu\text{m}$.

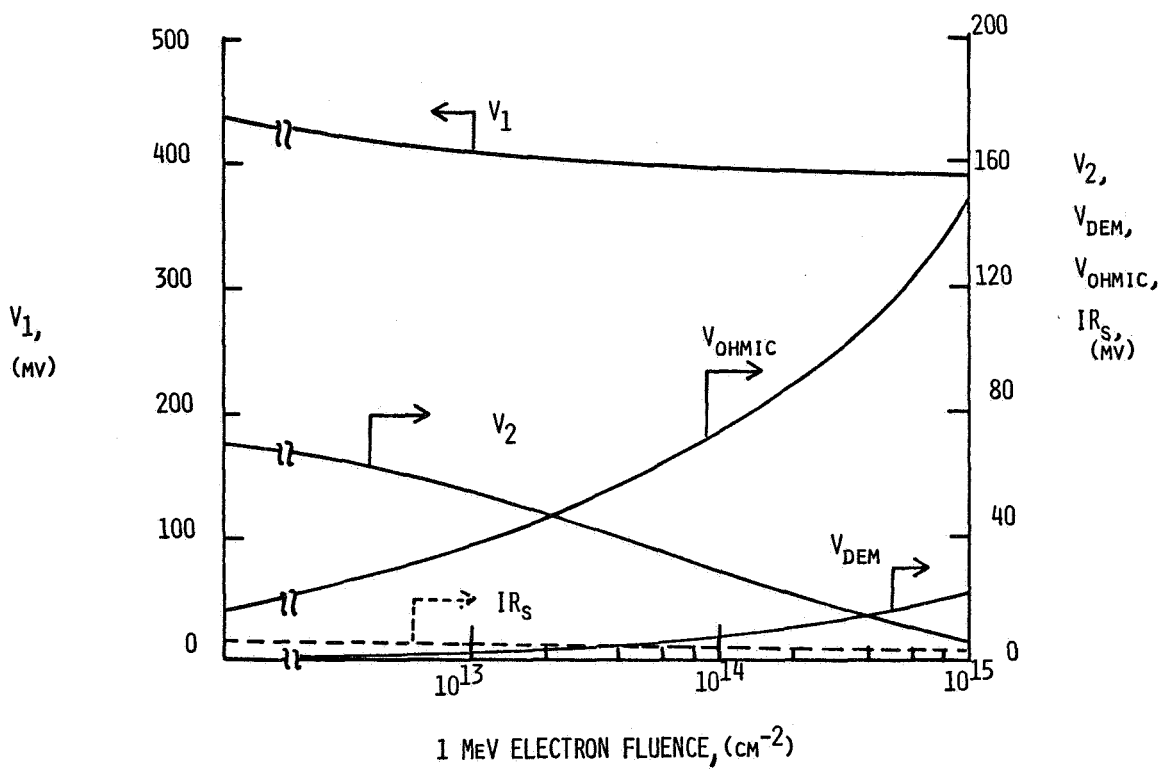


Figure 6. - Voltage components at P_{max} . $\rho = 1250 \Omega\text{-cm}$, $t = 250 \mu\text{m}$.

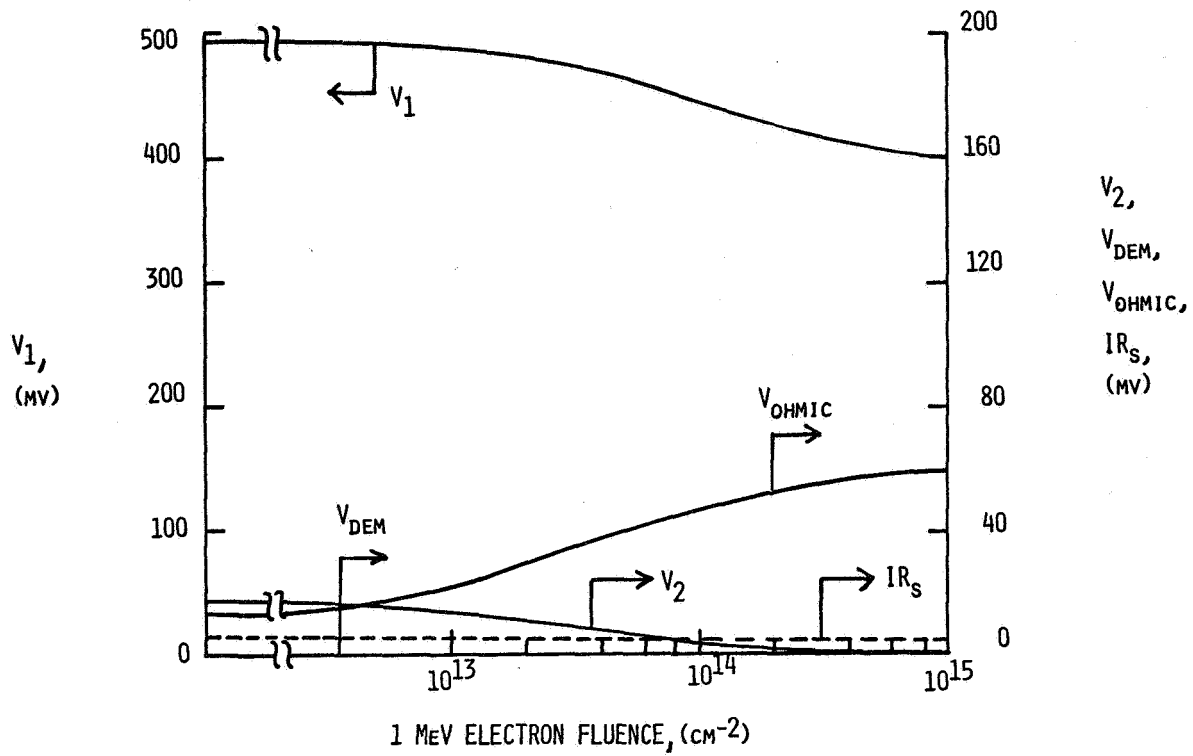


Figure 7. - Voltage components at P_{max} . $\rho = 84 \Omega\text{-cm}$; $t = 250 \mu\text{m}$.

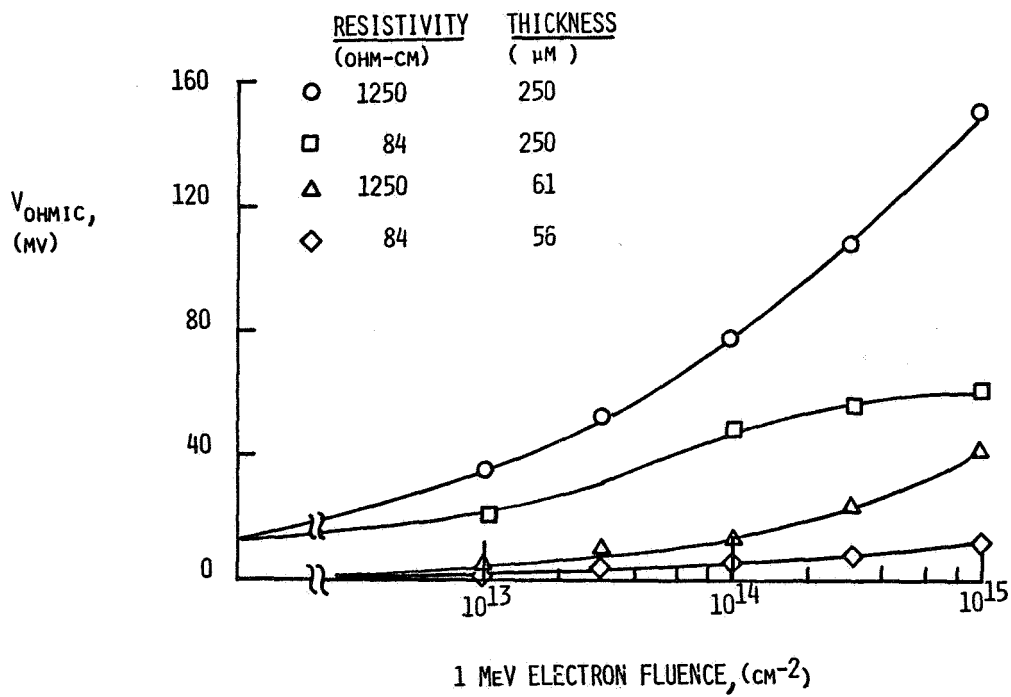


Figure 8. - Ohmic voltage component - all cells.

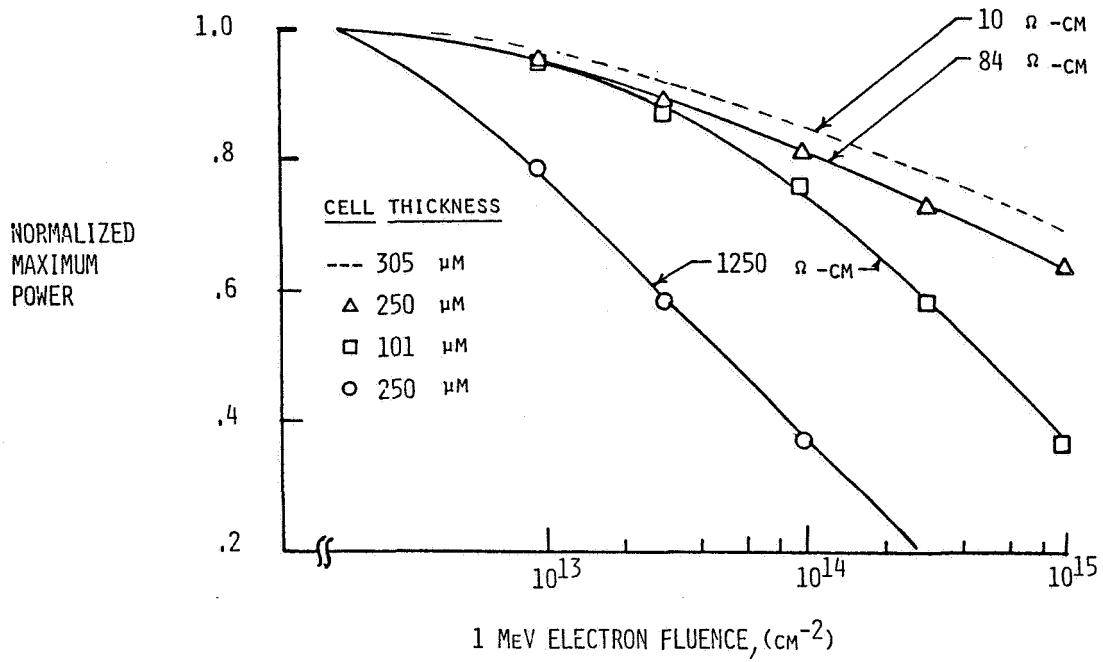


Figure 1. - Normalized maximum power versus 1-MeV electron fluence for high resistivity n^+pp^{++} cells. Cell thickness, 101 to 305 μm.

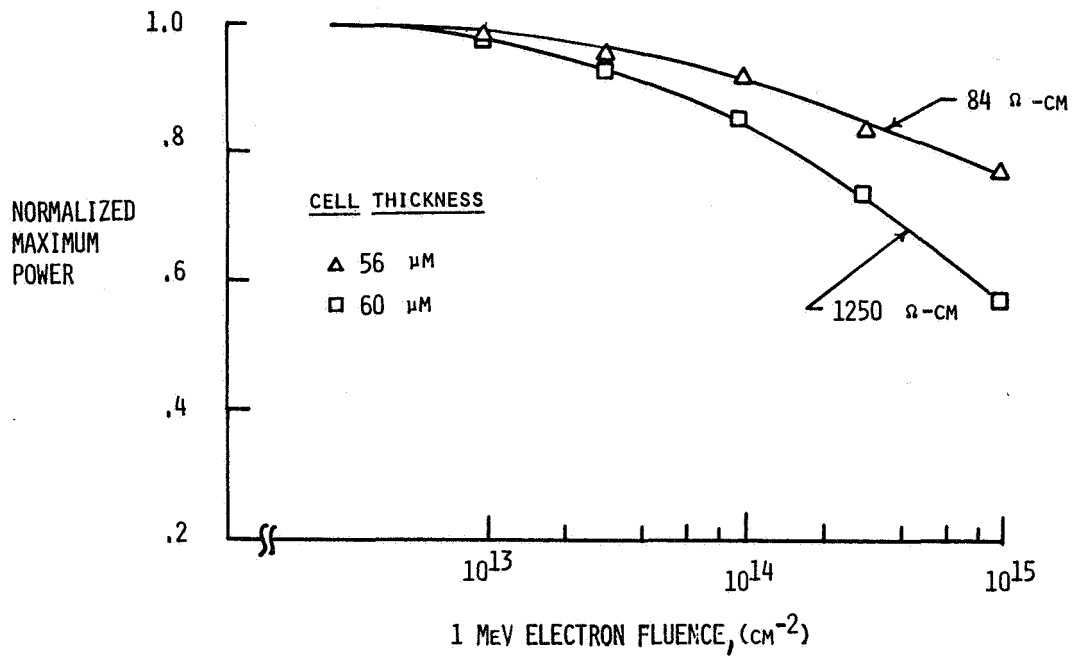


Figure 2. - Normalized maximum power versus 1-MeV electron fluence for high resistivity n^+pp^+ cells.

RADIATION DAMAGE AND ANNEALING IN LARGE AREA $n^+/p/p^+$ GaAs SHALLOW HOMOJUNCTION SOLAR CELLS

D.J. Flood, D.J. Brinker, C.K. Swartz, and R.E. Hart, Jr.
NASA Lewis Research Center
Cleveland, Ohio

and

John C.C. Fan
Lincoln Laboratory
Massachusetts Institute of Technology
Lexington, Massachusetts

SUMMARY

Annealing of radiation damage has been observed for the first time in VPE-grown, 2- by 2-cm, $n^+/p/p^+$ GaAs shallow homojunction solar cells. Electrical performance of several cells was determined as a function of 1-MeV electron fluence in the range of 10^{13} to 10^{15} e^-/cm^2 and as a function of thermal annealing time at various temperatures. Degradation of normalized power output after a fluence of 10^{15} 1-MeV electrons/ cm^2 ranged from a low of 24 to 31 percent of initial maximum power. Normalized short circuit current degradation was limited to the range from 10 to 19 percent of preirradiated values. Thermal annealing was carried out in a flowing nitrogen gas ambient, with annealing temperatures spanning the range from 125° to 200° C. Substantial recovery of short circuit current was observed at temperatures as low as 175° C. In one case improvement by as much as 10 percent of the postirradiated value was observed. The key features of these cells are their extremely thin emitter layers (approximately 0.05 μm), the absence of any $Al_xGa_{1-x}As$ passivating window layer, and their fabrication by vapor phase epitaxy.

INTRODUCTION

The GaAs shallow homojunction solar cell (refs. 1 and 2) is a potentially superior structure for space applications. Among the features of the cell which contribute to such performance are (1) the extremely thin (0.05 μm), highly doped n^+ emitter; (2) absence of the $Al_xGa_{1-x}As$ surface passivating layer; and (3) incorporation of the p-type base and p^+ back surface field region. The thin n^+ emitter assures that most of the electron hole pairs, created by incident photons with energies greater than the 1.43-eV bandgap of GaAs, are generated in the p-type base region of the cell. Since electrons are the minority carriers in the p-type base, minority carrier diffusion lengths are expected to be greater than in n-type material with the same doping density; hence, collection efficiency and resistance to radiation damage should be higher than in an equivalent $p^+/n/n^+$ structure.

The cells incorporated in this study were fabricated at the Lincoln Laboratory (ref. 3) using the chloride transport method of vapor phase epitaxy (VPE). All are 2 by 2 cm in total area with anodic oxide antireflection coatings and electroplated tin front contacts. Back contacts are electroplated gold. A cross section of the cell structure is shown in figure 1. The shallow n^+ emitter is sulfur doped to 5×10^{18} , while the p region dopant varied from 4×10^{16} to 6×10^{17} cm^{-3} .

RESULTS AND DISCUSSION

Irradiations by 1-MeV electrons were conducted at room temperature using the Lewis Research Center Dynamitron accelerator at five fluences ranging from 1×10^{13} to 1×10^{15} e⁻/cm². Characteristics were determined after each irradiation using a xenon arc solar simulator with a flight-calibrated GaAs reference cell as a standard. Six cells were irradiated in this study, these original efficiencies ranging from 13.6 to 15.6 percent AMO. Figure 2 shows the normalized short-circuit current as a function of 1-MeV electron fluence for its "best" cell (that cell showing minimum degradation after 10^{15} e⁻/cm² fluence). The short-circuit current was normalized to preirradiated values. The best cell degraded 10 percent, the worst cell 19 percent at a fluence of 10^{15} /cm² with an average degradation of 13.5 percent. Normalized maximum power degradation as a function of fluence is shown in figure 3. The best cell here, the same cell of figure 2, showed a degradation of 24 percent at a fluence of 10^{15} e⁻/cm². The worst cell degraded 31 percent while the average was 26.2 percent. A slight drop in fill factor was noticed in the cells when comparing preirradiation and postirradiation values, although the differences are barely outside the range of experimental error (+1.0 percent).

Annealing of this radiation damage has been observed for the first time in shallow homojunction solar cells. To date, annealing has only been reported in heteroface, liquid phase, epitaxially (LPE) grown cells. Thermal annealing was done in a flowing nitrogen gas ambient at room temperatures ranging from 125° to 200° C. Periodic measurements of I-V and spectral response were made to monitor cell performance. No annealing was seen at 125° C. Figure 4 shows the normalized short-circuit current as a function of annealing time at 175° and 200° C after irradiation at a fluence of 10^{15} e⁻/cm². The cell annealed at 175° C showed the largest degradation after irradiation, to 81 percent of the original value. It recovered to 88 percent after 15 hr; further annealing to 40 hr showed no additional increase. The cell annealed at 200° C exhibited less initial degradation, to 85 percent of preirradiated value, and recovered to 95 percent after 15 hr. Again, further annealing to 40 hr did not increase the response. Normalized maximum power as a function of annealing time is shown in figure 5. Twenty-five hours at 175° C raised the maximum power from 70 to 76 percent of preirradiation values. Recovery at 200° C was from 75 to 90 percent after 20 hr of annealing. Further annealing did not increase recovery. Figure 6 is the spectral response of a cell irradiated to a fluence of 10^{15} e⁻/cm² before and after annealing for 40 hr at 200° C. The data indicate that the loss in photocurrent is attributable entirely to damage in the base region of the cell. The shape of this recovery is compatible with the spectral response degradation seen in these cells as a function of 1-MeV fluence (ref. 4).

CONCLUSION

The GaAs shallow homojunction solar cells tested show good radiation tolerance. Annealing of radiation damage has been seen for the first time in these cells at temperatures as low as 175° C. Spectral response measurements indicate that the observed damage and subsequent annealing occurs entirely in the p-type base region of the cell. These results are an early indication that VPE-grown, shallow homojunction GaAs solar cells have great promise for use in space solar arrays in radiation environments

REFERENCES

1. Fan, J.C.C.; Bozler, C.O.; and Chapman, R.L.: Simplified Fabrication GaAs Homojunction Solar Cell with Increased Conversion Efficiencies, APL vol. 32, p. 390, 1978.
2. Fan, J.C.C.; Chapman, R.L.; and Bozler, C.O.: Shallow Homojunction GaAs Solar Cells with High Resistance to 1-MeV Electron Irradiation, APL vol. 36, p. 53, 1980.
3. Fan, J.C.C.: GaAs Shallow Homojunction Solar Cells. NASA CR-165167, Oct. 1980.
4. Flood, D.J.; Swartz, C.K.; and Hart, Jr., R.E.: GaAs Homojunction Solar Cell Development, 4th Space Photovoltaic Research and Technology Conference, Cleveland, Ohio, p.239, 1980.

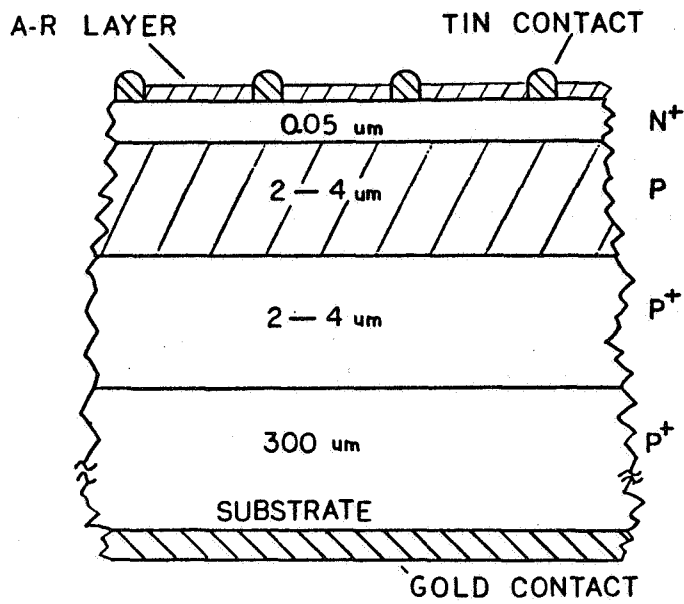


Figure 1. - Shallow homojunction cell structure.

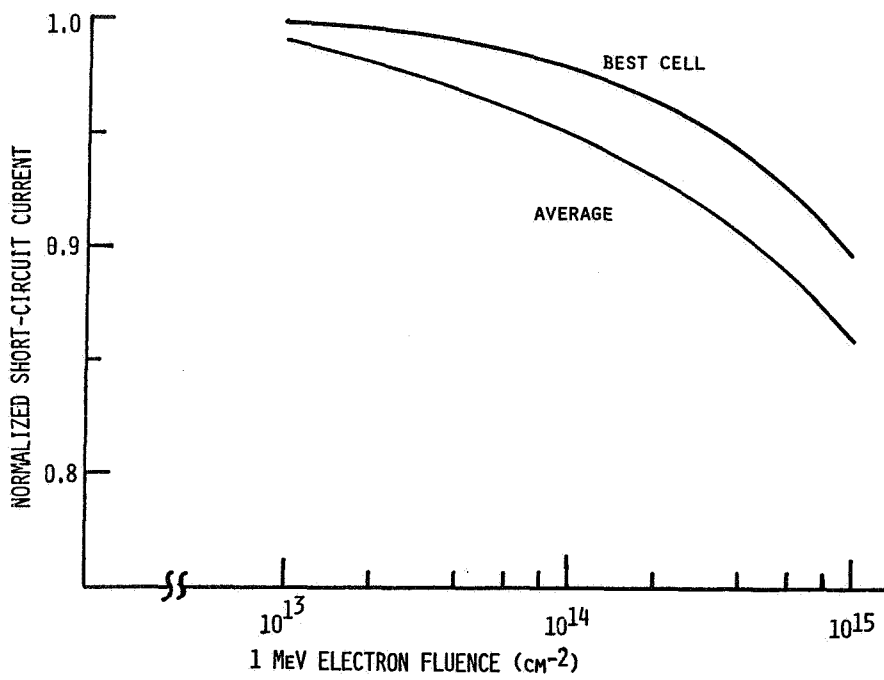


Figure 2. - Normalized short-circuit degradation in GaAs shallow homojunction solar cells.

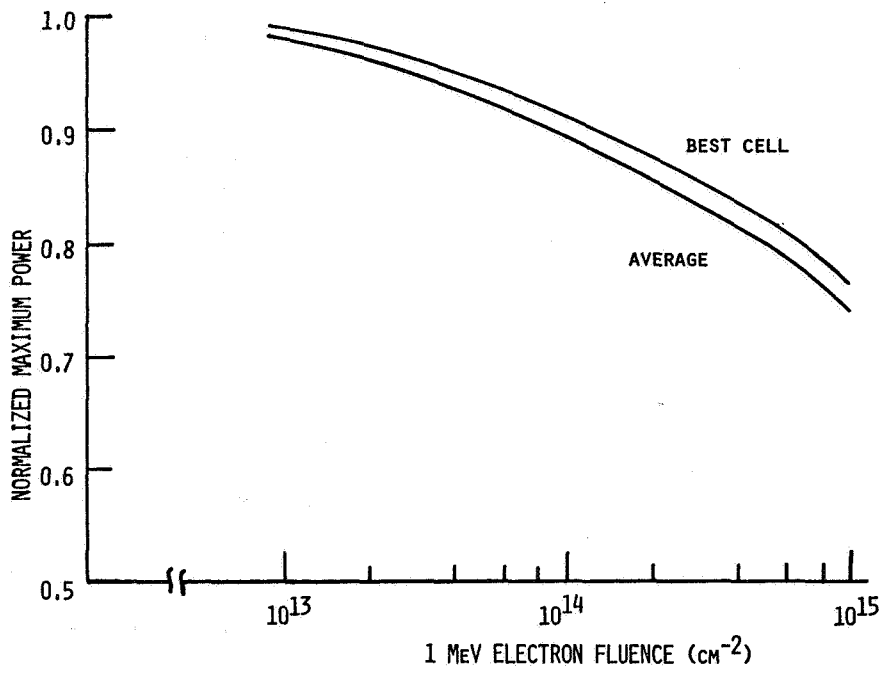


Figure 3. - Normalized maximum power degradation in GaAs shallow homojunction cells.

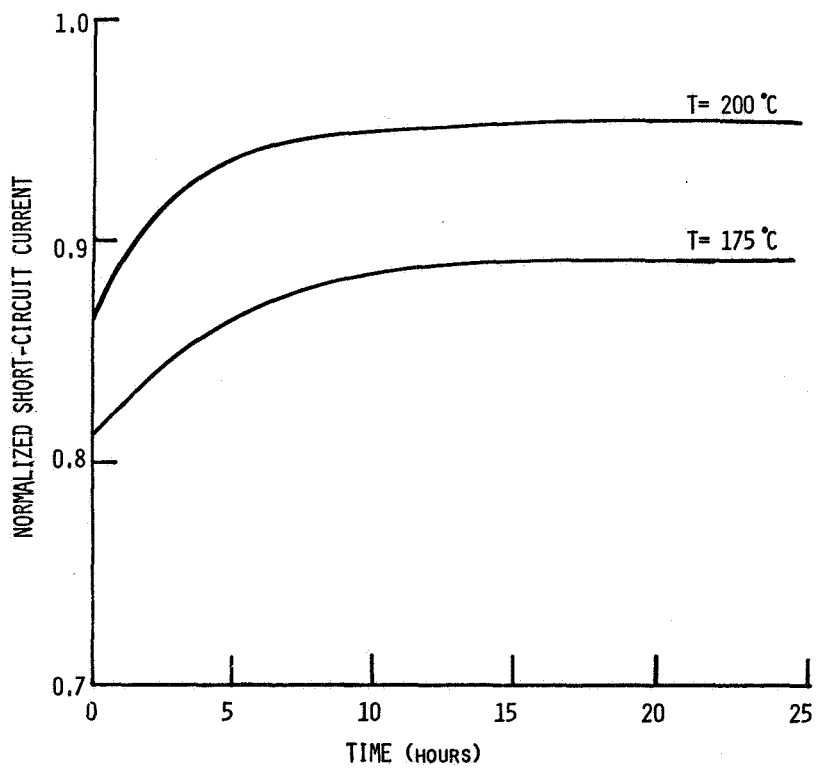


Figure 4. - Normalized short-circuit current versus annealing time.

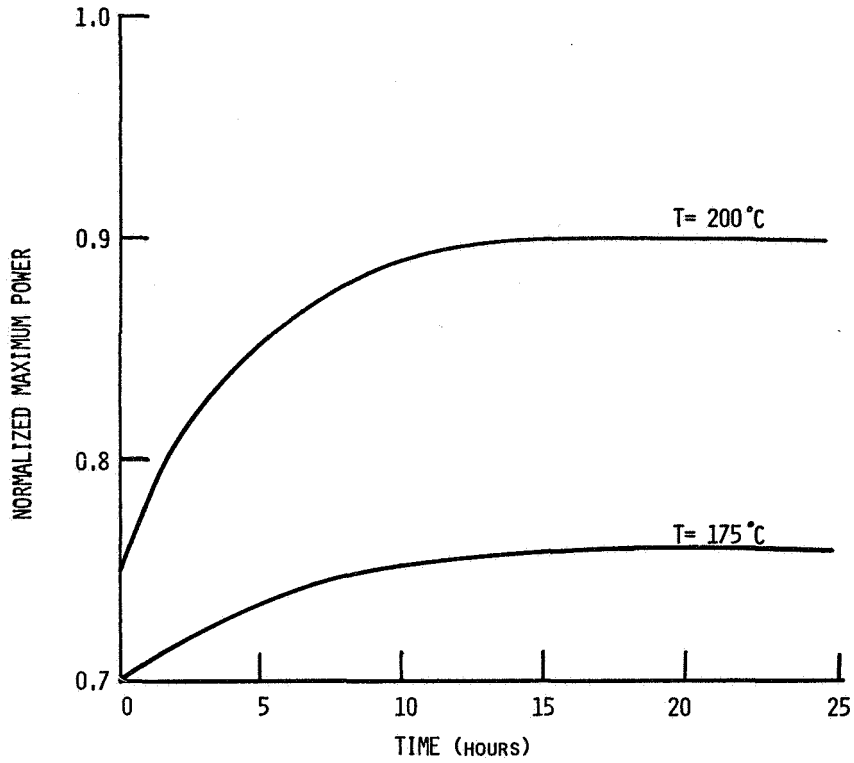


Figure 5. - Normalized maximum power versus annealing time.

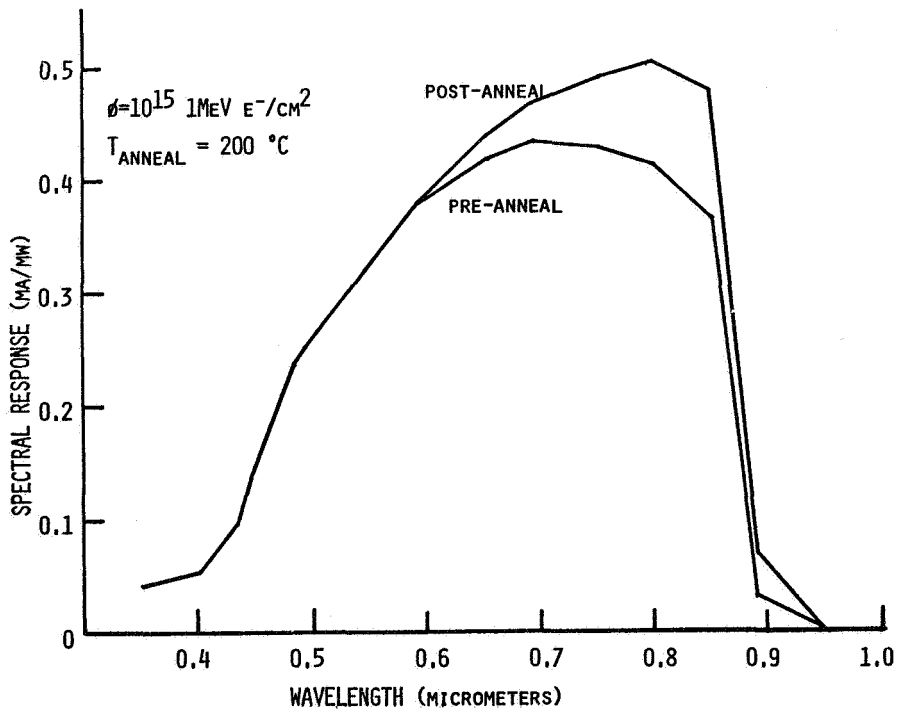


Figure 6. - Spectral response of an irradiated cell before and after annealing.

BASIS FOR EQUIVALENT FLUENCE CONCEPT IN SPACE SOLAR CELLS*

A. Meulenberg
COMSAT Laboratories
Clarksburg, Maryland

ABSTRACT

The equivalent fluence concept is defined, and its use and potential problems are noted. Silicon and GaAs solar cells are compared in a radiation environment. The analysis indicates that valid equivalent fluence values may be easier to obtain in GaAs than in silicon.

INTRODUCTION

Solar cells have been modified continually to improve their performance and lifetime for various space missions. Since an accurate simulation of the space radiation environment is very difficult, a means was sought to conveniently irradiate cells and use this information to predict performance in space with reasonable accuracy. For reasons described below, 1-MeV electrons were chosen as the single irradiation source that was both convenient and capable of simulating (at least to some extent) damage caused by the various components of the space radiation environment. Various means have been used to compare the damage to silicon solar cells by different energy protons and electrons with the damage resulting from 1-MeV electron irradiation. The "1-MeV electron equivalent fluence" concept is used to compare the damage calculated or measured for isotropic monoenergetic irradiation with the damage measured for normally incident 1-MeV electrons.

The 1-MeV equivalent fluence concept has been used with silicon cells for years with mixed success. The greatest application has been in standardizing the test procedure for comparing the radiation response of different cell designs or fabrication procedures. The concept has been less successful in the prediction of degradation in space, as explained below. Many problems that are experienced in the equivalent fluence concept for silicon will also be problems for GaAs. Two major questions need to be examined when considering an equivalent fluence model for GaAs:

- a. Was the concept really useful enough in the silicon solar cell field to warrant such a concept for GaAs?
- b. Is there a convenient and acceptable radiation type that can be used as the basis for comparison of radiation degradation studies in GaAs?

*This paper is based upon work performed at COMSAT Laboratories under the sponsorship of the Communications Satellite Corporation.

To answer these questions many factors must be considered. The following is an attempt to construct the appropriate framework for such an effort.

ASSUMPTIONS IN AN EQUIVALENT FLUENCE MODEL

The assumptions of an equivalent fluence model are 1) that a radiation type and energy level exist that, alone, can reproduce the extent and nature of radiation damage from the various space radiation environments; 2) that the space radiation components are known well enough (quantitatively and qualitatively) to substitute an equivalent fluence for the space radiation; and 3) that an equivalent fluence can be determined for all the major components and energies by a reasonable laboratory experiment. To the extent that the first assumption is valid, the model is useful. The third assumption may be false even if the first two are correct.

The major types of radiation damage to present space solar cells all involve displacement of atoms within the single crystal device. (Ultraviolet radiation damage to the solar cell coverslide assemblies is not considered here.) Electrons typically displace single atoms from their lattice site. Protons generally produce single displacements and multiple or "cluster" displacements. Neutrons (which can be ignored in the natural environment) primarily generate large clusters of displaced atoms. Population densities of the space electrons and protons normally decrease rapidly with increasing energy. This preponderance of low energy particles and the fact that they are generally isotropic means that the damage produced is much higher near an exposed surface of a device than in deeper regions within the cell. This nonuniform damage profile is the basis for effective shielding; however, it complicates the equivalent fluence model, which often assumes uniform damage to simplify mathematical analysis.

Different solar cells respond to the various radiation components in different ways. The nature of this damage depends upon the dominant damage mechanisms and the contribution to these mechanisms from each type of radiation. Since solar cells are minority carrier collection devices, reduction of the minority carrier diffusion length is generally the major damage mechanism. However, under certain circumstances, undoping (either by compensation or by coordination of a mobile defect with a donor or acceptor site) may be the primary source of solar cell power loss.

Each satellite orbit has a characteristic blend of electron and proton energies and densities. These energies and densities are not always well known and may even change from hour-to-hour or year-to-year. Under such conditions, the selected environment (the second assumption) will introduce a greater error in damage prediction than that caused by the uncertainties in equivalent fluences. As these environments become better defined by space experiments, the errors in equivalent fluence models can become critical. A major source for such errors is the laboratory experiment used to determine the equivalent fluence of a certain radiation type. Such errors (which influence the third assumption) have been observed to result from nonuniform damage, incorrect damage profiles, dose rate dependence, anneal characteristics, injection level effects, and inappropriate fluence levels. In many cases, the prediction of cell degradation in space by use of equivalent fluence models is very approximate unless the models have been verified or modified by space data for a particular environment. In some cases, the use of an equivalent fluence

can be misleading, even for only a comparison of cells, because the critical damage mechanisms may be different for the cells.

EQUIVALENT FLUENCE MODELS FOR SILICON CELLS

In the early 1960's, the concept of 1-MeV electron equivalent fluence values became accepted for damage to silicon solar cells (ref. 1). The Solar Cell Radiation Handbook* has carried on this tradition and tried to update its use. Instead of a historical development of this concept, reasons for present acceptance and reservations will be briefly described.

Cobalt 60 gamma cells and 1.5 to 2.5 MeV electron accelerators are common and easily used without the need for introducing cells into a vacuum system. The ^{60}Co gamma rays generate electrons with maximum energies less than 1 MeV and an average of ~600 keV. This radiation environment would then reproduce the space electron environment damage quite well. However, protons generate defect clusters and the gamma cell does not provide electrons with enough energy to generate more than a minute quantity of non-single displacement defects. The 1-MeV electrons will generate nearly an order of magnitude more divacancies than the gamma cell dose for the same generated electron fluence, and these defects are common in proton irradiated silicon. Use of higher energy electrons will increase the generation of divacancies, but will not provide cluster and higher-order defects necessary to better simulate proton damage. The 1-MeV electron is therefore a good choice for use as the basis for an equivalent fluence when proton generated damage from complex defects is not a major contribution to the total cell degradation.

The relative damage between 1-MeV electrons and other radiation has been determined in two ways (ref. 2). One way is a comparison of cells at the 25-percent degradation point. Cells are irradiated by normally incident protons or electrons of various energies; the fluences required to degrade the AMO I-V characteristics by 25 percent are compared to the fluence of 1 MeV normally incident electrons required to give the same degradation. The main advantages are the simplicity of generating the data and the comparison of data under illuminated conditions as expected in space. One disadvantage is that, in solar cells heavily damaged by a single type and energy of radiation, the nature of the damage is often too different from that generated by a space or 1-MeV electron environment to be realistically compared. Another problem is that the results compare normal incidence vs normal incidence irradiation, not the isotropic vs the normally incident irradiation of the 1-MeV equivalent fluence definition.

A second and mathematically satisfying method of specifying damage is the comparison of minority carrier diffusion lengths at different levels of normally incident monoenergetic irradiation. This latter method has a disadvantage in that the diffusion lengths are generally determined at low injection levels rather than under space illumination levels. This problem can be rectified, but the experiment is thereby made more complicated. In proton irradiated cells, the injection level effect can be as high as 2.5. This means that the equivalent fluence determined at

*JPL Publication 77-56.

low injection levels will be 2.5 x higher than that determined at higher levels (ref. 2).

Both methods of comparing damage are inaccurate when the damage from one or both sources is nonuniform (such as from low energy protons). Another source of error is the annealing or recovery of a portion of the radiation damage. Electron damage typically anneals over several weeks at room temperature, however, proton damage anneals after several days. In space, the damage anneals as it accrues; therefore, data must be compared after annealing is complete when establishing equivalent fluences or predicting degradation in space.

The technique of determining equivalent fluence compares the damage from isotropic monoenergetic radiation to the normally incident 1-MeV electrons (ref. 1). This method requires mathematical manipulation of normally incident radiation data, to calculate isotropic damage (refs. 3-5), or it requires actual isotropic irradiation. The mathematical manipulation is difficult, if no simplifying assumptions are made, and generally incorrect, if they are made. Only a few attempts have been made to actually irradiate solar cells from different angles to simulate an isotropic irradiation (refs. 3, 6, and 7). More efforts in this area have been completed [M. W. Walkden, results to be presented at the Photovoltaic Generators in Space Conference, Bath, England, May 1982] and are planned for 1982.

The mathematical conversion of normally incident radiation damage to isotropic radiation damage requires an accurate description both of the cell damage along the radiation path length and the geometry of the cell and its coverslide assembly. An assumption of equal damage probability along the path length makes calculations easy, but is not valid for protons with energies below ≈ 40 MeV. In addition to generating the wrong equivalent fluence with this assumption, an incorrect fluence dependence would be calculated for the equivalent fluence. This fluence dependence (fig. 1) is more correctly a diffusion length dependence and simply indicates the portion of a cell over which carriers are collected.

Actual experiments with simulated isotropic monoenergetic radiation will reduce many of the problems associated with the mathematical transformation from normal incidence to isotropic irradiation. Nevertheless, severe problems remain in silicon because the damage is nonuniform throughout the active region, and the solar cell electrical characteristics are generally calculated based on uniform diffusion lengths throughout the base of the cell. To correctly calculate the damage coefficients for nonuniform damage, the nature and profile of the damage must be known and included in the exact diode equations without the assumption of uniformity (ref. 8). The type and/or number of experiments must be increased to fulfill these requirements.

For an idea of the nonuniformities involved for proton damage in silicon, the displacement profiles for normally incident and isotropic irradiation can be examined. Nonpenetrating protons, normally incident on a silicon solar cell, will leave a region near the end-of-range which has a displacement density that may be orders of magnitude greater than in nearby parts of the cell (fig. 2a). An isotropic fluence of protons, with an energy spectrum representative of a solar proton flare environment at synchronous altitudes, would provide a factor of 5 to 10 difference in the displacement density from one side of the cell to the other (fig. 3). The narrow, heavily damaged region of the normally irradiated cell is somewhere within the cell bulk; its position depends upon the beam energy. The most heavily damaged region from the space environment is at the exposed surface; the damage gradient

depends upon the coverslide thickness. To compound this problem, four types of proton damage in silicon have been identified (ref. 4) and each has a different energy dependence. These different types of damage can also affect the cells differently, depending on the injection level and Fermi level within the cell. It is, therefore, exceedingly difficult to compare a monoenergetic normally incident proton beam (fig. 2a) to a monoenergetic isotropic proton beam (fig. 2b); however, this comparison is required to calculate an equivalent fluence from laboratory data. Ironically, the damage profiles from the space proton and electron environments are more similar than those produced by the laboratory sources. Therefore, an equivalent fluence is more accurately provided by comparing cell degradation in space with degradation by 1-MeV electrons in the laboratory. Unfortunately, this technique does not provide a good basis for a significantly different environment.

Two cases are mentioned as examples of using the equivalent fluence for predicting proton degradation of silicon solar arrays. The August 1972 solar flare was observed to degrade a number of solar panels on the INTELSAT IV series. Analysis of the degradation indicated much higher proton fluences than were then recorded by experiments on board ATS-1. When final corrections to the ATS-1 data were published a year later, the results were in excellent agreement with the numbers predicted by analysis (which involved use of the 1-MeV equivalent fluences) of the array degradation made one month after the event.

The second case is the solar cell experiment (ref. 9) on NTS-1, which followed an inclined orbit at 13,529 km. The observed cell degradation was much greater than that predicted from laboratory data and the equivalent fluence model.

What accounts for the apparent success of the equivalent fluence model in the first case and the gross failure in the second? A series of mistakes, made from necessity, canceled themselves out in the successful case, but showed up in the failed case. What mistakes can be identified in retrospect in the analysis and why did they occur?

The following are possible reasons:

- a. The only equivalent fluence values available were based on a simplistic model of radiation damage for 1 Ω -cm cells (but based on space data) from 1963 (ref. 1). The INTELSAT IV flight cells were 8-10 Ω -cm and fabricated nearly a decade later.
- b. The proton energy spectrum for synchronous altitudes was based on limited data obtained for solar proton flares during cycle 19. These data are overly severe in the low energy region (<10 MeV), thereby increasing the predicted damage.
- c. The third mistake, which compensated for the second, was in the modeling of the equivalent fluence which underestimated the equivalent fluence values for 1 Ω -cm cells. These mistakes canceled out in this case for synchronous orbit.

When the equivalent fluence model failed, conditions were different. The cells examined were ~ 2 Ω -cm; therefore, no significant uncertainty in the damage for different resistivities was encountered. The environment model did not have a bias in the most damaging proton energy range, which would increase the predicted damage. The equivalent fluence values were the same as those in the first case; but this time, there were no overestimated environment values to compensate for the incorrect model.

This incorrect model is still being used by many people because, for synchronous orbit, the results have not yet been proven false. Since the damage from protons for cells and coverslides >8 mils is less than that from electrons (even in the worst case), the errors in the model are not likely to be overly important. As cells, coverslides and back surface protection become thinner (<4 mils each), proton damage will begin to dominate. The environment is constantly being refined, and margins for error are constantly being reduced as spacecraft design is optimized. These trends indicate abandonment of the present equivalent fluence values and models unless someone is willing to pay for a corrected version. Many people who predict space degradation have in-house computer damage models and/or have an experimental base for their predictions. However, based on the above arguments, none of the published values or models for 1-MeV equivalent fluence values for single energy proton (and probably electron) damage to silicon appear to be correct (ref. 5).

GaAs VERSUS SILICON

It was pointed out in the previous section that for silicon, the concept of equivalent fluences, as presently defined, can vary from being a useful fiction to being a potentially dangerous trap. The situation may be different in GaAs for several reasons; some make it worse, some better.

The active region for GaAs cells is generally 5-10 μm compared to the >200 μm beginning-of-life active region of a silicon solar cell. This means the following:

- a. The influence on cell behavior from nonuniformities in normally incident proton damage observed in silicon is apparent at much lower energies in GaAs cells.
- b. The damage difference from front to back of the active region of a GaAs cell in the space environment is negligible; therefore, an assumption of uniform damage is reasonable for GaAs cells, but not for Si cells.
- c. The active region being limited to near the surface in GaAs cells implies that the average radiation within the active volume from the space environment is greater in a GaAs cell than in a silicon cell, even if the coverslide protection is identical.

The damage mechanisms for GaAs and Si cells are different:

- a. The voltage and fill factor in GaAs cells are generally dominated by junction recombination ($n = 2$) (ref. 10), compared to the bulk recombination dominance in silicon cells ($n = 1$).
- b. For uniform radiation damage, this dominance by the junction recombination in GaAs cells does not change (ref. 11).
- c. The nature of damage in silicon has been found to be fluence dependent (ref. 12); the damage in GaAs has been found to be fluence dependent (ref. 11) and dose rate dependent [Li et al., and Loo et al., to be presented at the 16th PVSC, San Diego, California, September 1982).

d. Present GaAs solar cells generally have a different spectral response degradation under irradiation than silicon solar cells, which show only degradation from the red end. The fact that the GaAs cells degrade throughout the full spectral range [the extent in each region depending upon the junction depth (ref. 11)], further complicates the prediction of space degradation for these cells.

After a survey of the differences between GaAs and silicon solar cells, it seems that an equivalent fluence would be easier to define and properly use in GaAs than in silicon. The critical factor would appear to be the relative uniformity of the space radiation damage throughout the active region of the GaAs cell. It may well be that 1-MeV electrons are not the preferred basis for the equivalent fluence. The 1-MeV protons at low fluence might be a better choice, although the electrons at high flux might provide an adequate simulation of proton damage.

CONCLUSIONS

The 1-MeV electron equivalent fluence concept has been often used, and misused, in place of an understanding of space radiation effects in silicon solar cells. A large quantity of laboratory data is being generated on radiation characteristics of GaAs solar cells, but until more space data become available and integrated with the laboratory data, an equivalent fluence concept is premature. Unless these tests are correctly interpreted (and hopefully correctly conceived), the equivalent fluence values determined for GaAs will be an unmarked scale, only useful to compare observed space data with some arbitrary laboratory radiation type and energy. In answer to the questions posed in the introduction, the 1-MeV electron equivalent fluence concept has been useful in silicon space cells despite its shortcomings; and, at least for many environments, a convenient and acceptable radiation type can probably be found to provide equivalent fluences for GaAs solar cells in space.

REFERENCES

1. Brown, W. L., Gabbe, J. D., and Rosenzweig, W., "Results of the Telstar Radiation Experiments," The Bell System Technical Journal, July 1963, pp. 1505-1559.
2. Meulenberg, A., and Treble, F. C., "Damage in Silicon Solar Cells from 2 to 155 MeV Protons," 10th IEEE Photovoltaic Specialists Conference, November 13-15, Palo Alto, California, 1973, Proc., pp. 359-365.
3. Bernard, J., Mottet, S., and Sarrant, D., "Protons Isotropic Irradiation of Solar Cells," 12th IEEE Photovoltaic Specialist Conference, Baton Rouge, Louisiana, November 15-18, 1976, Proc., pp. 216-223.
4. Meulenberg, A., "Proton Damage to Silicon from Laboratory and Space Sources," 12th IEEE Photovoltaic Specialist Conference, Baton Rouge, Louisiana, November 15-18, 1976, Proc., pp. 216-223.
5. Wilkinson, M. C., and Horne, W. E., "Limitations of the 1 MeV Equivalent Fluence Method in the Evaluation of Space Radiation Degradation," 11th IEEE Photovoltaic Specialists Conference, Scottsdale, Arizona, May 6-8, 1975, Proc., pp. 224-228.
6. Goldhammer, L. J., "Irradiation of Solar Cell Candidates for the ATS-F Solar Cell Flight Experiment," 9th IEEE Photovoltaic Specialists Conference, Silver Spring, Maryland, May 2-4, 1972, Proc., pp. 316-328.
7. Kalma, A. H., and Fischer, C. J., " 4π Space Radiation of Solar Cells," IEEE Transactions on Nuclear Science, Vol. NS-23, No. 6, December 1976, pp. 1789-1794.
8. Arndt, R. A., and Westerlund, L. H., "A Model for Nonpenetrating Proton Damage to Silicon Solar Cells," COMSAT Technical Review, Fall 1971, Vol. 1, No. 1, pp. 117-137.
9. Statler, R. L., Walker, D. H., and Lambert, R. J., "The NTS-1 Solar Cell Experiment after Two Years in Orbit," 12th IEEE Photovoltaic Specialist Conference, Baton Rouge, Louisiana, November 15-18, 1976, Proc., pp. 208-215.
10. Hovel, H. J., "The Effect of Depletion Region Recombination Currents on the Efficiencies of Si and GaAs Solar Cells," 10th IEEE Photovoltaic Specialists Conference, Palo Alto, California, November 13-15, 1973, Proc., pp. 34-39.
11. Loo, R., Kamath, G. S., and Knechtly, R. C., "Radiation Damage in GaAs Solar Cells," 14th IEEE Photovoltaic Specialists Conference, San Diego, California, January 7-10, 1980, Proc., pp. 1090-1097.
12. Weinburg, I., and Swartz, L. K., "Reduced Annealing Temperatures in Silicon Solar Cells," 15th IEEE Photovoltaic Specialists Conference, Kissimee, Florida, May 12-15, 1981, Proc., pp. 490-494.

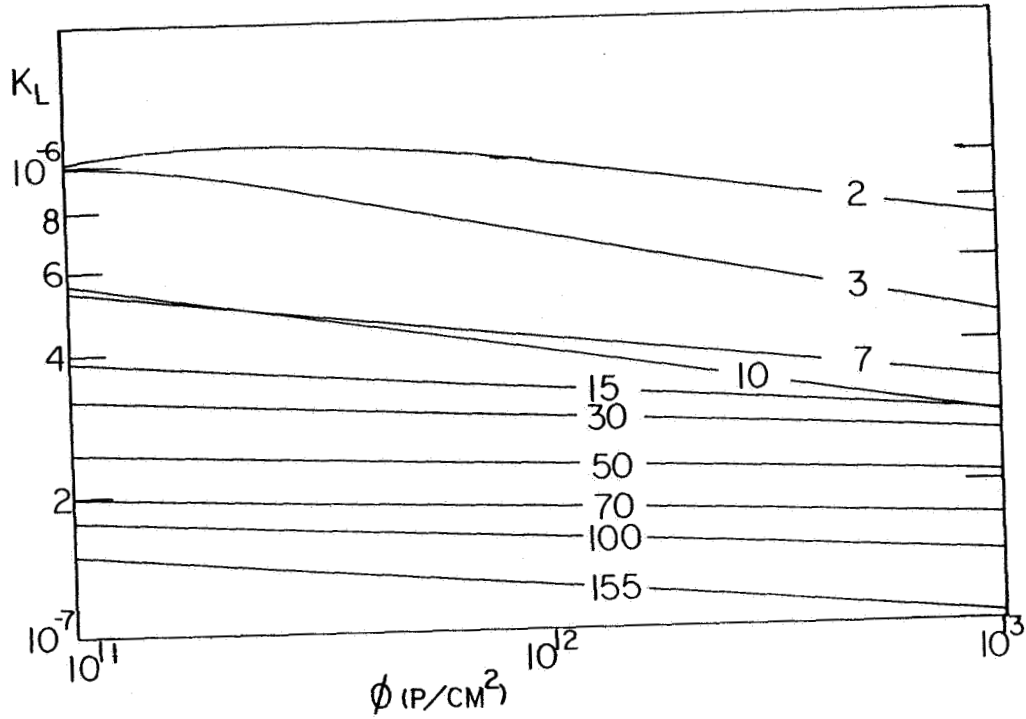


Figure 1. Diffusion Length Damage Coefficients vs Proton Fluence for Bare Cell Sets Measured at Low Injection Levels. The Curves are Labeled by the Incident Proton Energy in MeV.

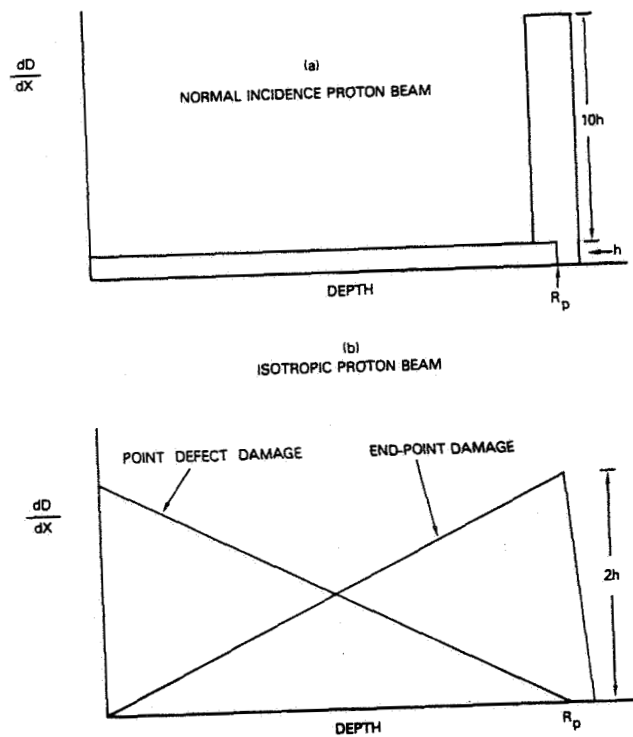


Figure 2. Damage Depth Profiles for Normally and Isotropically Incident Protons. The Proton End-of-Range is Denoted by R_p .

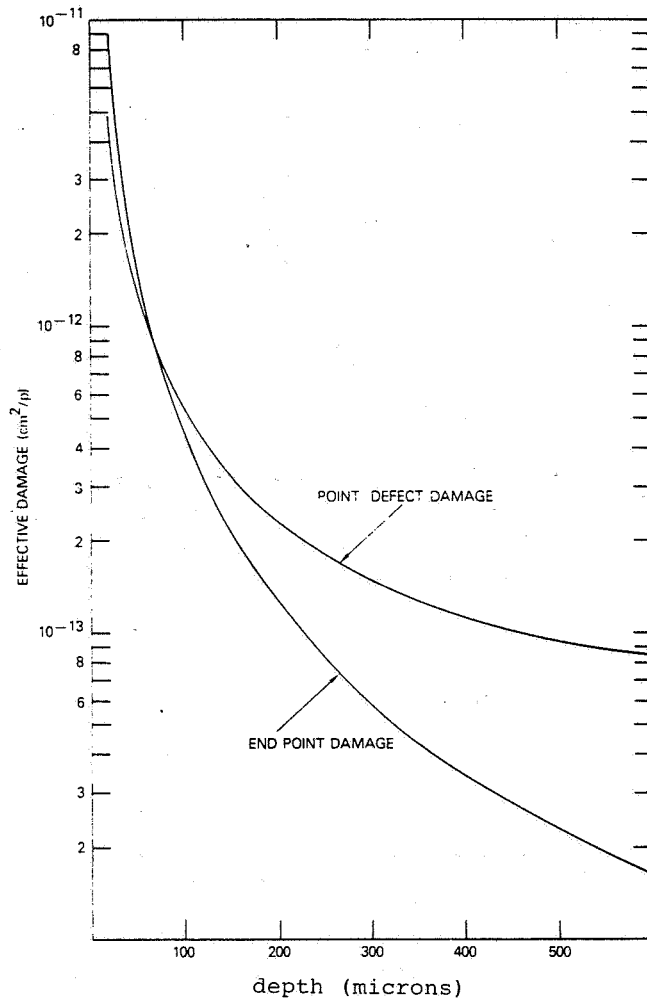


Figure 3. Components of Damage (Low Injection Level) from Solar Flare Protons at Synchronous Altitudes vs Depth into Silicon. The Relative Magnitude of the Components is Not Yet Determined (see text)

GROWN-IN DEFECTS AND DEFECTS PRODUCED BY 1-MeV ELECTRON IRRADIATION IN $\text{Al}_{0.3}\text{Ga}_{0.7}\text{As}$ P-N JUNCTION SOLAR CELLS*

Sheng S. Li, K.W. Teng, and D.W. Schoenfeld
University of Florida
Gainesville, Florida

W.P. Rahilly
Air Force Aeropropulsion Laboratory
Wright-Patterson Air Force Base, Ohio

EXTENDED ABSTRACT

Studies of grown-in defects and defects produced by the one-MeV electron irradiation in $\text{Al}_{0.3}\text{Ga}_{0.7}\text{As}$ p-n junction solar cells fabricated by liquid phase epitaxial (LPE) technique have been made for the unirradiated and one-MeV electron irradiated (with electron fluence of 10^{14} , 10^{15} , and 10^{16} e/cm²) samples, using DLTS and C-V methods. Defect and recombination parameters such as energy level, defect density, carrier capture cross sections and lifetimes were determined for various growth, annealing, and irradiation conditions. The results obtained from this study are discussed as follows: $\text{Al}_x\text{Ga}_{1-x}\text{As}$ p-n junction solar cells (area 1 mm²) grown by LPE technique were fabricated by S. Bedair at the Research Triangle Institute in conjunction with their $\text{Al}_x\text{Ga}_{1-x}\text{As}$ cascade p-n junction solar cell program supported by the Air Force Aeropropulsion Lab. Fig. 1 shows the four different solar cell structures which have been fabricated for our DLTS, C-V, and I-V measurements. Fig. 1 (b) is the cell's structure used in our study of deep-level defects produced by the one-MeV electron irradiation. This structure is identical to the top cell of the cascade solar cell, reported by Bedair et al^[1]. Fig. 2 shows the DLTS scans of the electron trap ($E_c-0.31$ eV) for three $\text{Al}_x\text{Ga}_{1-x}\text{As}$ p-n junction solar cells shown in Fig. 1 (a) through 1 (c). From our DLTS data, it is found that the Ge-doped $\text{Al}_x\text{Ga}_{1-x}\text{As}$ p-n junction solar cells usually have lower defect density than that of the Be-diffused p-n junction solar cells shown in Fig. 1 (a) and Fig. 1 (b). This is also the case for the hole trap shown in Fig. 3, where one hole trap with energy of $E_v+0.18$ eV was detected in both the Ge-doped and Be-diffused $\text{Al}_{0.3}\text{Ga}_{0.7}\text{As}$ p-n junction cells. Another interesting study is to investigate the effect of low temperature thermal annealing on the defect density in the $\text{Al}_{0.3}\text{Ga}_{0.7}\text{As}$ solar cell. Fig. 4 shows the DLTS scans of electron trap vs. annealing time (2 and 5 hrs. at 300°C). The results showed that the electron trap density was indeed decreased with increasing annealing time. Table 1 summarizes the defect parameters deduced from the DLTS and C-V data for the unirradiated $\text{Al}_{0.3}\text{Ga}_{0.7}\text{As}$ and GaAs solar cells shown in Fig. 1 for different annealing times. Table 2 summarizes the defect parameters for the unannealed and annealed $\text{Al}_{0.3}\text{Ga}_{0.7}\text{As}$ and GaAs solar cells shown in Fig. 4. To study the effect of one-MeV electron irradiation on the defects in the $\text{Al}_x\text{Ga}_{1-x}\text{As}$ p-n junction solar cells grown by the LPE technique, we performed (done at the Air Force Aeronautical Lab.) the one-MeV electron irradiation on the $\text{Al}_{0.3}\text{Ga}_{0.7}\text{As}$ p-n junction solar cells shown in Fig. 1 (b) for electron fluence of 10^{14} , 10^{15} , and 10^{16} e/cm². The results are shown in Fig. 5 and Fig. 6. Fig. 5 shows the DLTS scan of electron traps for the one-MeV electron irradiated $\text{Al}_{0.3}\text{Ga}_{0.7}\text{As}$ solar cells as a function of electron fluence. Note that three electron traps with energies of $E_c-0.12$, 0.20 , and 0.31 eV were observed in the one-MeV electron irradiated $\text{Al}_{0.3}\text{Ga}_{0.7}\text{As}$ cells; the dominant electron trap was due to $E_c-0.31$ eV. The density of this $E_c-0.31$ eV trap was found to increase with increasing electron fluence, while the other two shallower

electron traps showed less dependence on the electron fluence. In contrast to the GaAs p-n junction cells, no mid-gap deep-level traps were detected in the $\text{Al}_{0.3}\text{Ga}_{0.7}\text{As}$ p-n junction solar cells. Fig. 6 shows the DLTS scans of hole trap for the same cells shown in Fig. 5; only one hole trap with energy of $E_V+0.18$ eV was observed in these cells, and the density was found to vary from 2.75×10^{15} (for $\phi_e = 10^{14}$ e/cm²) to 5.93×10^{15} cm⁻³ (at $\phi_e = 10^{16}$ e/cm²). Again, no mid-gap hole trap or new hole trap was observed in these electron-irradiated $\text{Al}_x\text{Ga}_{1-x}\text{As}$ p-n junction solar cells. Table 3 summarizes the defect parameters deduced from the DLTS data for the electron traps shown in Fig. 5. From the results of this study, it is concluded that: (1) for the unirradiated $\text{Al}_{0.3}\text{Ga}_{0.7}\text{As}$ p-n junction cells, the dominant electron trap is due to $E_C-0.31$ eV and the dominant hole trap is due to $E_V+0.18$ eV; thermal annealing will effectively reduce the density of both electron and hole traps, (2) Ge-doped $\text{Al}_{0.3}\text{Ga}_{0.7}\text{As}$ p-n junction cells contain lower defect density than the Be-diffused cells, (3) one-MeV electron irradiation in the $\text{Al}_{0.3}\text{Ga}_{0.7}\text{As}$ p-n junction cells produces only one hole trap (i.e., $E_V+0.18$ eV) and three electron traps ($E_C-0.12$, 0.20 , and 0.31 eV); no mid-gap deep level defects were observed, (4) defect density does increase with increasing electron fluence, and (5) the DLTS data showed that $\text{Al}_{0.3}\text{Ga}_{0.7}\text{As}$ p-n junction solar cells may have more radiation tolerance than that of GaAs p-n junction solar cells reported in our previous paper[2].

*Research supported by Air Force Aeropropulsion Lab., AFWAL, subcontract through Universal Energy System Inc., task 6.

- (1) S. M. Bedair, M. Lamorte, and J. Hauser, Appl. Phys. Lett., vol. 34, p. 38 (1979).
- (2) In the same proceeding of this workshop.

Table 1. Measured and Calculated Defect Parameters in n-Al_{0.3}Ga_{0.7}As and n-GaAs LPE Layers.

Sample No.	Trap Density (cm ⁻³)		Energy Level (eV)		Capture Cross Section (cm ²)		Carrier Lifetime (μs)		Physical Origin	
	Electron	Hole	Electron	Hole	σ _n	σ _p	τ _n	τ _p	Electron	Hole
Y-015B	6.63x10 ¹²	6x10 ¹²	E _C -0.31	E _V +0.18	3.37x10 ⁻¹³	-	0.015	-	V _{Ga}	-
Y-015C	5.99x10 ¹¹	-	E _C -0.31	-	4.23x10 ⁻¹³	-	0.13	-	V _{Ga}	-
L-119D	9.34x10 ¹⁰	-	E _C -0.31	E _V +0.18	4.49x10 ⁻¹³	-	0.79	-	V _{Ga}	-
L-138D	7.1x10 ¹⁰	5.46x10 ¹⁰	E _C -0.42	E _V +0.40	1.29x10 ⁻¹²	-	0.35	-	-	A
	1.71x10 ¹¹	4.1x10 ¹¹	E _C -0.60	E _V +0.71	1.25x10 ⁻¹²	-	0.23	-	-	B

Table 2. Defect Parameters for the Unannealed and the Annealed Al_{0.3}Ga_{0.7}As and GaAs LPE Layers.

Sample No.	Annealing Condition	Electron Trap		Hole Trap		N _B (cm ⁻³)
		E _C -E _t (eV)	N _t (cm ⁻³)	E _V +E _t (eV)	N _t (cm ⁻³)	
Y-015C	Unannealed	0.31	6.0x10 ¹¹	0.18	<10 ¹⁰	2.6x10 ¹⁶
Y-015C	300°C, 2 hrs	0.31	4.4x10 ¹¹	0.18	<10 ¹⁰	5.7x10 ¹⁶
Y-015C	300°C, 5 hrs	0.31	3.6x10 ¹¹	0.18	<10 ¹⁰	3.5x10 ¹⁶
L-138D	Unannealed	0.42	7.1x10 ¹¹	0.40	5.5x10 ¹⁰	2.8x10 ¹⁵
		0.60	1.7x10 ¹¹	0.71	4.1x10 ¹¹	3.6x10 ¹⁵
L-138D	300°C, 2 hrs	0.42	1.2x10 ¹⁰	0.40	2.7x10 ¹⁰	2.1x10 ¹⁵
		0.60	4.7x10 ¹⁰	0.71	2.4x10 ¹⁰	2.4x10 ¹⁵
L-138D	300°C, 5 hrs	0.42	1.0x10 ⁹	0.40	1.3x10 ¹⁰	2.5x10 ¹⁵
		0.60	6.6x10 ⁹	0.71	1.5x10 ¹⁰	2.4x10 ¹⁵

Table 3. Electron Traps in One-MeV Electron Irradiated Al_{0.3}Ga_{0.7}As P-N Junction Solar Cells

Electron Fluence (e/cm ²)	N _B (cm ⁻³)	E _T (eV)	N _T (cm ⁻³)	σ _n (cm ²)	τ _n (ns)
0	1.14x10 ¹⁷	E _C -0.12	1.6x10 ¹⁴	-	-
		E _C -0.20	2.2x10 ¹⁴	2.63x10 ⁻¹⁵	172.8
		E _C -0.31	1.04x10 ¹⁴	1.64x10 ⁻¹³	5.86
10 ¹⁴	1.03x10 ¹⁷	E _C -0.12	2.1x10 ¹⁵	-	-
		E _C -0.20	4.3x10 ¹⁵	2.63x10 ⁻¹⁵	8.84
		E _C -0.31	7.8x10 ¹⁵	1.64x10 ⁻¹³	0.078
10 ¹⁵	1.26x10 ¹⁷	E _C -0.12	1.9x10 ¹⁵	-	-
		E _C -0.20	6.5x10 ¹⁵	2.63x10 ⁻¹⁵	5.85
		E _C -0.31	1.11x10 ¹⁶	1.64x10 ⁻¹³	0.055
10 ¹⁶	1.16x10 ¹⁷	E _C -0.12	2.2x10 ¹⁵	-	-
		E _C -0.20	3.9x10 ¹⁵	2.63x10 ⁻¹⁵	9.75
		E _C -0.31	1.8x10 ¹⁶	1.64x10 ⁻¹³	0.034

p ⁺ (Be)	Al _{0.3} Ga _{0.7} As
n	Al _{0.3} Ga _{0.7} As (UNDOPED)
n ⁺	GaAs (SUBSTRATE)

I.(a) Y-015C

p ⁺ (Be)	Al _{0.9} Ga _{0.1} As
n	Al _{0.3} Ga _{0.7} As (UNDOPED)
n ⁺	GaAs (SUBSTRATE)

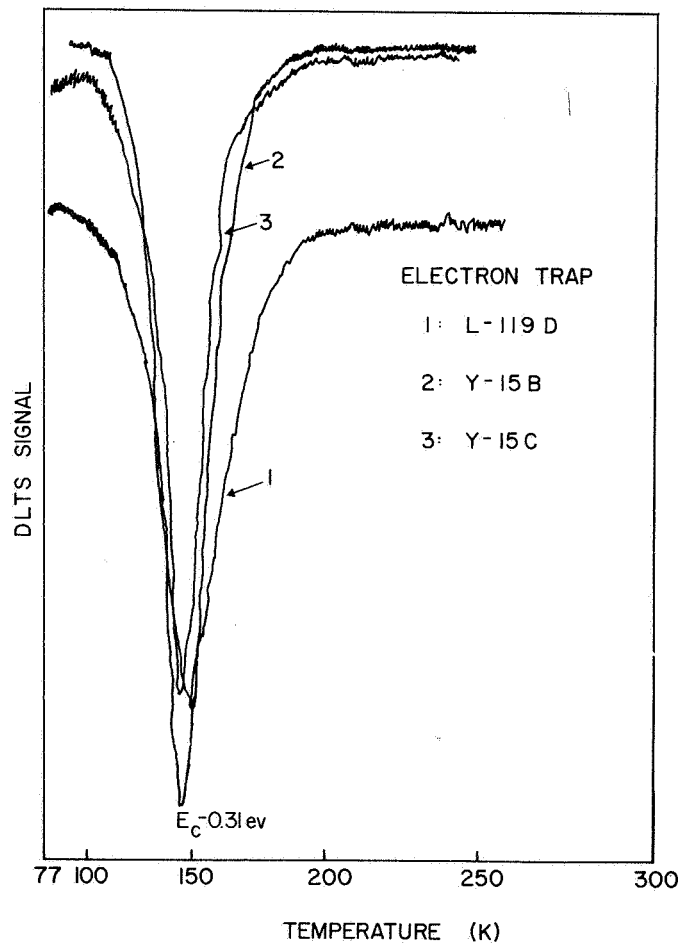
I.(b) Y-015B

p ⁺ (Ge)	Al _{0.3} Ga _{0.7} As
n	Al _{0.3} Ga _{0.7} As
n ⁺	GaAs

I.(c) L-119D

p ⁺ (Be)	Al _{0.3} Ga _{0.7} As
n	GaAs
n ⁺	GaAs

I.(d) L-138D

Fig. 1 Structure of Al_xGa_{1-x}As p-n junction solar cells for DLTS and C-V study.Fig.2 DLTS scans of electron traps in Be-diffused and Ge-doped Al_{0.3}Ga_{0.7}As p-n junction solar cells grown by LPE technique.

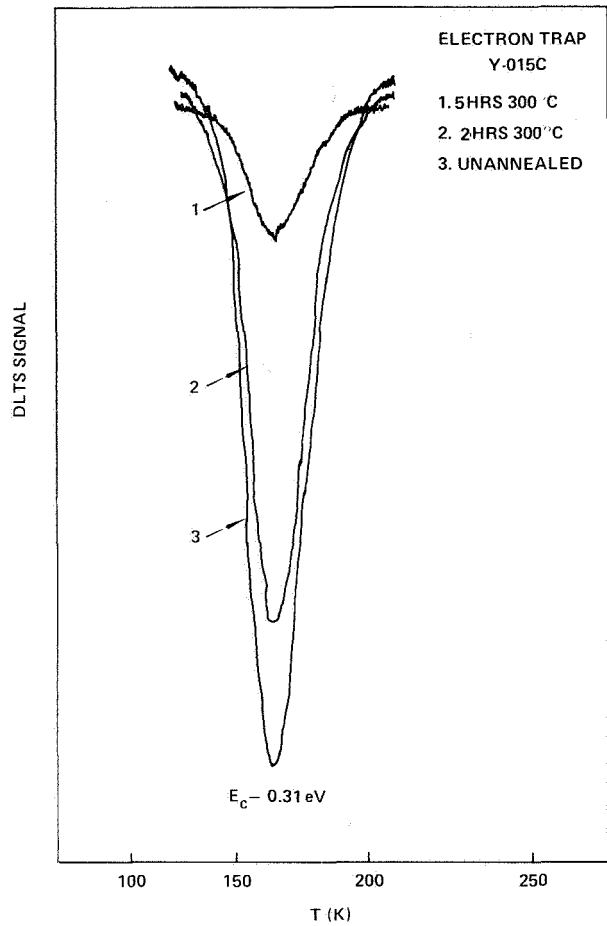


Fig. 3 DLTS scans of electron traps in $\text{Al}_{0.3}\text{Ga}_{0.7}\text{As}$ p-n junction solar cells annealed at 300°C for 0, 2, and 5 hours.

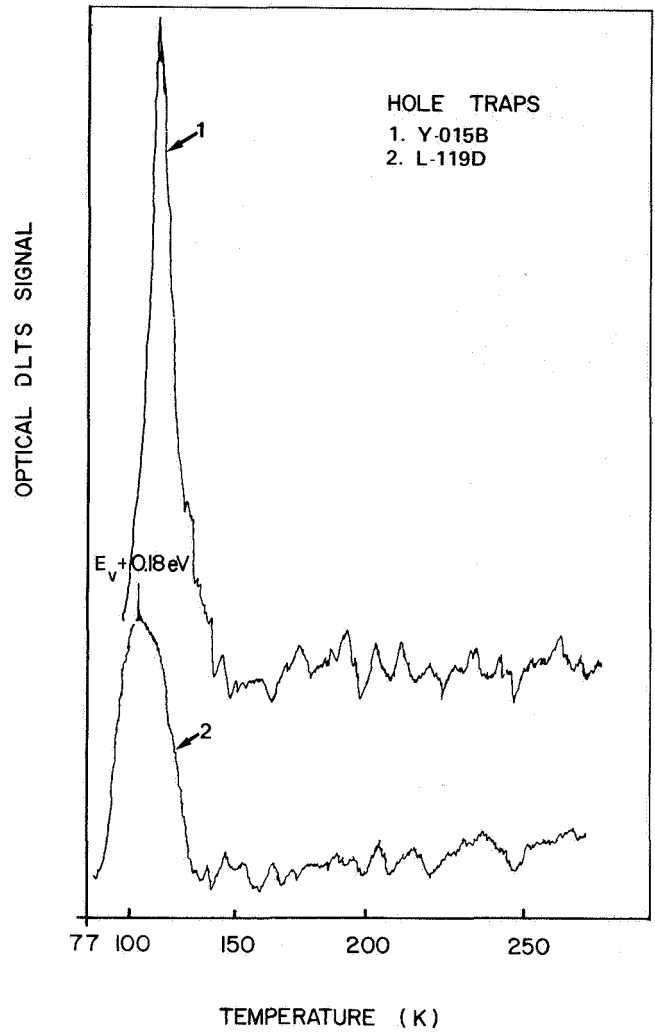


Fig. 4 Optical DLTS scans of hole trap in Be- and Ge-doped $\text{Al}_{0.3}\text{Ga}_{0.7}\text{As}$ p-n junction solar cells.

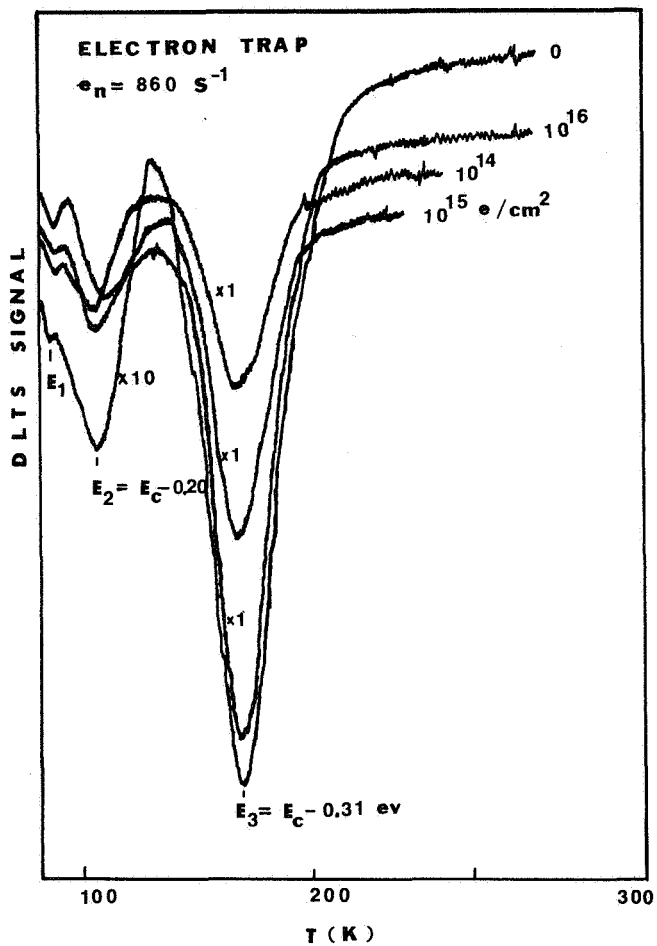


Fig.5 DLTS scans of electron traps in one-Mev electron irradiated $\text{Al}_{0.3}\text{Ga}_{0.7}\text{As}$ p-n junction solar cells for three electron fluences.

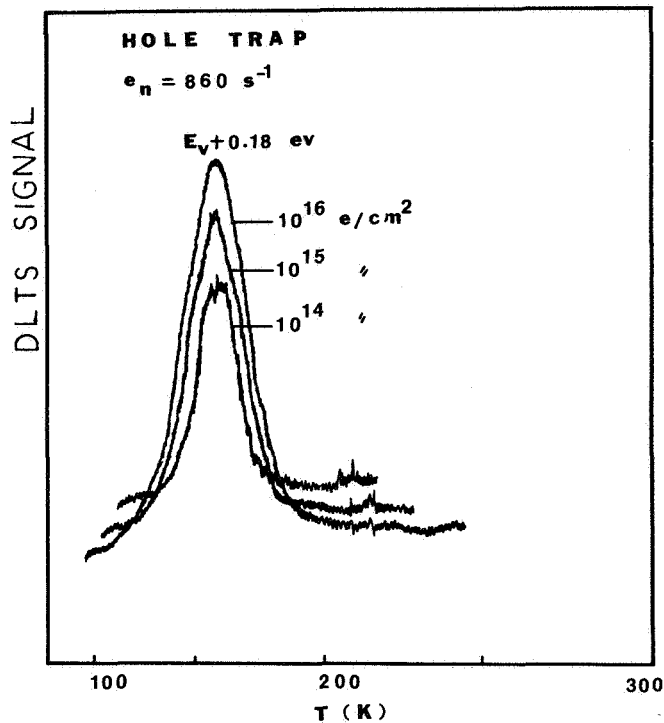


Fig. 6 DLTS scans of hole trap in one-Mev electron irradiated $\text{Al}_{0.3}\text{Ga}_{0.7}\text{As}$ p-n junction solar cells shown in Fig. 5.

PROGRESS IN DEVELOPING HIGH PERFORMANCE SOLAR BLANKETS AND ARRAYS*

John Scott-Monck
Jet Propulsion Laboratory
California Institute of Technology
Pasadena, California

INTRODUCTION

The development of high efficiency ($> 13\%$ AMO), ultrathin ($50 \mu\text{m}$) silicon solar cells offers both opportunity and challenge. It is possible to consider 400 W/kg blanket designs by using this cell in conjunction with flexible substrates, ultrathin covers and welded interconnects. By designing array structure which is mechanically and dynamically compatible with very low mass blankets, solar arrays with a specific power approaching 200 W/kg are achievable. Further improvements in blanket performance (higher power and lower mass per unit area), which could come from the implementation of higher efficiency cells operating at lower temperatures (silicon or GaAs), and the use of encapsulants, would result in the development of 300 W/kg solar arrays. There is a trend toward higher power.

There is a trend toward higher power and longer operating life in nearly every future mission being planned, whether for NASA, defense or commercial application. It is also becoming apparent that the Shuttle launch capability will not grow as rapidly as had been originally anticipated. Thus there is a need for the development of low mass solar arrays.

APPROACH

Figure 1 is a plot of beginning of life (BOL) array specific power as a function of array structure mass per unit area. It is possible to develop an optimum strategy for providing a high performance array by analyzing the relationship between array performance and the figures of merit for the blanket and structure components. It is apparent that increasing the specific power of the array blanket will provide much greater initial improvements in array specific power.

However as the blanket specific power increases (lower mass per unit area) for a fixed structure mass, the dynamics of the array begin to change. Thus it becomes necessary to modify the structure to bring the array into conformance with such requirements as stiffness and natural frequency. Even excluding array dynamics from consideration, lowering the structure mass becomes an attractive and even necessary option if array specific power is to exceed 150 W/kg BOL. Therefore once a relatively high performance blanket ($> 250 \text{ W/kg}$) is achieved, efforts to develop a low mass structure become the more effective method of increasing the array's specific power.

* The research described in this paper presents the results of one phase of research carried out by the Jet Propulsion Laboratory, California Institute of Technology, under contract with the National Aeronautics and Space Administration.

BLANKET DEVELOPMENT

Simple calculations show that the present SEP blanket (105 W/kg), which represents current state of the art, would be improved to nearly 150 W/kg by replacing the baseline cells and covers with ultrathin versions. Thus there is a strong incentive to develop a cost effective and scaleable approach to fabricating ultrathin solar cell blankets. The prospect that ultrathin GaAs solar cells will be available within this decade is another strong argument for pursuing this effort.

Manufacturing Methods

NASA-JPL is presently sponsoring three contracts aimed at devising a method for assembling ultrathin components. One effort seeks to retain as many conventional manufacturing processes as possible and concentrate on modifying only those that are proven to be incompatible. The rationale for this philosophy is that based on current projections for array demand and the fact that ultrathin cell blankets will not capture the near-term market, the expense to recapitalize for this new technology cannot be justified.

Substantial progress in producing ultrathin cell modules has been made using this approach, and a prototype module has been subjected to over 6000 thermal cycles (+80 to -80°C) without any significant electrical or mechanical degradation. The baseline process uses a kapton substrate, conventional DC 93-500 adhesive for substrate and cover bonding, welded silver-plated invar interconnects, 62 µm cells and 50 µm glass covers (ref. 1).

A second effort seeks to reduce the difficulty in handling these parts by investigating the use of automated machinery to interconnect the cell strings. In this approach ultrasonic welding of silver mesh is employed. Results to date indicate that weld joints with acceptable pull strength (200 gms in shear) and less than one percent electrical degradation can be achieved with this technique. Methods for bonding covers have also been developed.

A third parallel activity has developed special tooling, based on concepts proven effective for terrestrial module fabrication, to minimize the amount of handling operations the ultrathin cells and covers receive during assembly. The initial trial run using this cell-interconnect-registration tool (CIRT) showed a dramatic improvement in yield as compared to conventional handling processes. Further work is now underway to make improvements in the tool design. Although parallel-gap resistance welded interconnects were used for the proof test, a substantial effort will be made in this phase to investigate the possibility of laser welding as a joining method.

Ultrathin Solar Cells

The NASA-JPL pilot line program demonstrated that ultrathin silicon solar cells could be produced in quantity (ref. 2). Cells from this program, along with versions supplied by two space qualified sources, to a specification, are being used for the blanket development work. The newer versions incorporate such technology improvements as back surface reflectors, multiple antireflection coatings and an alternate back surface field technique. This recent procurement resulted in the delivery of cells with an average 28°C AMO efficiency of 12.5 percent, some cells exceeding 13 percent.

JPL also procured an improved version of the ultrathin cell from the original supplier. The device employs a gridded back contact to reduce cell mass, and

cells exceeding 13 percent AMO were provided (ref. 3). This second generation ultrathin cell is an important milestone for achieving even higher levels of blanket specific power. It offers the potential of reducing cell bowing, since the amount of contact metal is the same on both sides, reducing cell mass and lowering cell operating temperature because most of the back surface is free of metal.

It is expected that further modifications will be made to the ultrathin solar cell to improve operating efficiency and handling properties. The feedback received from the blanket development program will be used to write a specification for an optimized ultrathin solar cell compatible with whatever blanket fabrication process is developed.

Ultrathin Covers

Many mission orbits require only minimal shielding, but until the development of the ultrathin cell, the thinnest covers available were $\sim 100 \mu\text{m}$. Prototype ultrathin blankets used 50 to 75 μm microsheet glass which would not be acceptable for space use. Currently the blanket development programs are using 50 μm textured fused silica, but these covers do not have uv-rejection filters. Another alternative is to use ceria-doped microsheet. Sample quantities of 50 μm material have been obtained and will be used in the program.

Perhaps the most exciting candidate now being evaluated is a transparent polyimide polymer which was originally developed for commercial applications. Preliminary testing, which has been very encouraging, has been performed. Details of this evaluation are provided in another paper published in this volume (ref. 4).

A space qualified encapsulant is necessary in order to achieve a blanket specific power approaching 500 W/kg. By using an encapsulant, even thinner protective layers ($< 25 \mu\text{m}$) could be considered, and no adhesive would be necessary, thus saving additional mass. Encapsulation would also provide major benefits for blanket fabrication with respect to labor cost and yield.

Substrate

The baseline blanket design employs very thin (25 μm) kapton sheets. This may not be practical for two reasons. Thin, flexible substrates offer very little protection from the effects of the omnidirectional space radiation environment. For low earth orbital applications this is of little consequence, but for high earth or geosynchronous applications, where radiation levels are at least 6×10^{13} equivalent 1 MeV electrons/cm² annually, a thicker substrate may be necessary to protect the cells from backside radiation degradation. Trade-offs to determine the optimum substrate thickness for end of life array specific power will need to be done. Work is planned to determine the effects of space radiation on cells that have relatively little backside protection.

A second concern which has to do with transferring extremely thin substrates which have cell assembly (cell plus cover) circuits bonded to them. Although it is relatively easy to fabricate modules with thin substrates, it is much more difficult to join these modules into panels and ultimately integrate the panels into an array. Thus the present design will probably employ thicker (50 μm) composite, laminated or fiber reinforced substrates.

Adhesive

Processes to provide extremely thin ($\leq 25 \mu\text{m}$) adhesive bondlines for coverglass and circuit bonding have not been reduced to practice. Presently 50 μm bondlines are a realistic estimate for the blanket design. In the case of the coverglass, the implementation of an encapsulant such as the polyimide polymer now being evaluated, would eliminate adhesive. For substrate-circuit attachment, it may be necessary to consider "spot" bonding, wherein only certain areas of each cell are bonded to the substrate. This may cause the cell to run hotter, thus reducing power output. Therefore at some point it may be necessary to test this concept in order to obtain sufficient data to allow a trade-off to be made to determine the best approach to optimize end-of-life array specific power.

Interconnects

It is assumed that welding will be used for interconnecting. Currently three interconnect materials are being employed; silver, silver plated molybdenum and silver plated invar. The present practical lower limit of thickness for the base material is approximately 25 μm and in the latter two cases the amount of silver necessary to assure proper interconnect conductivity and weld suitability is in the order of 20 μm .

Ideally it would be better to either reduce the thickness of the interconnect base material or consider a low mass, highly conducting material such as aluminum. The prospect for securing thinner interconnects is not good unless funding is provided to develop the necessary etching and rolling technology. Based on the current situation, it is more likely that attempting to develop lower mass interconnect materials is the better approach.

However the mass advantages may be compromised by the substantial mismatch in thermal coefficient of expansion between the solar cell (silicon or GaAs) and an interconnect such as aluminum. Work will be undertaken in the future to investigate the possibility of using aluminum as an interconnect material, once the main problems associated with fabricating a space qualified ultrathin solar cell blanket are resolved.

Harness

In many analyses of blanket specific power, the mass of the harness or bus is not taken into consideration. Realistically the bus must be taken into account. The present harness material is copper and because of the low operating voltage of the array (30-40 volts), the harness mass is roughly 0.20 kg/m^2 for the current baseline design. As the mass of the other blanket components is reduced, the impact of the harness will act to constrain blanket performance. By increasing the operating voltage of the array to perhaps 120 volts and substituting aluminum for copper, the mass of the harness could be reduced to approximately .025 kg/m^2 .

STRUCTURE DEVELOPMENT

NASA-JPL sponsored an effort to develop array structure design concepts that would have low mass and be dynamically compatible with very low mass blankets (0.25 to 0.65 kg/m^2). Three concepts were evaluated; the Astromast used for the SEP array, a modified version of the extendible support structure used on the Seasat spacecraft, and the stacking triangular articulated compact beam (STACBEAM), which was finally chosen for further development.

The STACBEAM design has many attractive features including low mass, sequential deployment, high stiffness and the capacity for growth (ref. 5). Preliminary design work has begun and a working model of the beam, consisting of 8 bays or segments, has been built using graphite-epoxy. A breadboard model of the deployment mechanism has been constructed, and in the next phase a more accurate or "high fidelity" version will be constructed. Based on the progress to date, it appears that the STACBEAM will provide the low mass array structure that is necessary to achieve solar arrays with specific power in excess of 150 W/kg.

DISCUSSION

Table 1 represents the best estimate of the current status of high performance solar cell blankets and arrays. It is based on the present progress of the various NASA-JPL programs supporting this effort. In order to present the most realistic assessment, contingency factors have been applied to the cell performance at array operating temperature. This approach has borrowed heavily from the SEP array development program. For example, the cell output has been derated to account for fabrication losses, cell mismatch, diode losses, array packing factor and temperature. Although substantial progress has been made in the development of the STACBEAM array structure, enough work remains so that it is not realistic to state that it is ready at present for space flight operation. Whether the present SEP array structure would prove compatible with current blanket mass per unit area is still not settled, but in an optimistic analysis, it is assumed suitable.

Table 2 reflects the potential of the NASA-JPL programs now being pursued. As stated previously, a number of issues such as the thermal penalty associated with adhesive "spot" bonding and the practicality of aluminum interconnects remain to be resolved. Of even greater importance is the question of silicon solar cell efficiency at array operating temperature and the use of an encapsulation approach to replace conventional coverglass. It is expected that these will be major factors in determining the ultimate specific power of silicon solar cell blankets. A higher degree of confidence is attached to the efforts underway to develop a new, low mass array structure.

The utility of employing GaAs solar cells has not been addressed because sufficient information on the technology is still unavailable. However comments must address certain aspects of thin GaAs cells. Recently there have been published reports concerning the potential of ultrathin ($\leq 50 \mu\text{m}$) GaAs devices (ref. 6, 7 and 8). Much work remains before any of this technology can be realistically considered for space applications. If it were optimistically assumed that $10 \mu\text{m}$ GaAs solar cells with an AMO conversion efficiency, at operating temperature, approaching 18 percent could be achieved in a manner lending itself to a cost effective and practical approach to incorporation into space solar arrays, then space solar arrays with specific power at beginning-of-life exceeding 300 W/kg could be forecasted.

CONCLUSIONS

Encouraging progress towards achieving solar cell arrays capable of 300 W/kg (BOL) specific power has been made. Present technology involving advanced ultrathin silicon solar cells, welding and flexible substrates indicate that a solar array could be built, using current technology, that would be sixty percent better than the present state-of-the-art. Significant improvements will occur in the near future, provided the current programs continue. It is not unrealistic to consider attaining 300 W/kg (BOL) silicon solar array technology based on current progress.

REFERENCES

1. Mesch, H. G. and Rockey, D. E., "High Temperature, Low Mass Solar Blanket Development", 14th IECEC, Boston, August 1979, pp. 1264-1269.
2. Storti, G., Wohlgemuth, J. and Wrigley, C., "Thin Cells for Space", Solar Cell High Efficiency and Radiation Damage - 1979, Cleveland, June 1979, NASA Conf. Pub. 2097, pp 87-95.
3. Guiliano, M. and Wohlgemuth, J., "Short-Circuit Current Improvement in Thin Cells with a Gridded Back Contact", Space Photovoltaic Research and Technology 1980, Cleveland, October 1980, NASA Conf. Pub. 2169, pp 67-70.
4. Scott-Monck, J., "A Preliminary Evaluation of a Potential Space Worthy Encapsulant", These Proceedings.
5. Rockey, D. E., Hedgepeth, J. M., and Adams, L., "High Performance Silicon Solar Array Employing Advanced Structures", 16th IECEC, Atlanta, August 1981, pp 374-379.
6. Fan, J. C. C., Bozler, C. O. and McClelland, R. W., "The Cleft Process, A Technique for Producing Epitaxial Films on Reusable Substrates", Space Photovoltaic Research and Technology 1980, Cleveland, October 1980, NASA Conf. Pub. 2169, p 79.
7. Stirn, R. J., Wang, K. L., and Yeh, Y. C. M., "Epitaxial Thin Film GaAs Solar Cells Using OM-CVD Techniques", 15th IEEE Photovoltaic Specialists Conf., Kissimmee, May 1981, pp 1045-1050.
8. Gale, R. P., et al, "GaAs Shallow-Homojunction Solar Cells on Epitaxial Ge Grown on Si Substrate", 15th IEEE Photovoltaic Specialists Conf., Kissimmee, May 1981, pp 1051-1055.

TABLE 1.

Present Blanket and Array Status

COMPONENT	DESCRIPTION	kg/m ²	NOTES
Substrate	Kapton/50 μ m	.070	handling, radiation
Adhesive (substrate)	DC-93-500/50 μ m	.055	bondline limitations
Solar Cell	Silicon/62 μ m	.117	11% at op.temp.
Cell Contacts	Silver/4 μ m	.005	gridded back, welding
Adhesive (cover)	DC-93-500/50 μ m	.044	bondline limitations
Cover	CMS/50 μ m	.100	thinnest available
Interconnect	Mo, Invar, Silver/25 μ m	.018	thinnest available
Plating (IC)	Silver/20 μ m	.017	needed for Mo, Invar
Padding, etc.	-	.011	based on SEP
Harness	Copper	.046	based on SEP
TOTAL BLANKET		.483	80% packing factor
Array Structure		.581	SEP
TOTAL ARRAY		1.064	

Blanket Specific Power 231 W/kg (based on 112 W/m²)

Array Specific Power 105 W/kg

TABLE 2.

Anticipated Blanket and Array Performance

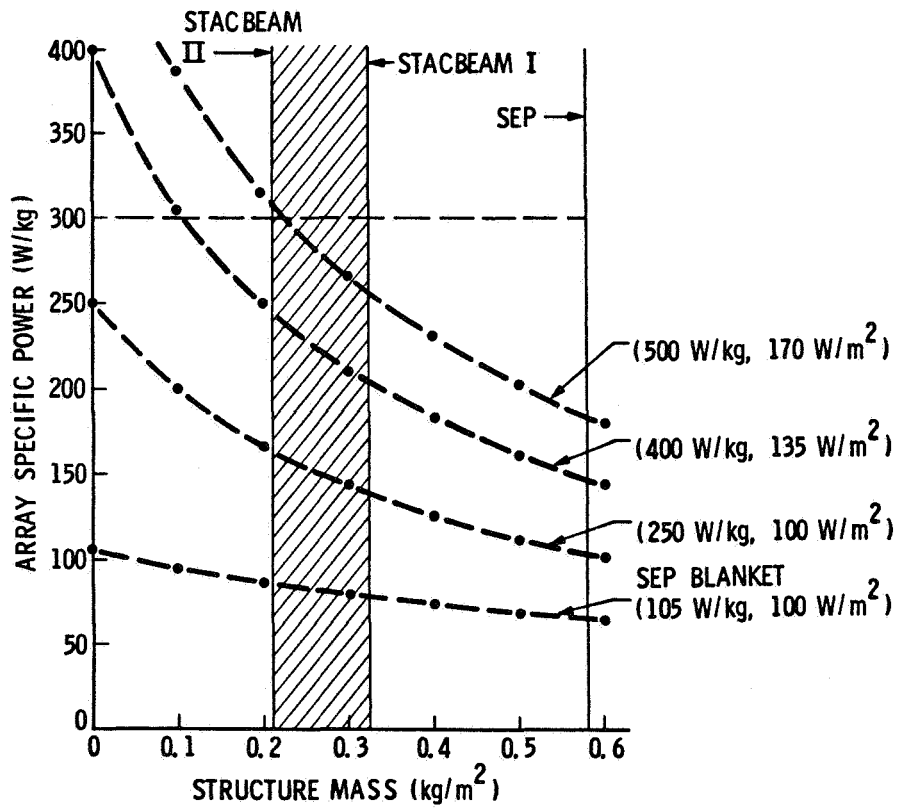
COMPONENT	DESCRIPTION	kg/m ²	NOTES
Substrate	Composite/50 μm	.070	handling, radiation
Adhesive (substrate)	DC-93-500/50 μm	.006	spot bonding
Solar Cell	Silicon/50 μm	.095	14% at op.temp.
Cell Contacts	Silver/4 μm	.005	gridded back, welding
Adhesive (cover)		-0-	none required
Cover	Encapsulant/25 μm	.034	shielding
Interconnect	Aluminum/30 μm	.007	conductivity
Plating (IC)	Silver/20 μm	.002	spot plating
Padding, etc.	-	.011	based on SEP
Harness	Aluminum	.025	advanced SEP concept
TOTAL BLANKET		.255	80% packing factor
Array Structure		.321	STACBEAM I
TOTAL ARRAY		.576	

Blanket Specific Power 557 W/kg (based on 142 W/m²)

Array Specific Power 247 W/kg

FIGURE 1

ARRAY SPECIFIC POWER vs STRUCTURE MASS



MINIATURIZED CASSEGRAINIAN CONCENTRATOR CONCEPT DEMONSTRATION

R.E. Patterson and H.S. Rauschenbach
TRW Space and Technology Group
Redondo Beach, California

INTRODUCTION

High concentration ratio photovoltaic systems for space applications have generally been considered impractical because of perceived difficulties in controlling solar cell temperatures to reasonably low values. A miniaturized concentrator system is now under development* which surmounts this objection by providing acceptable solar cell temperatures using purely passive cell cooling methods. An array of identical miniaturized, rigid Cassegrainian optical systems having a low f-number with resulting short dimensions along their optical axes are rigidly mounted into a frame to form a relatively thin concentrator solar array panel. A number of such panels, approximately 1.5 centimeters thick, are wired as an array and are folded against one another for launch in a stowed configuration. Deployment on orbit is similar to the deployment of conventional planar honeycomb panel arrays or flexible blanket arrays.

The miniaturized concept was conceived and studied in the 1978-80 time frame. Favorable results led to the present feasibility demonstration program which will span the period between 1980 and 1982. Progress in the feasibility demonstration phase made to date is reported in this paper. It is expected that the miniaturized Cassegrainian concentrator concept will be developed further in the future with space flight demonstration as a major target.

CONCENTRATOR SYSTEM DESCRIPTION

A typical solar panel of the miniaturized Cassegrainian concentrator solar array concept is illustrated in Figure 1. Groups of shallow concentrator elements are held rigidly within the gridded frame structure. The detailed design of a single element is depicted in Figure 2. The reflectors are made from relatively thick electroformed nickel in this feasibility demonstration phase. (In a later program phase, lower weight and lower cost fabrication approaches will be examined.) The solar cell radiator fin is shown as a flat square plate in Figure 1, and as a circular cup in Figure 2. This design change was made to accommodate assembly for large-scale production but is not considered final; low-cost high-volume production requirements will strongly influence the final element configuration. A materials and processes data base is presently being established that will assist in this determination.

*

This work was performed under contract NAS8-34131 for NASA MSFC (L. Crabtree, MSFC Technical Manager).

The nickel reflectors are coated as shown in Figure 3. The silicon monoxide (SiO) layer serves both to protect the reflector against terrestrial and space environments and to provide a high-emittance thermal control surface.

The operating temperature of the concentrator cell is controlled passively. Reference 1 describes the approach in detail; however, in brief summary it simply consists of radiating heat into space from both the front and back sides of the concentrator solar panel exactly as occurs for conventional planar arrays. Each concentrator element has a radiator fin, roughly the size of the entrance aperture, attached to the concentrator cell with a low thermal resistance bond. The radiator fin thickness is minimized for the desired cell operating temperature and the particular aperture size. The fin is radiatively coupled to the primary parabolic reflector to obtain front-side heat rejection and to reduce thermal gradients across the panel thickness. As Reference 1 demonstrates, only small diameter radiators, i.e., miniaturized elements, will result in low specific mass concentrator systems.

The concentrator element optical design, illustrated in Figure 4, results in the optical losses shown in Table 1. Under perfect sun-pointing conditions, the incident sunlight is reflected only twice without striking the tertiary reflector, also known as the light catcher cone. The light catcher cone improves the off-pointability of the concentrator element. Under conditions of perfect alignment and sun-pointing, the demonstration module concentrator elements have a theoretical geometrical concentration ratio of 163 and a nominal effective concentration ratio of 88.

EXAMINATION OF CRITICAL ISSUES

In this section the most critical issues affecting implementation of the concept are examined in four areas: optical design, thermal design, solar cell design, and assembly.

Optical Design

The initial problem of optical design was the design and procurement of a short-focal length (12.8 millimeters) nonimaging Cassegrainian system with a low f-number (0.25) and a high concentration ratio (163). Figures 5 and 6 and the performance data described below show that the initial design was successful.

The elements of the demonstration module are arranged orthogonally for assembly and test convenience only, rather than in a closely packed hexagonal pattern. Figure 5 shows the simple "spider" arrangement that supports the secondary hyperbolic reflector. The wide spider legs produce a large blockage loss contribution. No attempt was made to reduce this loss by substituting a more complex support structure since it was desired for the purpose of initial demonstration to use off-the-shelf commercial electroforming techniques without requiring complex mandrel tooling.

Current work is directed toward identifying practical methods of reducing the optical design losses to attain the goals shown in Table 1. The largest of the potential gains will result from an improvement in the reflective coating as indicated by Figure 7. By integrating the product of a spectral reflectance curve from this figure, the AMO solar spectrum, and the solar cell spectral response (Si or GaAs), the energy received by the solar cell after a double reflectance can be determined and, therefore, the comparative improvement obtained with candidate coatings other than aluminum. A silver coating is the obvious best choice. However, silver coatings, even with protective SiO overcoatings, are known to frequently exhibit problems in long-term terrestrial storage environments, usually due to hard-to-avoid pin holes in the SiO coating. Thus some development work will be required to make this coating system stable and economically viable.

Alignment sensitivity tests have shown that the three reflectors and the solar cell may be randomly misaligned with respect to the element's theoretical optical axis by as much as several tenths of a millimeter with no loss in element performance at normal incidence of sunlight (the Sun's ray parallel to the element's theoretical optical axis). Similarly, misalignment errors between reflectors and the cell in the direction of the optical axis up to several tenths of a millimeter are inconsequential at normal incidence.

Off-pointing tests in natural sunlight demonstrated the effectiveness of the light catcher cone (Figure 8). The off-pointing performance was good, but somewhat less than predicted analytically (for a 90 percent reflective cone surface) and from experience with alignment sensitivity measurements made with a laser in the laboratory. Several areas have been identified for potential improvements during the detailed design phase.

Thermal Design

For low earth orbit applications in which the Earth's albedo and IR emissions are significant, highly reflective high-emittance coatings are required for good thermal control. For this reason, both the spider and the aluminum radiator fin surfaces were painted with white thermal control paint. Thermal balance and thermal gradient tests in vacuum are presently under way to confirm the predicted silicon cell temperature of 80° to 100°C and cell-to-fin temperature gradients of less than 5°C. A natural sunlight test at Table Mountain, California at 8000 feet altitude and approximately 0.87 AMO sun equivalent intensity have yielded a cell temperature of 36°C with a still air ambient temperature of 19°C. This cell temperature compares favorably to similar flat plate array temperatures obtained under similar test conditions.

Solar Cell Design

The concentrator solar cell physical design, shown in Figure 9, represents a compromise in contact pad design between heat sinking and power losses in the nonilluminated cell junction area. A larger cell (with active area constant) improves heat sinking, however, it also increases power losses in the nonilluminated cell junction area. Concentrator cell designs should account for this loss mechanism and be coordinated with the

application so that it is minimized. Cell dimensions are not otherwise critical except that their tolerances must be compatible with assembly tooling requirements.

An important issue in optimizing the solar cell efficiency is that the concentrated light is typically nonuniform, especially under slight off-pointing conditions (see Reference 2). Grid line design should take this into consideration.

A desirable tradeoff yet to be conducted is between cell designs with textured and polished cell active areas. While texturing will improve the absorption of light by the cell, especially the light that impinges on the cell at angles of incidence between 0 and 30 degrees, it will also raise the cell's thermal absorptance and hence its operating temperature. Reference 2 discusses textured concentrator cells in greater detail.

Presently, the concentrator demonstration module contains silicon solar cells designed for maximum performance at 100 suns. They are 8 to 10 mils thick, are made from 0.5 Ω -cm base resistivity material. Junction depth is 4000 to 5000 Å. Contacts are Ti(400 Å)-Pd(800 Å)-Ag(10 μ m). The cells have evaporated aluminum back surface reflectors and SiO₂ (800 to 1300 Å) anti-reflective coatings.

NASA's Lewis Research Center is currently working on a GaAlAs cell for the miniaturized Cassegrainian concentrator. It is planned to build elements using these cells when they become available.

Assembly

The demonstration module was assembled in a way that attempted to anticipate and solve some of the problems that might occur during large-scale production. All parts shown in Figure 10 were stacked and soldered together at one time in a vapor phase solder reflow machine. The preassembly parts inspection using laser instrumentation mentioned earlier indicated that application of standard shop practices and techniques would result in elements of similar optical performance. The four holes in the cup bottom admitted pins of an assembly fixture that held all parts together. The assembled cups were then bonded in a honeycomb panel and electrically interconnected as shown in Figures 5 and 6, respectively. The nine elements were wired so that each could be tested individually and all could be tested together in a series circuit. The primary and secondary reflectors were installed, guided and aligned by the three tabs protruding upward from the cup (shown in Figure 10).

Summary and Conclusions

The work to date has identified the need for additional design optimization studies and related evaluation testing, for long-term space environmental testing, and for solar cell design and performance improvements. Nevertheless, the work accomplished thus far has demonstrated that the original assumptions and simplified mathematical models used in the formulation of the miniaturized Cassegrainian concentrator concept are valid and have predicted system performance quite well. No surprises or unusual

effects have been uncovered. The fabrication of single elements and a 9-element demonstration module has demonstrated the feasibility of the concept. Several different promising approaches toward achieving low-cost design suitable for flight have been identified and are under study. Many of the critical fabrication and assembly processes that are candidates for use with this concept are currently in use in other industries and fields of endeavor. Based upon these accomplishments, it is concluded that the original multikilowatt solar array cost reduction goal of one order of magnitude is both reasonable and feasible with space performance comparable to that of state-of-the-art nonconcentrating planar solar arrays.

REFERENCES

1. R. E. Patterson, H. S. Rauschenbach, M. D. Cannady, and U. S. Whang, "Low Cost, High Concentration Ratio Solar Cell Array for Space Applications," TRW Space and Technology Group, Redondo Beach, California 90278. W. L. Crabtree, Marshall Space Flight Center, Huntsville, Alabama 35812. 16th IECEC, August 9-14, 1981.
2. H. Rauschenbach, and R. Patterson, "Design Requirements for High-Efficiency High Concentration Ratio Space Solar Cells," TRW Space and Technology Group, Space Photovoltaic Research and Technology, 1980, NASA Conference Publication 2169, October 1980.

Table 1. Optical System Transmission Comparison:
 Demonstration Module Versus Design Goal

PARAMETER	DEMONSTRATION MODULE HARDWARE		ULTIMATE DESIGN GOAL	
PRIMARY REFLECTOR REFLECTANCE LOSS	16%		5%	
SECONDARY REFLECTOR REFLECTANCE LOSS	16%		5%	
SECONDARY REFLECTOR BLOCKAGE LOSS	6%	20%	6%	11%
SECONDARY REFLECTOR SUPPORT BLOCKAGE LOSS	14%		5%	
OTHER LOSSES (MISALIGNMENT, ETC)	4%		2%	
OPTICAL SYSTEM TRANSMISSION	54%		79%	

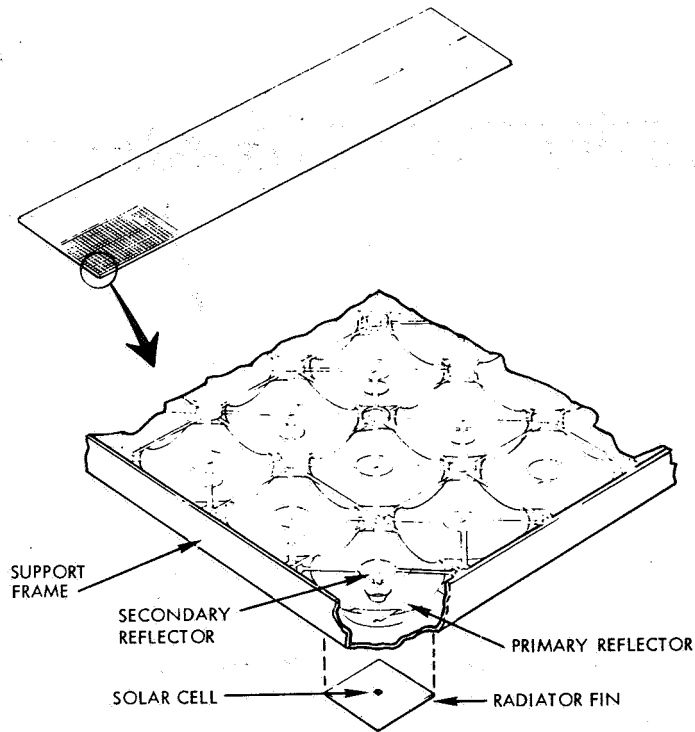


Figure 1. Mounting of Concentrator Element or Subassemblies into Panel Frame

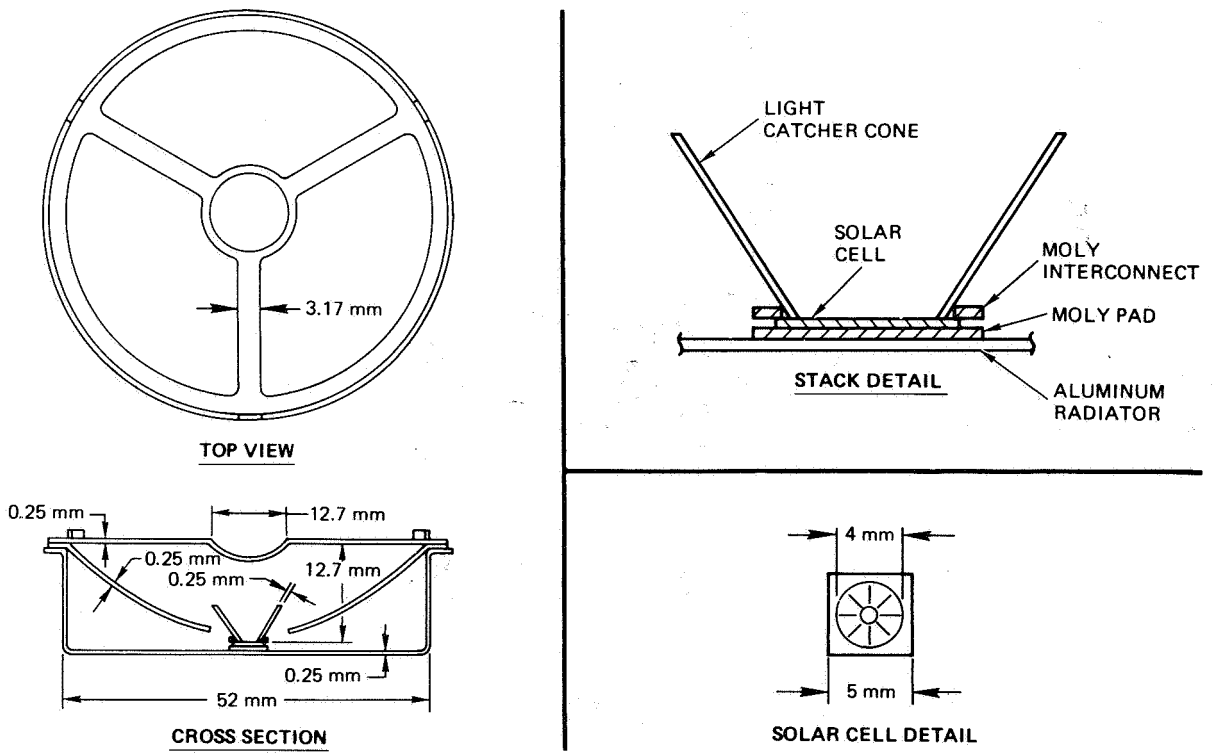


Figure 2. Baseline Concentrator Element Design

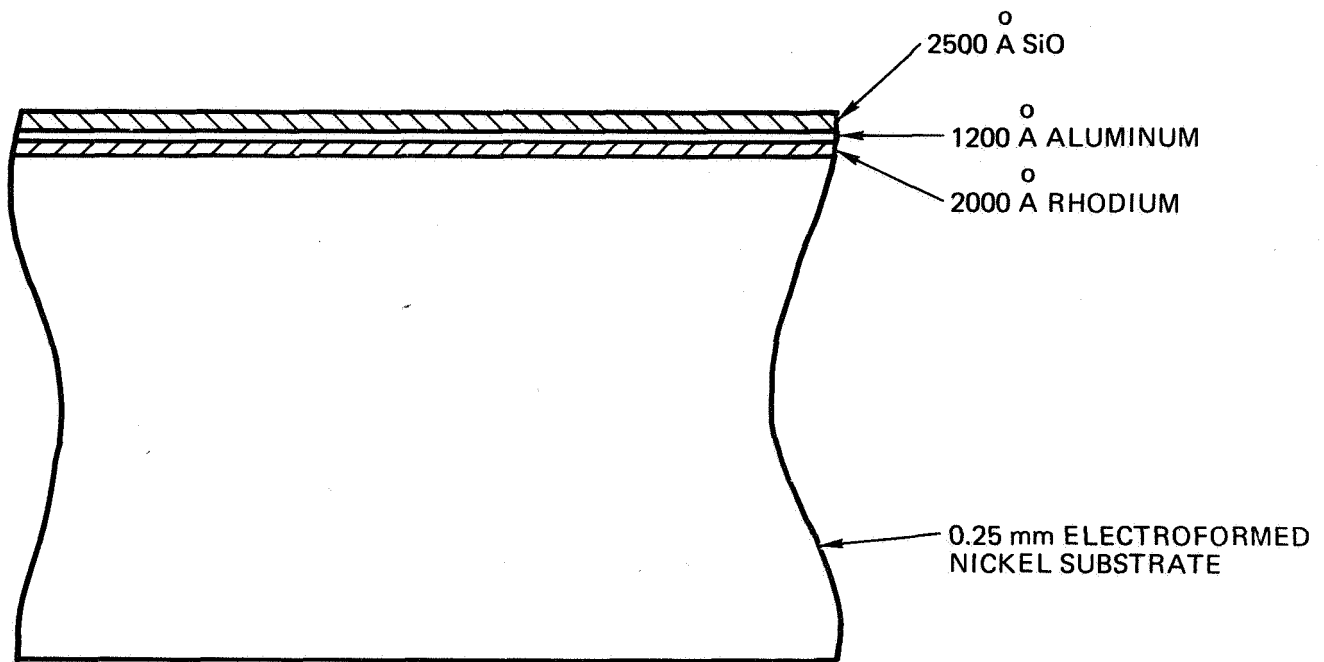


Figure 3. Reflector and Coating Configuration

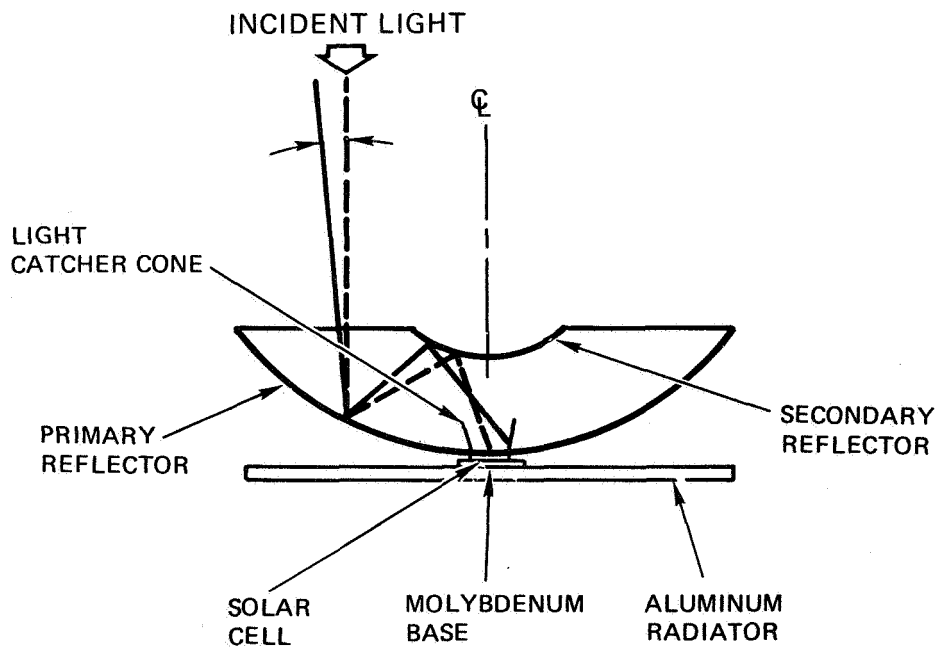


Figure 4. System Schematic

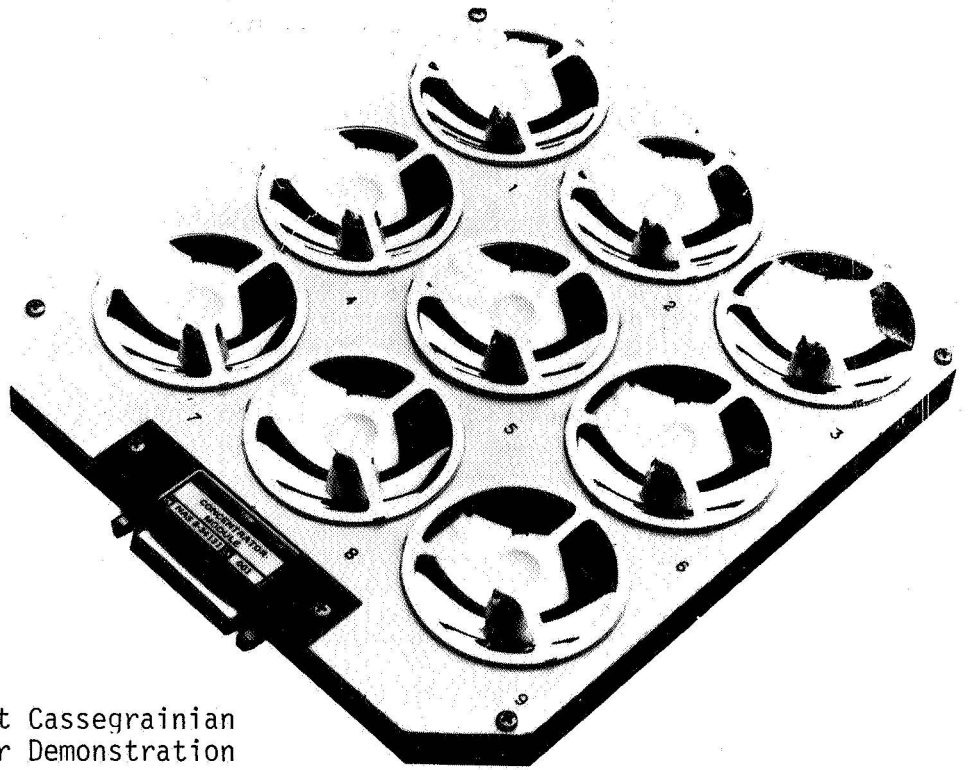


Figure 5. Nine-element Cassegrainian Concentrator Demonstration Module

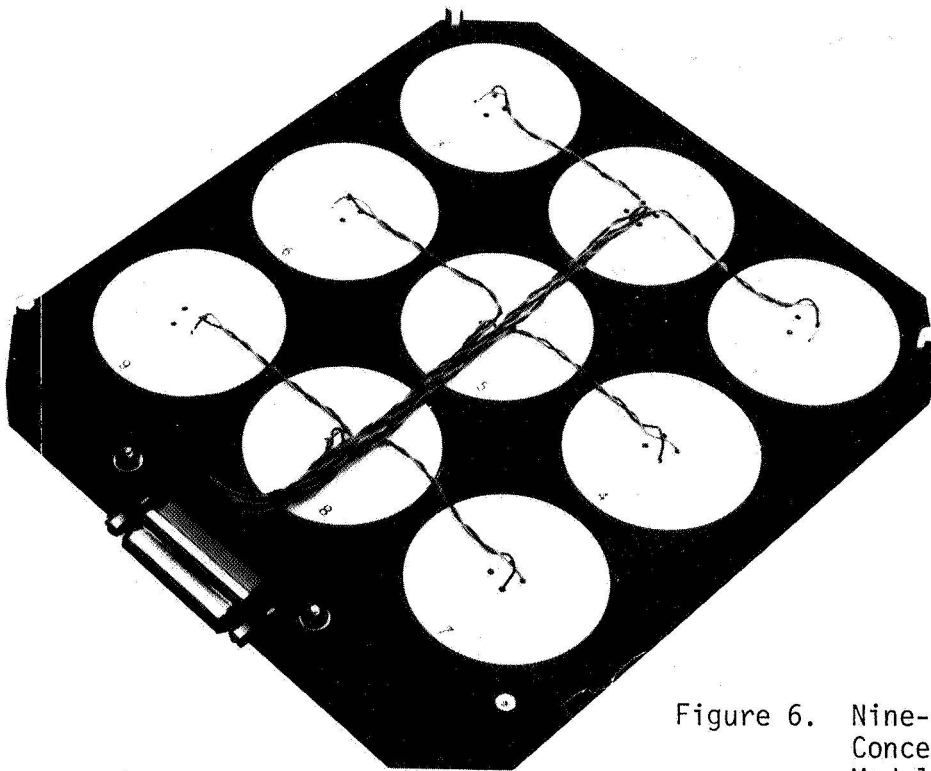


Figure 6. Nine-element Cassegrainian Concentrator Demonstration Module (Back View)

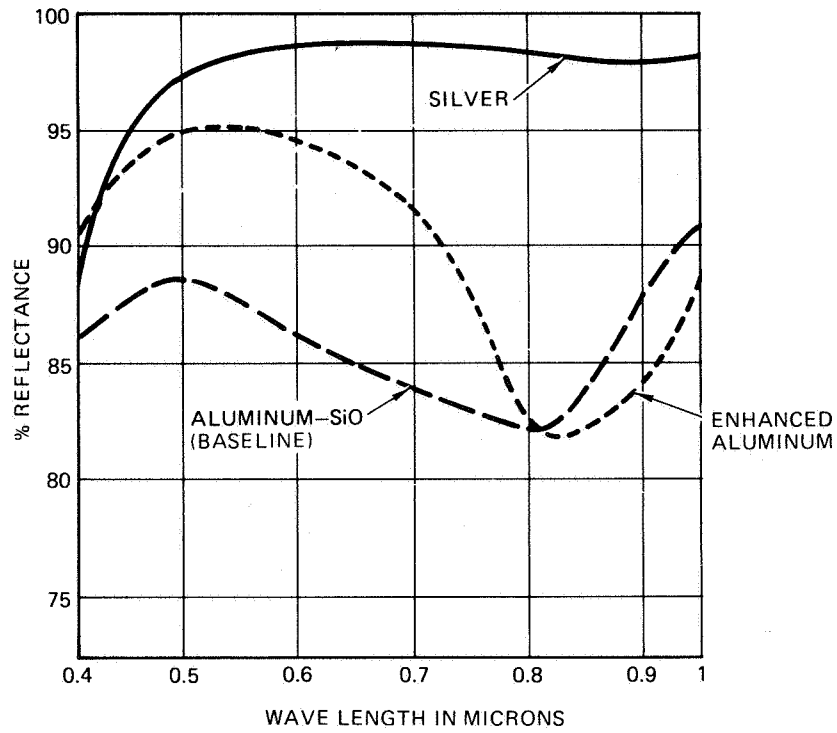


Figure 7. Alternate Reflector Coatings Offer Improved Reflectance

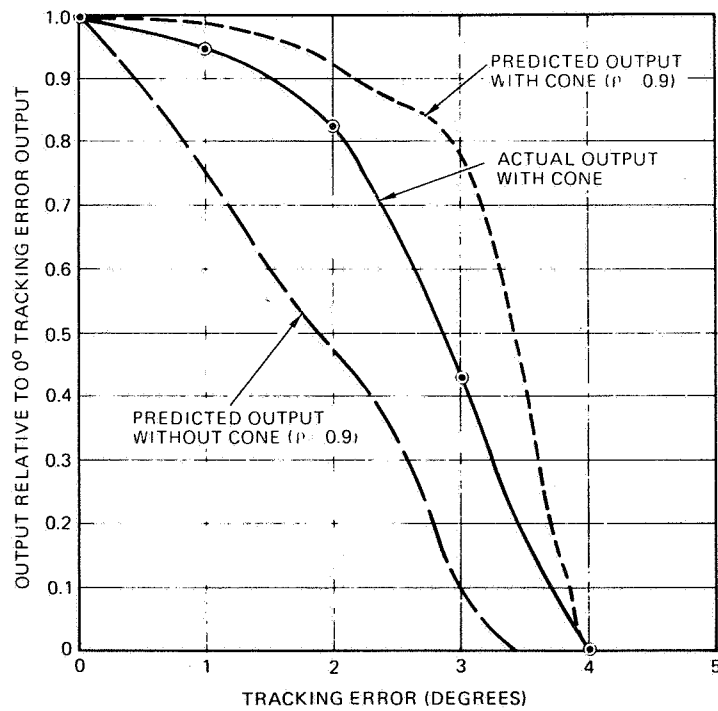


Figure 8. Single Element Off-Pointing Test Results

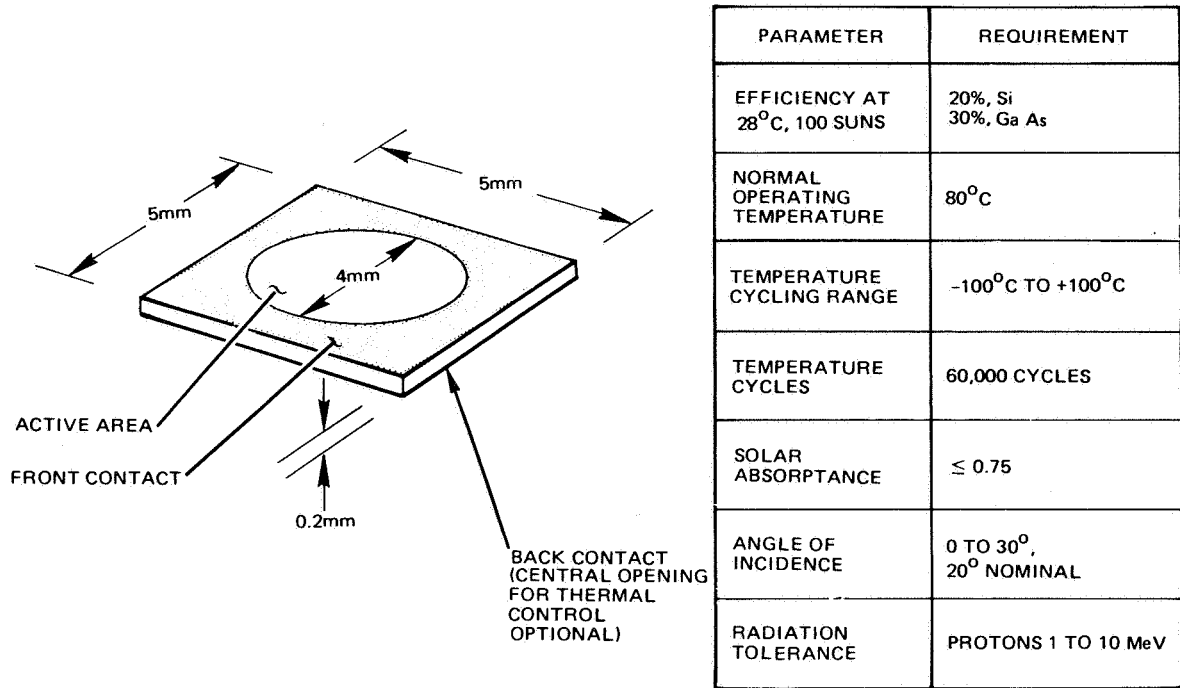


Figure 9. Concentrator Solar Cell Reference Design and Requirements

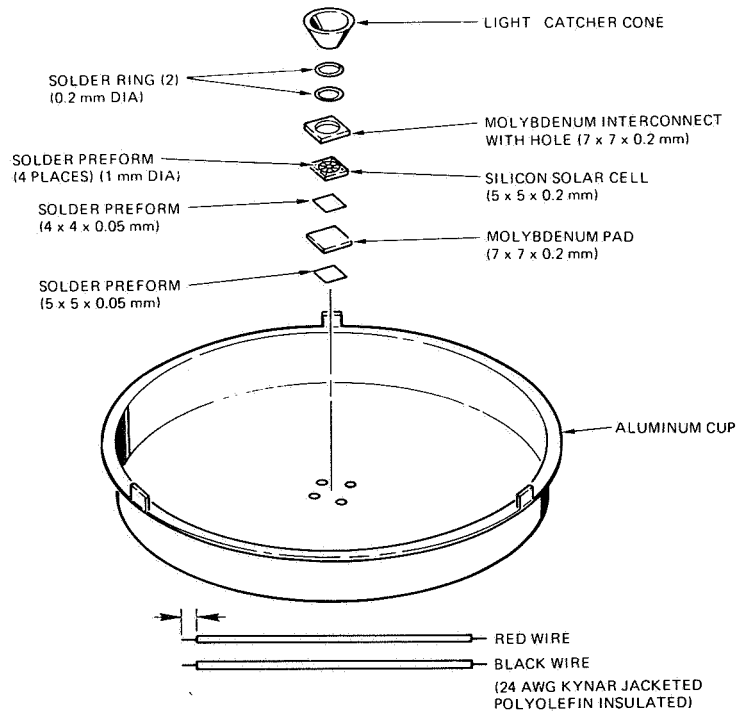


Figure 10. Cell Stack Assembly Parts Diagram

THE COURSE OF SOLAR ARRAY WELDING TECHNOLOGY DEVELOPMENT*

Paul M. Stella
Jet Propulsion Laboratory
California Institute Of Technology
Pasadena, California

SUMMARY

Solar array welding technology is examined from its beginnings in the late 1960's to the present. The U.S. and European efforts are compared, and significant similarities are highlighted. The utilization of welding technology for space use is shown to have been influenced by a number of subtle, secondary factors.

INTRODUCTION

Since the time of the first satellite solar power systems, the preferred method of solar cell interconnect attachment has been solder. Yet for over a decade there has been a continuing if not always steady development of a "better" method. Although a number of satellite solar arrays have been assembled with welding methods by the European industry (ref. 1), welding has not achieved a similar level of application in the U.S. Even though solder has proven suitable for past space efforts, future requirements will most likely exceed its capabilities. For this reason NASA is planning to initiate a U.S. welding program that will provide the knowledge and confidence required to achieve flight ready status. This paper will provide a background to that effort, examining past activities and results in welding for U.S. and European efforts. It will be shown that the two efforts exhibit considerable similarity and that the greatest impediment to weld acceptance has been the lack of suitable in-process NDE (nondestructive evaluation) methods. The following discussion will generally follow a chronological format.

SOLDER

Early studies have shown solder to have a number of critical limitations both at high temperature where creep and even melting can occur, and at low temperatures where fatigue induced failure is of concern (ref. 2). The former limit is readily observable since the melting points of the solders are well documented. The low temperature situation was, and still is, much more difficult to quantify.

Due to thermal expansion mismatches between the cell, solder, and interconnect, various stress distributions will occur depending on temperature limits, bond area, and component thicknesses. Analyses indicated that a small number of very low temperature exposures or a moderate number of less severe low temperature exposures could lead to cracking in the solder (ref. s 2 & 3). Since the acceptance of a solder bond has been tied to the appearance of the solder fillet, changes in ap-

* The research described in this paper presents the results of one phase of research carried out, at the Jet Propulsion Laboratory, California Institute of Technology, under Contract with the National Aeronautics and Space Administration.

pearance which were observed during thermal cycling were occasions for concern. It was felt that these changes ultimately lead to bond failure including possible silicon divoting. The correlation between solder cracking and observable surface appearance changes and actual bond or silicon failure was not however, clearly demonstrated. At the same time since actual stresses within the bond were influenced by the materials used, stress reduction could be achieved by means of changes in materials or thickness (ref. 4). As a result, the present day solder system is considerably improved over that used in the late 1960's. Solder pressing and preforms have reduced the solder thickness in the bond, and interconnectors with coefficients of expansion close to silicon's, such as molybdenum, both create a more favorable situation than the earlier systems. As a result, it is now possible to withstand over 1000 cycles typical of GEO (equivalent to over 10 years orbit), something that might not have been expected from early analyses (ref. 5). By comparison early tests of soldered interconnects with less optimum configurations typically suffered modest to severe damage under similar thermal cycle conditions (ref. 2).

The case for long term LEO use of solder has not been as optimistic. Even though temperature extremes are less pronounced, the need to demonstrate survival capability for tens of thousands of cycles means that the costs and time required to adequately test the LEO simulations is considerable and as a result a greater reliance must be placed on theoretical analyses for guidance. These analyses indicate that the solder system should be replaced with a welded (brazed) one. As time has shown, this has not been a trivial task. Solder's easy repairability, relative insensitivity to process parameters, suitability to visual inspection, and large bond area with resultant high bond strength, have proved a challenging combination to overcome.

WELDING TECHNOLOGY DEVELOPMENT (EXPLORING ALTERNATIVES 1965-1970)

The beginning of serious solar cell weld development can be traced to the development of the palladium passivated cell contact. This meant that humidity resistance could be achieved without the use of solder (ref. 6), allowing non-solder interconnection methods to be freely pursued. During this early phase, European and U.S. organization pursued a great number of interconnecting schemes such as ultrasonic, thermal diffusion, thermocompression, parallel gap resistance welding (R.W.) and even laser welding (ref. 7). These were examined for use with a wide variety of interconnector materials including silver, aluminum, gold, silver plated copper, molybdenum, and Kovar. Various degrees of success were obtained in these exploratory efforts resulting in a narrowing of options by 1970. The European choice was primarily R.W. in conjunction with silver plated molybdenum tabs, although pulse welding has continued to receive significant although limited development (ref. 8). Pulse welding is actually a version of the more familiar R.W. technique where the heat for the bond fusion is formed in one of the two weld electrodes rather than in the cell/interconnector contact region.

By contrast, a consensus was not as rapidly attained in the U.S. This can be traced primarily to the emphasis on development of Al contacted cells for satisfying military requirements. As a result the U.S. effort was initially biased towards ultrasonic welding of aluminum interconnectors to cells with aluminum (Al) contacts. The Al-Al system did not prove highly successful, so it wasn't until after 1970 that the U.S. effort focussed on the R.W. method. Similar to the Europeans, a single significant alternative method has survived this initial explora-

tory period. In this case, it is ultrasonic welding, now used with Ag interconnects and conventional silver contacted cells (ref. 3).

It is interesting at this point to compare the European and U.S. efforts resulting from the exploratory period. Both ultimately emphasized the R.W. method, based on use of the Hughes MCW 550 power supply. The interconnectors of primary choice were usually silver plated rigid materials with thermal expansion coefficients somewhat matched to silicon's. Yet both efforts also resulted in a single significant alternate method, pulse welding in Europe and ultrasonic in the U.S., that were tied to the use of a relatively flexible interconnect material, silver. In fact both these alternates have received continuous although limited support through the present. They share another similarity--rather than rely on spot bonds such as occur with R.W., they use tooling that provides a linear bond.

A EUROPEAN COMMITMENT, 1970-1974

By 1972 the European effort achieved a milestone with the commitment of R.W. to the Helios solar probe (ref. 9). Due to the high temperature environment that the probe would observe, it was obvious that solder would not be suitable and welding was necessary. However, excluding the high temperature exposure (175°C) the mission thermal cycling environment was not particularly severe. At the same time, a number of developments served to reduce the concern over individual weld bond integrity such as the cell interconnector-cover (CIC) "sandwich" assembly, and increased interconnect redundancy (ref. s 9 & 10).

Studies of bond joints had indicated that solder bonds are subject to high stress not only due to the thermal coefficient mismatch, but also because of the large bond area. Advantages for welded systems then, would be to reduce the thermal coefficient mismatch and also to provide a smaller bond area. Both would serve to minimize stresses. However, the smaller bond area translates to reduced bond strengths, particularly under torsional loading of rigid interconnectors, such as were in use (ref. 7).

The use of the CIC not only provided protection to the cell's complete top surface, but it also mechanically constrained the tab at the weld joint, providing protection against torsional loading. It is even possible that under a debond situation the mechanical coupling provided by the CIC assembly might allow full electrical contact, simulating a sliding contact.

The cell design used with the CIC assembly allows the use of 3 bond joints per side of the cell. This redundancy reduces the need for 100% bond integrity since only one joint per side would be needed for useful cell output. Since it was not possible to verify the quality of each individual bond this approach provided a practical method for using an "imperfect" weld process. As a further attempt at maximizing the bond integrity, automated indexing and welding of the CIC assemblies was introduced so as to minimize operator dependence. The combination of weld, CIC, and redundancy, thus allowed an unproven technology to provide a confident interconnect method. This was all applied to an almost perfect first mission need for a weld interconnect system.

During this period although evaluation of weld schedules and the influence of component variations continued, the emphasis of U.S. and European welding was placed on developing methods for ensuring individual bond quality since the basic weld optimizations had been performed. The primary problem was that, unlike solder,

the bond was not visible for inspection, particularly for rigid interconnect systems. Some correlation between the bond characteristics and deformations in the welded interconnect was possible with the silver system (ref. s 4 & 7), but in general visual inspection was not felt to be sufficiently reliable. Since the R.W. method relies on current flow in the bonding components to generate sufficient but not excessive heat (which could degrade the cell junction), initial efforts were based on pre-weld measurements of resistances between the electrodes, interconnector, and cell in order to establish go/no-go conditions of resistance that would impact the weld process. The heat generated in the weld bond was then related to characteristics of the weld pulse such as current and energy flow so that conditions of over (excess melting) and under (insufficient heat) welding could be estimated for each individual weld (ref. s 11, 12, 13 & 14).

These of course are secondary approaches to accounting for actual heat flow at the bond surface, but have proven to be reasonably reliable. For example, in one study, the application of these methods was evaluated against weld pull strengths and it was determined that for a moderately large sample size, it was possible to identify nearly 92.5% of the bad welds (over or under welds) (ref. 11). During this period AEG Telefunken reported that they had accumulated experience with over one hundred thousand weld processes, a significant quantity.

In the U.S. encouraging thermal cycle results were reported using ultrasonic welding and silver interconnects. After 700 cycles of a simulated GEO environment no electrical degradation was observed for sample test modules. However, it was noted that soldered samples performed as well (ref. 15).

TECHNOLOGY EVOLUTION-QUALITY ASSURANCE CONCERNS (1975-1982)

By 1975 the European program was moving rapidly with a variety of new welded solar arrays being assembled for missions. In fact 5 space projects were well underway, and the number of weld joints that had been made was estimated to be well over a million (ref. 13). However, this was not to imply that the R.W. method was completely reduced to practice since work on weld parameter optimization and on inprocess controls continued to be published. For example, work continued on determination of an optimum range for the parallel gap weld pulse duration. This was of interest since a number of studies had shown that good welds (based on pull strengths and cell electrical effects) could be achieved for a wide range of pulse durations as long as the pulse voltage was simultaneously adjusted (ref. s 4 & 13). Along with earlier results (ref. s 7 & 14), the new work indicated an optimum duration of approximately 100 msec (ref. 13). Also this time, AEG Telefunken proposed that the weld pulse shape be changed from the "standard" rectangular wave to a trapezoidal shape (ref. 13).

In the U.S., similar activities were conducted although again without any significant flight program application. The use of a combination of preweld, in weld, and post weld tests was examined and found to be a reasonable predictor of weld strength. In fact, one study showed a 93% correlation could be made with acceptable bond quality (ref. 17), a value surprisingly similar to European results published somewhat earlier.

The similarity of the U.S. and European efforts and results to this point can be dramatically shown by examining the data presented for independent weld optimizations done on similar interconnect systems.

In 1970 AEG Telefunken reported that Ag (5 μM) plated molybdenum (30 μM) could be best welded with the following conditions (ref. 7):

pressure = .75 \rightarrow 2.5 kg
duration = 100 msec
voltage = .65V front, .70V rear

In 1974 Lockheed reported that optimum conditions for a similar interconnect system were (ref. 14):

pressure = .68 kg
duration = 100 msec
voltage = .64V front, .72V rear

The results are very similar. In view of the many possible subtle differences in cells and interconnectors such as contact thicknesses, surface smoothness, and plating methods, these results indicate a strong consistency in the R.W. weld process.

After 1976, less welding work was being reported, but the concern for NDE methods was still evident. Clearly the problem of individual weld integrity has not been solved. Both U.S. and European efforts report encouraging results in using Infrared (IR) monitoring to detect the temperature of the weld. Although detection of heat from portions of the interconnector and weld electrodes can interfere with actual temperature measurement at the bond line (ref. 18), the method is felt to be sufficiently useful that it has been incorporated into one manufacturer's weld process. In practice the detected thermal signal is used to terminate the weld pulse when a preset IR sensor output value is measured, compensating for variations in the cells and interconnectors (ref. 19).

Competitive alternates continued to show progress on both continents. The MBB pulse weld method is combined with Ag mesh to provide CIC assemblies for Intel-sat V (ref. 20). Hughes Aircraft determined that the small bonds obtained with ultrasonic spot welding methods were unacceptable and developed a rotary ultrasonic seam welder that when used with Ag mesh can provide a strong and highly redundant interconnect system (ref. 3). Advanced methods such as laser welding continue to receive support (ref.'s 21 & 22).

CONCLUSION

A review of weld technology developments shows many similarities between the U.S. and European efforts. The major difference has been one of flight hardware experience. At the same time, with the exception of the high temperature Helios mission, the environmental requirements of those welded arrays flown could have been met by use of solder, somewhat mitigating these as full endorsements of weld capabilities. In fact, it is the influence of a number of secondary factors, shown in Table 1, rather than basic differences in welding capabilities that have determined the use of welding for space applications.

Extensive work on weld optimization, when combined with pre-weld and in-weld monitoring, has lead to a fairly reliable technique on both continents. Ultimately a temperature detection system might prove more valuable than the weld pulse monitoring methods commonly used since it should avoid uncertainties involved in the indirect measurement of the bond temperature.

The single most significant impediment to weld technology acceptance is the lack of a non destructive inspection technique to evaluate an individual bond. Recent work on viewing of the internal weld structure, using IR and ultrasonic techniques (ref. s 19 & 23) may provide a solution to this limitation and lead to full confidence in the welding process.

REFERENCES

1. D. J. Curtain and W. J. Billerbeck, "Development of Advanced Interconnects for Solar Cells", COMSAT Technical Journal, V4, N1, Spring 1974, pp 53-68.
2. W. Luft, "Solar Cell Interconnector Design", IEEE Transactions on Aerospace and Electronic Systems, Vol. AES-7, No. 5, Sept. 1971, pp 781-791.
3. G. J. Pack and R. W. Opjorden, "Advanced Interconnect for Use with Ultrasonic Seam Welding on Solar Cells", Proceedings of 12th IEEE PVS Conf., Baton Rouge, LA, 1976, pp 368-374.
4. P. M. Stella and E. F. Zimmerman, "Silicon Solar Cell-Interconnect System Development", Final Report, INTELSAT Contract CSC-SS-273, 1972.
5. F. C. Treble and A. Dunnet, "Comparative Deep Thermal Cycling of Solar Cell Panels", Proceedings of 11th IEEE PVS Conf., Scottsdale, AZ, pp 145-152.
6. H. Fisher and R. Gereth, "New Aspects for the Choice of Contract Materials for Silicon Solar Cells", Seventh PVS Conf. Proceedings, Pasadena, CA, 1968, pp 70-76.
7. J. J. Capart and K. K. Reinhartz, "Welded Solar Cell Interconnections", Proceedings of the International Colloquium on Solar Cells, Toulouse, France, 1970, pp 389-405.
8. E. Nitsche et al, "A New Type of Solar Cell Array for A Solar Probe Mission", Proceedings of the 8th IEEE PVS Conf., Seattle, WA, 1970, pp 293-302.
9. H. J. Durre, B. Gorgens and J. Rath, "The Helios Solar Array", International Congress on Sun in the Service of Mankind, Paris, 1973, pp 407-416.
10. H. W. Boller et at, "Solar Cells and Generator Technology for the Helios Sun Probe", Proceedings of the 9thd IEEE PVS Conf., Silver Springs, MD, 1972, pp 226-236.
11. R. M. Jenkins, D. G. Powley and J. C. Larue, "Non-Destructive Testing of Welded Solar Cell Interconnections", Proceedings of the 10th IEEE PVS Conf., Palo Alto, CA, 1973, pp 287-205.
12. H. G. Mesch, "Parallel Gap Welding of Silver-Plated Solar Cells", Proceedings of the 10th IEEE PVS Conf., Palo Alto, CA, 1973, pp 275-280.
13. R. Buhs, H. Durre, H. Boller, "Welding of Solar Cells in a Production Line", Proceedings of 11th IEEE PVS Conf., Scottsdale, AZ, 1975, pp 126-133.

14. J. S. Katzeff, "Solar Cell Welded Interconnection Development Program", International Conf. on Photovoltaic Power Generation Proceedings, Hamburg, Germany, 1974, pp 405-421.
15. T. C. Eakins, "Results of Solar Cell Welded Interconnection Development", Proceedings of the 7th IECEC, San Diego, CA, 1972, pp 651-660.
16. H. S. Rauschenbach and A. F. Ratajczak, "FEP-Teflon Covered Solar Cell Array Advancements", Proceedings of the 10th IEEE PVS Conf., Palo Alto, CA, 1973, pp 264-271.
17. D. R. Lott, et al, "NDT Evaluation of Solar Cell Weld Joints with Details of Selected Post-Bond, and Pre-Bond Systems", Proceedings of the 11th IEEE PVS Conf., Scottsdale, AZ, 1975, pp 134-144.
18. H. W. Boller and J. Koch, "Non-Destructive Testing (NDT) of Solar Cell Weld Joints", 12th IEEE PVS Conf. Proceedings, Baton Rouge, LA, 1976, pp. 397-405.
19. J. S. Katzeff, "Non-Destructive Testing of Solar Cell Welds", 12th IEEE PVS Conf. Proceedings, Baton Rouge, LA, 1976, pp 388-396.
20. D. C. Briggs, et al, "Intelsat V Solar Array Design and Development Summary", 13th IEEE PVS Conf. Proceedings, San Diego, CA, 1978, pp 110-117.
21. J. Koch and Lydorf, "Latest Developments in Solar Array Technology at AEG-Telefunken", 13th IEEE PVS Conf. Proceedings, San Diego, CA, 1978, pp 215-220.
22. JPL Contract 956020, Lockheed Missiles and Space Company.
23. P. Stella, D. Yuhas and C. Vorres, "SLAM Examination of Solar Cells and Solar Cell Welds", 15th IEEE PVS Conf. Proceedings, Orlando, FL, 1981, pp 218- 224.

Table 1

Factors Influencing Weld Development

- ° Passivated Cell Contact
- ° Aluminum Cell Contact
- ° Cell-Interconnector-Cover Assembly
- ° Redundant Interconnections
- ° Helios Near-Sun Probe
- ° Pre-Weld, In-Weld Monitoring
- ° NDE Techniques for Bond Evaluation

A PRELIMINARY EVALUATION OF A POTENTIAL SPACE WORTHY ENCAPSULANT*

John Scott-Monck
Jet Propulsion Laboratory
California Institute of Technology
Pasadena, California

INTRODUCTION

The development of 50 μm silicon solar cell technology (ref. 1), which offers a major improvement in array weight reduction, has added a new stimulus for developing an alternative to conventional fused silica coverglass. Although it is necessary to protect the cell from the catastrophic effects of low energy protons (ref. 2), for many mission applications the required shielding thickness is less than 25 μm (fused silica equivalent). However it is difficult to obtain, or work with, coverglass less than 100 μm for array assembly.

The concept of encapsulating the interconnected cell modules offers important weight and cost advantages (ref. 3). The materials and labor required to bond individual covers to cells would be significantly reduced. By optimizing the required shielding and eliminating adhesives, major weight savings would occur. This paper will describe the results of a preliminary evaluation of a new organic material which has the potential for providing the cost and weight benefits associated with encapsulation.

BACKGROUND

This polyimide polymer was developed by the Hughes Aircraft Technology Support Division for commercial utilization. Recognizing the potential of this material, a joint program was initiated with NASA-JPL to evaluate the polyimide for space applications. A test matrix was set up to provide a number of gates (go/no go) in order to minimize program cost.

JPL provided silicon solar cells which had been characterized with respect to electrical output and spectral response. Hughes TSD prepared and deposited the polyimide onto the cells, providing two groups of samples, one having $\sim 5 \mu\text{m}$ of polymer, the other $\sim 12.5 \mu\text{m}$. JPL then retested the samples to investigate the effect of the deposition process and the optical properties of the polyimide on the cells' electrical output. The 20 cell sample group was then divided into a number of test subgroups.

JPL investigated the effect of electrons and low energy protons on the polyimide while Hughes TSD did thermal shock and humidity tests as well as thermo-

* The research described in this paper presents the results of one phase of research carried out at the Jet Propulsion Laboratory, California Institute of Technology, under contract with the National Aeronautics and Space Administration.

gravometric analysis. Then a 1350 hr vacuum ultraviolet test was performed. The results of these tests are given in the following section.

TEST RESULTS

Deposition Effects

The polymer was deposited on the cells using a spray technique, then cured for 2 hours at 225°C. In some cases the film overlapped the front contact bar and had to be removed, which provided a very practical demonstration of the adherence and durability of the coating. Post deposition electrical measurements showed that the average loss in I_{SC} for the 10 samples which received a 5 μm deposition was 3.5% while for the other 10 cell group coated with 12.5 μm of polyimide, the reduction in I_{SC} was 3.1% (Figure 1). There was no evidence of curve factor degradation in any sample.

A comparison of pre and post deposition spectral response curves for a typical cell sample is shown in Figure 2. It can be seen that the response was reduced in the region below approximately 5000 nm and above approximately 7000 nm; while there was an increase in response between 5000 and 7000 nm. Obviously the polyimide refractive index is contributing to these results, but it is not possible to assess its impact on these results until the index has been determined.

Electron Effects

This is a gross test of the polyimide's optical properties under simulated space radiation conditions. Since the films are very thin, it was not anticipated that penetrating radiation would have any significant effect. Three samples from each test group were irradiated with 1 MeV electrons to 1×10^{14} and then 1×10^{15} e/cm² using the JPL Dynamitron facility. Spectral response comparisons were made for the pre and post irradiated samples between 3600 and 6000 nm, since this response region in the cell is relatively insensitive to the effects of electrons. There was no change in the spectral response for any of the samples irradiated.

Low Energy Proton Effects

This was a critical test since the energy selected guaranteed that the protons would be absorbed within the polyimide coating. Test samples from both groups were given two separate irradiations, each consisting of exposure to 1×10^{11} 50 keV protons/cm². Electrical and spectral response data was obtained after each test. In the second test, an uncovered control cell was included. Based on the severe degradation in output experienced by the control cell (Figure 3), the protons were stopped within the polyimide for both the 5 and 12.5 μm samples.

Spectral response and I-V measurements indicated no significant change between pre and post proton test data, showing that the optical properties of the films were not degraded by the protons. However, this result is slightly compromised since "bleaching" of proton induced color centers could have occurred in the period of days between the irradiation and the spectral response measurements.

Thermal Shock and Humidity Effects

Samples were exposed to 25 cycles from 20°C (room temperature) to -196°C (liquid nitrogen). Following this they were subjected to a tape peel test. There was no evidence of delamination of the polyimide coating from the solar cell. However, exposure to 168 hours of 95% relative humidity while being cycled from 25 to

65°C did show some evidence of film cracking and "crazing". Subsequent tape peel tests of these samples resulted in a loss of film adherence over approximately 25 percent of the sample. This is not unexpected since the polyimide film being evaluated has a less than optimum molecular weight.

Vacuum Ultraviolet Effects

A carefully controlled vacuum ultraviolet test was performed on 5 cell samples and a quartz plate coated with the polyimide. The test chamber was designed so that it could be removed from the test area for electrical measurements while retaining the samples in vacuum. Two control cells, one covered with quartz, the other unprotected, were included in the test matrix to provide information on system's effects such as window darkening from the uv and deposition of foreign material on the surface of the test samples.

The uv source provided an intensity of 1.5 ± 0.5 suns and the samples were held between 30 to 40°C under a vacuum better than 10^{-6} torr. The short circuit current, at 28°C, of each sample was measured periodically during the test. The results are given in Figure 4. After factoring out the system's effects, the polyimide coated cell samples (5 and 12.5 μm) were calculated to have lost between 8 to 8.5 percent in I_{sc} after 1350 hrs of uv exposure. The test was terminated when the change in polyimide transparency had appeared to cease (Figure 4). There is some evidence, based on the behavior of the control cells, to argue that the polyimide had actually degraded only 6.5 to 7.0 percent.

Pre and post test transmission measurements of the polyimide coated quartz sample show that the major loss in optical transmission occurred in the region between 3500 and 7000 nm. Unfortunately the polyimide cell samples were destroyed during an attempt to remove them from the test plate. Thus there is no post test spectral response data on the cells.

DISCUSSION

These results are highly promising since the polymer that was evaluated is an unrefined version, made from materials that were not purified to the levels that could be achieved using more sophisticated synthesizing processes. The successful demonstration that this material can be deposited by a simple spraying process and the fact that absorbed protons do not appear to cause darkening is most encouraging. The apparent stabilization and magnitude of polyimide transmission loss in uv is additional evidence to support optimism that this material has the potential to meet the requirements for space utilization. It is known that the molecular weight of the present polyimide is much less than what can be achieved. It is expected that by increasing the material's molecular weight, increased resistance to the effects of humidity can be provided.

The pre and post deposition and uv data are consistent in that no polyimide film thickness dependence was observed. It is possible that even the unrefined version of this material may be much better than results indicate. Surface contaminations or interactions between the polyimide and the cell antireflection coating might be responsible for some portion of the degradation observed in this preliminary screening.

CONCLUSIONS

A new polymer polyimide possessing optical and mechanical properties potentially suitable for space applications now exists. A preliminary evaluation of the material indicates that in its present state of development, the polyimide is not ready for space qualification. Further efforts to increase molecular weight and purify the constituents used to synthesize it are warranted. Activities addressing these needs are now being pursued. If these approaches prove successful, additional testing will take place with an emphasis on synergistic effects.

REFERENCES

1. Lindmayer, J. and Wrigley, C., "A New Lightweight Solar Cell", 12th IEEE Photovoltaic Specialists Conf., Baton Rouge, Nov. 1976, pp. 53-54.
2. Stofel, E.J. and Joslin, E.D., "Low Energy Proton Damage to Silicon Solar Cells", Aerospace Report No. TR-0059, (6250-20)-8., Oct. 1970.
3. Forestieri, A.F. and Broder, J.D., "Improvements in Silicon Solar Cell Cover Glass Assembly and Packaging Using FEP Teflon", 8th IEEE Photovoltaic Specialists Conf., Seattle, Aug. 1970, pp. 179-181.

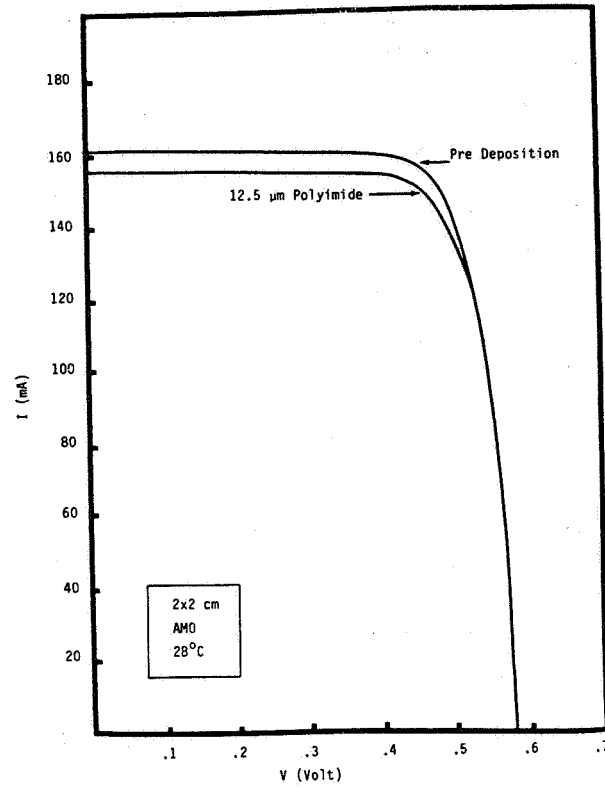


Figure 1. Effect of Polyimide on Cell Output

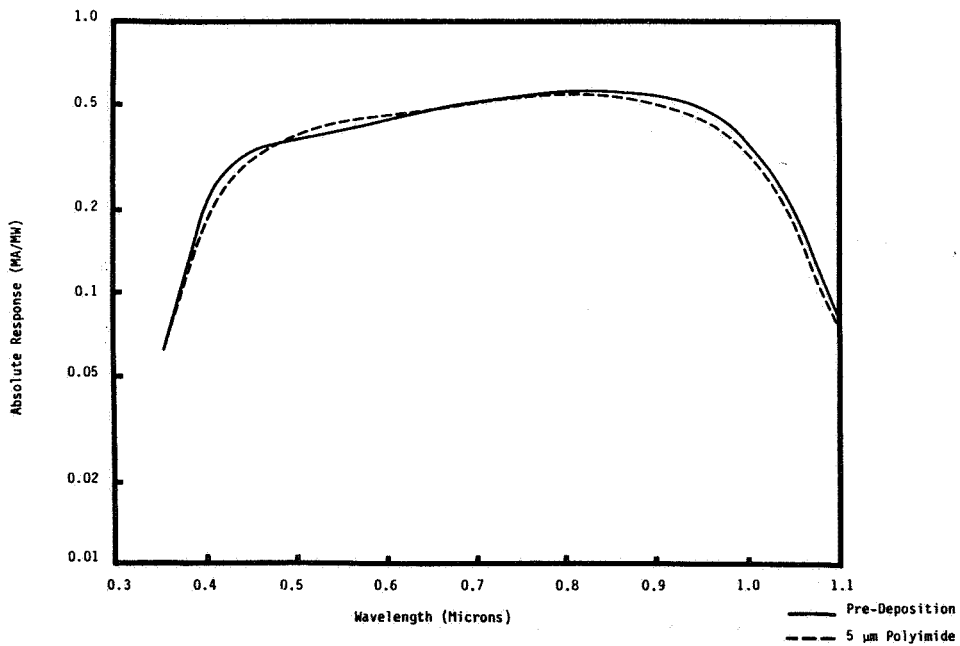


Figure 2. Effect of Polyimide on Cell Spectral Response

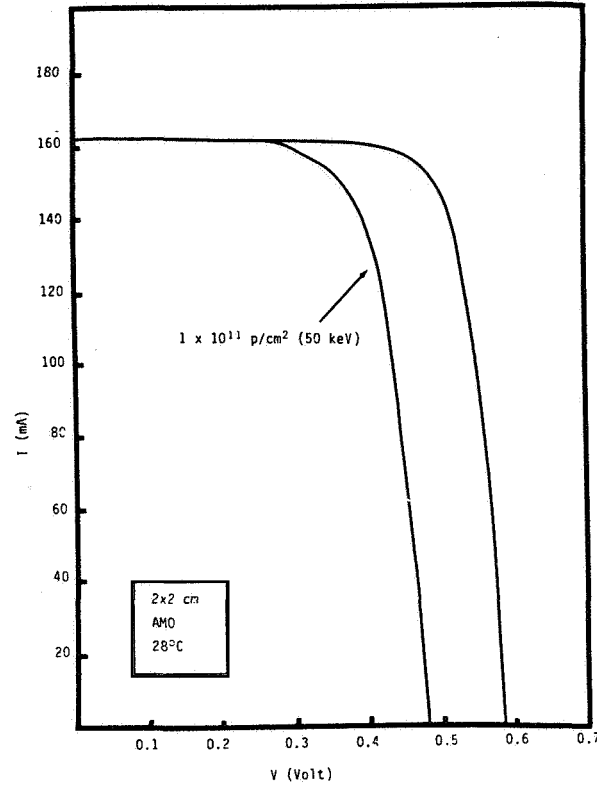


Figure 3. Effect of Protons on Unshielded Cell

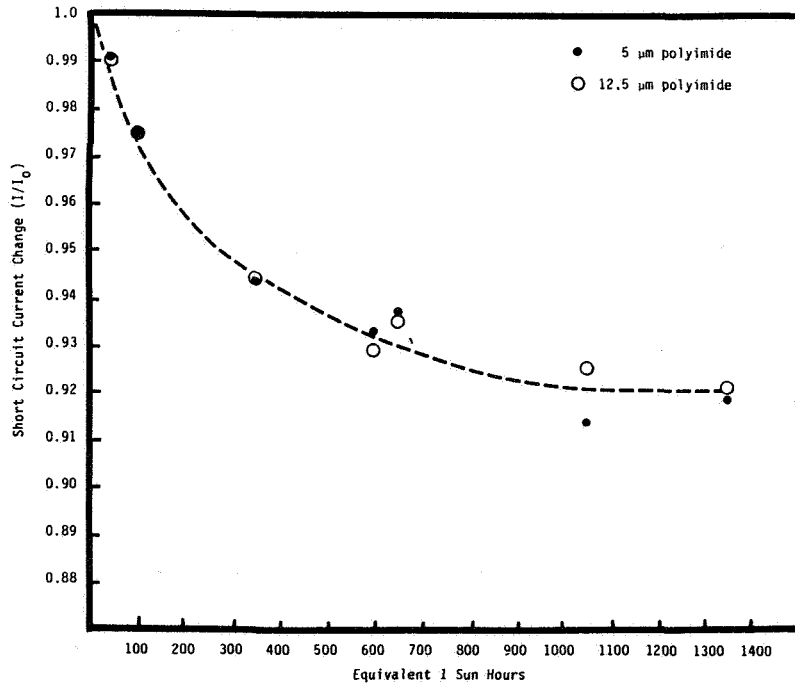


Figure 4. Effect of UV on Polyimide Coated Solar Cells

MICROSTRUCTURAL ANALYSIS OF SOLAR CELL WELDS

T.J. Moore, G.K. Watson, and C.R. Baraona
NASA Lewis Research Center
Cleveland, Ohio

SUMMARY

Parallel-gap resistance welding of silicon solar cells with copper interconnects results in complex microstructural variations that depend on the welding variables. At relatively low heat input solid-state welds are produced. At medium heat the Ag-Cu eutectic forms resulting in a braze joint. High heat produces a fusion weld with complete melting of the silver layer on the silicon-solar cell. If the silicon is also melted, cracking occurs in the silicon cell below the weld nugget. These determinations were made using light microscopy, microprobe, and scanning electron microscopy analyses.

INTRODUCTION

Parallel-gap resistance welding (PGRW) has been used extensively in the production welding of interconnects to solar cells for space-power applications. Despite the fact that thousands of welds have been made, little information has been published on the microstructure of solar-cell welds. This investigation, though limited in scope, is an attempt to characterize the various microstructures that can be obtained when welding 39- μm (1.5-mil) thick copper interconnects to 200- μm (8-mil) thick silicon solar cells by PGRW. Solar-cell welds, made using three different weld schedules, were examined by optical and scanning electron microscopies. Compositional traces were obtained with an electron probe microanalyzer.

American Welding Society (AWS) terms and definitions are used throughout this report to make the technical discussions as clear as possible. The AWS Joint Method Diagram (fig. 1) is based on the physical state of the materials at the weld interface during coalescence (ref. 1). Thus, three metallurgical classifications of welding processes are defined:

- Fusion welding for liquid/liquid reaction
- Solid-state welding for solid/solid reaction
- Brazing and soldering for liquid/solid reaction

The authors are grateful to Frank M. Terepka, who performed the electron probe analysis.

MATERIALS

Cross sectional sketches of the silicon solar cell used in this study are shown in figure 2. These cells had 2-ohm cm, P-type base resistivity, shallow

junctions and wraparound insulator type contacts. At the P contact areas, four layers of material were deposited on the silicon (Si) cell:

- (1) Aluminum (Al) about 2000 Å thick
- (2) Titanium (Ti) about 1000 Å thick
- (3) Palladium (Pd) about 250 Å thick
- (4) Silver (Ag), 9 μm thick (7 to 13 μm by metallography)

The outer layer of silver was applied for electrical conductivity. The wraparound N-type contacts had the same silver, palladium, and titanium metal layers as the P contacts. However, instead of aluminum, the first layer deposited on the silicon cell was silicon dioxide (SiO₂) dielectric about 1 μm thick. This SiO₂ layer provided electrical insulation between the N-type contacts and the P-type silicon base layer.

The copper interconnect tab was cold-rolled stock with an average thickness of 39 μm. Metallographic examination showed a thickness variation of 37 to 46 μm.

PROCEDURE

Welding Equipment

Parallel-gap resistance welding is a variation of series resistance welding in which the electrodes are placed very close together. This electrode placement tends to produce relatively high heating and formation of a fusion weld nugget between the electrode. However, by controlled adjustment of the welding variables, it is possible to produce individual solid-state welds under each electrode.

In the welding head, an assembly with two molybdenum electrodes is used. Each side is electrically insulated from the other. Both electrodes move downward together on activation of their common supporting arm. Each electrode is permitted a controlled degree of flexing, which compensates for minor irregularities in flatness or thickness. This is important because good mechanical fit insures proper electrical contact between the electrodes and the work.

A constant-voltage power supply is used to produce a dynamically controlled single pulse of welding current. Welding is accomplished at a constant, preset voltage. Initiation of the welding power is automatic when a predetermined force is applied to the work by the electrodes.

Welding Schedules

Three weld schedules were applied in welding the copper interconnects to the silicon cells. Weld voltage is a primary variable because of the direct proportionality with welding current. Heat is generated in all portions of the circuit according to the formula:

$$H = I^2Rt$$

where H is the heat in joules, I is the current in amperes, R is the resistance in ohms, and t is the time of current flow in seconds. Welding time was

the second variable in this program (table I). Electrode force, which controls interfacial resistance, and the gap between the electrodes were held constant. Thus, the three weld schedules can be described as follows:

- Schedule A: Low heat for a long time
- Schedule B: Moderate heat for an intermediate time
- Schedule C: High heat for a short time

Welds were made with the same schedules for both the P and N contact areas in the solar cells.

Weld Examination

The solar-cell welds were mounted in clear epoxy for sectioning and metallographic polishing. Cross sections of the welds were examined at various locations along the electrode footprint denoted by section A-A in figure 3. Specific examples shown in this report were at positions 30 percent and 40 percent through the joints. A flat was polished on the side of the cylindrical metallographic mounts so that the weld footprint could be clearly seen. The specific location of the weld cross section after metallographic polishing could then be measured optically.

All of the weld cross sections were polished using standard metallographic techniques. The cross sections were examined optically up to 1000x. Although the welds were examined in both the unetched and etched conditions, all of the photomicrographs shown are in the unetched condition.

Selected samples were examined using a scanning electron microscope (SEM). Various areas of the samples were qualitatively analyzed using energy dispersive spectroscopy (EDS). In addition, an electron probe microanalyzer was used to obtain quantitative elemental distribution along continuous-line traverses through the weld regions.

RESULTS AND DISCUSSION

In the results to follow, an overview showing the electrode positions and the kinds of welds that were obtained with the various weld schedules will first be shown at 100x magnification. Higher magnification light photomicrographs with corresponding microprobe chemical analyses of the various weld joints will then be presented and discussed. The SEM was used to further examine braze areas, the solid-state weld interface and the SiO₂ layer at N contact area of the cells.

Schedule A Welds

The N contact weld shown in figure 4 (40 percent through the joint, table I) is a combination of solid-state welding and brazing. The SEM photomicrograph in figure 5 shows that dendrites in the braze metal are oriented normal to the braze interface, which is parallel to the expected direction of solidification. This shows that Cu interconnects can be joined to the Ag layer on the cell by resistance brazing rather than by conventional fusion resistance welding.

Ag-Cu solid-state welded areas (fig. 4) were present towards the outsides of the electrode footprints beyond the brazed regions.

Solid-state welding is achieved instantaneously when the resistance heated Ag and Cu surfaces are brought into intimate contact. Welding occurs at about $0.8 T_m$ of Ag (710°C), where T_m is the absolute melting point of silver. Since the metallic bonds are believed to form on contact, since diffusion is not the cause of adhesion (ref. 2), and since the welding time is short (100 ms or less), the term solid-state resistance welding is a more appropriate term than is diffusion welding (ref. 1). Solid-state welding was judged to be achieved if microexamination of unetched joints up to 1000x revealed no unwelded areas. Subsequent microprobe examination showed that in the solid-state weld areas, only a small amount of interdiffusion had occurred between Ag and Cu.

An instant after solid-state welding occurred under the electrodes, a Ag - 40-atomic-percent-Cu eutectic composition formed at, or very near, the solid-state weld interface and became a liquid phase when the joint was heated to 779°C (fig. 6 and ref. 3). When the eutectic formed, it flowed by capillary action and brazed unwelded areas of the joint. The brazing action can continue with Ag-Cu alloys of varying composition as resistance heating increases the temperature of the melt well above the eutectic temperature. The complexity of the metallurgical situation is considerable. For example, when initially solid-state welded areas are heated above the Ag-Cu eutectic temperature, they become molten and thus part of the brazed area of the joint. Note in figure 4 that there are unwelded areas between the electrodes and towards the outside of the electrode footprints. The former area is believed to contain trapped air which, as will be shown later, can result in voids in braze metal or in a weld nugget.

At the N contact weld just discussed, less heating effect was observed than at a P contact weld where brazing occurred between the electrodes (not shown). However, insufficient data are available to demonstrate whether this effect correlates with the contact area welded or with other welding variables.

Schedule B Welds

The two weld cross sections in figure 7 show a considerable difference in microstructure for the same weld schedule. This variation is at least partly due to the fact that maximum heating occurs midway through the joint. The P contact weld cross section (fig. 7(a)), was taken 30 percent through the joint. It shows a braze joint in the electrode gap and under the inside of the electrode footprints. A line of small pores is present in the Ag-Cu braze metal. Solid state welding took place beyond the braze.

More heating is evident at the N contact cross section of figure 7(b), 40 percent through the joint. In this case all of the silver has been melted between the electrodes to form a fusion weld nugget. This nugget is a Ag-Cu alloy. A brazed region borders the nugget, and solid-state welding took place beyond the limits of the braze.

The small pores in the braze joint of figure 7(a) and the large pores in the fusion weld of figure 7(b) are believed to be air bubbles formed in the molten braze or weld metal (discussed previously regarding fig. 4). The localized trapped air effect is also believed to have produced the bulge in the copper interconnect between the electrodes (fig. 7(b)).

Schedule C Welds

In figure 8 two fusion welds are shown with brazes and solid-state welds towards the outside of the electrode footprints. The weld nugget at the N contact (30 percent through the joint) is a Ag-Cu alloy (fig. 8(a)). The 1- μm SiO_2 layer on the cell acted as a refractory material to contain the Ag-Cu melt and thus prevent the nugget from alloying with the silicon. The SiO_2 layer also inhibited solid-state diffusion and possible formation of the Ag-15.4 atomic percent silicon eutectic which melts at 830° C (ref. 3 and fig. 9). Although no cell cracking is evident in figure 8(a), fine cracks in the silicon cell were observed under another similar Ag-Cu weld nugget.

At the P contact weld (40 percent through the joint) (fig. 8(b)) no protective SiO_2 layer was present on the silicon cell. This weld is similar to the N contact weld except that the weld nugget here is a Ag-Cu-Si-Pd alloy. The lens-shaped crack, observed under the weld nugget in fig. 8(b) is typical for all cases where the silicon cell was melted. Several factors contribute to the cracking. First of all the silicon cell has essentially no ductility at room temperature. Thus, local thermal shock alone could produce cracking. Second, solidification shrinkage of the pancake-shaped weld nugget must produce some deformation, that is, dishing under the weld nugget. Third, residual stresses are produced when the weld nugget contracts on cooling from the solidification temperature to room temperature, with the maximum residual stress being limited to the yield strength of the Ag-Cu-Si-Pd alloy (refs. 4 and 5).

Electron Probe Microanalysis

Electron-probe, continuous-line traverses were run on all three metallurgical classes of welds between the copper interconnect and the silicon cell:

- (a) Solid-state weld between Ag and Cu
- (b) Ag-Cu braze joint
- (c) Two fusion weld nuggets; one Ag-Cu, the other Ag-Cu-Si-Pd

For each weldment examined, microprobe traces confirmed the presence of thin layers of titanium and palladium, which had been intentionally deposited on the contact surface of the Si cells during manufacturing. These titanium and palladium microprobe traces are not shown in the figures for purposes of clarity. No attempt was made to confirm the presence of aluminum at the P contacts.

The solid-state weld joint of figure 10 shows a small amount of Ag-Cu interdiffusion. Interdiffusion between silver and silicon was nil. The dark band (about 1 μm wide) between the silicon and silver and the increase in microprobe specimen current in this vicinity gave evidence of the SiO_2 layer on the cell at this and other N contact areas.

This Ag-Cu braze joint (fig. 11) is only about 2.5 μm wide. Because of equipment limitations, it could not be established that the braze metal was of the eutectic composition. But the microprobe trace does show significant alloying near the Ag-Cu interface. Interdiffusion between silver and silicon was nil. Since this is a P contact area, no SiO_2 layer was present.

A microprobe trace of a Ag-Cu fusion weld nugget containing large trapped voids is shown in figure 12. In this case the silver coating was com-

pletely melted and formed an alloy of about 50 Ag - 50 Cu (weight percent). The 1- μm SiO_2 refractory layer in the N contact area protected the cell. Thus, the molten weld metal nugget was prevented from alloying with the silicon solar cell.

The fusion weld nugget (fig. 11) is an alloy of Ag-Cu-Si and palladium. Although the quantity of palladium was very slight, the microprobe traverse showed alloying of palladium in the weld nugget. The melting and alloying of the silicon cell is evident by the wavy nugget/cell weld interface and by the microprobe trace. Since this was a P contact, there was no protective SiO_2 coating on the cell. Two cracks are shown in figure 13 in the silicon below the weld nugget. Lens-shaped cracking of this type occurred below the nugget in all cases where the silicon was melted, and thus became part of the weld.

CONCLUSIONS

1. Three metallurgical categories of resistance welds were identified under various conditions of parallel-gap resistance welding:

(a) Low heat for a long time: Combination solid-state welding and brazing under each electrode with an unwelded area between the electrodes.

(b) Moderate heat, intermediate time: A Ag-Cu braze joint between the electrodes with solid-state welding at the periphery.

(c) High heat for a short time: A conventional fusion weld nugget between the electrodes with brazing and solid-state welding at the periphery. This kind of weld is always accompanied by cracking in the Si cell if melting of the Si occurs.

2. The 1- μm layer of SiO_2 at the N contact areas of the cell proved to be a refractory barrier that contained the molten weld nugget and prevented interaction with the Si cell.

RECOMMENDATIONS

1. Programs to develop solar array welding technology should start with well-defined metallurgical goals.

2. The weld joint metallurgy required to give optimum solar-cell reliability should be identified.

3. The welding process, associated control systems, and NDE procedures should be tailored to give assurance that the metallurgical goals are achieved.

REFERENCES

1. Welding Terms and Definitions. American Welding Society, A3.0-80, 1980.
2. Ludemann, W. D.: A Fundamental Study of the Pressure Welding of Dissimilar Metals Through Oxide Layers. UCRL-50744, 1969.
3. Hansen, M.: Constitution of Binary Alloys. McGraw-Hill Book Co., Inc., 1958.
4. Linnert, G. E.: Welding Metallurgy. Vol. 2. American Welding Society, 1967.
5. Lancaster, J. F.: The Metallurgy of Welding, Brazing and Soldering. George Allen and Unwin Ltd., 1965.

TABLE 1. - PARALLEL-GAP RESISTANCE
WELDING SCHEDULES

[Electrode force, 8.9 N (2.0 lb); electrode pressure, 6.1×10^6 N/m² (885 psi); electrode gap, 0.30 mm.]

Schedule	Weld voltage, V	Weld time, ms (a)
A	0.58	100
B	.63	80
C	.68	50

^aApproximate

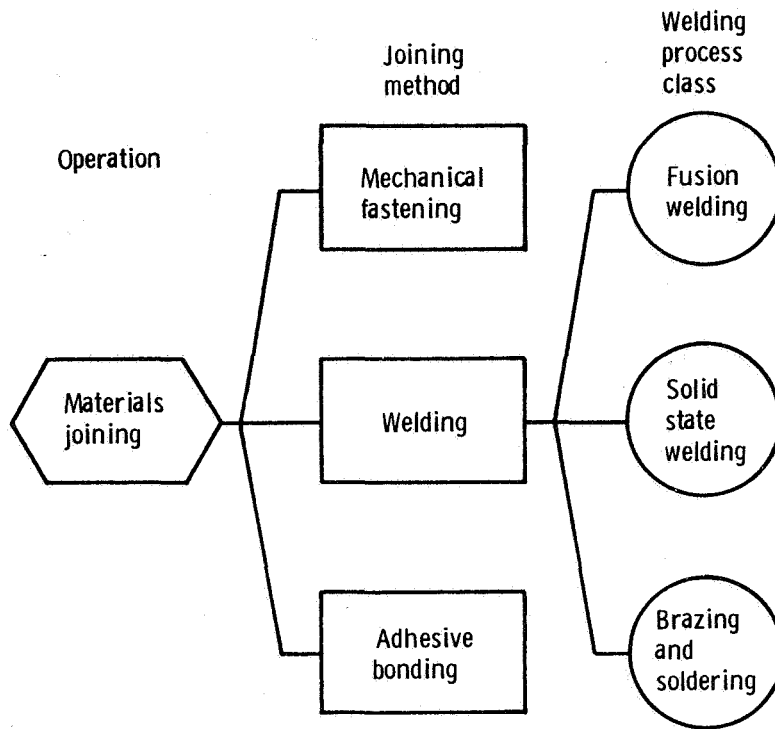


Figure 1. - Joining method diagram.

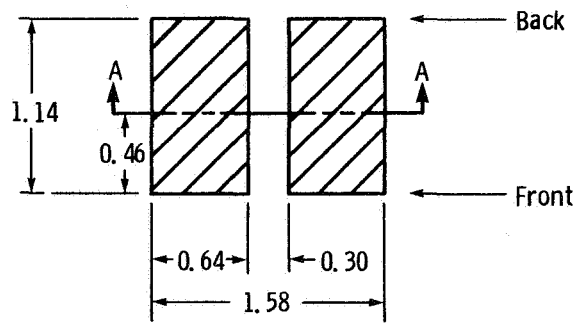


Figure 2. - Sectioning procedure.

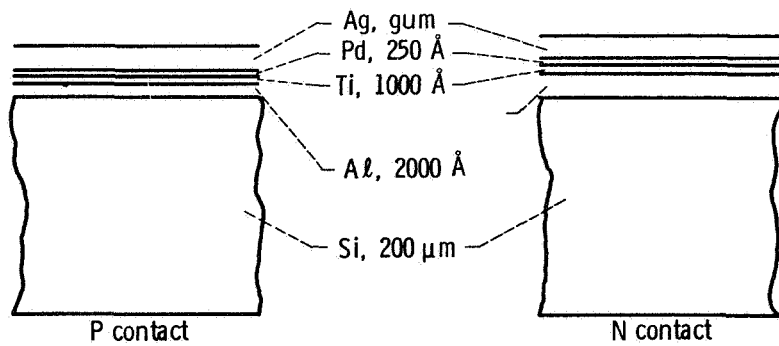


Figure 3. - Cell contacts.

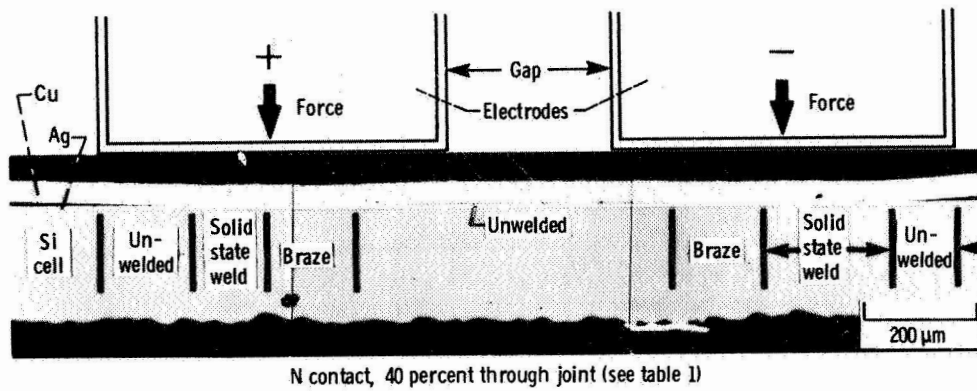


Figure 4. - Schedule A combination solid-state weld and braze joint. Air is believed to be in the unwelded area between the electrodes.

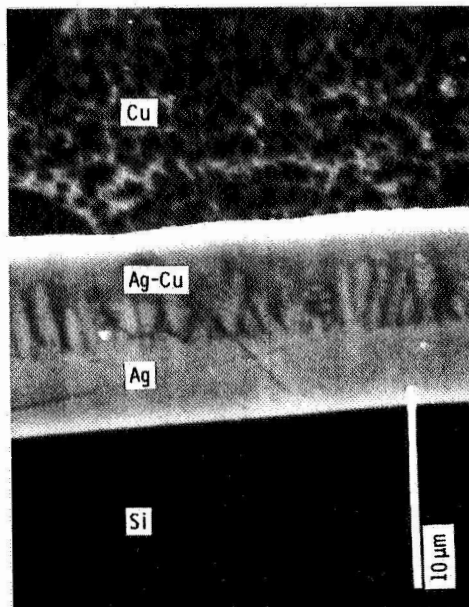


Figure 5. - Dendritic structure of an Ag-Cu braze metal in a schedule A weld at an N contact.

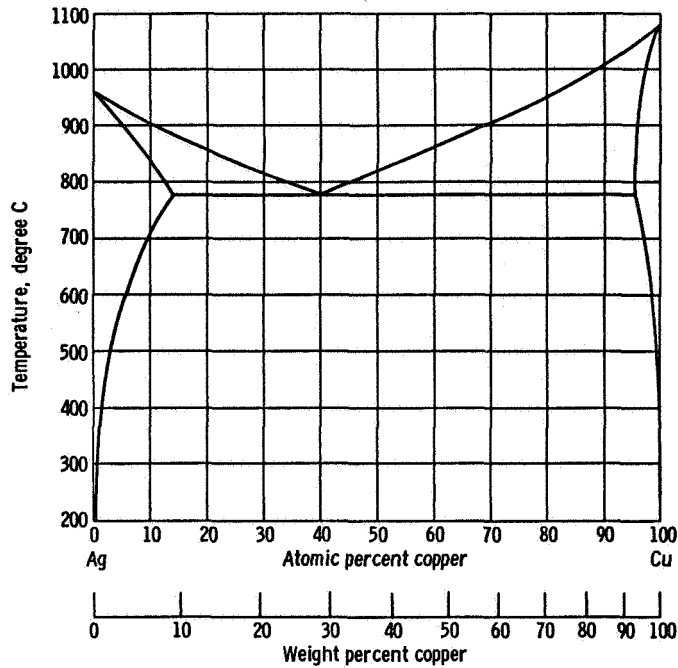
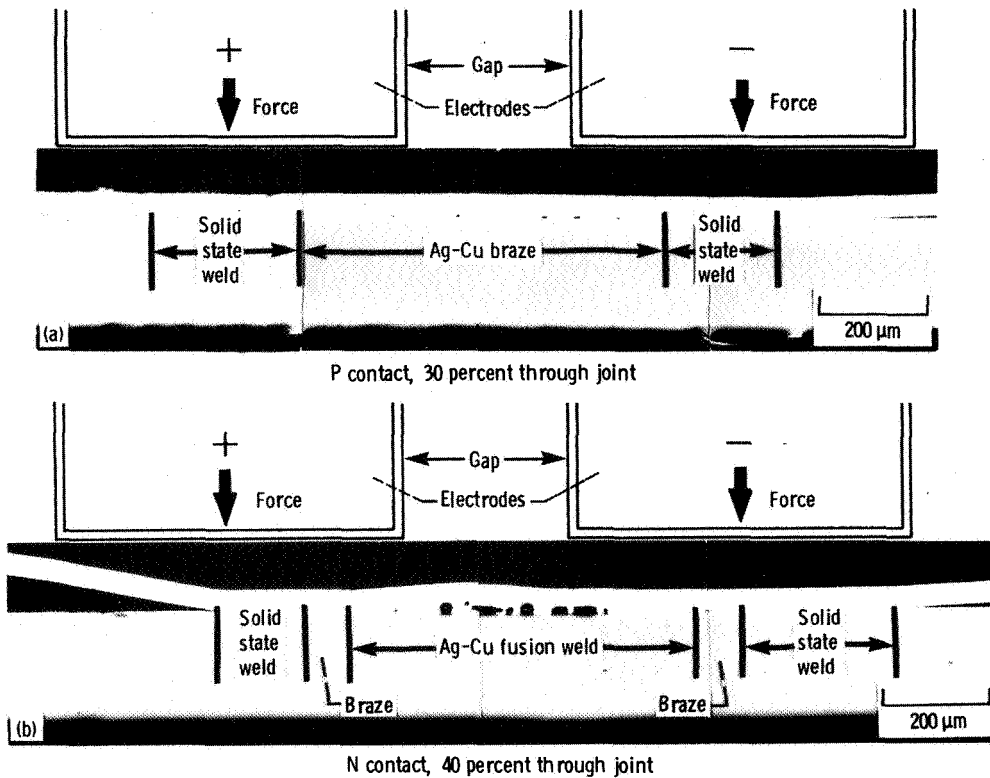
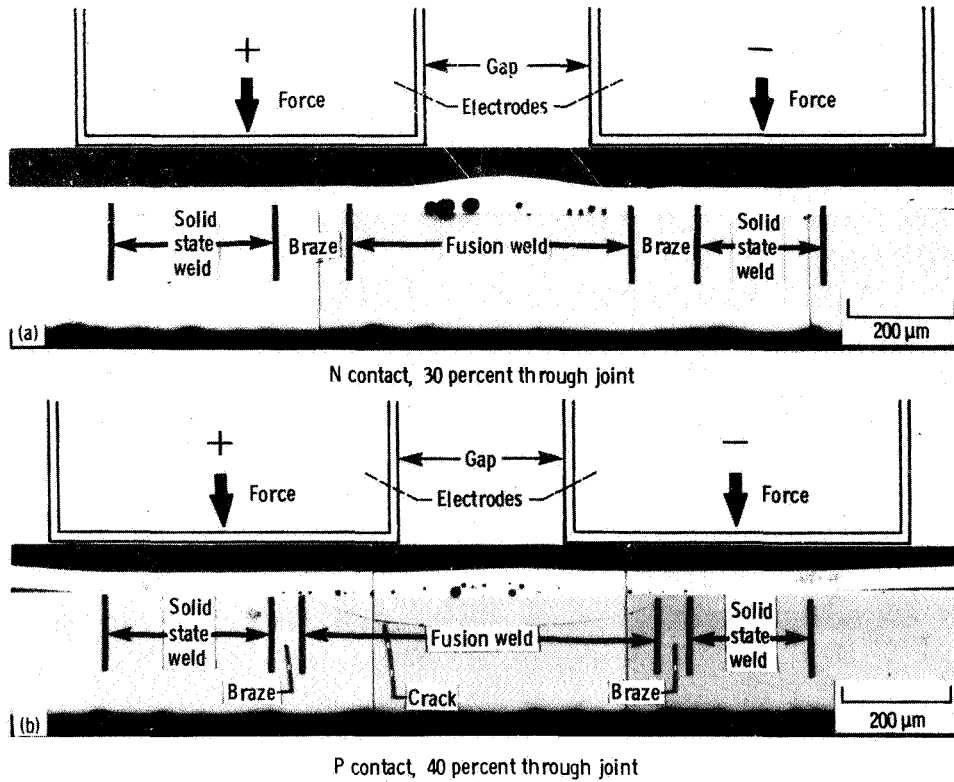


Figure 6. - Silver-copper equilibrium diagram (ref. 3).



- (a) Braze between electrodes with small voids in braze metal. Solid-state welds are outside of braze region.
- (b) Porous Ag-Cu fusion weld nugget producing bulge with brazing and solid-state welding outside of the nugget.

Figure 7. - Microstructural variations in schedule B welds.



- (a) Porous Ag-Cu fusion weld nugget with brazing and solid state welding outside nugget.
- (b) Porous Ag-Cu-Si-Pd fusion weld with brazing and solid state welding beyond the nugget. A lens-shaped crack in the silicon cell is present under the fusion weld.

Figure 8. - Microstructural variations in schedule C welds.

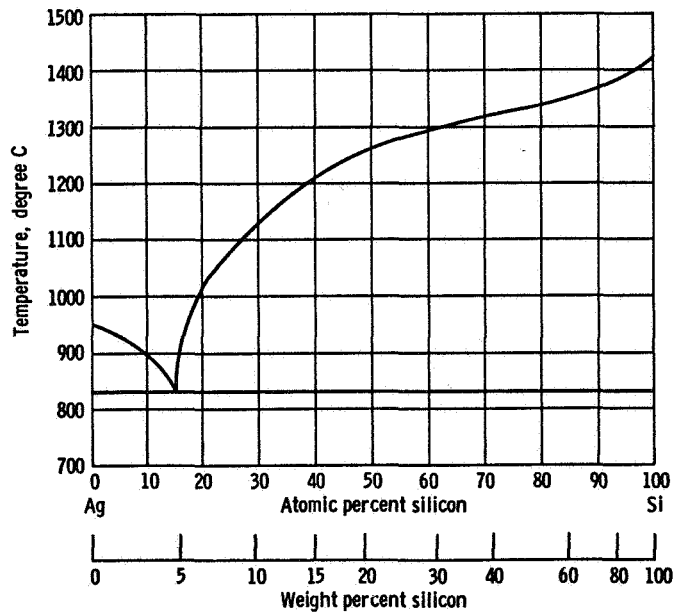


Figure 9. - Silver-silicon equilibrium diagram (ref. 3).

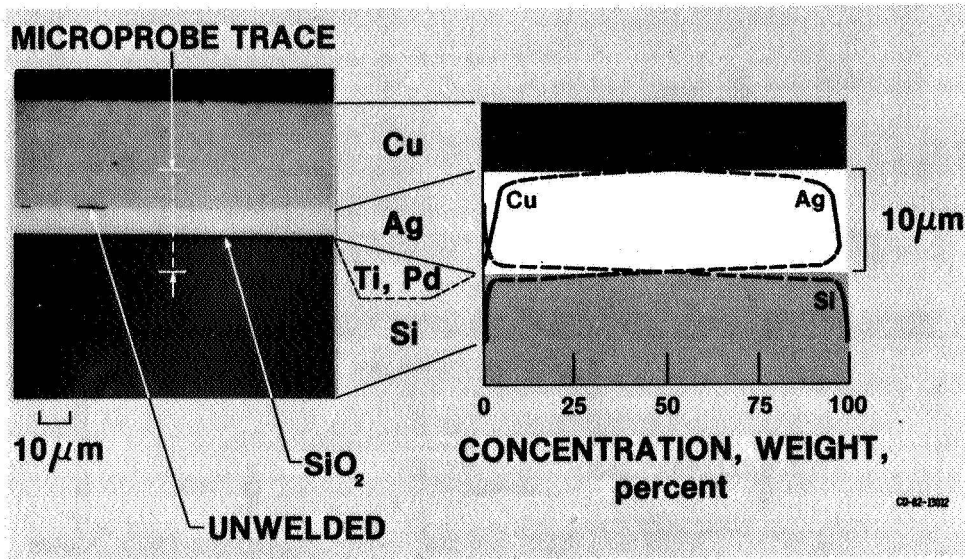


Figure 10. - Solid state weld at N contact area showing slight interdiffusion between silver and copper. Schedule C; weld under electrode.

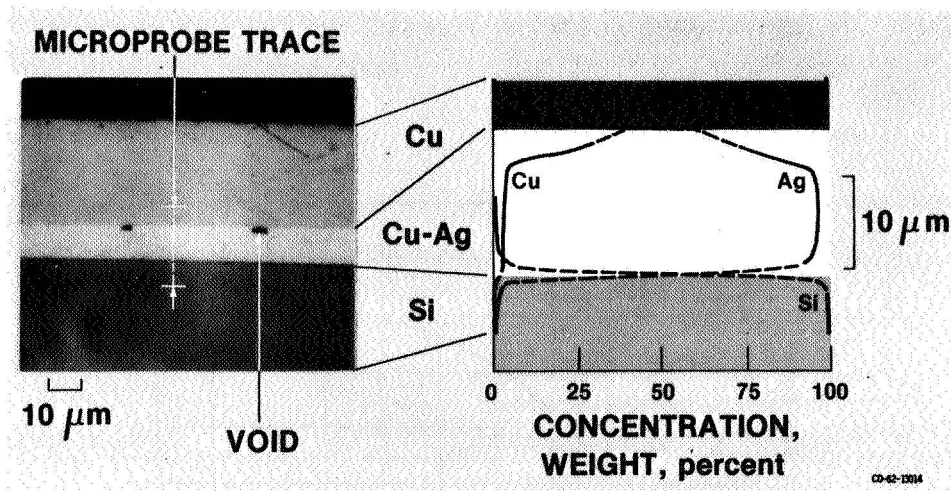


Figure 11. - Silver-copper braze joint, approximately 2.5 μm wide, with small voids in braze metal. Significant Ag-Cu alloying is shown at braze in this P contact joint.

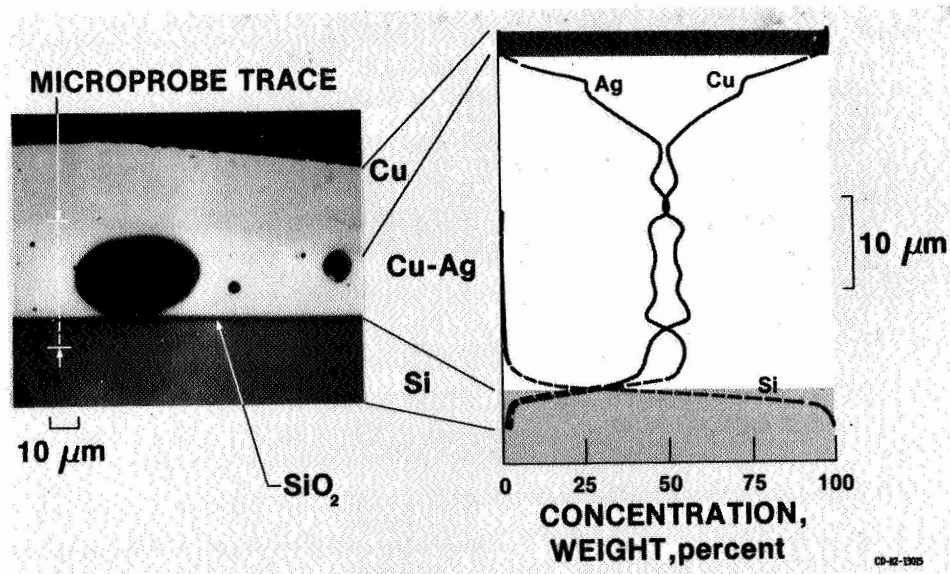


Figure 12. - Fusion weld nugget of Ag-Cu alloy at N contact with complete melting of silver layer. Schedule C; weld between the electrodes.

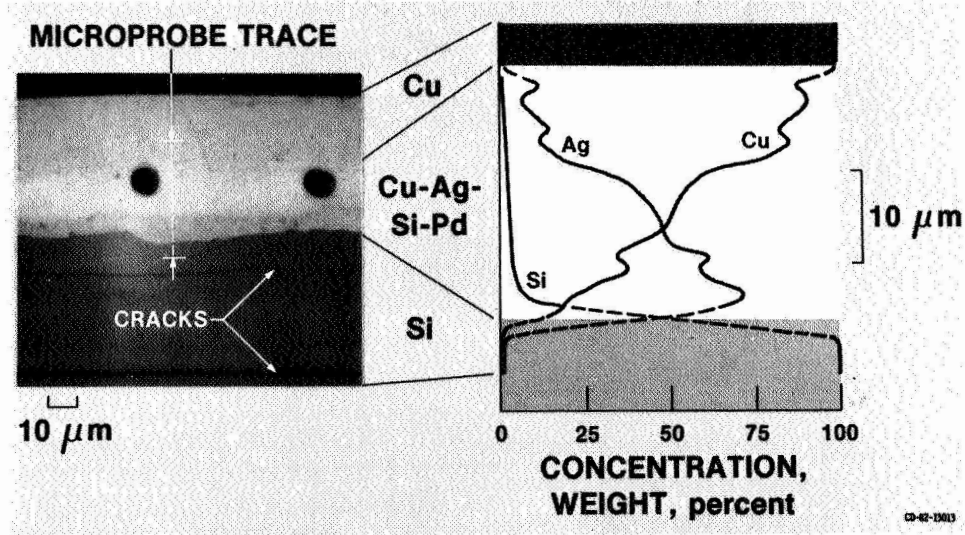


Figure 13. - Fusion weld nugget of Ag-Cu-Si-Pd alloy at P contact showing cracking in the silicon cell layer. Schedule C; weld between the electrodes.

EVALUATION OF SOLAR CELL WELDS BY SCANNING ACOUSTIC MICROSCOPY

S.J. Klima, W.E. Frey, and C.R. Baraona
NASA Lewis Research Center
Cleveland, Ohio

SUMMARY

Scanning laser acoustic microscopy was used to nondestructively evaluate solar cell interconnect bonds made by resistance welding. Both copper-silver and silver-silver welds were analyzed. The bonds were produced either by a conventional parallel-gap welding technique using rectangular electrodes or new annular gap design with a circular electrode cross section. With the scanning laser acoustic microscope, it was possible to produce a real time television image which reveals the weld configuration as it relates to electrode geometry. The effect of electrode misalignment with the surface of the cell was also determined. A preliminary metallographic analysis was performed on selected welds to establish the relationship between actual size and shape of the weld area and the information available from acoustic micrographs.

INTRODUCTION

Welding is becoming an increasingly attractive alternative to soldering as a means of joining interconnect tabs to solar cell contact surfaces. The potential advantages include reduced weight, ability to withstand higher peak operating temperatures, increased thermal fatigue resistance, and improved automation capability for fabricating large arrays. Although the idea of welded solar cell interconnects is not new (ref. 1), acceptance of the technology remains limited due to a lack of experience in space flight applications and the need for a reliable technique for nondestructively evaluating bond quality. Whereas visual examination is generally sufficient for evaluating solder joints, welded joints require more sophisticated procedures because the bond area is hidden from view. Therefore, welded solar cell interconnect joints can be nondestructively evaluated only by indirect methods. The scanning laser acoustic microscope, which combines laser technology with ultrasonic technology, appears to be a good choice for this application. The instrument is capable of operating at high ultrasonic frequencies with resultant high resolution and, at 100 MHz, can produce a real-time image of an area about 2.3 by 3 mm in size at a magnification of 75.

It has previously been shown (ref. 2) that acoustic images of welded solar cell interconnect joints can be produced with the scanning laser acoustic microscope. However, substantiating evidence relating weld geometry to the acoustic information was not presented. It was the purpose of this investigation, therefore, to show that a relationship does exist between actual weld area and the results obtained with the acoustic microscope. This was accomplished by generating acoustic micrographs of welds having various geometric configurations and using the acoustic images to map out areas to be sectioned for metallographic analysis. Correlations between acoustic results and bond area were thus obtained.

MATERIALS, APPARATUS, AND PROCEDURE

Welding

Two types of electric resistance weld electrodes (fig. 1) were used to make the welds that were analyzed in this program. Figure 1(a) shows a pair of conventional parallel-gap electrodes made of molybdenum. The tips were rectangular in cross section measuring 0.65 by 1.25 mm on a side, with a gap of 0.25 mm. Figure 1(b) shows a new annular-gap electrode design, also made of molybdenum, which consists of a center electrode surrounded by an annular electrode. (The annular gap design was developed at the Lewis Research Center by C. R. Baraona and A. F. Forestieri). The outside diameter of the annulus was 2.0 mm and the inside diameter was 1.5 mm. The gap width was 0.13 mm.

The interconnect materials were either copper or silver foil, 0.05 mm thick. Solar cells were 2 by 4 centimeters and had wraparound contacts. The cells were not encapsulated in or attached to a solar array substrate or blanket material such as Kapton or aluminum honeycomb. The parallel-gap welds were made on glass covered cells, 400 μm thick, while the annular-gap welds were made on uncovered cells, 225 μm thick. The interconnects were welded to both positive and negative contact surfaces. Voltage settings ranged from 0.6 to 1.0 V, applied for 50 to 100 ms. The electrode tips maintained a load of 9 to 36 N on the tab for the duration of the welding operation.

Nondestructive Evaluation

The scanning laser acoustic microscope and its principles of operation are described in detail in reference 3. Figure 2 shows a sketch illustrating the application of the acoustic microscope for evaluation of solar cell welds. The solar cell is placed on the sample stage with the interconnect tab on top. A coverslip consisting of a clear plastic material and a film of gold a few angstroms thick on one surface is placed on top of the tab. The purpose of the coverslip is to provide a reflective surface for the laser beam in instances where the surface of the material being evaluated is not sufficiently reflective. The ultrasonic transducer, located at the bottom of a shallow well in the top surface of the sample stage, produces continuous waves at a frequency of 100 MHz and an incident angle of 10° to the cell surface. The ultrasonic waves are transmitted through the water couplant and into the solar cell. The energy is further transmitted into the interconnect tab wherever bonding exists. The interaction of sound waves at an angle to the top surface of the interconnect tab sets up a dynamic ripple which is then transmitted to the cover slip by a water coupling medium. A laser beam constantly scans the area in raster fashion. The intensity of the reflected laser light is modulated by the dynamic ripple and is proportional to the amplitude of sound waves at the reflective surface of the coverslip. These variations in light intensity are seen by the photodetector as an AC signal which is processed and used to produce a real-time TV image in black and white. The brightest regions on the screen represent areas of highest ultrasonic amplitude and black regions are indicative of little or no ultrasonic transmission. The real-time image covers an area 2.3 by 3 mm on a side at a magnification of 75. Acoustic micrographs at a magnification of 32 were made by photographing the TV screen using Polaroid film.

Metallography

To determine the ability of the acoustic microscope to provide visual evidence of the integrity of interconnect-cell bonds, it was necessary to perform a destructive analysis on selected welds. This was accomplished by selecting welded joints that produced unique or interesting patterns on the acoustic micrographs and sectioning the cell to permit a cross sectional view of the bond line between the interconnect tab and the solar cell contact. Sectioning was done with a dicing saw. The weld specimens thus removed were mounted on edge in an epoxy encapsulation that served as a specimen holder. The encapsulated specimens could then be ground in specified increments to obtain views of planes at predetermined locations within the weld joint. The extent of the bond or nonbond in each plane was determined metallographically. Standard techniques were used to polish the metallographic specimens. Since a complete microstructural study of the weld joint was not required, photo-micrographs were taken of the surfaces in the unetched condition only. Surfaces were considered to be bonded when no interfacial features indicative of disbond could be detected at a magnification of 750.

RESULTS AND DISCUSSION

Results obtained with the scanning laser acoustic microscope and the related metallographic analyses are presented in figures 3 to 5. Each figure shows a photograph of the surface of the interconnect tab after welding, an acoustic micrograph of the region of the weld, and a photomicrograph of a crosssection through the middle of the weld. The ability of the acoustic microscope to describe the size and shape of the bonded area is discussed.

Figure 3 shows the results obtained from an analysis of a joint made by welding a copper interconnect tab to a silver solar cell contact using the parallel-gap resistance welding technique. A partial imprint of the electrode pair was embossed in the surface of the relatively soft copper (fig. 3(a)). The partial imprint indicates that the electrodes applied nonuniform pressure to the tab, probably because of a minor misalignment relative to the solar cell surface. A complete imprint would consist of two parallel rectangles which resemble footprints. Figure 3(b) is an acoustic micrograph of the weld and surrounding area. On first observation it was not clear whether the weld zone was represented by the white region of the acoustic micrograph only or by the white area plus the smaller gray area immediately to the left. Thus, the actual size and shape of the weld had to be accurately determined by other means. This was accomplished in two ways. First, it was found that the unbonded part of the copper tab could be removed by folding it back over the bonded part and carefully tearing it at the perimeter of the weld nugget with tweezers, leaving the welded part of the tab in place. The result of this operation is shown in figure 3(c). The welded copper material is intact in the center of the picture, surrounded by the silver solar cell contact surface. The black residue on the contact surface is a material of unknown origin which was present beneath the unbonded part of the tab. Note the partial footprint of the right hand electrode which covers almost half of the welded copper tab. It is obvious that the weld nugget was not centered between the electrodes nor was it confined to the region beneath the electrodes. It is also apparent that, although the electrode footprints provide some information regarding the general location, they say little about either the size or the shape of the weld. Figures 3(b) and (c) show that the weld is represented only by the white area on

the acoustic micrograph, which closely approximates the size and shape of the weld nugget. Although not apparent in this series of photographs, it was further observed that the acoustic microscope can also reveal the location of the weld relative to a feature such as the edge of the tab, which is visible in the top of figure 3(a).

Additional information about the dimensions of the weld zone as well as the nature of the bond was obtained through a metallographic analysis. Figure 3(b) shows two dark spots within the white region of the acoustic micrograph, indicating the presence of defects which blocked ultrasonic transmission. A cross section through the larger of these defects is shown in figure 3(d). The photomicrograph reveals a bonded section measuring 0.78 mm long with a nonbonded portion in the middle. The nonbond, which corresponds to the dark spot on the acoustic micrograph, is 225 μm long and only 4 μm wide. Other bondline pores less than 30 μm in diameter are visible in the photomicrograph but were not resolved individually in the acoustic micrograph.

Figure 4 presents the results of an analysis of a joint made by welding a silver interconnect tab to a silver solar cell contact using the annular-gap electrodes. The electrode imprint on the tab surface is shown in figure 4(a). The circular feature was made by the annular electrode, and the spot in the middle is the result of pressure applied by the center electrode. The imprint on the tab is closely approximated in size and shape in the acoustic micrograph (fig. 4(b)), indicating that welding occurred beneath a major portion of the circumference of the annular electrode and the middle part of the center electrode. Supporting evidence is shown in the photomicrograph of a cross section through the middle of the weld (fig. 4(c)). Two bonded sections, one in the middle of the photomicrograph and one on the right side, correspond to white areas of ultrasonic transmission in the acoustic micrograph. Little or no bonding is evident on the left side of the photomicrograph, which agrees with the information in the acoustic micrograph.

Figure 5 shows the results obtained from another silver-silver weld made with annular-gap electrodes. The imprint embossed in the tab surface (fig. 5(a)) looks similar to the one in figure 4(a). However, the acoustic micrograph (fig. 5(b)) indicates that the weld geometry is quite different from that in figure 4. Bonding appears to have taken place primarily under one side of the annular-gap electrode, completely spanning the gap. Little bonding appears to have taken place under the other half. The photomicrograph (fig. 5(c)) of the cross section through the middle of the weld confirms the information obtained from the acoustic micrograph. With the exception of some bondline porosity, the bond between the tab and the metallized contact is continuous under the right hand side of the electrodes. On the left, little or no bonding exists, again confirming the evidence presented in the acoustic micrograph.

CONCLUDING REMARKS

The scanning laser acoustic microscope appears to be a viable tool for non-destructive evaluation of solar cell interconnect bonds made by welding. Metallographic analyses of selected welds showed that acoustic microscopy can accurately determine the size and shape of welded areas in both uncovered cells and cells with a protective glass cover adhesively bonded to the front surface. Although the glass cover and adhesive increase scatter and decrease

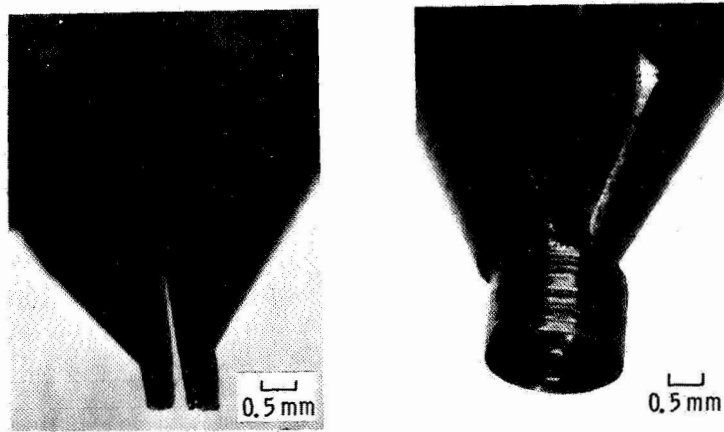
resolution, the adverse effects appear to be small, and the final result is acceptable for cells in the thickness range evaluated in this investigation.

In addition to generally describing the size and shape of weld areas, the acoustic microscope demonstrated a capability for detecting small nonbonded areas of the order of 200 μm diameter within an otherwise continuous weld zone. Conversely, it is expected that welded areas 200 μm diameter and larger could be detected against a background of unwelded material.

The results of this investigation suggest that application of scanning laser acoustic microscopy can be extended from individual solar cells to solar cell arrays, providing the cells are not encapsulated or attached to a substrate or blanket material in such a way as to block the transmission of acoustic energy. Any air gap between the substrate and the cell in the region to be nondestructively evaluated would preclude evaluation by ultrasonic transmission. It is therefore recommended that array manufacturers consider the requirements for successful nondestructive evaluation in the design stage to insure that accommodations for adequate inspection are made.

REFERENCES

1. Reinhartz, K.; and Capart, J.: Status of Welded Solar Cell Module Technology at ESRO, Proceedings of the Eighth IEEE Photovoltaic Specialists Conference, 1970.
2. Stella, P. M.; Vorres, C. L.; and Yuhas, D. E.; SLAM Examination of Solar Cells and Solar Cell Welds. Presented at the Fifteenth IEEE Photovoltaic Specialists Conference, May 12-15, 1981.
3. Kessler, L. W.; and Yuhas, D. E.: Acoustic Microscopy - 1979. Proceedings of the IEEE, Vol. 67, No. 4, April 1979.



(a) Conventional parallel-gap electrodes.
 (b) Annular-gap electrodes.

Figure 1. - Resistance weld electrodes used for joining solar cell interconnects.

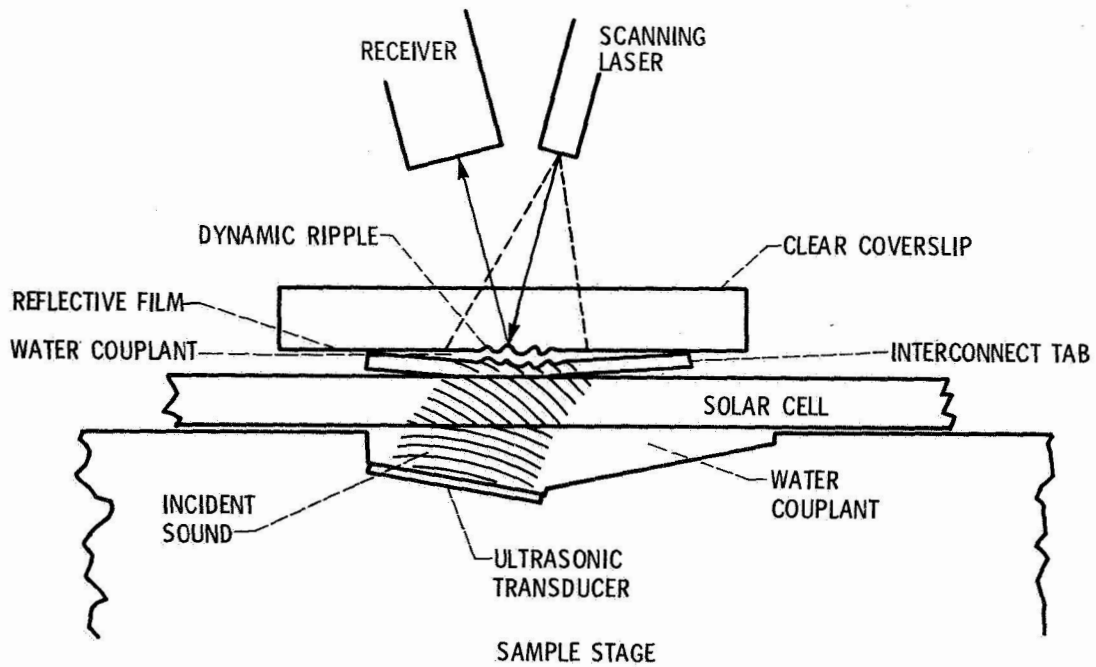
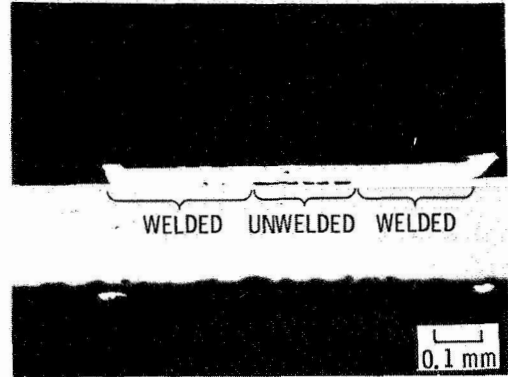
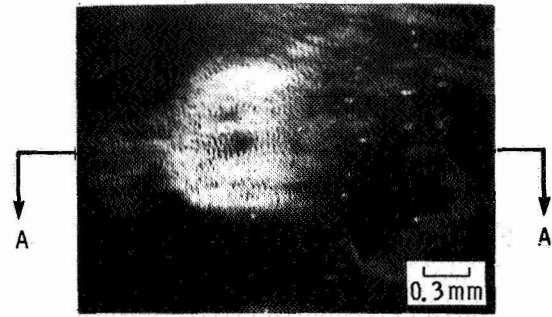
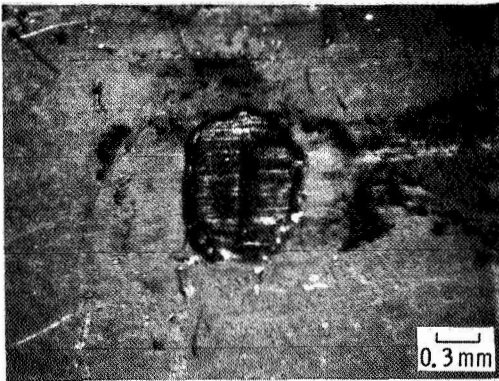
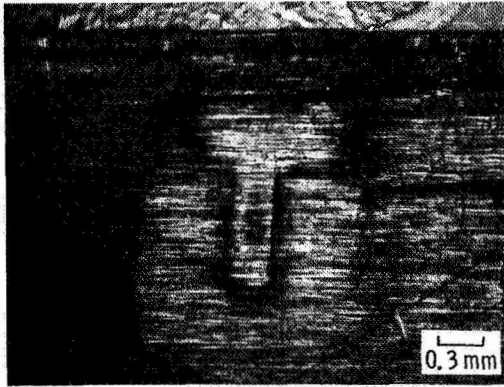
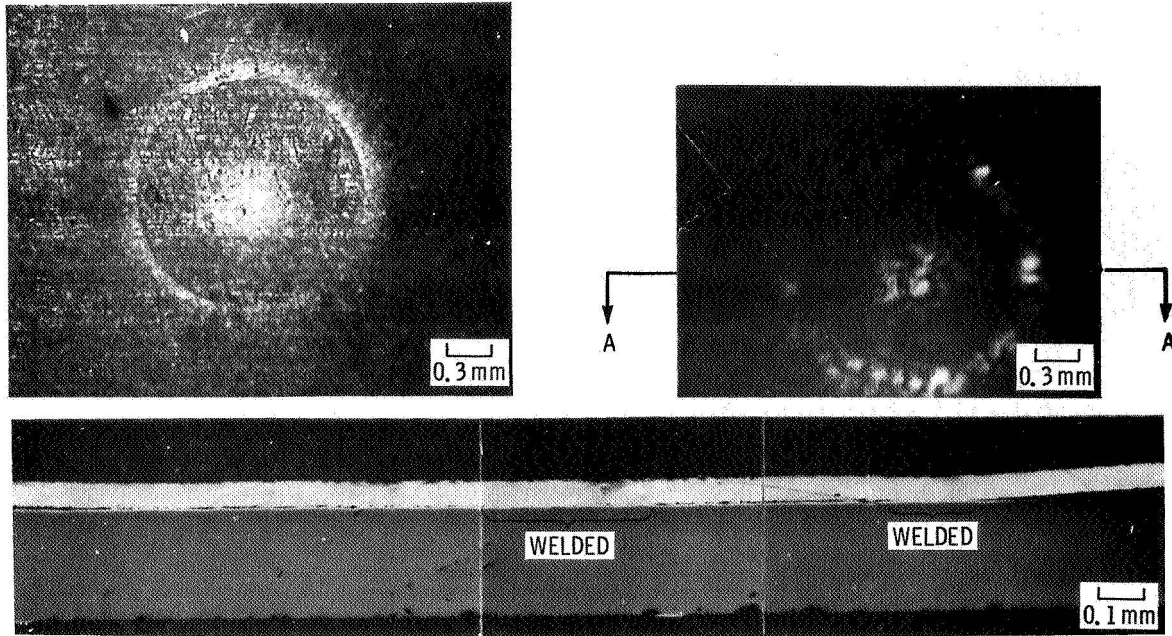


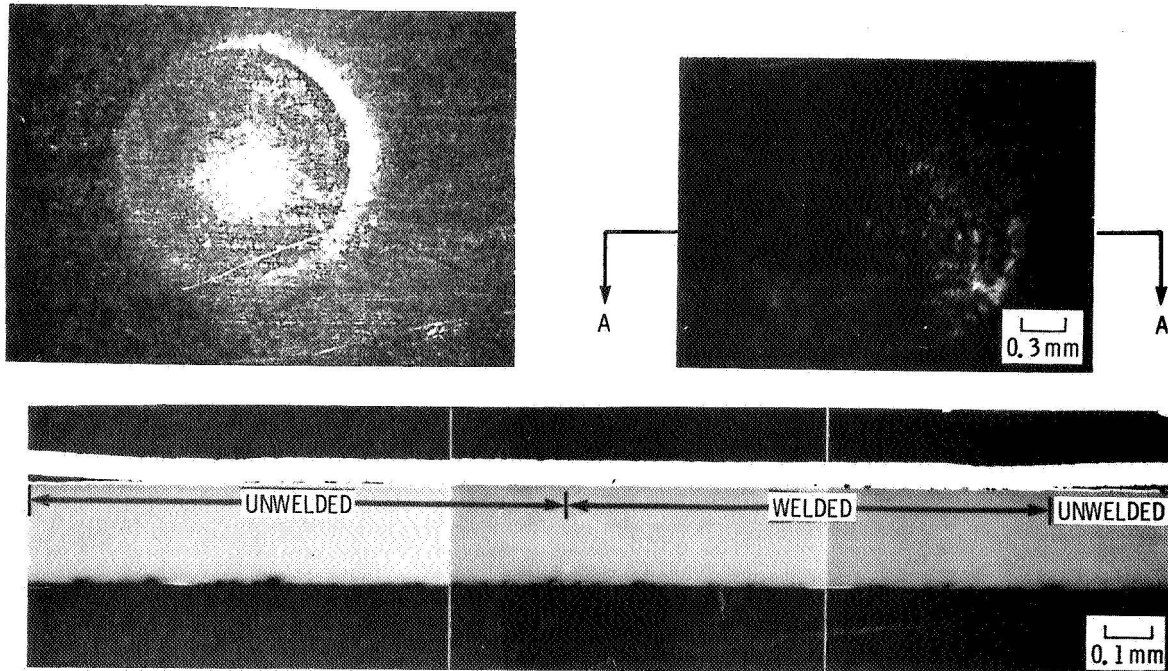
Figure 2. - Application of the scanning laser acoustic microscope for nondestructive evaluation of solar interconnect welds.



(a) Partial imprint on tab surface.
(b) Acoustic micrograph of weld zone.
(c) Nugget size revealed by removal of unwelded portion of tab.
(d) Photomicrograph of cross section A-A through middle of weld zone.
Figure 3. - Results of destructive and nondestructive analysis of Cu-Ag parallel-gap weld.



(a) Complete electrode imprint of tab surface.
 (b) Acoustic micrograph on nearly complete weld.
 (c) Photomicrograph of cross section A-A through middle of weld zone.
 Figure 4. - Results of destructive and nondestructive analysis of Ag-Ag annular-gap weld zone.



(a) Complete electrode imprint of tab surface.
 (b) Acoustic micrograph on nearly complete weld.
 (c) Photomicrograph of cross section A-A through middle of weld zone.
 Figure 5. - Results of destructive and nondestructive analysis of Ag-Ag annular-gap weld zone.

SILICON RESEARCH AND TECHNOLOGY

A. Meulenberg
COMSAT Laboratories
Clarksburg, Maryland

The mood of the silicon R&T Workshop was not one of optimism this year in contrast to that of the 1980 workshop. The cause(s) of this depression may have been: (1) the inability of the silicon community to fulfill the optimism of the last meeting which foresaw an 18 percent silicon cell; (2) the present emphasis on increased radiation hardening [e.g., 15 percent efficiency end-of-life (EOL) after $10^{15}/\text{cm}^2$ 1 MeV electrons] which did not seem feasible; or (3) the pressure from GaAs work with its potential for higher BOL and EOL power output.

In spite of the failure to date to achieve an 18 percent efficient silicon solar cell (AMO at 25° C), there are presently indications that the goal is approachable. The best results are open circuit voltages in excess of 690 mV in an MINP structure. Other work has pointed to surface recombination velocity (SRV) as the limiting factor (in diffused cells) and possible ways of bypassing this problem. Evidence that indicates a reduction in the predicted bandgap narrowing (resulting from heavy doping) and an increase in the Auger lifetime in heavily doped silicon is also encouraging for further improvements in diffused junction silicon solar cells.

Optimism for success in overcoming the present problems, without immediately encountering further problems in an already highly optimized device, was muted. However, since major voltage gains were a result of new technology (for the diffused silicon group), infusion from other fields might make another major improvement. Techniques borrowed from other solid state devices could be keys to a further increase in silicon solar cell efficiency. Such improvements could complement or supplement the boost in voltage achieved by the MINP cell which is an outgrowth of MIS technology. Such modified or hybrid silicon cells could provide the benefits of silicon technology with much higher initial output. Again, enthusiasm for such improvements was dampened by the recognition that perhaps none of these improvements would survive a radiation environment. Only after we were reminded that many satellites do not fly in the radiation belts and others need more power early in a mission was the cloud over BOL efficiency improvements lifted somewhat.

Hybrid structures using GaP, ASi (amorphous silicon) or some other such wide bandgap semiconductor on the silicon surfaces could provide a "window" to lower the SRV for both the front and the back of a silicon cell. This could overcome the problems observed in forming an effective p^+ back contact on 0.1 Ω -cm material. The use of electrostatic bonding and perhaps ion implantation into the cover glass was proposed as a possible way of forming an MINP cell which is less sensitive to radiation than presently predicted.

Other areas of potential cell improvement included: (1) Ingot material modification, where the Air Force program for altered doping (Ga vs. B), ultrahigh purity FZ, and cold crucible techniques were mentioned; (2) processing changes, to take advantage of surface gettering and to prevent defect generation; (3) counter doping, the introduction of internal getters or compensation for radiation damage; and (4) use of n-type rather than p-type substrates and/or processing modifications have been shown to improve BOL performance. The material modification or counter doping is expected to improve EOL performance, but no encouraging data are yet available.

Some useful tools in studying SRV of emitter surfaces have been tried or suggested. Electrostatic charge applied to the AR coating of a completed cell is perhaps the simplest means of testing the effectiveness of surface passivation and/or n+ (or p+) surface layers. More quantitative methods would include special structures which can use C-V techniques on heavily doped surfaces and voltage applied to water drops on isolated surface areas. An idea that might have interest as a test structure or as a future solar cell would be an FET cell, where the gate would be a thin tin oxide conductive layer for application of voltage between the grids. An integrated circuit cell could provide self-biasing for this structure which could improve radiation hardening over a trapped charge structure.

A final question addressed the user's preference of a commercially produced 20 percent GaAs cell vs. a commercially produced 18 percent Si cell, assuming equal costs and weight. The most important answer to this question was a sobering declaration that, despite obvious advantages of the GaAs cells, the most important difference would be flight experience and many inferior systems fly and will continue to fly until requirements force a change.

A short congress of the Silicon R&T, the Radiation Damage, and the Blanket Technology Workshops was most useful in emphasizing the basic conservatism of project offices in general and their reluctance to change unless forced to do so. Nevertheless, diversity in cell characteristics was encouraged; particularly if sufficient test or flight data become available to allow clear and comfortable choices to be made for specific missions.

The participants in the Silicon R&T Workshop were

Mike Giuliano	Solarex
Bob Nasby	Sandia Labs
Richard J. Schwartz	Purdue Univ.
Peter Iles	ASEC
Stan Solomon	Spire
Steve Tobin	Spire
Dick Statler	NRL
Mark Spitzer	Spire
Paul Stella	JPL
Dan Meier	Westinghouse
Ed Gaddy	GSFC
M. Wolf	Univ. of Pa.
Darryl Peterson	Lockheed
Paul Dillard	Lockheed
Bernie Sater	NASA LeRC
Vic Weizer	NASA LeRC
Chandra Goradia	Cleveland State Univ.
Michael Piszczor	CSU
Peter J. Drevinsky	RADC/ESR
Hans Rauschenbach	TRW
L. Perkes	NASA LeRC
J. Minahan	Spectrolab
T. Trumble	AFWAL WPAFB
N. Mardesich	Spectrolab
A. Meulenber	COMSAT Labs

ADVANCED DEVICES

Peter Bordin
Varian Associates
Palo Alto, California

The working group on Advanced Devices addressed five questions:

1. Has sufficient progress been made to warrant confidence that the 30 percent efficiency at 100x and 80° C goal can be achieved? If so, what are the most promising approaches; if not, how should the program be altered?
2. What approaches seem likely to achieve efficiency beyond 30 percent? What barrier problems ought to be attacked?
3. What cascade cell manufacturing problems do you envision?
4. What approaches are most likely to succeed for interconnecting a cascade cell stack?
5. How can we overcome the requirement for lattice constant matching in monolithic cascade cells? Is the direct bandgap requirement too stringent?

The working group obtained the following responses to these questions:

1. Has sufficient progress been made toward the 30 percent goal?

In general, substantial progress has been made and there is no reason to change the goal at this time. The metal interconnected cascade cell reported at this conference demonstrated considerable improvement in both cell area and efficiency over the state-of-the-art 1 year ago. Progress is being made in both materials and processes required to achieve the goal.

The question of minimum efficiency was also addressed. For a new technology to be accepted, it must show some advantage over the existing technology. Cascade cells should exhibit about 3 percentage points of efficiency above that of GaAs to justify their consideration as a replacement, with all else being equal.

As cascade cells become a proven technology, questions about their application need to be addressed. Among these, three emerged as most important:

(1) Radiation effects need to be considered, especially in series connected cascades, where degradation in one cell's short circuit current affects of the stack's short circuit current.

(2) Laboratory evaluation procedures and standards must be developed. In many cases, these cells will require new test procedures.

(3) To reach the 30 percent goal, we will use concentration. More work is needed to evaluate what concentrator designs are most appropriate for high efficiency cascade cells. Specifically, what concentration and concentrator design are appropriate for various potential missions?

2. What approaches are likely to exceed 30 percent efficiency, and what barrier problems must be addressed

The main barrier problem with existing technology is the photovoltaic effect itself, and higher efficiency technologies probably will not be photovoltaic, at least as we see it today. We really do not know what these future technologies are. Use of surface plasmon effects was one idea reported at this meeting. For very high power, in the megawatt range, nuclear might be preferable, assuming political and safety problems do not stand in the way.

This question is very difficult for a group of experts in photovoltaics to address. We recommend that future SPRAT conferences invite input from nonphotovoltaic technologies to encourage us to think innovatively.

3. What cascade cell manufacturing problems are envisioned

This question was somewhat difficult to address, because the devices to manufacture have not themselves been defined. Manufacturing engineers are very innovative and have tackled difficult semiconductor devices in the past (such as 64K RAMs), so that concern about manufacturability is not warranted at this time.

Some discussion centered on epitaxial growth technology. OM-VPE and LPE have been used, and both are funded technologies. OM-VPE has been used to make the best working device to date and is a versatile and reproducible technique. LPE has been used to make large area, multilayer devices in the laser and LED industries and is also being used to make good GaAs solar cells. As a general statement, if the attractive cascade cell has more than five or six layers, some or all of which require close thickness control, then OM-VPE will be the preferred technology.

4. What approaches seem most likely to succeed for interconnecting a cascade cell stack

Five techniques for making cascade cell stacks were mentioned, two of which form series interconnects and three of which leave open the option of either forming a series interconnect or addressing cells individually. The latter might be worth a further consideration if the reduced process yields or lessens radiation hardness. The techniques are

MIC² (metal Interconnect). - This has been used to make the best monolithic cascade cells to date. It is also a useful diagnostic tool since it allows addressing of individual cells. This feature allows its use in a nonseries-connected configuration. Its drawback is added processing.

Tunnel junction. - This has been demonstrated with LPE growth over small areas. Because the cells do not require extra processing after growth, it would be attractive, but only if reproducible low resistance, large area tunnel junctions are feasible. As the 30 percent cell will require three junctions, and tunnel junctions are hard to achieve in high gap materials, it is possible that a future cell will be a MIC²-tunnel junction hybrid, with the top interconnect MIC² and the bottom tunnel junction.

Ge interconnect layer. - Possibly, a thin layer of Ge placed between the two cells will provide a good shorting junction. This is especially attractive in the GaAs-AlGaAs system, where Ge is lattice matched.

Mechanically bonded stack. - It is possible to mechanically bond two individual cells together. Such a configuration provides the option for individual addressing of cells. This could circumvent various interconnect and materials growth problems.

Spectrum splitting using, for example, dichroic filters. - This eliminates the interconnect problems at the price of a more complex mechanical system, and the cost of additional components such as the filter.

All of these approaches are being examined, and it is not possible to recommend a preferred one at this time.

5. How can we overcome the requirement for lattice constant matching in monolithic cascade cells? Is the direct bandgap requirement too stringent?

The lattice matching requirement has evolved from many years of experience in crystal growth. While it is a general rule, there are some exceptions, such as Ge on Si and possibly GaAsP on GaAs. Thus, while lattice matching is important to bear in mind, processes and cell designs should not be rejected a priori because they violate lattice matching requirements. Spectrum splitting and mechanically stacked structures do not require lattice matching.

Indirect gap materials are usable for both the top and bottom cells. Because the top cell is grown epitaxially, it must be relatively thin. One way to use an

indirect gap material there is to use the spill-through current match technique, in which above-gap light passes through to the bottom cell, bearing in mind that even indirect materials collect blue light in a relatively short length. The bottom cell can use the bulk of the substrate, and can be an indirect material as well.

In summary the group's observations and recommendations were as follows:

1. Cascade cell development is progressing toward the 30 percent goal. A minimum efficiency advantage of 3 percent is required to ensure use in competition with the next best existing technology, all else being equal. Radiation effects and concentrator designs need to be considered more carefully. Laboratory procedures and standards must be developed.

2. We must encourage innovation to identify next generation high efficiency technologies. Future SPRAT conferences should include inputs from nonphotovoltaic technologies to encourage this innovative thinking.

3. Manufacturing problems are not envisioned at this time, because the cascade cell is not well defined. LPE and OM-VPE epitaxial technologies are being developed. If the best cell requires a relatively complex epitaxial structure, OM-VPE will probably be preferred.

4. A number of interconnect approaches are possible and are being investigated. Those that do not require series connection may be useful if the series connection significantly reduces process yield or radiation hardness.

5. Lattice constant matching is not always required. Indirect gap materials may be used for both the top and bottom cells.

Working Group Participants

Lynn Anderson	NASA Lewis
Bruce Anspaugh	JPL
Allen Barnett	University of Delaware
Peter Borden	Varian Associates
J.M. Borrego	Rensselaer Polytechnic Institute
David Brinker	NASA Lewis
Lee A. Cole	SERI
Henry Curtis	NASA Lewis
John Fan	MIT Lincoln Labs
Dennis Flood	NASA HQ
Lan Hsu	Rockwell International
Jim Hutchby	Research Triangle Institute
G.S. Kamath	Hughes Research Labs
R. Knechtli	Hughes Research Labs
Sheng S. Li	University of Florida
Robert Loo	Hughes Research Labs
Bob MacKunas	Research Triangle Institute
Jim McNeely	M/A-Com Laser Diode
Shing Mao	UTL Corporation
Ken Masloski	Air Force AFWAL/POOC
Pat Rahilly	AFWAL/POOC/WPAFB
D.A. Vance	Lockheed Palo Alto Research Lab
Irv Weinberg	NASA Lewis
Howard Weiner	Aerospace Corporation
John Woolam	University of Nebraska
Y.C. Milton Yeh	JPL

GaAs SOLAR CELLS

E.J. Conway
NASA Langley Research Center
Hampton, Virginia

The GaAs Solar Cell Workshop considered a range of topics from "high efficiency" to "novel ideas." A majority of the 17 participants were interested, directly or indirectly, in the first GaAs production cell. This produced a lively discussion on the identification and solution of near-term problems.

The major thrusts proposed for GaAs were increased efficiency and improved radiation damage data. Current laboratory production cells consistently achieve 16 percent AMO one-Sun efficiency. The user community wants 18-percent efficient cells as soon as possible, and such a goal is thought to be achievable in 2 years with sufficient research funds. A 20-percent research cell is considered the efficiency limit with current technology, and such a cell seems realizable in approximately 4 years. Future efficiency improvements await improved substrates and materials. For still higher efficiencies, concentrator cells and multijunction cells are proposed as near-term directions.

When the efficiency is driven up by changes of cell structure, measurement techniques become more unreliable. The Workshop participants called for renewed, low-cost flight calibration of cells. Such a service through Lewis Research Center is terminating. Replacement options include another aircraft, balloon flights, or the shuttle. (A decision has been made by Lewis since the meeting to provide another aircraft for high-altitude calibration of solar cells.)

Radiation damage is the central problem impeding application of GaAs solar cells. Data sufficient to define its relatively unknown radiation behavior cannot be achieved only in the laboratory (with reasonable funds and time). Space flight data are needed (and may be obtained in planned DoD missions). The group recommended initiation of a continuing program to (1) characterize the practical degradation of production cells in space and in the laboratory; (2) understand the degradation in order to improve cell stability; and (3) promote interaction between the application community and the research community through damage modeling.

Annealing of radiation damage was considered a separate and more long range problem. Cell annealing would require a more complex or specialized array, which is well beyond current concepts. However, advanced concepts for annealing, such as current annealing and elevated temperature operation within a concentrator, were discussed. The application of annealing is expected to depend on whether annealing becomes mission enabling.

Thin cells are those which offer low cost, low weight, and high specific power. The long-term advantages of thin cell research to advance cell technology were recognized. A multibandgap cell is similar in general concept to

several thin cells in optical series. Because heat conduction can be a critical problem for concentrator applications, thin cells may have special importance for high intensity uses. Also, if thin cells do not require as much total growth time (substrate plus active layers) as current GaAs cells, then shortened manufacturing time may translate into reduced cost. However, near-term application for a thin cell is limited by the mass of radiation covers, contact and cable size, and array weight and cost. The Workshop participants proposed that current cell technology be developed to the point of diminishing returns and that an effective concept for employing thin cells be developed before initiating development of very thin GaAs cells.

Concentrator cells appear potentially useful. Their development is progressing at a rate that permits practical application of GaAs concentrator cells. The applications offer cost reduction and radiation resistance. However, concentrators may pose special thermal management problems.

The price of GaAs cells is expected to decline sharply when an Air Force Manufacturing Technology program achieves its production goals. Two factors could further reduce the price of GaAs solar cells: (1) a volume of cells reaching 1 MWe/year; and (2) reduced price of substrates, which currently cost approximately \$30 per square inch.

Among the new concepts endorsed by this Workshop are back surface fields and other built-in fields and materials tailoring for maximum efficiency (especially $Al_xGa_{1-x}As$).

In summary, the major recommendations are

1. Achieve 18-percent production cell and a 20-percent research cell (2 to 4 years).
2. Begin a continuous radiation damage program involving practical assessment of damage, understanding of damage mechanisms and modeling.

GaAs Workshop Participants

Edmund J. Conway	NASA Langley Research Center
Y. C. Milton Yeh	NASA Jet Propulsion Laboratory
J. B. McNeely	M/A - Com Laser Diode
G. S. Kamath	HRL, Malibu, California
J. M. Borrego	Rensselaer Polytechnic Institute
Peter Iles	ASEC
Terry Trumble	AFWAL
Henry Curtis	NASA Lewis Research Center
Darryl Peterson	Lockheed
George Mazanis	NASA Lewis Research Center
David Brinker	NASA Lewis Research Center
R. T. Chen	Rockwell
Lee A. Cole	SERI
S. K. Ghandhi	Rensselaer Polytechnic Institute
Steve Tobin	SPIRE
Peter Borden	Varian Associates
Shing Mao	UTL Corporation

RADIATION DAMAGE

I. Weinberg
NASA Lewis Research Center
Cleveland, Ohio

The radiation damage workshop considered a variety of topics among which were the need for equivalent electron fluences in gallium arsenide, the possibility of 15 percent end-of-life efficiencies for silicon, increasing radiation resistance in gallium arsenide, annealing of radiation damage and the need for radiation damage studies in cascade cells.

The workshop members agreed that a high priority should be assigned to obtaining equivalent electron fluences for gallium arsenide cells. It was suggested that 1 MeV would be a reasonable electron energy for this purpose. Special care should be given to proton irradiations particularly for energies below 1 MeV. In addition, omnidirectional rather than normal incidence protons should be used. It was also agreed that there was a need for obtaining damage coefficients in gallium arsenide. In silicon, there is a requirement for additional flight data, especially in proton dominated orbits. These data are needed to further check the accuracy of the 1 MeV equivalence fluences.

Attainment of 15 percent end-of-life efficiencies, after 10 years in geosynchronous orbit, was judged to be a practical goal for silicon. This is conditioned on attainment of BOL efficiencies of 16 to 18 percent. Several cell types were suggested as possible candidates, provided the required efficiencies could be attained. Configurations suggested were the structure proposed by Martin Wolf at the present conference, gallium-doped thin drift field cells, gallium-doped vertical junction cells, if used with heavy backshielding, and 0.1 Ω -cm cells if annealable. Defect concentrations should be kept low in the starting silicon.

Several approaches show promise for attaining increased radiation resistance in gallium arsenide solar cells. The major radiation induced defect, located at midgap, is vacancy and stoichiometry related. Processing to minimize the concentration of this defect in the starting material and irradiated cell would be desirable. Decreased junction depths, especially in the present AlGaAs/GaAs heterojunction cells, together with use of better quality substrates should lead to increased radiation resistance. Radiation damage research using techniques such as DLTS should be correlated with the processing and fabrication procedures and used as a guide to further improvements.

Reduction of annealing temperatures below 200°C together with decreased annealing times are desirable goals for both silicon and gallium arsenide cells. The efficacy of periodic versus continuous annealing was considered, and it was concluded that additional data are needed to decide between the two techniques. Some concern was expressed concerning possible methods to accomplish annealing in space. Although no method was specified, several members of the workshop felt that accomplishing this in practice would present highly undesirable problems in spacecraft design and operation. However, it was pointed out that pulsed current annealing had accomplished defect reduction and performance recovery in gallium arsenide cells and that this technique, if used, would present a minimum of problems to spacecraft

design and operation. At any rate, the question of how to accomplish annealing in space deserves further consideration.

In addition to damage removal, it was suggested that studies of annealing kinetics could be pursued as a technique to characterize radiation defects. This would be especially important for gallium arsenide where defect identification is difficult and minimal. Radiation damage and annealing studies, in cascade cells, were considered but assigned a low priority. These studies, if pursued should at present be used to redirect materials related research in the cascade cell area.

In summary: The need for 1-MeV damage equivalent fluences in gallium arsenide was emphasized. End-of-life efficiencies of 15 percent after 10 years in geosynchronous orbit were considered attainable for silicon, and suggestions were offered to attain this goal. Radiation resistance in gallium arsenide can be increased by improvements in processing and fabrication, which should be correlated with the results of defect studies. Annealing studies should continue in both silicon and gallium arsenide. These should have the twofold goal of reducing annealing temperatures and aiding in defect characterization especially in gallium arsenide. Finally, consideration should be given to devising a simple method for achieving annealing in space.

RADIATION DAMAGE WORKSHOP PARTICIPANTS

Irving Weinberg	NASA Lewis
Bruce Anspaugh	Jet Propulsion Laboratory
Stan Solomon	Spire
Mark Spitzer	Spire
Marty Gandel	Lockheed
Harry Gatos	MIT
Pat Rahilly	AFWAL
Vic Weizer	NASA Lewis
Cliff Swartz	NASA Lewis
Richard Schwartz	Purdue University
Robert Loo	Hughes
Sheng San Li	University of Florida
A. Meulenberg	COMSAT Labs
P. J. Drevinsky	RADC/ESR-Hanscom Field
R. D. Nasby	Sandia
R. L. Statler	NRL
Henry Brandhorst	NASA Lewis
Russ Hart	NASA Lewis
Hans Rauschenbach	TRW

BLANKET TECHNOLOGY

John Scott-Monck
Jet Propulsion Laboratory
California Institute of Technology
Pasadena, California

The workshop participants felt that the questions presented for their consideration were too amorphous, with respect to definition of terms, to address quantitatively. There was general agreement that the subject of "welding" or "joining" was a significant issue. It was concluded that systems requirements would force a reassessment of the conventional approach to interconnecting cells into blanket or array modules. Defense applications (hardening) were identified as the key requirement that would force a movement away from the standard method (solder) of forming array circuits. The panel also agreed that requirements associated with the impending NASA Space Station and in-bound missions would lead to alternative interconnecting approaches. It was concluded that the diverse requirements of future space missions (high temperature and extended thermal cycling) might not be met by one approach, such as parallel-gap resistance welding. The panel suggested that other options such as high temperature solders and brazing be considered for the various mission requirements that were anticipated.

The panel agreed that blanket technology was potentially suitable for in-orbit annealing to temperatures of 200°C provided that conventional soldered connecting techniques were replaced by "welding". Some concern was expressed about the ability of adhesives to retain their optical properties after this type of thermal excursion. The members stated that annealing would require new types of qualification testing since most thermal cycling failures occurred at elevated temperatures.

Approaches to providing 200°C in-orbit do exist. However, the panel strongly recommended that trade-offs must be performed between the added weight, cost and risk associated with blanket annealing and the end-of-life (EOL) advantages gained. The consensus was that the method of providing the required temperature must be simple (low risk) or annealing will not be considered by mission planners. The panel stated that the annealing conditions (continuous versus periodic) must be more adequately defined before a complete answer to the subject of annealing could be provided.

The issue of GaAs blanket technology was addressed by the panel. It was agreed that the results of the WPAFB sponsored GaAs Solar Cell Manufacturing Technology (MANTECH) program, aimed at demonstrating production capability, would be the determining factor in deciding whether to pursue GaAs blanket development. The need for reliable, pertinent information on the behavior of GaAs solar cells under simulated space operating conditions was deemed critical in order to provide planners with sufficient data to determine the merits of employing GaAs blankets and arrays for future missions. Until significant quantities of well characterized GaAs solar cells are available, no serious attempt to initiate development of GaAs blanket technology will likely occur.

The question of future progress in the development of high performance blankets and arrays prompted a lively discussion focused on what properties constitute "high performance" and what was the present status of blanket and array performance with respect to specific power (W/kg). This discussion led to the conclusion that mission system's level requirements usually forced the utilization of technically "compromised" or "detuned" blankets and arrays, with less than optimum specific power, for mission applications.

The panel suggested that the Space Telescope array which is 20 W/kg beginning-of-life (BOL) is most representative of current state-of-the-art array technology. It should be noted that the Space Telescope blanket specific power is approximately half of what is forecasted for the "SEP" blanket (~55 vs 105 W/kg). It was concluded that blanket components, and their associated mass contributions, can vary dramatically depending on the design approach provided to satisfy system requirements.

To further illustrate this conclusion, it was observed that many future mission requirements, especially those involving defense and manned applications, will demand that arrays and blankets be designed for "toughness" and survivability, conditions which will lead to a reduction in specific power. It was suggested that the technologists need to consider such "realistic" mission requirements in their approaches to achieving "high performance" blankets and arrays.

Having established the fact that beginning and end-of-life specific power were not easy subjects to define, the members addressed the question of future advancements in this area, providing both assessments and goals. It was the general opinion that further progress would be evolutionary (conservative) in order to satisfy mission reliability concerns. Thus it was anticipated that the next step in blanket progress would incorporate 100 μm silicon solar cells and covers to replace the current assemblies (200 μm cells, 150 μm covers). It was also agreed that flexible substrates could probably be reduced to ~ 75 μm thickness.

The group anticipated that by 1990, blankets with a specific power of approximately 100 W/kg would be used for space missions, and during the 1990s this figure would probably increase to 150 W/kg, depending on mission requirements. It was pointed out that the shortfall in Shuttle launch capability could very likely demand blankets with even higher BOL specific power. It was therefore suggested that blanket goals expressed in terms of kg/m^2 and W/kg be established. These goals (see Table 1) are much higher than what the group projected for space flight use. This was done because of the realization that system's requirements inevitably lead to a reduction in specific power. There was consensus that no realistic forecast of array specific power, either BOL or EOL, could be made without information on the spacecraft and its associated mission requirements.

A special joint session was held with the Silicon Research and Technology workshop group. This meeting was extremely productive since it exposed the researchers to the complex decision making process that must be performed by the blanket technologists, and made the technologists aware of the frustrations associated with developing advancements that do not gain acceptance for flight use. A discussion followed on the subject of what factors determine mission acceptance of new technology. It should be mentioned at this point that the blanket workshop members feel strongly that this type of interaction between researchers and technologists is extremely beneficial and recommended that this type of combined workshop become a feature of any subsequent SPRAT Conference, since this is the only meeting where the entire spectrum of photovoltaic technology is represented.

Suggestions were made on how to increase the chances that research innovations will find acceptance for space flight use. It was agreed that a key interface between the two disciplines was the device manufacturers who must demonstrate that research derived advancements can meet the requirements of a given subsystem mission requirement. Researchers must be aware that the information needed to determine flight acceptance covers a wide area that goes beyond the more obvious figures of merit such as efficiency and resistance to the space radiation environment.

A schematic illustrating the relationship between mission requirements, technology selection and the ongoing effort in developing advanced photovoltaic technology is presented in Figure 1. The mission generates a series of performance requirements based on the expected environment and an estimate of technology readiness. As these requirements filter down to the array subsystem, the element of risk becomes a dominant factor and the constraints placed on the array increase due to the requirements of each major system for subsystem support. This results in technology compromises.

Assessment of risk is largely determined by the existing data base that is available for any blanket or array component being considered for use. This approach often precludes "better" components from being implemented, since the trade-off between risk and a less than optimum subsystem usually results in the selection of an engineering compromise that accomodates the component which has the larger supporting base of statistically significant performance data. Therefore every effort must be made to assure that advanced technology is tested thoroughly and transferred to the device manufacturers in a timely fashion.

It should be pointed out that although NASA and DOD provide most of the support for space photovoltaic research, not enough attention is devoted to assuring that a proper transfer of this technology is made to the manufacturers. This topic might make a very interesting subject for future SPRAT Conference workshops to address.

Workshop Participants

Cosmo Baraona - NASA LeRC
Paul Dillard - LMSC
Ed Gaddy - NASA GSFC
John Hedgepeth - Astro Research Corp.
Stan Klima - NASA LeRC
Ron Knechtli - Hughes Research Labs
Nick Mardesich - Spectrolab, Inc.
Ken Masloski - USAF

Tom Moore - NASA LeRC
Bob Patterson - TRW
Bernie Sater - NASA LeRC
John Scott-Monck - JPL
Paul Stella - JPL
Dave Vance - LMSC
Howard Weiner - Aerospace Corp.
John Woollam - Univ. Nebraska

Table 1

Goals for Blanket Technology

Year	Mass Per Unit Area	Specific Power (BOL)*
1982	1.05 kg/m ²	105 W/kg
1985	0.65 kg/m ²	170 W/kg
1995	0.50 kg/m ²	280 W/kg

* EOL cannot be stated without knowledge of specific mission environment

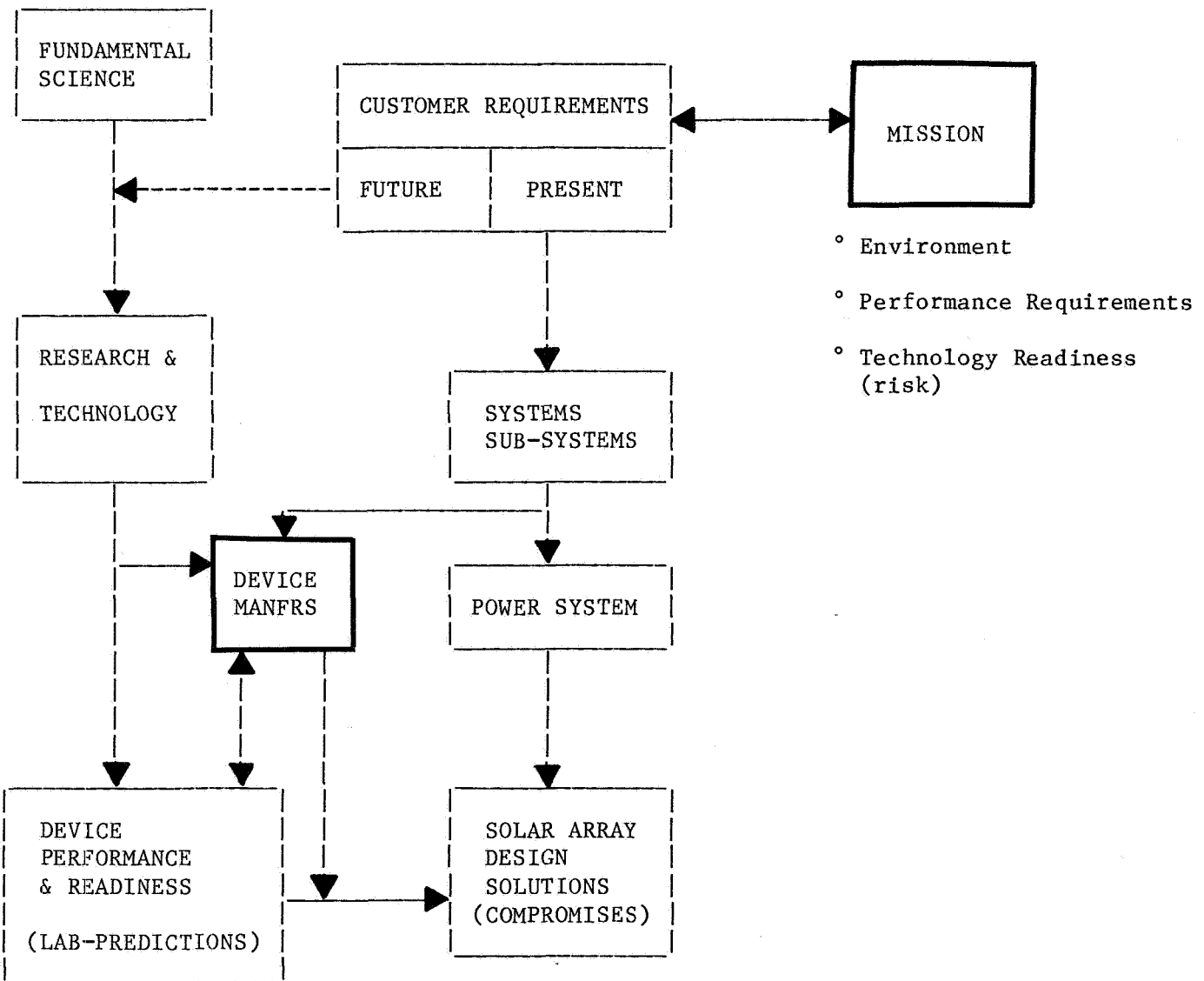


Figure 1. Technology Relationships for Mission Applications

1. Report No. NASA CP-2256	2. Government Accession No.	3. Recipient's Catalog No.	
4. Title and Subtitle SPACE PHOTOVOLTAIC RESEARCH AND TECHNOLOGY - 1982 High Efficiency, Radiation Damage, and Blanket Technology		5. Report Date	
		6. Performing Organization Code 506-55-42	
7. Author(s)		8. Performing Organization Report No. E-1303	
		10. Work Unit No.	
9. Performing Organization Name and Address National Aeronautics and Space Administration Lewis Research Center Cleveland, Ohio 44135		11. Contract or Grant No.	
		13. Type of Report and Period Covered Conference Publication	
12. Sponsoring Agency Name and Address National Aeronautics and Space Administration Washington, D. C. 20545		14. Sponsoring Agency Code	
15. Supplementary Notes			
16. Abstract <p>This three-day conference, fifth in a series that began in 1974, was held at the NASA Lewis Research Center on April 20-22, 1982. The conference provided a forum for the discussion of space photovoltaic systems, their research status, and program goals. Papers were presented and workshops were held in a variety of technology areas, including silicon research and technology, gallium arsenide solar cells, advanced devices blanket technology, and radiation damage.</p>			
17. Key Words (Suggested by Author(s)) Photovoltaic cells Solar cells Solar arrays		18. Distribution Statement Unclassified - unlimited STAR Category 44	
19. Security Classif. (of this report) Unclassified	20. Security Classif. (of this page) Unclassified	21. No. of Pages 280	22. Price* A13

* For sale by the National Technical Information Service, Springfield, Virginia 22161